EARLY-AGE GGBS CONCRETE HYDRATION TEMPERATURE DEVELOPMENT AND MODELLING

A thesis submitted in accordance with the requirements of

Brunel University London for the degree of Doctor of Philosophy

By

YAOWEN TAN

July 2024

ABSTRACT

Early-age hydration temperature development in concrete plays a crucial role in determining its structural performance and long-term durability. Excessive temperature rise and thermal gradients can induce stresses, leading to early-age cracking, particularly in mass concrete and large-span structures. The incorporation of Ground Granulated Blast Furnace Slag (GGBS) as a supplementary cementitious material helps mitigate these risks due to its lower heat of hydration compared to CEM I. However, knowledge gaps remain regarding the effects of variable ambient temperatures, the influence of coarse aggregates, and the applicability of existing hydration models developed for CEM I-only concrete. This study addresses these gaps through experimental investigations and numerical modelling.

The experimental program involved semi-adiabatic and isothermal calorimetry tests. Semi-adiabatic calorimetry tests on concrete specimens with varying GGBS replacement levels (0%–50%) assessed the impact of GGBS on hydration temperature development under uncontrolled conditions. Results demonstrated that increasing GGBS content reduced peak hydration temperatures and prolonged the induction period, confirming its thermal mitigation effect. Isothermal calorimetry tests were conducted on micro-concrete and equivalent mortar specimens at curing temperatures of 20, 30, 40, and 50°C to analyse hydration heat evolution. Higher curing temperatures accelerated early hydration but did not proportionally enhance long-term cumulative hydration heat. The presence of coarse aggregates slightly delayed hydration kinetics and increased cumulative hydration heat at later stages, though the observed differences were minimal, making it unclear whether they were due to experimental variability or an actual material effect.

A finite element model (FEM) was developed using COMSOL Multiphysics 6.1 to predict the early-age temperature development of in-situ concrete. The heat source for the model was derived from isothermal calorimetry data and adjusted using an Arrhenius-based equivalent age approach to reflect actual hydration heat evolution in concrete. The FEM was validated against semi-adiabatic calorimetry test results. The modelling results underscored the necessity of incorporating real-time ambient temperature variations, as constant-temperature boundary conditions led to discrepancies in predicted temperature profiles. Additionally, models using equivalent mortar hydration heat data overestimated peak temperatures, highlighting the importance of considering coarse aggregate effects.

The study also evaluated the applicability of the Three-Parameter Equation (TPE) hydration heat model, originally developed for CEM I, in predicting temperature development in GGBS-containing concrete. While the model provided reasonable accuracy, it consistently overestimated peak hydration temperatures for high-GGBS content mixes, likely due to its assumption of immediate GGBS hydration rather than

its delayed activation. Refining hydration models to incorporate the two-stage reaction mechanism of GGBS could improve predictive accuracy.

Although this research enhances understanding of early-age concrete temperature development, certain limitations remain. The hydration heat differences between micro-concrete and equivalent mortar were small, making it difficult to determine whether the effect of coarse aggregates on hydration kinetics was genuine or within the range of experimental error. More advanced experimental techniques are required to clarify this issue. Additionally, the FEM was validated under laboratory-controlled conditions, necessitating future field-scale validation to account for real-world thermal interactions.

This study enhances the predictive capabilities of hydration temperature models by integrating experimental data with numerical simulations. The findings emphasize the importance of precise boundary condition inputs, improved hydration models for blended cement, and the necessity of incorporating micro-concrete data for accurate temperature predictions. Future research should focus on refining hydration models for GGBS-containing concrete, conducting field-scale validations, and integrating thermal stress analysis to further mitigate early-age cracking risks in concrete structures.

ACKNOWLEDGMENTS

I would like to express my sincere gratitude to my supervisors, Dr. K. Tang and Prof. X. Zhou, whose expertise, patience, and encouragement were essential in guiding me through my research. Your insightful feedback and unwavering support have been crucial in the completion of this thesis.

I also wish to thank the technicians at the Brunel University Civil Engineering Laboratory, Mr. C. Morrison, Mr. A. Smith, and Mrs. R. Liu, as well as the technician at the Brunel University Experimental Techniques Centre, Dr. S. Haghani, for their assistance and guidance with my experimental work. Additionally, I am grateful to Mr. R. Thomas from the Brunel IT Centre for his help with the necessary engineering software setup and related script development. I also extend my thanks to my colleague, Mr. B. Wong, for his assistance during the experimental process.

I am grateful to Hanson UK for providing free TEES SF REGEN GGBS, which was vital throughout the entire process of this research.

My heartfelt thanks go to my parents, Mr. H. Tan and Mrs. X. Dong, for their financial support, spiritual encouragement, and unconditional love and support. Your patience and understanding have been my anchor during the most challenging times of this journey.

Finally, I would like to express my sincere appreciation to all my family and friends for their prayers, care, and understanding during my studies. Your support has been invaluable.

TABLE OF CONTENTS

CHAPTER 1 INTRODUCTION

1.1 Background

Early-age temperature development in concrete is a critical factor influencing the structural integrity and safety of concrete structures. During the initial stages of hydration, the exothermic reactions of cementitious materials generate significant amounts of heat, leading to an increase in the internal temperature of the concrete. This temperature rise induces thermal expansion within the concrete matrix. As the temperature subsequently decreases, thermal contraction occurs. This thermal contraction can become problematic when it is restrained by adjacent structures or due to temperature gradients within the concrete itself. Such restraints result in the development of tensile stresses within the concrete. Since concrete at an early age has not yet fully developed its strength, particularly its tensile strength, these stresses can exceed the material's capacity, leading to early-age thermal cracking [1-3]. This type of cracking is especially concerning in mass concrete and long-span concrete structures, where the large volume and extensive surface area exacerbate temperature gradients and restraints. The occurrence of thermal cracking not only compromises the immediate structural integrity but also has long-term implications for durability, potentially allowing the ingress of deleterious substances that can accelerate deterioration processes such as reinforcement corrosion [4].

To mitigate the risks of early-age thermal cracking in concrete, various methods, including pre-cooling ingredients, using insulating formwork, and incorporating supplementary cementitious materials (SCMs) like Ground Granulated Blast-Furnace Slag (GGBS), have been employed in construction. GGBS is favoured for its lower hydration heat compared to ordinary Portland cement (CEM I), effectively reducing peak temperatures, and associated thermal cracking risks [1, 5, 6]. As a by-product of the iron and steel industry, GGBS not only recycles industrial waste but also enhances concrete's durability, permeability, and resistance to sulphate attack and alkali-silica reactions [7-9]. However, GGBS hydrates slower than CEM I, leading to lower early-age strength, which necessitates a careful mix of design and curing practices to ensure adequate early strength without compromising long-term benefits [1, 10, 11]. The sustainable integration of GGBS in concrete mix designs aligns with modern environmental goals by reducing CO_2 emissions from cement production [12, 13]. Despite slower early-age hydration, GGBS's benefits in reducing thermal cracking risk and enhancing durability justify its continued use and further research to optimize its application.

Accurately predicting early-age hydration temperature development in in-situ concrete is essential for designing effective mitigation measures. Finite Element Method (FEM) modelling offers a computational framework to simulate hydration heat generation, thermal properties of concrete, and environmental effects, enabling detailed analysis of

temperature distributions and gradients. Such models are indispensable for assessing the impact of factors like concrete composition, coarse aggregates, and ambient temperature variations on temperature development.

1.2 Research Gaps and Significance

Accurate prediction of early-age temperature development in concrete is crucial for ensuring structural integrity and preventing issues such as thermal cracking. Despite significant advancements in the field, several gaps and limitations persist in existing research, which this study aims to address.

First, current research often neglects the impact of coarse aggregates on the hydration heat and temperature development of concrete. Previous studies assumed that the hydration heat development in equivalent mortar samples could represent that of concrete [14-18]. However, this assumption has not been conclusively proven and could lead to discrepancies between experimental results and actual concrete behaviour. The presence of coarse aggregates influences the thermal properties and heat distribution within the concrete, and ignoring this effect may result in errors in both experimental observations and simulation outcomes.

Second, existing concrete temperature modelling studies frequently overlook the influence of fluctuating ambient temperatures on the temperature development of in-situ concrete. Current concrete temperature modelling studies employ constant temperature conditions [19-21] or sinusoidal wave equations [22] to simulate ambient temperature variations, they often do not fully capture the complex and dynamic nature of real-world environmental conditions. This limitation can lead to inaccurate predictions of concrete heat dissipation and temperature distribution, affecting the reliability of subsequent assessments of thermal stresses and potential cracking.

Third, the mathematical models currently used to describe the hydration heat development based on the equivalent age of concrete were originally developed for Ordinary Portland Cement (CEM I). The applicability of these models to CEM-GGBS blended mixes remains controversial [23, 24]. GGBS has a distinct hydration mechanism, characterised by a delayed reaction due to its reliance on the alkaline environment produced by the hydration of CEM I [1, 25, 26]. The hydration process of CEM-GGBS blended mixes has been reported not adequately captured by existing hydration models, potentially compromising the accuracy of temperature and strength predictions for GGBS-containing concrete.

This research addresses these gaps by emphasizing the importance of accurate and realistic heat source and boundary conditions in concrete temperature FEM modelling. The modelling results highlight the unignorable presence of variable ambient temperatures and the critical role of coarse aggregates in the hydration heat and temperature development of concrete, arguing against the substitution of mortar

hydration heat development for concrete. Additionally, the study suggests further investigation into the hydration mechanisms of CEM-GGBS blended mixes and the development of specialized mathematical models to better describe their hydration heat development. By tackling these issues, this research aims to provide more reliable temperature predictions for in-situ concrete containing GGBS, enhancing the safety and durability of concrete structures.

1.3 Research Aims and Objectives

1.3.1 Research Aims

This research aims to investigate the early-age hydration temperature development in Ground Granulated blast Furnace Slag (GGBS) concrete and improve the accuracy of predictive models for in-situ concrete temperature evolution. By addressing existing gaps in knowledge, such as the influence of coarse aggregates and variable environmental conditions, this study seeks to enhance the reliability of hydration heat simulations and contribute to better-informed structural design and construction practices.

1.3.2 Research Objectives

This research addresses key gaps in predicting early-age hydration temperature development in GGBS concrete as descripted in Section 2.6.4, focusing on the influence of environmental conditions, coarse aggregates, and hydration modelling limitations. The specific objectives are:

1. **Incorporate Variable Ambient Temperatures in FEM Modelling:**
   Develop a Finite Element Method (FEM) model that integrates fluctuating ambient temperatures to reflect real-world environmental conditions. This includes assessing their impact on hydration rates, heat dissipation, and temperature profiles in in-situ concrete.

2. **Validate the Influence of Coarse Aggregates on Hydration Heat:**
   Investigate whether hydration heat curves derived from mortar accurately represent those of concrete, particularly addressing the role of coarse aggregates. This validation ensures the reliability of hydration heat data as a thermal source for FEM simulations.

3. **Assess the Applicability of Hydration Models for GGBS-CEM Mixes:**
   Assess the accuracy and reliability of existing mathematical models, initially developed for CEM I, in predicting hydration heat development in GGBS-CEM blended mixtures, particularly for high GGBS content concrete.

1.4 Research Methodology

In response to the research objectives highlighted in Section 1.3, this section delves into the research methodology adopted for this study, encompassing both experimental approaches and simulation strategies. This methodology is meticulously designed to address the identified research gaps, enhancing the precision and reliability of predicting early-age hydration temperature evolution in in-situ concrete containing GGBS.

The research method contains two principal components: experimental works and numerical modelling. The experimental segment comprises an extensive series of semi-adiabatic and isothermal calorimetry tests. These tests are crucial for capturing the temperature development and heat release characteristics of GGBS concrete under varying curing temperature conditions. The gathered data not only underpin the subsequent development of concrete temperature models but are also instrumental in verifying the accuracy of these models. Upon completion of the experimental phase, the study progresses to advanced numerical simulations employing the Finite Element Method (FEM). These simulations aim to accurately replicate the temperature dynamics within in-situ GGBS concrete, factoring in the complexities of environmental influences, concrete mix designs, and the distinctive thermal properties imparted by GGBS.

The following research methodologies will be implemented:

1.4.1 Semi-Adiabatic Calorimetry for Concrete Temperature Development

The first research approach delineated in this thesis encompasses conducting semi-adiabatic calorimetry tests on concrete specimens to investigate the impact of substituting cement with GGBS at varying proportions (10%, 20%, 30%, 40%, and 50%) on the early-age hydration temperature evolution of in-situ concrete. Concrete specimens will be subjected to semi-adiabatic curing conditions, exposed directly to ambient environmental conditions rather than being placed within temperature-controlled curing chambers. This methodology is designed to emulate the typical heat dissipation mechanisms and boundary conditions of in-situ concrete as closely as possible, allowing the monitored concrete temperature development curves to fully reflect the impact of variable environmental temperatures. Continuous real-time monitoring of both concrete and ambient temperatures will be conducted using type-K thermocouples.

These experiments aim to investigate the impact of GGBS content on the early-age hydration temperature development of concrete. The findings will address the objective set out in Section 3.1.1. Upon determining the temperature variations under different GGBS contents, another goal of this experiment is to validate the accuracy of subsequent FEM modelling of concrete temperature. Essentially, the geometry, material

properties, and boundary conditions of the FEM models will be based on the prototypes established by these experiments.

1.4.2 Isothermal Calorimetry for Evaluating the Effect of GGBS Content and Curing Temperature on Hydration Heat

As outlined in Section 2.4.3, isothermal calorimetry tests offer a convenient and precise method for measuring the heat output power of cement hydration at constant curing temperatures. Compared to adiabatic calorimetry tests, isothermal calorimetry requires significantly smaller sample masses (in this work, not exceeding 50 grams), obviating the need to derive hydration heat power from the thermal properties of the sample, such as specific heat capacity and thermal conductivity, and eliminating the need for complex adiabatic systems to maintain “adiabatic” conditions.

This study employs the isothermal calorimetry technique to measure the hydration heat rate and cumulative hydration heat curves of micro-concrete samples with varying GGBS contents (the same replacements as those used in the semi-adiabatic calorimetry tests mentioned previously) over the first three days at different curing temperatures (20°C, 30°C, 40°C, and 50°C).

These isothermal calorimetry tests aim to capture the hydration heat development of samples with different GGBS contents at temperatures ranging from 20°C to 50°C. The obtained hydration heat curves will be utilized to assess the impact of temperature and GGBS content on cement hydration heat development. These results will also be used to calculate the hydration heat development characteristics of different samples at various temperatures, such as the delayed hydration phenomenon associated with GGBS and other important hydration heat characteristic parameters. Crucially, an Arrhenius-based mathematical model of hydration heat will be further employed to simulate the hydration heat development under different curing temperatures, providing insights into the hydration heat development of in-situ concrete under varying thermal conditions. The simulation data will then serve as the heat source input for FEM models, simulating temperature variations within concrete structures. These outcomes will support the objective outlined in Sections 3.1.1 and 3.1.3.

1.4.3 Isothermal Calorimetry Test for Micro-concrete Specimen

Given the prevalent use of isothermal calorimeters with small container volumes (20 mL) that cannot accommodate coarse aggregates, there is ongoing debate regarding whether the hydration heat curves of equivalent cement paste and mortar can be considered representative of concrete.

Considering that the focus of this research is on predicting the temperature development in in-situ concrete rather than mortar, it is crucial to investigate the role of coarse aggregates in the development of cement hydration heat and, subsequently, in concrete

temperature evolution to avoid potential errors in subsequent concrete temperature modelling. This experiment will employ the TAM Air 3-channel isothermal calorimeter with a container volume of 125 mL, thereby accommodating coarse aggregates. Micro-concrete specimens (not exceeding 50 grams) with the same mix used in the semi-adiabatic calorimetry tests will be prepared for isothermal calorimetry tests. It should be noted that micro-concrete does not refer to the microscopic scale, but rather to the fact that the weight of the concrete sample containing the coarse aggregate in the isothermal calorimetry test is less than 50g, which is much smaller than that of the conventional concrete specimen in the laboratory or of the concrete structure in the field construction. These micro-concrete samples will be produced simultaneously with the equivalent mortar samples and measured in the isothermal calorimeter concurrently to ensure synchronization of the hydration initiation and measurement times, facilitating subsequent comparative analyses. The impact of coarse aggregates on hydration heat development will be assessed across different mixes (different GGBS replacement ratio) and curing temperatures. Likewise, the hydration heat results from the micro-concrete specimens, processed in the same manner as the mortar specimens, will be used as a heat source for the concrete temperature FEM model to further evaluate the impact of omitting coarse aggregates from the thermal source on concrete temperature simulations.

This methodology focuses on bridging the gap between small-scale laboratory tests and the real-world conditions of concrete structures. By incorporating coarse aggregates into the isothermal calorimetry tests, this research aims to enhance the accuracy and relevance of the FEM models, ensuring they reflect the effect of coarse aggregate on the temperature development of in-situ concrete. These outcomes will support the objective outlined in Sections 3.1.2 and 3.1.3.

1.4.4 Finite Element Modelling of Early-Age Concrete Temperature Development

The results from the isothermal calorimetry tests will be adjusted using Arrhenius-based hydration heat models to simulate the development of cement hydration heat in in-situ concrete. These results will then be integrated as the thermal source component in the concrete temperature FEM modelling. The commercial FEM software package COMSOL Multiphysics [27] will be employed to simulate the temperature development of concrete specimens, using the semi-adiabatic calorimetry tests as a prototype. The accuracy of the simulation results from the FEM will be validated against the temperature monitoring data obtained from the semi-adiabatic calorimetry tests. This study will evaluate the impact of various factors, such as the GGBS content, the presence of coarse aggregates, and the applicability of current hydration heat models, on the accuracy of the FEM results. The ultimate goal is to establish a model to simulate the temperature development of in-situ concrete containing GGBS accurately.

The graph below describes the Research Methodology of this study, and the relationship between the various works:

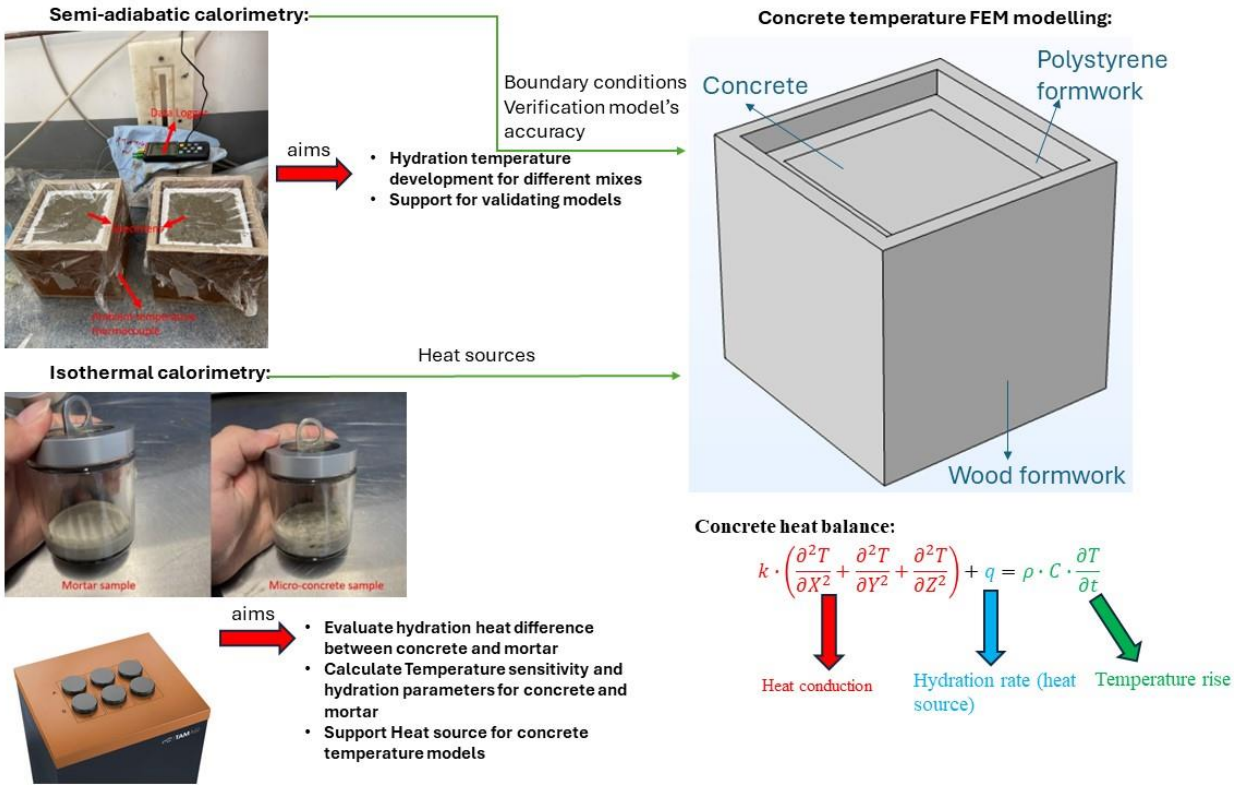

Figure 1.1 Research methodology summary

1.5 Research Contents

Chapter 2 provides the literature review on the early-age hydration and temperature development in concrete. The hydration processes of CEM I and Ground Granulated Blast-Furnace Slag (GGBS) are explored, along with factors influencing cement hydration and concrete temperature development, such as cement type, supplementary cementitious materials (SCMs), and environmental conditions. The principles and limitations of various calorimetry methods (adiabatic, semi-adiabatic, and isothermal) and their applications in measuring cement hydration and concrete temperature development are discussed. Chapter 2 emphasizes the application of the maturity method, which assumes that concrete strength and hydration heat development are functions of temperature and age, as a critical approach for predicting concrete hydration heat and temperature development. By reviewing existing finite element method (FEM) models for predicting concrete temperature, the chapter identifies research gaps that may lead to model inaccuracies, thus laying the groundwork for establishing the research aims and objectives of this study.

Chapter 3 presents the trial mix, selected mixture proportions and material properties utilized in this study.

Chapter 4 presents and analyses the test procedure and results of the semi-adiabatic calorimetry tests, with a particular focus on the impact of varying GGBS replacement ratios for CEM I on the temperature development of concrete samples. Chapter 5

presents the results of isothermal calorimetry tests, which investigate the effects of temperature and GGBS replacement ratios for CEM I on the development of hydration heat. The isothermal calorimetry results also explore the differences in hydration heat development between equivalent mortar and concrete samples, highlighting the significant influence of coarse aggregates and underscoring that concrete hydration heat cannot be represented by mortar.

Chapter 6 presents and analyses the results of concrete temperature modelling. By comparing the simulation results with semi-adiabatic calorimetry data, the accuracy and applicability of the model are evaluated. The findings underscore the importance of precise boundary conditions and heat source inputs, including environmental temperature fluctuations, concrete initial temperature, and the presence of coarse aggregates. Additionally, the necessity for further research into the hydration mechanisms of GGBS-CEM blended mixes is highlighted to enhance model reliability and predictive capability.

Finally, Chapter 7 presents a summary of the main findings and conclusions of this study, along with recommendations for further research.

CHAPTER 2 LITERATURE REVIEW

2.1 Introduction

In-situ concrete is extensively utilized in the construction industry due to its myriad advantages. Compared to precast concrete, steel, or timber, in-situ concrete demonstrates superior longevity, enhanced strength, and greater cost-effectiveness in various applications, including but not limited to bridges, high-rise buildings, and underground structures. Despite these advantages, in-situ concrete is not without its complexities and challenges. One significant issue arises during the early-age stage of cement hydration, where the temperature of the concrete increases, potentially leading to thermal cracking and impacting the performance and durability of the structure. This highlights the necessity of accurately predicting and controlling the early-age temperature development of in-situ concrete to ensure the structure's longevity. This literature review will delve into the complexities surrounding this issue.

This chapter will first explore hydration reaction processes of various cementitious materials. This will lay the groundwork for understanding the fundamental principles that govern the behaviour of in-situ concrete, including a detailed discussion on the nature of cement-based materials and the intricacies of the hydration process. The review will then delve into the main factors influencing exothermic cement hydration and concrete temperature development. This chapter will thoroughly analyse the variables that impact the hydration process and temperature progressions, such as environmental conditions, the type and fineness of cement, and the concrete specimen size. Subsequently, the causes and mechanisms of early thermal cracking in in-situ concrete will be addressed. This will involve exploring how the above factors contribute to thermal cracking and the formation of thermal loading in concrete. Additionally, this chapter will review common methods employed in engineering to mitigate thermal cracking, providing an understanding of the practical approaches currently in use.

The review will then present the analysis of diverse methods for measuring and calculating cement hydration and concrete temperature, including maturity methods and various calorimetry methods. Additionally, the application of the finite element method (FEM) in predicting the early-age hydration temperature of concrete will be reviewed.

Finally, the review will critically discuss the limitations and potential issues of existing methods for predicting the development of hydration temperature in concrete. This will set the stage for the subsequent chapters of this PhD thesis, which aim to address these research gaps.

2.2 Cementitious Materials and Hydration Process

The hydration process of cementitious materials plays a critical role in determining the temperature development and potential thermal cracking risks in concrete structures. During hydration, exothermic reactions generate heat, leading to a temperature rise that, if unmanaged, may result in thermal stresses and cracking. Understanding the properties and hydration behaviour of cementitious materials is therefore essential for predicting early-age temperature development and implementing effective mitigation measures in concrete.

Cementitious materials, including hydraulic cement and supplementary cementitious materials (SCMs), serve as key binding agents in concrete mixtures. According to BS EN 197-1:2011 [28], hydraulic cement is classified into various types based on clinker content and supplementary components, influencing hydration heat and thermal behaviour. CEM I, with a high clinker content, generates substantial heat during hydration, making it more prone to early-age thermal cracking. In contrast, blended cements such as CEM II and CEM III, which incorporate SCMs like fly ash or slag, produce lower hydration heat, thereby reducing thermal cracking risks.

SCMs, particularly Ground Granulated Blast-Furnace Slag (GGBS), are widely used to partially replace CEM I in concrete to reduce hydration heat and improve long-term durability. GGBS enhances concrete properties, including workability, permeability reduction, and resistance to sulphate attack, while mitigating early-age temperature rise and thermal cracking risks in mass concrete structures [29-31]. This section focuses on the properties of GGBS and its impact on the hydration heat development of in-situ concrete.

2.2.1 CEM I

CEM I cement clinker predominantly comprises four mineralogical components: tricalcium silicate (C_3S), dicalcium silicate (C_2S), tricalcium aluminate (C_3A), and tetra-calcium aluminoferrite (C_4AF). But its chemical composition is usually expressed in terms of oxides, including calcium oxide (CaO), silicon dioxide (SiO_2), aluminium oxide (Al_2O_3), iron oxide (Fe_2O_3), and small amounts of other minerals such as magnesium oxide (MgO) and sulfur trioxide (SO_3) [32-36]. This is primarily attributed to quantifying chemical compositions being considerably less challenging and cost-intensive (including test equipment and requirements for operators) compared to the analytical determination of compounds. Once this oxide content has been established, the four principal mineral components of the cement can be quantitatively derived via the Bogue formula, which has been widely used in cement research and has been incorporated into ASTM C150 [37] as a standard method for calculating the mineral content of cement.

The hydration reactions of cement are the process of combining cement and water to form various hydration products, such as calcium silicate hydrate (C-S-H), calcium aluminate hydrate (C-A-H), calcium sulfoaluminate hydrate (C-S-A-H), and calcium

hydroxide (CH) [38]. To better understand the kinetics and thermodynamics of this complex process, it is helpful to divide it into five main stages, including Initial mixing reaction, Dormancy, Acceleration, Speed reduction, and Steady development [22, 34, 39-41]:

1. The first stage is the initial mixing reaction, where the cement particles encounter water, leading to the dissolution of various mineral phases and the release of ions into the aqueous solution. The primary reaction at this stage is between C_3A and gypsum, which forms a sharp peak in the heat of the hydration curve. This reaction is quickly suppressed as the ettringite produced by the reaction encapsulates the C_3A. This stage lasts around 15-30 minutes.

2. The initial mixing reaction stage is followed by a period of dormancy, during which the hydration process appears slow, and no significant changes occur. This is mainly due to the formation of a protective layer of ettringite around the C_3A particles, which inhibits further hydration. The dormancy stage will generally last 5-6 hours.

3. The dormancy stage is followed by an acceleration stage, during which there is a rapid development of calcium silicate hydrate (C-S-H) and calcium hydroxide ($Ca(OH)_2$) gels. This is mainly due to the dissolution of C_3S and C_2S particles, which are less affected by the ettringite layer than C_3A. The acceleration stage contributes to the enhancement of the strength of the cement paste. During this stage, the hydration heat development also becomes significant due to the high exothermic nature of the reaction.

4. The acceleration stage is followed by a speed reduction stage, during which the hydration process slows down due to the depletion of reactants and the buildup of reaction products. This results in a decrease in both strength development and heat generation. Depending on the curing conditions, the speed reduction stage may last for several days or weeks.

5. The speed reduction stage is followed by a steady development stage, during which the hydration process continues slowly and steadily, gradually strengthening the cement paste. Unlike the speed reduction stage, where the hydration rate is still influenced by the availability of reactants and the porosity of the paste, the steady development stage is mainly controlled by the diffusion of water and ions through the hardened matrix. The steady development stage may last for months or years until the hydration reaches equilibrium with the environment. A typical heat of hydration rate curve of cement in Figure 2.1 describes the five stages of cement hydration. These stages reflect the dynamic and complex nature of the hydration process, which affects the properties and performance of concrete.

The acceleration and speed reduction stages are particularly relevant to early-age hydration temperature development. The acceleration stage, characterized by high heat release, is crucial for understanding early thermal behaviour in large concrete pours. The speed reduction stage highlights the diminishing rate of temperature rise and the gradual development of thermal stresses over time, both of which are critical for predicting potential thermal cracking in in-situ concrete.

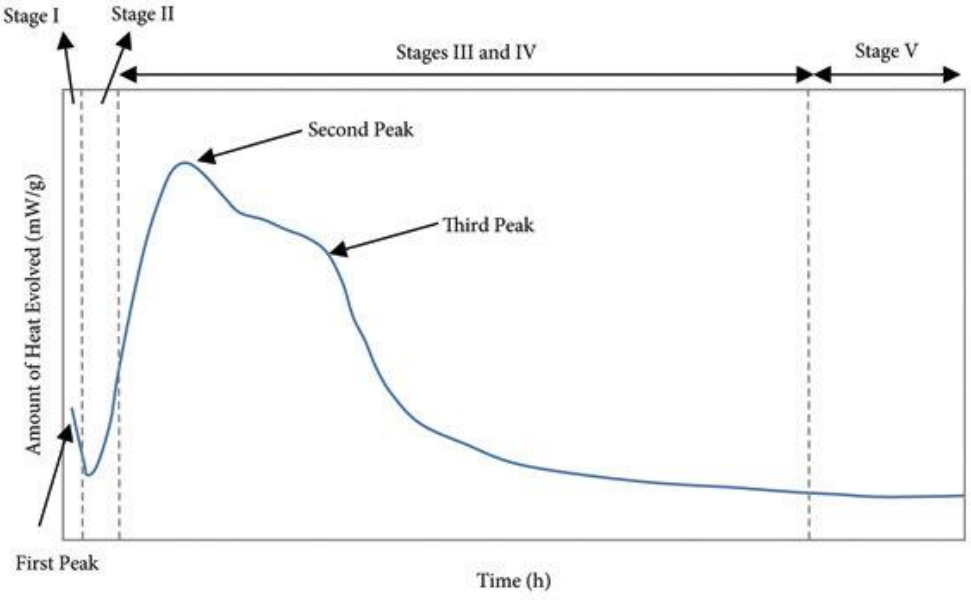

Figure 2.1. Five stages of cement hydration process [42].

2.2.2 Ground Granulated Blast Furnace Slag (GGBS)

GGBS, as defined in BS EN 15167-1:2006 [43], is a finely ground byproduct of the iron and steel industry obtained through rapid cooling of molten slag. GGBS exhibits lower hydration heat compared to CEM I, making it an effective SCM for reducing early-age temperature rise in concrete.

In GGBS-CEM blended mixes, the hydration process involves both cement and GGBS reactions. Initially, CEM I hydrates to form C-S-H and $Ca(OH)_2$, creating an alkaline environment that activates the GGBS. The subsequent hydration of GGBS contributes to additional C-S-H formation, enhancing concrete strength and durability while reducing hydration heat. This process can be summarized in three stages [44-46]:

1. Initial Hydration: CEM I hydrates first, producing C-S-H and $Ca(OH)_2$. This initial hydration generates the necessary alkaline environment to activate the GGBS.

2. Activation of GGBS: The $Ca(OH)_2$ from the CEM I hydration activates the GGBS, leading to its dissolution and subsequent formation of additional C-S-H. This interaction enhances the density and durability of the concrete matrix.

3. Continued Hydration: The hydration of both GGBS and CEM I continues, with GGBS contributing to the long-term strength development of the concrete. This stage is characterized by a slower but sustained release of heat and a gradual increase in strength over time.

Studies indicate that replacing CEM I with GGBS can reduce peak hydration temperature and mitigate thermal cracking risks in mass concrete structures [1, 5, 6]. However, GGBS also delays early strength development due to its slower hydration rate [47, 48]. Therefore, optimizing the replacement ratio and curing conditions is essential to balance early-age strength and temperature control.

In the UK, GGBS is widely used in concrete production to reduce carbon emissions and improve sustainability. According to the Cementitious Slag Makers Association (CSMA) [49], GGBS production requires significantly less energy and emits substantially lower carbon dioxide compared to CEM I. Despite these benefits, recent analyses have raised questions about the long-term sustainability of GGBS in the UK. Kelly's [50] review in 2023 points out that while GGBS effectively reduces carbon emissions at the project level, its broad utilization has not significantly impacted the national emissions profile. The material has been maximally utilized in the UK for over two decades, favoured for its affordability and positive impact on concrete properties. This extensive use has sparked concerns about the future availability of GGBS.

The challenge surrounding GGBS's sustainability intensifies when considering its global demand versus limited supply. A report of the Institution of Structural Engineers in 2023 [51] highlights that GGBS is a globally constrained resource. Its increased use in one area often leads to decreased availability elsewhere, creating a zero-sum situation regarding global greenhouse gas emissions. Furthermore, the UK's steel production, a key source of GGBS, is projected to decline in the coming years, potentially leading to a 30% reduction in GGBS supply. This decline indicates that GGBS is approaching a saturation point in the UK market and may no longer be a viable and sustainable SCMs. Therefore, the industry must explore other SCMs and enhance the efficiency of GGBS utilization.

2.2.3 Factors Influencing Hydration Rate and Temperature Development in Concrete

The hydration of cement is a complex process that can be influenced by various factors. To investigate the early-age temperature development of in-situ concrete, a review of the factors that influence the hydration reaction of cementitious materials is necessary. The most important factors affecting cement hydration in concrete are cement type, cement fineness, water-cement ratio, mineral admixture, temperature, and specimen size. The influence of these factors on cement hydration in concrete will be reviewed

and discussed in this section.

2.2.3.1 Influence of Cement Type on Hydration Heat

Different types of cement will have varying types and amounts of clinker and mineral admixtures, which can affect the rate and degree of hydration, as well as the final hydration product. It is therefore the type of cement used will have an impact on the heat generated during hydration. For instance, a higher content of C_3A and C_3S in cement can lead to a greater rate of heat evolution during early stages [22]. Figure 2.2 and Figure 2.3 illustrate the variation of cement's heat of hydration development with different C_3A and C_3S content, respectively. Different cement types can have different rates of heat evolution over time (Figure 2.4 illustrates the heat of hydration curves for different types of cement), which can affect the temperature development in mass concrete structures and potentially lead to thermal cracking. ACI 207.2R-95 [52] reports on adiabatic temperature rise for various cement types at identical place temperatures and concrete densities (Figure 2.5). As can be seen in Figure 2.5, the rate of temperature rises, and maximum temperature of the adiabatic concrete specimen varies with different types of cement. Therefore, selecting the appropriate cement type is an important consideration when designing concrete structures with specific performance requirements, including controlling the heat of hydration and thermal cracking.

In practical applications, the choice of cement type should align with the specific performance requirements of the concrete structure. For instance, in scenarios such as highway bridges requiring high corrosion resistance to chloride, high aluminate cement might be the preferred choice due to its superior resistance to chloride penetration. High aluminate cement has a lower C_3S content and higher C_3A content, which can offer enhanced durability in environments with high chloride exposure, such as coastal areas or regions where de-icing salts are used [53, 54].

For applications where early strength development is crucial, such as in fast-track construction projects, a high early strength cement, which typically has a higher C_3S content, may be more suitable [55]. This type of cement generates more heat during the initial hydration stages (Figure 2.3), promoting faster strength gain. However, careful consideration must be given to the potential risk of thermal cracking due to the higher heat evolution.

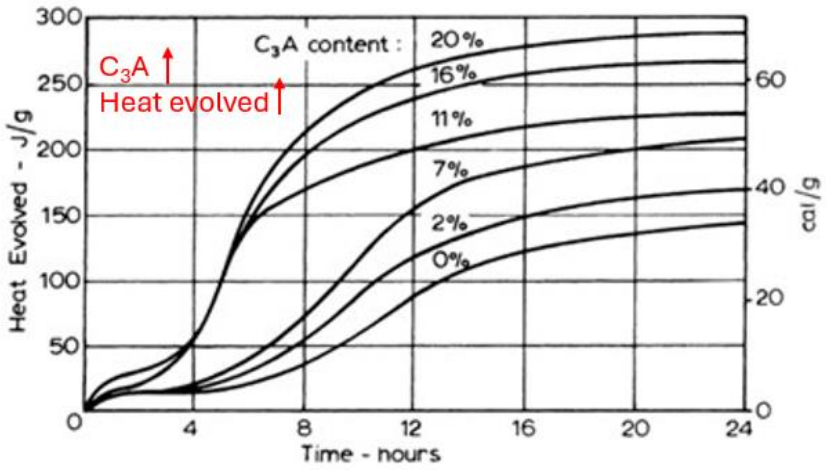

Figure 2.2. Cement hydration heat development in relation to C_3A content [34].

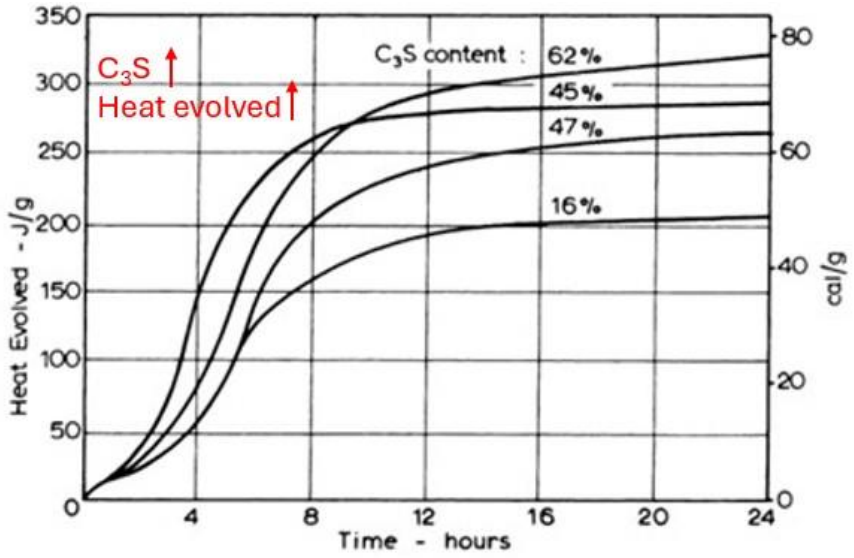

Figure 2.3. Cement hydration heat development in relation to C_3S content [34].

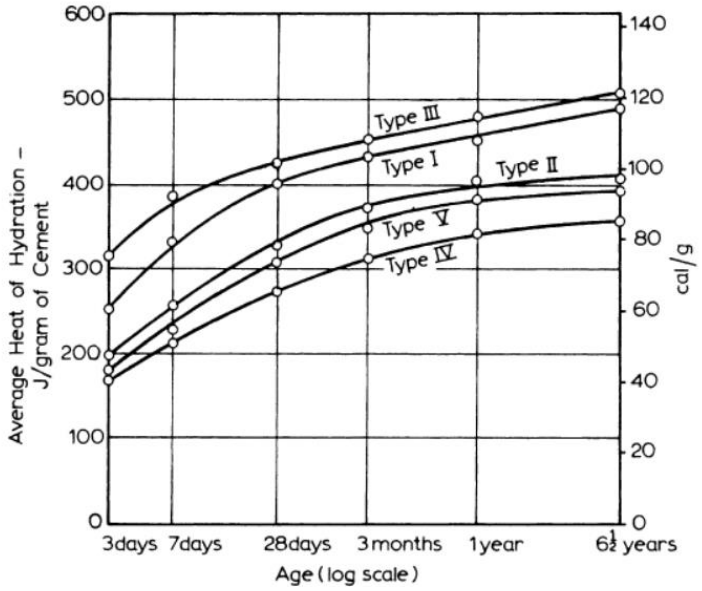

Figure 2.4. Hydration curves of different types of cement (cured under 21 °C with a w/c ration of 0.4) [34].

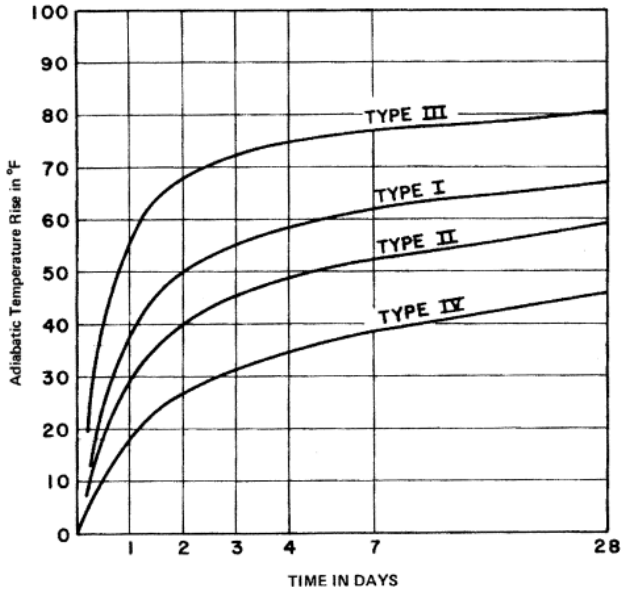

Figure 2.5. Adiabatic temperature for different types of cement form ACI 207.2R-9 [52].

2.2.3.2 Influence of Binder Particle Fineness on Hydration Heat

Binder particle fineness, described as the specific surface area per unit mass, influences the hydration process and heat development in concrete. Finer particles, with larger surface areas, accelerate hydration by providing more contact points with water. This increases the early hydration rate and initial heat release but does not significantly impact the total cumulative heat at later stages [33, 56].

The particle size distribution of supplementary cementitious materials (SCMs), such as GGBS, also affects their reactivity. Fine GGBS particles enhance early hydration and strength development, contributing to better concrete performance. However, excessive fineness can result in high early heat release, creating thermal gradients that increase the risk of thermal cracking in mass concrete structures.

Therefore, balancing binder fineness is crucial. While finer particles promote early strength, overly fine binders may compromise thermal stability. Proper control of particle size distribution ensures optimal hydration performance and reduces the potential for thermal cracking.

2.2.3.3 Influence of Water-cement Ratio on Hydration Heat

The water-to-cement ratio (w/c ratio) represents the proportion of water to cementitious materials in a concrete mixture. It is a critical parameter affecting cement hydration

reactions. As previously discussed, cement hydration involves a series of chemical reactions between cement and water. To enable the continuation of hydration reaction, it is crucial to ensure that an adequate amount of water is available. In the presence of sufficient free water, the cement hydration reaction will continue until the cement is fully hydrated or the available spaces within the cement paste/concrete are completely filled with hydration products. Thus, in conditions where external water is plentiful (such as concrete curing in a water bath), the hydration process persists until the cement is fully hydrated or until the available space within the paste is occupied by the hydration products.

Byfors [57] reported that the w/c ratio does not affect the early stages of the hydration rate since, during this period, there is always sufficient space for the hydration products and enough free water for the reactions. However, Byfors [57]also pointed out that in the later stages of hydration, the heat generation rate decreases with a decreasing w/c ratio mix. Figure 2.6 shows the adiabatic calorimetry results for concrete with different w/c ratios as reported by RILEM [58], which nicely validates Byfors' conclusions.

Van Breugel [59] proposed that a water-cement ratio (w/c) of at least 0.4 is required to achieve complete cement hydration. Mindess and Young [60] also noted that the hydration process ceases when there is insufficient water available to form a saturated C-S-H gel, and to achieve complete hydration, a minimum w/c ratio of 0.42 is necessary. The limitation of these findings is that they may only apply to the specific mix proportions and cement types used in these studies. A higher water-cement ratio results in more water present in the concrete mixture, which means that some of the water may not participate in the reaction and instead remain in the concrete's pores. This surplus water can lead to the formation of voids in the concrete that can be filled with air or other materials, ultimately reducing the concrete's strength and durability [61, 62]. The w/c ratio should be carefully controlled and can be determined either through calculation or experimental methods to optimize the hydration process. This control ensures the generation of sufficient hydration to form durable concrete without inducing thermal cracking. Calculations typically involve existing empirical equations and mix design methods, such as the BRE mix design method [63], which provides guidelines based on extensive empirical data. Experimental determination might include trials with various w/c ratios to assess the resultant heat of hydration, strength, and durability. This process involves selecting the w/c ratio based on the specific needs of the concrete application, including mix design, environmental factors, and curing methods. By balancing these factors, it is possible to achieve the desired performance characteristics of concrete, ensuring both its structural integrity and longevity.

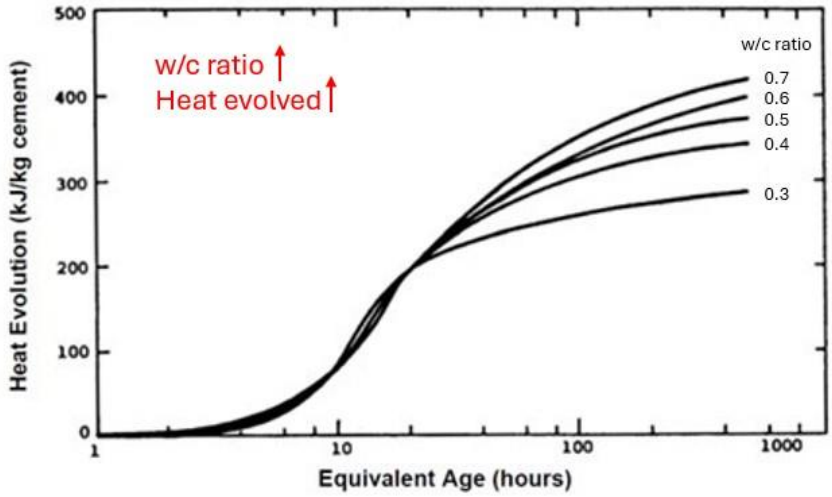

Figure 2.6. Adiabatic calorimetric results for concrete with different w/c ratios [58].

2.2.3.4 Influence of GGBS Replacement on Hydration Heat

When Ground Granulated Blast-Furnace Slag (GGBS) partially replaces CEM I cement in concrete mixes, it significantly influences the hydration process and heat development. GGBS reduces the production of calcium hydroxide ($Ca(OH)_2$) during cement hydration, which lowers the alkalinity of the pore solution and slows the dissolution rate of GGBS [25, 26]. Additionally, GGBS reacts with $Ca(OH)_2$ to form calcium silicate hydrate (C-S-H) and calcium aluminate hydrate (C-A-H), compounds that enhance the strength and durability of concrete [25, 64].

One of the key impacts of GGBS replacement is the reduction in hydration heat, which lowers the peak temperature in concrete and helps mitigate the risk of thermal cracking. The hydration curve of GGBS-CEM blends typically exhibits two distinct peaks: the first peak corresponds to the rapid hydration of CEM I, while the second peak reflects the slower hydration of GGBS. De Schutter [65] proposed a model based on this two-peak behaviour, describing GGBS hydration as a process superimposed on CEM I hydration. However, some researchers, such as Zheng *et al.* [66], argue that this simplification does not fully capture the complexity of the hydration process.

Studies have shown that increasing the GGBS content in concrete decreases the early hydration rate and peak heat output while delaying the time to reach peak hydration. For example, Tan and Tang [67] demonstrated that mixes with higher GGBS content exhibit a slower hydration rate and a lower hydration peak value during hydration (as shown in Figure 2.7). Zheng *et al.* [69] confirmed these findings through isothermal calorimetry tests, observing that the relationship between GGBS content and hydration heat development varies with curing temperature. At lower temperatures, the relationship is linear, whereas at higher temperatures, it becomes non-linear.

In summary, replacing part of the cement with GGBS offers several benefits, such as

reducing early-age hydration heat and mitigating thermal cracking risks. GGBS lowers the intensity of early exothermic reactions and the total heat release during the curing process, making it a valuable component in concrete mix designs for mass and long-span structures. Despite concerns about the long-term sustainability of GGBS due to supply constraints [49-51], its contributions to reducing hydration heat and enhancing concrete durability remain significant.

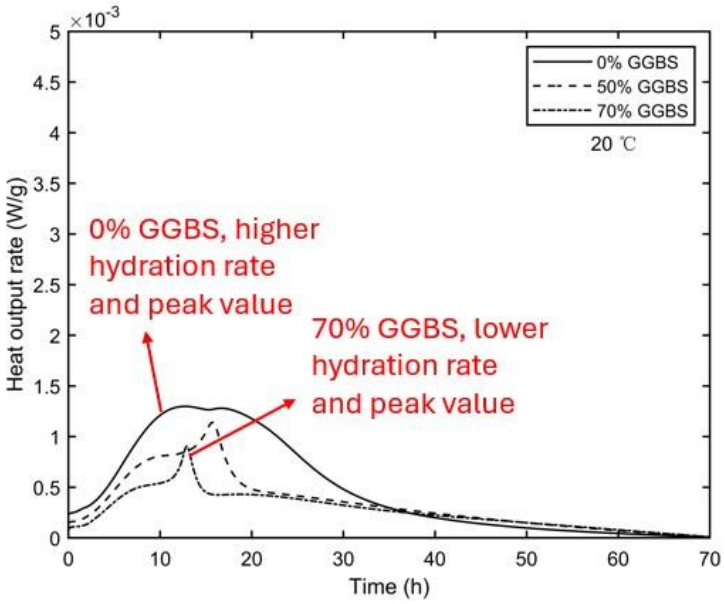

Figure 2.7. Effect of GGBS content on hydration heat generation rate [67].

2.2.3.5 Influence of Temperature on Hydration Heat

In the context of concrete curing, the term "temperature" encompasses a broad range of concepts, including the initial temperature of the concrete, the self-temperature (internal temperature) of the concrete, and the curing/environmental temperature. The initial temperature is the temperature of the fresh concrete mixture before it is placed in the formwork. The self-temperature is the temperature of the hardening concrete during the hydration process. The curing/ambient temperature is the temperature of the surrounding environment of the concrete specimen during the curing process, such as the temperature of the environmental chamber in the lab or the variable on-site temperature at which the concrete is located in the field. Each of these temperature aspects influences the cement hydration heat development and the concrete hydration temperature development, albeit in different ways. A thorough understanding and distinction between these temperature variables are crucial for accurately predicting the temperature development of concrete. This differentiation is essential to ensure precise modelling and effective management of the thermal behaviour of concrete during the early stages of hydration, thereby mitigating risks such as thermal cracking and ensuring the long-term durability and performance of the structure.

The concrete self-temperature significantly impacts the rate of hydration and the

temperature development of concrete. The relationship between the hydration rate of cement and self-temperature is often described by the Arrhenius equation (as shown in Eq. (2.1), which will be discussed in detail in later sections), which shows that the cement hydration reaction rate is proportional to the exponential function of the temperature. The initial temperature of the concrete can be considered as T_0 in this equation, which represents the baseline state before the onset of cement hydration. As the hydration process progresses, the evolving self-temperatures within the concrete are expressed as T_1, T_2, ..., and T_n. It's crucial to underscore that the curing temperature or ambient temperature does not directly influence the cement hydration process within the concrete. Instead, it governs the concrete's heat dissipation capacity by establishing a temperature differential between the concrete and its environment. Consequently, this external temperature parameter alters the concrete's internal temperature, thereby indirectly affecting the cement hydration process.

$$k(T) = A \cdot \exp\left(\frac{-E_a}{R \cdot \mathrm{T}}\right) \tag{2.1}$$

where k(T) is the rate constant at temperature T, T is the concrete temperature (T), A is a rate constant, R is the universal gas constant = 8.314 (J/K·mol), and E_a is the apparent activation energy (J/mol).

The increase in concrete self-temperature, therefore, accelerates the hydration reaction and leads to the rapid development of the heat of hydration. The correlation between the rise in temperature and the acceleration of the hydration reaction results in a quick release of the heat of hydration, consequently amplifying the internal temperature within the concrete structure. This elevation in temperature, in turn, further expedites the hydration process. As indicated in Eq. (2.1), it is essential to note that the heat discharged during the hydration of cement is not a linear function of temperature. Instead, it exhibits an exponential relationship, substantially intensifying the pace of the temperature increase within the concrete. This phenomenon can precipitate the risk of thermal cracking (will be discussed in the Section 2.3).

The cement hydration rate undergoes a dynamic shift at high temperatures, characterized by an acceleration in the early stages followed by a deceleration in the later stages. This phenomenon can be explained by forming a "coating" or "shell" of early hydration products enveloping the cement particles under high-temperature conditions. This shell impedes the continuation of the hydration process [6, 22]. The density of this protective shell tends to increase as the temperature escalates. Furthermore, it is noteworthy to mention that early-age curing at elevated temperatures may detrimentally impact the ultimate strength of the concrete, and this phenomenon has been widely verified [1, 22, 47, 68, 69]. This could be due to the formation of this dense shell, which restricts the progression of hydration and potentially leads to less homogeneous and denser hydration products, thereby compromising the mechanical properties of the resultant concrete.

Wang *et al*. [47] measured the strength development of cement mortar and cement-GGBS mortar at 20 ℃ and 65 ℃. The results demonstrated that early age curing at elevated temperatures enhances the initial hydration reactions in cement, while conversely impeding the subsequent ones. This imbalance engenders a microstructure characterized by large pore spaces. Consequently, the longevity of the strength of cement mortars subjected to high-temperature conditioning at an early stage is lower to those treated at temperatures below 20°C. In addition, it was found that the hydration reaction of cement-GGBS composites demonstrates a higher sensitivity to temperature changes than that of cement alone. Consequently, the rate of strength development of cement-GGBS mortars conditioned at high temperatures in the early stage outpaces that of cement mortars. Similar findings were reported by Tang *et al.* [1, 6], which indicated that the deleterious impact of incorporating GGBS on the early strength of concrete diminishes with the escalation of the curing temperature. These observations intimate the necessity to establish an equilibrium between the advantageous thermal cracking mitigation properties of GGBS in concrete and its potentially detrimental effects on early strength development. Such a balance would ensure the attainment of the designed concrete strength while concurrently minimizing the evolution of thermal cracking.

Conversely, initiating and curing hydration reactions at lower temperatures can decelerate the rate of heat evolution, inducing a more gradual temperature elevation within the concrete. This condition, often deemed beneficial, can mitigate the probability of thermal cracking. However, it is crucial to acknowledge that excessively low temperatures can also impart detrimental effects on the hydration process, manifesting as diminished strength development and potential susceptibility to freeze-thaw durability issues [70, 71].

The effect of temperature on cement hydration rate can be determined using various calorimetric methods, including isothermal calorimetry, adiabatic calorimetry, and semi-adiabatic calorimetry. The review and discussion of these testing approaches will be undertaken in Section 2.4.

In conclusion, the placement and curing temperatures play a cardinal role in the hydration reactions of cement and the consequential development of hydration temperature in concrete. The reactivity of cement is temperature-dependent, leading to different hydration kinetics and temperature evolutions within the concrete. While higher temperatures can hasten the early hydration process, they may induce the formation of a dense shell around cement particles, hindering subsequent hydration and potentially affecting the ultimate strength and durability of the concrete. On the other hand, lower temperatures, while beneficial for mitigating thermal cracking and enhancing strength development, could affect concrete's freeze-thaw durability if the temperatures are excessively low.

The temperature sensitivity of cement hydration and the resulting temperature evolution

in concrete underscore the importance of careful temperature management to prevent thermal cracking and ensure the desired strength and durability of the concrete structure. This balance is particularly critical when supplementary cementitious materials like GGBS are incorporated into the concrete mixture. This knowledge will provide valuable insights for concrete mix design and curing procedures, contributing to constructing more durable and sustainable concrete structures.

2.2.3.6 Influence of Concrete Specimen Size on the Concrete Temperature

As this research will delve deeper into the study of the hydration temperature of concrete, it becomes apparent that the size and thickness of concrete specimens play a crucial role in the rate of hydration of cement and the development of concrete temperature. In contrast to the study of pure heat of hydration of cement, this unique influencing factor in the field of concrete demands a more comprehensive analysis.

During the cement hydration process in mass concrete structures, or those with substantial thickness, the material's low thermal conductivity coupled with the large concrete volume poses a significant challenge for effective heat dissipation. As a result, the core temperature within such structures often escalates to high levels. Consequently, this core temperature within mass concrete is frequently utilized to simulate the conditions in adiabatic thermal method tests, providing a realistic examination of the thermal behaviours intrinsic to large-scale concrete structures [1, 72, 73]. The heat transfer in concrete is determined by a combination of thermal conductivity and temperature gradient, which can be expressed by the Fourier heat transfer equation (Eq. (2.2)). Further, the heat equilibrium within the concrete structure can be encapsulated via the heat diffusion equation (Eq. (2.3)), a model predicated on Fourier's heat transfer principle. This mathematical formulation serves as a critical framework for understanding the thermodynamic behaviour of concrete. Eq. (2.3) indicates that the velocity of the thermal transformation at a specific spatial location is proportionate to the second spatial derivative, fundamentally the rate of alteration of the spatial gradient of the temperature at that location. In essence, thermal diffusion transpires from regions of elevated temperature towards regions of diminished temperature, and the pace of temperature alteration is at its apex, where the thermal gradient is steepest. The role of concrete's thickness emerges prominently in this context, influencing the rate of thermal dissipation. The greater the concrete thickness, the longer the duration required for heat to transfer to the concrete surface, thus underscoring the pivotal role of the physical size of the concrete in its thermal behaviour.

$$q = -k \cdot \Delta T \tag{2.2}$$

where q indicates the heat transfer per unit time and per unit area (W/m^2), k is the thermal conductivity of the concrete (W/(m·K)), ΔT is the temperature gradient (K/m^2).

$$k \cdot \left(\frac{\partial^2 T}{\partial X^2} + \frac{\partial^2 T}{\partial Y^2} + \frac{\partial^2 T}{\partial Z^2} \right) + Q = \rho \cdot C_p \cdot \frac{\partial T}{\partial t} \quad (2.3)$$

where Q is the heat generation rate of the cement (W/m^3), X, Y, Z represent three different axes in the concrete, T is the concrete temperature (°C), ρ is the density of the concrete (kg/m^3), and C_p is the heat capacity of concrete (J/kg·K).

Huang *et.al* [74] established a Finite Element Method (FEM) model to simulate the thermal progression at various points within a sizable concrete pier. By leveraging this well-structured FEM model, they conducted a parametric analysis to explore the influence of ambient temperature shifts on the thermal trajectory at each point within the pier structure. Their investigation revealed that points close to the core of the pier demonstrated remarkable resistance to the impacts of changes in ambient temperature. Conversely, locations closer to the external surface of the pier section were considerably impacted by these environmental shifts. This deduction sheds light on the intricate dynamics at play in the hydration process of concrete. Specifically, it underscores the susceptibility of the concrete regions, which are conducive to heat dissipation, to variations in ambient temperature. Moreover, this study resonates with the earlier discussion on the influential role of concrete specimen size and thickness in the rate of hydration and the subsequent development of concrete temperature. The concrete structure's thickness directly impacts the heat dissipation rate: larger thicknesses lead to slower diffusion of heat to the concrete surface. Consequently, heat retention in larger concrete structures causes the core temperatures to remain high for extended periods.

The understanding of the relationship between concrete size/thickness and temperature development is paramount in predicting and controlling the thermal behaviour of large-scale concrete structures. Such insights can guide the design and construction processes to optimize structural integrity while mitigating potential thermal cracking risks.

2.3 Early-Age Thermal Cracking in Concrete and Mitigation Strategies

The preceding sections of this chapter offered a review of cementitious materials and the hydration process. They highlighted various factors that affect the hydration reaction and the temperature development of in-situ concrete. These fundamental aspects are essential for tackling the issues related to early-age thermal cracking of in-situ concrete.

Concrete is a widely used building material composed of cementitious material, water, aggregates, and sometimes, additives. The hydration process of cementitious materials in concrete results in the formation of binders, which contribute to the strength and durability of the concrete matrix. BS EN 206:2013 [75] defines concrete as: "material formed by mixing cement, coarse and fine aggregate and water, with or without the

incorporation of admixtures, additions or fibres, which develops its properties by hydration."

In-situ concrete is concrete that is poured and cured on site. During the early stages of hydration, the temperature of concrete can rise significantly. This issue is especially pronounced in in-situ concrete due to the difficulty in controlling temperature and humidity conditions during curing. Elevated temperatures can cause problems with durability, which can reduce the service life of the concrete structure [4].

The knowledge of the hydration process and thermal cracking is particularly relevant in the modern construction industry, which extensively utilizes mass concrete structures, such as pad foundations, bridge dams, and long-span concrete structures. These structures are vulnerable to several challenges and risks during their early stages, with thermal cracking posing a significant concern.

In the early stages of concrete casting and hardening, the heat generated by the hydration reaction causes an increase in temperature and thermal deformation within the concrete. When the thermal deformation of concrete is restrained by external constraints or by its uneven thermal deformation, thermal stresses will be generated. Early-age thermal cracking will occur when the tensile stress in the concrete exceeds its tensile strength. Early-age thermal cracking affects the durability, aesthetics, and safety of concrete structures.

Therefore, effective measures are needed to prevent and control early-age thermal cracking. The following parts of this section will delve into the specific characteristics and risks associated with early-age thermal cracking in these structures. This section will also explore common mitigation methods, such as temperature control during curing and using certain additives, to enhance the longevity and safety of these structures.

2.3.1 Thermal Loading in Concrete Structures

Thermal loading in concrete structures refers to the changes in temperature within the concrete mass that led to thermal expansion and contraction. This phenomenon is a critical aspect of concrete behaviour, especially during the early stages of hydration. As cement hydrates, it generates heat, causing the temperature within the concrete to rise. This temperature rise is unevenly distributed due to the varying thermal properties and boundary conditions, leading to thermal gradients.

Thermal loading can significantly impact the structural integrity of concrete. When the temperature increases, the concrete expands. If this expansion is restrained, either internally by the concrete mass itself or externally by formwork or adjacent structures, it generates thermal stresses. Similarly, when the temperature decreases, the concrete contracts. If this contraction is restrained, it also creates stress. Both expansion and

contraction can lead to cracking if the induced thermal stresses exceed the tensile strength of the concrete.

2.3.2 Internal Thermal Constraints in Mass Concrete

Temperature increases in the concrete lead to volume expansion, and as the concrete reaches its peak temperature, the temperature gradually decreases, resulting in volume contraction. In mass concrete, the large volume and low thermal conductivity of the material make heat dissipation from the core difficult (ACI 301 [76] recommends that concrete exceeding 1.4m in size be considered mass concrete). However, the outer surface of the concrete directly contacts the air, allowing heat dissipation and creating a temperature gradient from the concrete surfaces to the core. This gradient results in a lower temperature at the concrete surface than at the core. Consequently, the outer surface undergoes thermal contraction while the core remains at a higher temperature and experiences less shrinkage or even thermal expansion.

Furthermore, during the early curing phase, if the concrete surface is exposed to sudden temperature drops, such as during sudden demoulding, a sharp decrease in surface temperature occurs, creating a temperature gradient and uneven deformation within the concrete. These differential deformations between the surface and the core result in restrained thermal contraction at the surface, generating thermal tension stress [4, 77]. The strength of concrete in its early stages is far from reaching the design strength, making it easy for the thermal stress to exceed the strength at that time, resulting in thermal cracking on the concrete surface. ACI 207.2R [52] advises that the temperature difference between the surface and core of concrete should not exceed 20°C. Figure 2.8 shows the typical cracking location and crack distribution of the experimental blocks of Lawrence *et al.* [4], the red circles in the figure indicate prominent instances of thermal cracking. This figure visualizes the preceding discussion, illustrating the thermal stress differential caused by temperature gradients and uneven deformation between the surface and the core, emphasizing the role of temperature gradients and differential deformations in the generation of thermal tensile stress and subsequent cracking.

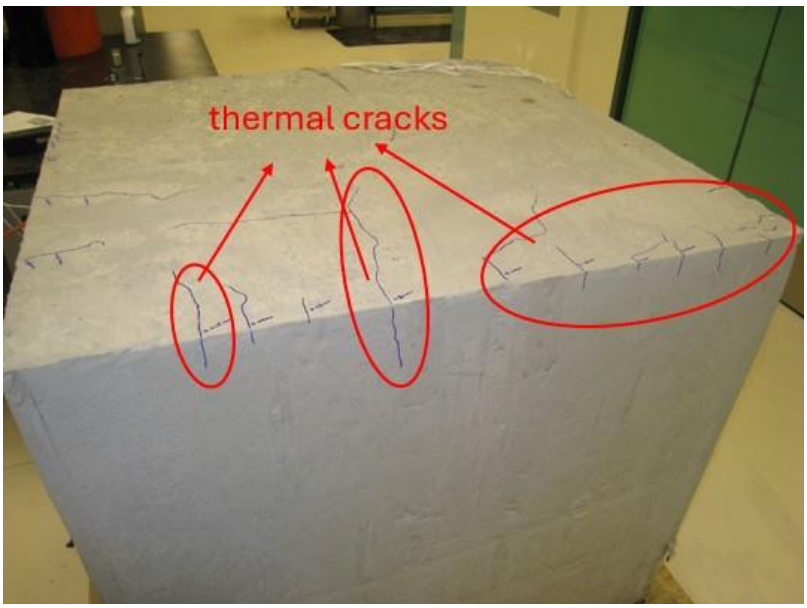

Figure 2.8. Thermal cracking on mass concrete surfaces [4].

2.3.3 External Thermal Constraints in Long-Span Concrete Structures

While mass concrete structures face thermal cracking issues due to what is referred to as “internal restraint”, long-span concrete structures, especially long-span thin-slab structures, encounter a different set of challenges. The ability of the concrete core to dissipate heat quickly in these structures helps reduce temperature gradients and uneven deformation. However, constrained temperature deformation in suspended concrete structures may also lead to significant stresses and cracking.

Although thin-slab structures are generally less prone to internal restraint, the large spans and connections to vertical structures in suspended concrete structures limit their deformation under temperature changes [1, 5, 78]. As a result, thermal expansion is restricted when the concrete heats, leading to compressive stresses, while limited thermal contraction during cooling results in tensile stresses. Due to the non-linear nature of concrete, its tensile strength is much lower than its compressive strength. Therefore, tensile stresses resulting from constrained contraction are more likely to cause cracking in these structures.

Adenidi [79] created a schematic illustration of the mechanism within a concrete slab to better comprehend the challenges associated with thermal shrinkage as shown in Figure 2.9. The upper half of the figure (the first two slab sketches) depicts a diagrammatic representation of thermal contraction in a concrete slab without external constraints. Without external restraint, the slab can shrink freely, thus avoiding the stresses induced by constraints. The lower half of the figure (the latter two slab sketches) illustrates a concrete slab subjected to external constraints at both ends. During the thermal contraction phase, the restraint at the slab’s ends generates tensile stresses within the slab’s interior. Cracking occurs when these tensile stresses exceed the

concrete's tensile strength at this stage. This diagram effectively visualizes the process of thermal shrinkage cracking, elucidating the relationship between thermal contraction, the development of tensile stresses, and the eventual cracking of the concrete structure.

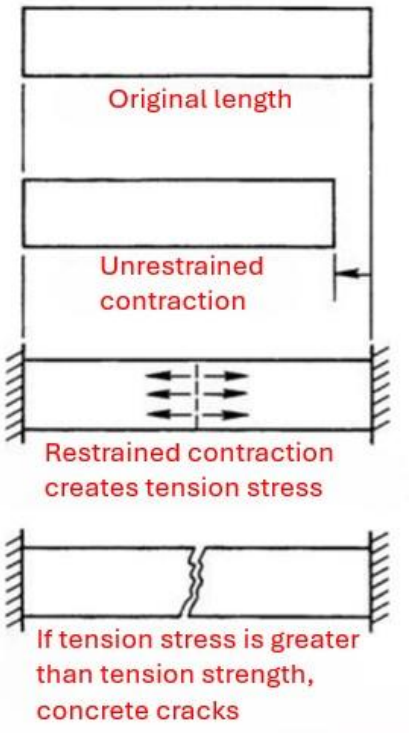

Figure 2.9. Sketch of concrete slab thermal contraction cracking [79].

2.3.4 Thermal Cracking in Other Concrete Structures

Like mass and long-span concrete structures, other types of concrete structures, such as pavements and slabs exposed to the external environment, also face potential risks of thermal cracking. These structures are exposed to a wide range of temperatures on their upper surfaces, while their lower surfaces are relatively protected. When a significant temperature differential exists between the two surfaces, thermal cracking is a potential risk [80]. According to the Federal Highway Administration Research and Technology [81], the thermal coefficient of expansion for concrete ranges from 8-12e-6 (1/°C). In hot climates, a concrete pavement cast at 35°C can experience temperatures as high as 70°C in summer and as low as -7°C in winter, resulting in an annual temperature cycle of 75°C (data in Arizona, USA) [82] and potential thermal cracking risks.

In conclusion, thermal cracking is a common issue in various types of concrete structures, from mass and long-span structures to pavements and slabs. Despite the differences in the specific mechanisms and factors contributing to thermal cracking in these structures, the underlying cause is the same: the temperature gradients and uneven deformation caused by the hydration reaction and temperature development of the concrete. Understanding these issues and the factors that contribute to them is crucial for developing effective strategies to prevent thermal cracking and enhance the

durability and longevity of concrete structures.

2.3.5 Methods for Mitigating Thermal Cracking

Mitigating thermal cracking in concrete structures requires a comprehensive approach that addresses the key factors influencing thermal stress and strain. These strategies aim to control thermal expansion, manage temperature gradients, reduce hydration heat, and optimize construction practices. By integrating these measures, the risk of thermal cracking can be significantly minimized, enhancing the durability and performance of concrete structures.

Material Selection: Choosing aggregates with a low thermal expansion coefficient can effectively reduce the overall thermal strain in concrete. Since aggregates constitute a large proportion of the concrete mix, their thermal properties greatly influence the concrete's expansion behaviour. Reducing the thermal expansion coefficient lowers the risk of thermal cracking by minimizing internal stresses caused by temperature changes [83].

Temperature Gradient Management: Managing temperature differentials between the surface and core of concrete is critical to preventing thermal cracking. Two key techniques are commonly employed:

- **Cooling Water Pipes:** Embedding cooling pipes within mass concrete structures helps dissipate heat from the core, reducing temperature gradients. Circulating cool water through these pipes lowers internal temperatures and decreases the likelihood of thermal cracking [84, 85].
- **Formwork Insulation:** Insulating the formwork helps maintain uniform temperatures throughout the concrete mass. However, caution is needed, as insulation can increase the peak core temperature, potentially causing issues such as spalling, delayed ettringite formation (DEF), and loss of mechanical properties [86-89]. The decision to insulate should consider specific project conditions to achieve a balance between reducing gradients and avoiding excessive core temperatures.

Reducing Hydration Heat: Since hydration heat is the primary cause of temperature rise in concrete, reducing it is essential to control thermal strain:

- **Use of Supplementary Cementitious Materials (SCMs):** Replacing part of the cement with SCMs like GGBS or PFA reduces the overall heat of hydration, thereby lowering the temperature rise. SCMs also enhance long-term durability through pozzolanic reactions [1, 5].
- **Lower Cement Content:** Reducing the cement content directly decreases hydration heat. However, this must be carefully managed to maintain the

required strength and durability of the concrete. Finding the optimal balance is crucial to minimizing thermal cracking risk without compromising performance.

Optimized Construction Practices: Incorporating construction techniques such as joints and pour gaps provides space for thermal expansion and contraction, preventing cracking caused by temperature changes. Proper joint spacing and depth are critical for ensuring structural integrity. For example, joints should be placed around 30 times the slab thickness apart and cut at least a quarter of the slab's thickness [90-92].

By implementing these mitigation techniques, engineers can effectively manage thermal stresses and minimize the risk of early-age thermal cracking in concrete structures. These strategies contribute to safer, more durable concrete designs, ensuring long-term performance and structural integrity.

2.4 Methods for Measuring Cement Hydration and Concrete Temperature

After exploring the fundamental aspects of cementitious materials, the hydration process, and the challenges associated with early-age thermal cracking in in-situ concrete, this section will focus on the critical task of measuring cement hydration and concrete temperature. This is a pivotal step in the investigation, as accurate measurement and understanding of these parameters are essential for predicting the early-age temperature development in in-situ concrete.

The measurement of cement hydration and concrete temperature is a multifaceted process, with various techniques available, each offering unique advantages and potential limitations. Among these, calorimetry stands out as a particularly valuable tool. Calorimetry allows for estimating the heat evolution during the hydration process, providing insights into the rate and degree of hydration, which are key factors influencing the temperature development in concrete.

This section delves into the specifics of calorimetry, examining its various forms: adiabatic calorimetry, semi-adiabatic calorimetry, and isothermal calorimetry, and discussing their respective advantages and potential drawbacks. Each of these techniques offers a unique perspective on the hydration process. However, only isothermal calorimetry can directly measure the heat flow of cement hydration. In contrast, adiabatic calorimetry and semi-adiabatic calorimetry can only measure the temperature development of concrete or mortar specimens and then infer the heat of hydration based on the thermal properties of the specimen. Understanding these differences is crucial for selecting the most appropriate method for a given situation.

Finally, this section contrasts the three calorimetry methods and evaluates their suitability for different scenarios. This comparative analysis provides an overview of the strengths and limitations of each technique, facilitating the selection of the most appropriate approach for predicting early-age temperature development in in-situ

concrete. This understanding is crucial for mitigating the risk of thermal cracking in concrete structures, thereby enhancing their durability and longevity.

2.4.1 Adiabatic Calorimetry

The adiabatic calorimetry test is a method to measure the heat evolution of concrete specimen under adiabatic conditions, i.e., without heat loss or gain to the surroundings. The primary purpose and application of this test is to simulate the temperature development within the core of mass concrete structures, where the large volume and low thermal conductivity result in most of the generated hydration heat being retained. Consequently, the temperature rise within the core can approach adiabatic conditions. Additionally, since theoretically there is no heat loss, this test is also used to obtain the complete hydration heat of the specimen.

As discussed in Section 2.3.2, mass concrete structures tend to retain most of the heat generated by cement hydration within their core, resulting in a significant temperature rise that may approach the adiabatic temperature. This can cause various durability problems, such as delayed ettringite formation (DEF) when the temperature exceeds 70 °C, and thermal cracking when the temperature gradient between the core and the surface is too large. Therefore, the adiabatic calorimetry test can provide valuable information for predicting and controlling the temperature development and thermal cracking risk of mass concrete structures. Moreover, with its specific heat, the adiabatic calorimetry test results can also be used to obtain the hydration curve and the hydration parameters of concrete, which can further support the numerical modelling and simulation of concrete temperature behaviour (this will be discussed in detail in Section 2.5).

However, it should be noted that achieving perfect adiabatic conditions in practical tests is impossible. Therefore, some test standards allow for a small amount of heat loss during the adiabatic calorimetry test. For example, the RILEM TC 119-TCE [93] guidelines specify that the temperature loss of the specimen should not exceed 0.02 K/h, while the BS EN 12390-15:2019 [94] sets this limit at 0.05 K/h. These tolerances reflect the practical difficulties of maintaining adiabatic conditions and aim to improve the reliability and accuracy of the test results.

As discussed above, the adiabatic calorimetry test imposes very stringent requirements on the heat loss of concrete specimens. To comply with these heat loss limitation, modern adiabatic calorimetry devices often employ a temperature control system that dynamically adjusts the temperature around the specimen to match the temperature inside the specimen, thus minimizing heat dissipation from the specimen as much as possible. This system may consist of a feedback loop that measures the specimen temperature and regulates the heating or cooling of the surrounding environment accordingly. The main components of an adiabatic calorimetry system comprise a concrete holding mold, a chamber with temperature control capabilities, and

temperature sensors for monitoring both the concrete and the chamber. The principle behind the test is to align the chamber's temperature with the hydration temperature of the concrete during the hydration process. This alignment facilitates an adiabatic condition for the concrete, thereby eliminating any heat transfer into or out of the concrete [95, 96].

In Lin and Chen's [97] adiabatic calorimetry test system, a temperature-regulated water bath serves as the aforementioned "chamber". The insulated mold houses the concrete specimens and is fully submerged within this water bath. Temperature sensors continuously monitor the thermal conditions of both the concrete specimen and the water bath. This data is relayed to the temperature control system, which in turn, adjusts the temperature of the water bath to match that of the concrete. This intricate feedback mechanism ensures that heat transfer from the water bath to the concrete during hydration is effectively mitigated, thereby achieving a state of "adiabatic". Figure 2.10 shows the schematic diagram of the temperature control system designed by Lin and Chen [97] for the adiabatic calorimetry test. This design underscores the importance of maintaining a consistent temperature environment to simulate the adiabatic conditions inherent in mass concrete structures accurately. The adiabatic calorimetry system in BS EN 12390-15:2019 [94] has a sophisticated closed-loop control mechanism. The sketch of this adiabatic calorimetry system is shown in Figure 2.11. This mechanism ensures a consistent temperature distribution across the external enclosure of the calorimeter cell. The system is designed to automatically adjust the temperature of the calorimeter cell to maintain adiabatic conditions. Specifically, it ensures that the temperature difference between the sample and the calorimeter cell is non-negative and does not exceed 0.5 K.

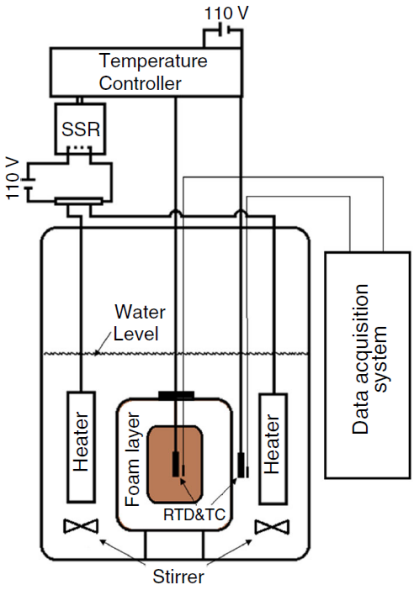

Figure 2.10. Adiabatic calorimetry temperature control system, designed by Lin and Chen [97].

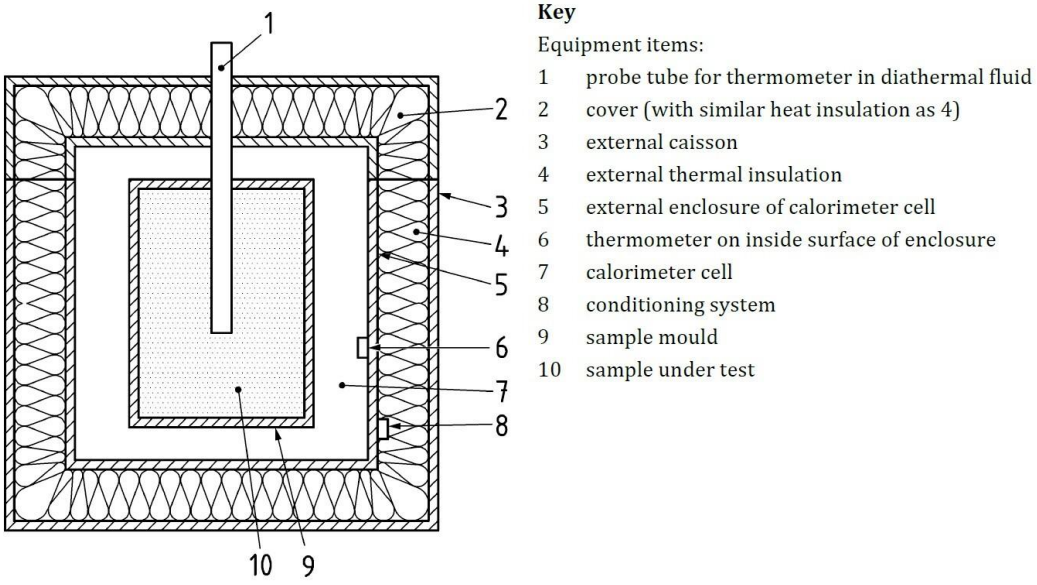

Figure 2.11. Adiabatic calorimetry temperature control system in BS EN 12390-15:2019 [94].

The data directly obtained from the adiabatic calorimetry test is the evolution of the temperature of the concrete specimen. Upon obtaining the adiabatic temperature rise curve of the concrete, given that this test is considered to have no heat loss, the heat of the hydration curve of the binder in the concrete can be calculated by multiplying the temperature difference at each time step with the initial temperature by the specific heat capacity of the concrete. This calculation process can be represented by Eq. (2.4) and (2.5).

$$\Delta T(t) = T(t) - T_0 \tag{2.4}$$

$$H(t) = \frac{\Delta T(t) \cdot C_c}{m_c} \tag{2.5}$$

where Δ T(t) is the concrete temperature rise value at time t (℃), T(t) is the concrete temperature at time t (℃), T_0 is the initial temperature of concrete (℃); H(t) is the cumulative heat of hydration at time t (J/kg), C_c is the total heat capacity of concrete (J/K), and m_c is the mass of concrete specimen (kg).

Concrete adiabatic calorimetry test has various applications and research values in concrete research. One of the applications is to analyse the temperature change and thermal stress in mass concrete structures at early ages, as mentioned above, and to provide a reference for temperature control and crack prevention in mass concrete. By simulating the adiabatic condition of mass concrete, the temperature rise curve can be used as an input for finite element analysis software to predict the internal temperature

distribution and thermal stress development in mass concrete structures under different environmental and construction conditions [24, 98].

Furthermore, given that the concrete adiabatic temperature rise test is designed to prevent heat loss, the concrete temperature and heat of the hydration curve derived from this test can be employed to study cement hydration. The cement hydration parameters obtained can be utilized to simulate the temperature and temperature stress modelling of any concrete structure with the same mix [74, 96, 99]. This approach has a broader range of applications and yields more accurate results than merely simulating the temperature rise of mass concrete through the concrete adiabatic temperature rise curve.

Another aspect is evaluating the effect of different types of cement, admixtures, and additives on the heat of hydration of concrete, which can provide a basis for concrete mix design. By performing adiabatic calorimetry tests on different concrete mixtures, the peak temperature, time to peak temperature, and total heat release can be obtained, indicating the potential for thermal cracking and delayed ettringite formation in mass concrete structures. These parameters can help to optimize the concrete mix design and to select appropriate preventive measures such as insulation and cooling water pipes discussed in Section 2.3.4.

In conclusion, concrete adiabatic calorimetry is a wide-application technique for measuring the heat of hydration of concrete and predicting the thermal performance of mass concrete structures. It has critical applications and research values in the field of concrete technology. However, there are also some challenges and limitations in performing adiabatic calorimetry tests, such as the high set-up cost of the temperature control system and difficulty in achieving actual adiabatic conditions [96]. Therefore, further research and development are needed to improve the accuracy and reliability of concrete adiabatic calorimetry.

2.4.2 Semi-adiabatic Calorimetry

Semi-adiabatic calorimetry is a technique for measuring the temperature development of concrete or mortar specimens under uncontrolled curing temperature conditions. The primary purpose of this test is to simulate the temperature development of concrete in real-world situations, where heat loss to the environment is inevitable. It is similar to adiabatic calorimetry but allows for a certain degree of heat loss, meaning the specimen is not in a completely adiabatic condition [93]. This characteristic eliminates the need for a complex temperature control system, requiring only a sufficient insulation setup to cover the specimen. This simplification reduces the cost and operational difficulty of semi-adiabatic calorimetry [96] and brings it closer to the actual temperature state of concrete structures [1].

In semi-adiabatic calorimetry, the specimen undergoes a certain degree of heat exchange with the external environment. This heat exchange results in a non-uniform

temperature distribution within the specimen, gradually decreasing from the centre to the surfaces. As the cement in the concrete hydrates and releases heat, the temperature of the concrete initially rises, reaching a peak value. However, as the heat release rate of the hydration reaction becomes lower than the heat loss rate of the concrete, the temperature of the concrete begins to drop until it gradually approaches the ambient temperature. The non-adiabatic, non-isothermal curing state of the semi-adiabatic calorimetry specimen closely resembles the insulation mode of in-situ concrete. Therefore, semi-adiabatic calorimetry is recognized as an effective method for simulating the temperature development of in-situ concrete in a laboratory setting [1, 5].

In addition to simulating the temperature development of in-situ concrete, semi-adiabatic calorimetry can also be used to obtain the hydration curve of cement in concrete. This is achieved by monitoring the heat loss during the hydration process of concrete with a specific device and obtaining the complete hydration heat of concrete through a heat loss compensation procedure.

BS EN 12390-14 [100] specifies a semi-adiabatic calorimetry method for quantifying the heat released by concrete during its curing process. The necessary apparatus for this test includes a semi-adiabatic calorimeter, a temperature monitoring and control system, thermometers, and a balance. The semi-adiabatic calorimetry system in BS EN 12390-14:2018 is illustrated in Figure 2.12. The system requires two calorimeters with similar heat loss coefficients (α) at 20 °C and heat capacities (C_c) within 15 % of each other. One calorimeter holds the test specimen, while the other holds the calibration specimen. Each calorimeter has a calorimetric cell with an insulated cover that can be removed, and an outer enclosure made of a material with high thermal conductivity, such as steel or another suitable material. The calorimeter cell is enclosed by an insulating layer covered by a rigid casing. The test procedure commences with replacing the test sample in the calorimeter with a calibration cylinder of identical size equipped with electrical resistance. The heat released by this cylinder over time is then measured. This test is conducted at a constant temperature of 20°C ± 2°C. The heat released by the concrete sample is calculated using the calibration curve derived from the calibration cylinder. The masses of the concrete sample, the added water, and the aggregates are also measured. These measurements are used to compute the heat of hydration of the concrete. The results obtained from on-site experimentation should be considered informative, and the same precision requirements as in the laboratory should be maintained. The total heat loss coefficient α of the calorimeter is determined by measurement during a steady-state mode, using the heat released by the Joule effect inside the calibration cylinder and the warming of this cylinder compared to the temperature of the inert cylinder placed in the control calorimeter. Once thermal equilibrium has been achieved (typically around 14 days), the heat generated is fully dissipated towards the external environment. The loss coefficient α can be expressed as Eq. (2.6).

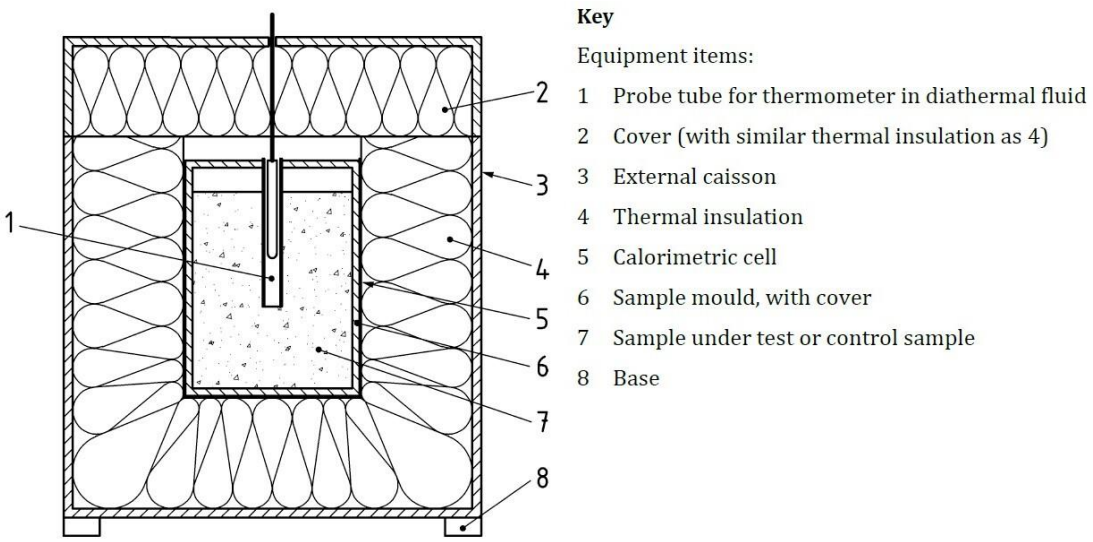

Figure 2.12. Semi-adiabatic calorimetry temperature control system in BS EN 12390-14:2018 [100].

$$\alpha = \frac{3600 \cdot V^2}{R \cdot \theta} \tag{2.6}$$

where θ is the temperature difference of the calibration cylinder, V is the volume of the calibration cylinder, and R is the resistance value of the calibration cylinder. This calculation is crucial for accurately determining the heat the concrete sample releases during the testing procedure.

Once the heat loss coefficient α of the calorimeter has been obtained, the heat of hydration of the concrete can be calculated using the heat released by the concrete sample during the testing procedure. The heat released H(t) expressed in joules per kilogram of concrete is calculated at time t using the Eq. (2.7):

$$H(t) = \frac{C_t}{m_c}\big(\theta(t) - \theta(0)\big) + \frac{1}{m_c}\int_0^t \alpha(\theta) \cdot \theta(u) \cdot du \tag{2.7}$$

where C_t is the total heat capacity of the system, and m_c is the mass of the concrete sample, u and du are mathematical integration variable. The first component of Eq. (2.7) on the right-hand side signifies the heat of hydration, which is responsible for the temperature increase in the concrete specimen. The second component represents the heat loss from the concrete specimen. The sum of these two components represents the cumulative heat of hydration of the concrete specimen at a specific time point. This equation provides the understanding of the heat dynamics within the concrete specimen during the hydration process.

Beyond the semi-adiabatic calorimetry system outlined in BS EN 12390-14:2018, numerous scholars [95, 101-103] have devised their semi-adiabatic calorimetry systems to derive the adiabatic hydration curve of concrete. These systems operate on a principle analogous to that of BS EN 12390-14:2018, where they monitor the heat loss from semi-adiabatic specimens and subsequently compute the cumulative heat of hydration of the concrete via a heat loss compensation step. This approach has been employed in various research contexts, including investigating the hydration characteristics of different cement paste samples and studying the early-age thermal properties of concrete under different ambient temperatures. The versatility and adaptability of these systems underscore their potential for broad application in concrete research.

In conclusion, semi-adiabatic calorimetry, as outlined in BS EN 12390-14:2018 and further developed by various researchers, is a robust and versatile method for studying the hydration characteristics of concrete. This method, which closely simulates the insulating conditions of in-situ concrete, provides valuable insights into the heat dynamics within the concrete specimen during the hydration process. The ability to monitor the heat loss from semi-adiabatic specimens and subsequently compute the cumulative heat of hydration of the concrete via a heat loss compensation step has proven to be a valuable tool in concrete research. The semi-adiabatic calorimetry method is cost-effective and operationally more straightforward than adiabatic calorimetry, but it also provides a more realistic representation of the actual temperature state of concrete structures. This makes it an effective tool for predicting the maximum temperature rise of mass concrete and investigating the hydration characteristics of various cement paste samples. Furthermore, the adaptability of the semi-adiabatic calorimetry systems, as demonstrated by the various designs developed by researchers, underscores its potential for broad application in concrete research. As such, semi-adiabatic calorimetry is expected to continue playing a pivotal role in advancing our understanding of concrete hydration and temperature development, thereby contributing to developing more durable and efficient concrete structures.

2.4.3 Isothermal Calorimetry

Isothermal calorimetry is a test method for the direct measurement of the hydration heat power in watt (heat release rate) of cement or mortar at a constant temperature. The primary purpose of this test is to simulate the curing conditions of concrete or mortar under controlled, constant temperature environments, allowing for precise monitoring of the hydration process. This is crucial for understanding the heat evolution and kinetics of cement hydration, which directly impact the temperature development and performance of the material in practical applications. The descriptor “isothermal” as applied to the isothermal calorimetry bears a conceptual resemblance to the “adiabatic” label in the adiabatic calorimetry. When referring to an isothermal heat conduction calorimeter as “isothermal”, it underscores the minimal temperature deviations during the test. As recommended by the BE EN 196-11:2018 [104], the permissible temperature fluctuation of the thermostat should be less than 0.2 °C. For instance, if an

experimental procedure mandates a temperature of 20 °C, the operational temperature of the equipment throughout the experiment should remain within the range of 20 ± 0.2 °C. Such deviations are so negligible that, for all practical intents and purposes, the outcomes align closely with those expected under ideal isothermal conditions [104].

As delineated in the above description, isothermal calorimetry necessitates the measurement of the heat output rate of cement hydration under constant temperature conditions. Consequently, an isothermal calorimeter must be equipped with mechanisms to maintain both the apparatus and the specimen at a consistent temperature, as well as capabilities to monitor the thermal power of the sample. The maintenance of a consistent temperature within the isothermal calorimeter, as well as for the specimen, is facilitated by a computer-controlled thermostat. Figure 2.13 presents a schematic representation of an isothermal calorimeter as described in ASTM C1702-09a [105]. The outermost component is the thermostat, ensuring a consistent temperature environment. All other equipment components, as well as the samples, are situated within this thermostat to guarantee temperature stability throughout the experiment. As delineated in ASTM C1702-09a [105], an isothermal calorimeter is a sophisticated instrument designed for precise thermal measurements. At its core, it features a stable temperature heat sink, to which two heat-flow sensors and sample holders are meticulously attached, ensuring optimal thermal conductivity. One of these sensors and its sample holder houses the test sample, while the other serves as a reference with an inert sample that does not produce heat. The criterion for the reference sample mandates that its specific heat capacity should approximate that of the test sample. This congruence ensures that the reference and test samples exhibit consistent thermal responses with equivalent time constants. Such alignment is pivotal for maintaining a stable baseline and mitigating background noise in the measurements. In isothermal calorimetry tests for cement/mortar, water or sand is often selected as the reference sample. Figure 2.14 provides a sectional view of the interior of the isothermal calorimeter. The upper component, designated as the “Heat Sink Plug”, functions as the entry point for introducing ampoules filled with both test and reference samples into the instrument. The heat emanating from the sample’s hydration initially traverses through the base of the ampoule, entering the heat flow sensor, before being subsequently channelled to the heat sink. As the cementitious sample undergoes hydration, the liberated heat traverses the sensor, dissipating into the heat sink. The calorimeter’s output is derived from the differential heat flow between the sample and reference sample. Notably, the heat-flow sensor detects a minute temperature gradient across itself. However, the heat extraction from the hydrating sample is so efficient that the sample essentially remains isothermal. The sensor’s output is an electrical signal, mirroring the sample’s thermal power, which requires calibration against a known thermal benchmark. This calibration is achieved using a consistent, known power-emitting heat source. The cumulative thermal power over the test duration represents the hydration heat.

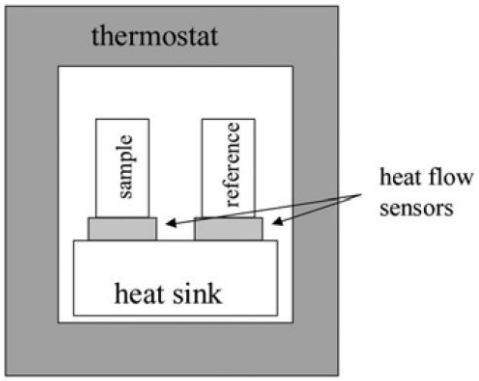

Figure 2.13. Schematic diagram of an isothermal heat transfer calorimeter from ASTM C1702-09a [105].

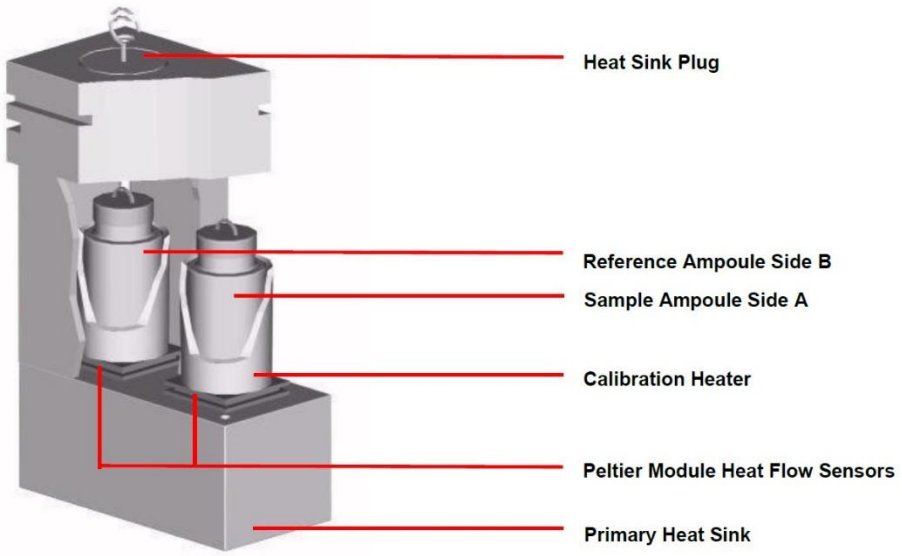

Figure 2.14. Cutaway view of the TAM Air isothermal calorimeter [106].

In isothermal calorimetry experiments, the sample mass is typically minimal. For instance, the ampoule capacity of an 8-channel TAM Air isothermal calorimeter is merely 20 mL, often accommodating samples weighing around 10g. Even the more giant 3-channel TAM Air calorimeter, designed for greater capacity, has an ampoule volume of just 125 mL, which can hold samples up to 50g. Figure 2.15 illustrates the ampoules of both TAM Air isothermal calorimeter models, highlighting their design and capacity differences. It is imperative to note that those above “10g” and “50g” do not represent the mass of the sample sufficient to fill the ampoule. On the contrary, it is not advisable to overfill the ampoule with the sample. As illustrated in Figure 2.14, the heat generated from the sample’s hydration is transmitted to the heat flow sensor through the ampoule base. As the mass of the sample increases, the height of the sample within the ampoule also rises. This elevation could potentially hinder the heat produced by the upper portions of the sample from reaching the heat flow sensor at the base, leading to experimental discrepancies. Furthermore, the specified “10g” and “50g” are not dictated by standardized guidelines or testing manuals. Instead, they are derived

from the empirical observations of previous researchers [1, 18, 107, 108] and the author's own experimental experiences. The precise mass of the sample to be used in experiments should be determined based on specific experimental requirements and the inherent properties of the sample.

Figure 2.15. TAM Air isothermal calorimetry ampoule [106] (left: 20mL, right: 125mL).

Isothermal calorimetry is widely used in the cement research. As previously discussed, it allows the heat output of cement hydration to be measured under constant temperature conditions. Modern isothermal calorimeters, such as the TAM Air [106], offer a wide range of operating temperatures from 5°C to 90°C. This versatility allows practical evaluation of the influence of temperature on hydration reactions. It also helps to estimate critical parameters such as the maximum heat of hydration [1, 5, 66], apparent activation energy [109-111] and hydration parameters [18, 99, 112]. Such information can be further used to predict the early-age hydration temperatures development in concrete and the risk of concrete thermal cracking [4]. It is essential to note that although instruments such as the TAM Air calorimeter can measure several samples simultaneously (up to eight in the case of the TAM Air), each experimental run is limited to a single temperature. This is due to the role of the thermostat in maintaining a uniform temperature throughout the calorimeter, including all inner components and samples, as shown in Figure 2.13. In addition, modern isothermal calorimeters usually have multiple channels that allow researchers to measure various samples simultaneously. For example, researchers can investigate the effects of supplementary cementitious materials or admixtures on the hydration reactions and their retardation. These capabilities enhance the applicability and efficiency of isothermal calorimetry in cement research.

In obtaining the heat of hydration of cement, isothermal calorimetry presents notable advantages when compared with semi-adiabatic and adiabatic calorimetry. One of the primary merits of isothermal calorimetry lies in its direct measurement capability of the hydration heat power of the sample. As delineated in the prior two sections, semi-adiabatic and adiabatic calorimetry methods necessitate extrapolating the hydration heat curve based on observed temperature development in the concrete. This approach can introduce potential experimental inaccuracies due to factors such as the insulating capacity of the adiabatic calorimeter and errors in the thermal compensation process in

semi-adiabatic calorimetry. Furthermore, some researchers [113-116] posit that the thermal properties of early-stage concrete, specifically its thermal conductivity and specific heat capacity, may evolve throughout its curing duration. Consequently, employing a fixed specific heat capacity for deducing hydration heat could engender additional errors. The nature of isothermal calorimetry, which directly measures the power of the heat of hydration, eliminates the need for the experimenter to know the thermal properties of the sample, thus avoiding possible errors in this respect. Additionally, as discussed above, the specimen size required for isothermal calorimetry is substantially smaller than that for semi-adiabatic and adiabatic methods, offering a more streamlined sample preparation process. Furthermore, modern isothermal calorimeters are often characterized by their high precision and robust stability. Such instruments typically do not necessitate frequent calibration. For instance, the TAM Air user manual [106] recommends a calibration frequency of four times annually, provided there are no alterations in the operational temperature of the device. In contrast, adiabatic calorimetry requires calibration prior to each experimental run [16], underscoring the operational efficiency of the isothermal calorimetry.

Wang *et al*. [117] investigated the effects of different mixing times on the heat release during the hydration process. They evaluated various mixing durations to determine their impact on the precision and consistency of the hydration heat measurements. The study employed external mixing (EM) and internal mixing (IM) procedures to assess the heat release. For the EM procedure, different mixing times were tested to find the optimal duration that ensures adequate dispersion of cement particles without excessive heat loss. They found that a mixing time of 75 seconds at 2000 r/min provided the best balance, resulting in consistent and reliable hydration heat measurements. Wang *et al.* observed that shorter mixing times (45 s) led to insufficient mixing, resulting in lower heat release values due to the inadequate dispersion of cement particles. Conversely, longer mixing times (120 s) caused excessive loss of hydration heat during the mixing period, which also skewed the results. Their findings underscore the importance of standardized mixing times to achieve accurate and reproducible calorimetric data. Furthermore, the study highlighted the precision of isothermal calorimetry in capturing early-age hydration heat, emphasizing its advantages over traditional methods such as the solution calorimetry described by ASTM C186-05 [118]. Isothermal calorimetry provides direct measurement of hydration heat flow, eliminating the need for complex calculations based on thermal properties like specific heat capacity and thermal conductivity. This precision makes it an invaluable tool for evaluating the effects of variables such as mixing time and aggregate content on cement hydration. By adopting a 75-second mixing duration, Wang *et al.* ensured that their calorimetric measurements were both precise and representative of the true hydration behaviour of the cement samples.

One potential drawback of isothermal calorimetry in concrete research stems from the limited capacity of its ampoules or channels designated for sample containment. This restriction often results in the fact that the coarse aggregate in the concrete cannot be

added to the ampoules. As a result, the typical study subjects in isothermal calorimetry tend to be cement pastes or mortars rather than concrete compositions. Wadsö [16] used an 8-channel TAM Air isothermal calorimeter to examine the influence of aggregate addition on cement hydration heat development. The maximum capacity of 20mL per channel for this calorimeter restricted the experiments to aggregates with a maximum particle size of 5mm. The results showed that samples with aggregates had an increased peak heat release rate compared to pure cement pastes. The difference in peak heat release rate was about 0.3mW/g, as inferred from the graphs presented by Wadsö. Based on this slight difference, Wadsö suggested that isothermal calorimetry results from equivalent mortars or cement pastes could represent the heat of hydration in concrete. However, Wadsö also recognized the limitations imposed by the channel capacity, which prevented the inclusion of larger-sized coarse aggregates commonly used in actual concrete mixes. On the contrary, Xu *et al.* [18, 99] obtained concrete hydration parameters by using semi-adiabatic calorimetry (concrete specimens) and isothermal calorimetry (mortar specimens) tests separately. These parameters were subsequently utilized in numerical simulations to predict the evolution of hydration temperatures in concrete pavements. The results showed that the semi-adiabatic calorimetry-based numerical model was more accurate than the one based on isothermal calorimetry. Xu *et al.* suggested that this discrepancy might arise from the inherent differences between the mortar used in isothermal calorimetry and the actual concrete composition. Thus, the isothermal calorimetry method might fall short of capturing the influence of coarse aggregates on the hydration heat of concrete. This issue stands as a contentious point in the realm of concrete research. Further experimental investigations are imperative to assess this contentious point, which constitutes one of the primary experimental works undertaken by the author's PhD work for a detailed understanding of this matter. Thus, while isothermal calorimetry offers valuable insights into the hydration process, its potential limitations warrant meticulous scrutiny and validation, especially concerning the role of coarse aggregates on the cement hydration heat.

In conclusion, isothermal calorimetry is a pivotal tool in cement and concrete research, offering direct and precise measurements of the hydration heat power under constant temperature conditions. It has inherent advantages, such as directly measuring the hydration heat power of cement and requiring less sample preparation, underscoring its significance in the field. The TAM Air is an example of a modern isothermal calorimeter that offers high precision, stability, and multi-sample testing capabilities. However, the method has its limitations. The small capacity of the calorimeter's containers often prevents the inclusion of coarse aggregates, which might affect the results when applied to actual concrete compositions. While studies like those of Wadsö [16] suggested that mortars or cement pastes can be representative of concrete hydration heat. Others, such as the findings of Xu *et al.* [18, 99], believed that coarse aggregates in concrete affect the development of the hydration heat of cement, which further affects the subsequent prediction of concrete temperatures. This divergence accentuates the need for a holistic understanding and further empirical exploration, especially concerning the influence of coarse aggregates.

2.4.4 Comparison of Different Calorimetry Techniques

The three calorimetry methods discussed above, adiabatic, semi-adiabatic, and isothermal calorimetry, each have unique strengths and limitations in measuring the heat evolution during cement hydration. Selecting the appropriate approach requires a nuanced evaluation of these techniques in the context of specific research objectives.

Adiabatic calorimetry is pivotal for simulating the temperature progression within the core of large-volume concrete structures. This method necessitates a specialized system to ensure adiabatic conditions and negligible heat loss during the measurement phase, facilitating the acquisition of the concrete's adiabatic temperature rise curve. The hydration heat evolution curve can be deduced by utilizing the specific heat capacity of the concrete specimen. Given the assumption of no heat loss, the derived hydration curve represents the entire cement hydration process. Such data is instrumental for subsequent calculations related to cement hydration parameters and predictive modelling of concrete temperature evolution. However, achieving actual adiabatic conditions requires intricate and costly temperature control systems, making it a challenge in practical applications.

Semi-adiabatic calorimetry offers a more streamlined approach compared with adiabatic calorimetry. The semi-adiabatic method permits some heat dissipation from the concrete specimen. The designed calorimetry monitors this dissipation, and a subsequent heat loss compensation procedure is employed to deduce the concrete's adiabatic temperature rise curve. The ensuing procedures for deriving the hydration heat closely mirror the adiabatic method. Its efficacy has garnered validation from multiple studies, positioning it as a robust alternative to the adiabatic calorimetry. Its primary advantage lies in its cost-effectiveness and operational simplicity, eliminating the need for elaborate equipment.

However, both the adiabatic and semi-adiabatic methods share inherent limitations. Their primary focus is on the temperature evolution of specimens, meaning that various factors can influence subsequent hydration heat deductions. These include the accuracy of the concrete specimen's specific heat capacity, which might fluctuate, especially in early-age concrete, the device's adherence to standard adiabatic conditions, and the calibration status of the equipment.

In contrast, isothermal calorimetry directly measures cement hydration heat power under constant temperature conditions, circumventing the errors inherent in the other two methods. Typically requiring minimal specimens, it presents a cost-effective alternative in terms of raw material preparation. Modern isothermal calorimeters have enhanced sensitivity and stability, ensuring precise measurements. However, its limitation arises from the small capacity of its ampoule, which challenges its ability to accommodate the larger aggregate sizes found in real concrete. The debate on whether

the isothermal calorimetry curve of cement paste or mortar can truly represent equivalent concrete remains contentious, emphasizing the need for rigorous experimental validation. Table 2.1 provides a structured comparison of the three calorimetry methods, highlighting their specific applications, insulation materials, data measurement techniques, and potential challenges.

This section explored three distinct calorimetry methods for assessing the heat evolution in cementitious materials: adiabatic, semi-adiabatic, and isothermal calorimetry. Adiabatic and semi-adiabatic methods derive the heat evolution of cement hydration through the adiabatic temperature rise curve of concrete. On the other hand, isothermal calorimetry offers the advantage of direct heat power measurements under constant conditions. However, each method presents its own set of challenges. While the adiabatic and semi-adiabatic techniques require intricate devices and procedures, isothermal calorimetry, despite its precision, cannot incorporate coarse aggregates in its specimens. Each calorimetry method has its advantages and challenges. It is essential to be aware of each method's potential errors and inherent limitations.

Table 2.1. Comparison of different calorimetry methods.

Criteria	Adiabatic Calorimetry	Semi-adiabatic Calorimetry	Isothermal Calorimetry
Purpose	Simulate temperature development in mass concrete under near-adiabatic conditions.	Simulate temperature development in in-situ concrete with some heat loss.	Direct measurement of hydration heat power under constant temperature.
Curing Conditions	Near-adiabatic conditions (no heat loss).	Semi-adiabatic conditions (some heat loss allowed).	Isothermal conditions (constant temperature).
Common Insulation Measurement Employed	Specialized temperature control systems to ensure adiabatic conditions.	Sufficient insulation setup to cover the specimen.	Thermostats for maintaining constant temperature.
Project Applications	Mass concrete structures such as dams, large foundations.	In-situ concrete structures, general construction applications.	Laboratory studies, cement and mortar research.
Specimen Size	Larger specimens (mass concrete size).	Intermediate size specimens (closer to actual in-situ concrete size).	Smaller specimens (cement paste, mortar).

Data Measured	Temperature evolution, hydration curve (indirect heat of hydration).	Temperature evolution, hydration curve (indirect heat of hydration).	Direct heat power of hydration, hydration curve.
Heat Loss Consideration	Designed to have negligible heat loss (ideal conditions).	Allows for heat loss, compensated in data analysis.	No heat loss (ideal constant temperature).
Accuracy and Precision	High accuracy if conditions are perfectly adiabatic.	Moderate accuracy, influenced by heat loss compensation accuracy.	High accuracy, direct measurement with modern calorimeters.
Cost and Complexity	High cost and complex setup due to temperature control systems.	Lower cost and simpler setup compared to adiabatic method.	Moderate cost, simpler setup, but limited by specimen size.
Challenges	Achieving perfect adiabatic conditions, expensive setup.	Ensuring accurate heat loss compensation, non-uniform temperature distribution.	Limited capacity for coarse aggregates, potential discrepancies with actual concrete.
Standards and Guidelines	BS EN 12390-15:2019 [94].	BS EN 12390-14:2018 [100].	ASTM C1702-09a [105], BE EN 196-11:2018 [104].

2.5 Maturity-Based Models for Cement Hydration

While the experimental methods discussed in Section 2.4 provide valuable insights into the direct or indirect measurement of heat evolution due to cement hydration in concrete, they present limitations when extrapolated to real-life concrete structures (in-situ concrete). The data obtained from these laboratory tests predominantly represent the specific conditions of the test specimens and may not necessarily mirror the complexities of in-situ concrete temperature development. Modern construction often involves the use of large-volume or long-span concrete structures. These structures, due to their sheer size and geometry, inherently influence the temperature development within the concrete and concrete heat dissipation, further affecting the progression of cement hydration. Additionally, the ambient conditions surrounding in-situ concrete are dynamic and multifaceted, adding complexity to the hydration heat development. Such intricacies make it challenging to apply laboratory findings to real-world applications directly.

Considering these complexities, it becomes essential to employ mathematical methods

to establish a bridge between laboratory results and actual in-situ concrete scenarios, ensuring that laboratory findings can serve as a component in predicting the temperature development of in-situ concrete. This leads to the exploration of the maturity method. The maturity theory offers a framework that considers the time and temperature histories of concrete, bridging the gap between laboratory measurements and actual temperature development in-situ concrete structures. In the forthcoming Section 2.5, the different theories and methodologies underpinning the concrete maturity concept will be delved into, elucidating how they can be employed to predict early-age temperature development in concrete with greater precision.

Firstly, this section introduces two widely recognized concrete maturity formulas: the Nurse-Saul Maturity and the Equivalent Age Maturity. These formulas are mathematical functions that describe concrete's relative degree of hydration at different times and temperatures. They are based on the assumption that concrete strength is proportional to its degree of hydration. These formulas are recommended by ASTM C1074 [119] as standard methods for estimating concrete strength from its temperature history. Secondly, this section explains the concept of apparent activation energy, a decisive parameter in the maturity formulas. The apparent activation energy represents the effect of temperature on the hydration reaction rate. It can be determined by experimental tests or empirical equations. Subsequently, this section discusses the relationship between concrete maturity and hydration heat evolution, which is the first and fundamental step to using laboratory data to predict the temperature development of in-situ concrete. The heat evolution curve for concrete is derived by scaling its degree of hydration curve with a constant factor known as the ultimate heat of hydration per unit mass of cement. This factor epitomizes the cumulative heat liberated upon the complete hydration of a unit mass of cement. By differentiating this heat evolution curve with respect to time, one can ascertain the heat power or the rate of heat flow in concrete at any given moment. Finally, this section discusses the relationship between concrete maturity and hydration heat evolution, which is the first and fundamental step to using laboratory data to predict the temperature development of in-situ concrete, which details how the experimental results in Section 2.4 can be used in the derivation process for predicting the hydration heat rate development of cement under variable self-temperatures and on-site conditions. This maturity method-based iteration process allows the derivation of the rate of hydration at each time step of concrete hardening in the field. This result will be used as the heat source part of the numerical model for concrete temperature prediction.

2.5.1 Nurse-Saul Maturity Method

The concrete maturity method describes the combined effect of curing temperature and time on the development of the mechanical properties of concrete [113]. The basic assumption of the maturity method is that concrete of the same mix and the same maturity has approximately the same strength, regardless of the temperature and time history. This principle was proposed by Saul [120] in the early 1950s. The maturity

equation is a mathematical expression that describes the maturity of concrete as a function of time and temperature as can be written as follows:

$$M = \sum_{0}^{t} (T - T_0)\,\Delta t \tag{2.8}$$

where M is the maturity of the concrete, t is the concrete age, T is the average temperature during the time interval Δt, t_0 is the age at which concrete begins to develop strength, T_0 is the datum temperature.

Eq. (2.8) is recognized as the Nurse-Saul Maturity equation. It is often termed the "temperature-time factor" since it is derived by multiplying the mean temperature of the concrete over a specific time duration with the concrete's age. A pivotal component in this equation is the datum temperature, the critical threshold below which the hydration reaction of cement in concrete is arrested. When the curing temperature falls below this datum temperature, the hydration reaction of cement ceases, leading to a halt in the development of both concrete strength and heat of hydration. Saul [120] proposed -10°C as the datum temperature for the concrete maturity equation. However, it is crucial to note that this suggested value is a rough estimate derived under the specific experimental conditions of that time. According to ASTM C 1074 [119], the datum temperature can fluctuate based on the cement type, the kind and amount of admixtures incorporated, other components influencing the hydration speed, and the temperature spectrum the concrete undergoes during hardening. ASTM C 1074 provides a standardized procedure to determine the datum temperature for concrete through mortar strength tests.

While the Nurse-Saul maturity method offers valuable insights, it is imperative to recognize its inherent assumptions and limitations. A core assumption is a linear relationship between concrete strength development and temperature, which might not universally hold across varied concrete compositions or thermal scenarios. Saul himself highlighted certain constraints of his maturity equation. His empirical observations revealed that the equation tended to underestimate the early strength of concrete cured at elevated temperatures while overestimating its strength at later stages.

Despite its widespread use and standardization by ASTM C1074 [119], the Nurse-Saul maturity method has notable limitations. A fundamental assumption of this method is the linear relationship between temperature and the rate of strength gain, which can be overly simplistic. This linear approximation often fails to accurately capture the actual strength development under varying temperature conditions, especially those outside the typical range of 0-40ºC. The method's reliance on a fixed datum temperature, commonly set at 0ºC, -5ºC, or -10ºC, further complicates its accuracy. This temperature, below which concrete is presumed not to gain strength, can vary based on specific mix designs and environmental factors, leading to potential errors in maturity calculations

if not correctly estimated [121, 122].

Moreover, concrete strength development exhibits non-linear behaviour with respect to temperature, a nuance that the Nurse-Saul method does not account for. Advanced models, such as the Arrhenius maturity function (will be discussed in the next section), provide a more accurate representation by considering the activation energy required for hydration reactions. Comparative studies [123-125] have demonstrated the superior accuracy of the Arrhenius approach, particularly under varying temperature regimes. While the simplicity and ease of application of the Nurse-Saul method make it popular for routine use, its limitations suggest that alternative methods like the Arrhenius function are preferable for more precise strength estimation in critical projects or environments with significant temperature fluctuations. Therefore, while the Nurse-Saul method remains a valuable tool, its inherent assumptions necessitate cautious application and, where possible, supplementation with more robust predictive models.

2.5.2 Equivalent Age Maturity Method

Based on Saul's foundational work and acknowledging the constraints of the Nurse-Saul Maturity equation, Rastrup [126] introduced the concept of "equivalent age". The equivalent age delineates the time required for a concrete mix to be cured at a designated reference temperature to attain a maturity index analogous to what it would achieve under a different curing temperature condition. Rastrup's modified maturity equation and equivalent age as illustrated in Eq. (2.9) and Eq. (2.10) respectively.

$$M = \int_0^t K(T)dt = \int_0^{t_{eq}} K(T_r)dt \tag{2.9}$$

$$t_e = \int_0^t \frac{K(T)}{K(T_r)}dt \tag{2.10}$$

where t_e is the concrete equivalent age, T_r is the reference temperature, usually taken at 20°C. K is the hydration reaction rate constant.

Since cement hydration is an exothermic reaction that causes strength development, Tank and Carino [127] proposed a hyperbolic Arrhenius equation to describe the effect of temperature on the rate constant, as follows:

$$K(T) = Ae^{\left(\frac{-E_a}{R \cdot T}\right)} \tag{2.11}$$

where K(T) is the rate constant at temperature T, A is a constant of proportionality, E_a is the activation energy (J/mol), which is a key parameter and will be discussed in detail

later. R is the universal gas constant = 8.314 (J/Kmol), T is the temperature (K).

By associating Eq. (2.10) and Eq. (2.11), an Arrhenius-based expression for the equivalent age of concrete can be derived in Eq. (2.12), known as the Equivalent Age Maturity equation.

$$t_e = \sum e^{\frac{-E_a}{R}\left(\frac{1}{T}-\frac{1}{T_r}\right)} \cdot \Delta t \tag{2.12}$$

The following equation is a general expression of the equivalent age concept:

$$t_e = \sum f(T) \cdot \Delta t \tag{2.13}$$

where f(T) is the "age conversion factor". An "age conversion factor" translates the curing interval Δt at curing temperature T into an equivalent curing interval Δt_e at a reference temperature T_r. This allows for the conversion between curing times at different temperatures by applying the age conversion factor as a translation coefficient.

From the Equivalent Age Maturity equation, it is evident that the relationship between equivalent age (or maturity) and temperature is non-linear, contrasting with the linear relationship between maturity and temperature posited by the Nurse-Saul Maturity equation. Numerous studies [22, 128-131] have corroborated that the accuracy of the Equivalent Age Maturity equation in predicting the development of concrete strength surpasses that of the Nurse-Saul Maturity equation. This has led to the predominant adoption of the Equivalent Age Maturity as the foundational theory in contemporary research on predicting concrete strength and hydration temperature. Concurrently, it serves as one of the fundamental theories underpinning the author's work on concrete temperature prediction.

Venturing further, the Equivalent Age Maturity serves as a conduit to derive the cement hydration heat rate equation, anchored in the concrete equivalent age concept. This transformation enables the extrapolation of laboratory-acquired hydration heat data to in-situ concrete conditions at distinct temporal and thermal junctures, laying the foundation for the heat source component in the concrete temperature prediction model. This process requires further integration of theories related to the degree of cement hydration and hydration kinetic, etc., which will be discussed in the following sections.

2.5.3 Apparent Activation Energy in Hydration Models

In chemical kinetics, the activation energy represents a paramount parameter that delineates the minimum energy threshold required for reactant molecules to transition to an activated complex or transition state, thereby facilitating the progression of a chemical reaction. Essentially, it quantifies the energy barrier that reactants must overcome to convert into products. The magnitude of activation energy profoundly

influences the temperature sensitivity of the reaction rate. As encapsulated by the Arrhenius equation, a higher activation energy implies that the reaction is more sensitive to temperature variations. Conversely, a reaction with a lower activation energy exhibits diminished temperature sensitivity [22, 132, 133]. The expression for the activation energy can be derived by doing a simple mathematical transformation of Eq. (2.12):

$$E_a = -RT \cdot \ln\left(\frac{K}{A}\right) \tag{2.14}$$

The Arrhenius equation (Eq. (2.11) or Eq. (2.14)) is a mathematical model that describes how the temperature affects the rate of a simple chemical reaction. However, applying this law to the case of cement hydration is only an approximation because cement hydration is not a single reaction but a complex process that involves several interrelated reactions of different cement components (as described in Section 2.2.1). Theoretically, the activation energies for each of the four principal compounds in cement can be individually determined using the Arrhenius equation. However, current methodologies for measuring the activation energy of concrete treat specimens as an integrated whole, ascertaining it through compressive strength tests or isothermal calorimetry (the discussion on these testing methods will be presented subsequently). Therefore, the derived activation energy values represent the entirety of the cement hydration process rather than any individual reaction. The activation energy, in this case, is not the actual energy barrier for a specific reaction but an empirical parameter that reflects how sensitive the overall reaction rate is to temperature changes. This is why the activation energy is called "apparent" in the context of cement hydration [133-135].

Within the Equivalent Age Maturity equation context, the apparent activation energy emerges as the singular undetermined parameter essential for the computation of the equivalent age. As such, the precision associated with determining the apparent activation energy bears direct implications on the accuracy of the equivalent age estimation and the subsequent modelling of cement hydration heat and the concrete temperature development. Numerous researchers and established national standards have proffered methodologies for gauging the apparent activation energy.

Freiesleben-Hansen and Pedersen [136] are recognized as the researchers who first proposed the equation for calculating the apparent activation energy of concrete. They suggested that the apparent activation energy of concrete is not contingent upon the concrete mix but is solely influenced by temperature. They proposed that when the curing temperature exceeds 20°C, the apparent activation energy remains constant at 33,500 (J/mol). Conversely, when the temperature falls below 20°C, a linear relationship exists between the apparent activation energy and the temperature. The formulations posited by Freiesleben-Hansen and Pedersen for the apparent activation energy can be articulated through Eq. (2.15) and Eq. (2.16).

For T ≥ 20°C,

$$E_a = 33500\ J/mol \tag{2.15}$$

For T ≤ 20°C,

$$E_a = 33{,}500\ + 1450 \times (20\ - T\ )\ J/mol \tag{2.16}$$

However, considering contemporary research, such a rudimentary assumption appears simplistic. Malhotra and Carino [137] have indicated that the value of activation energy is influenced by various properties of the concrete mix, including the chemical composition, the type and amount of cement and admixtures incorporated, and the fineness of the cement. This is especially true considering the plethora of cement types, supplementary cementitious materials, and additives in today's market. As delineated in Section 2.2.3, the type of cement and the incorporation of various cementitious materials and additives can significantly influence the rate of cement hydration and the peak heat of hydration. Consequently, different concrete mixes are bound to exhibit distinct apparent activation energy values. This underscores the need for more rigorous experimental investigations and mathematical derivations to determine the apparent activation energy accurately. The following section will introduce several test and calculation procedures for determining the apparent activation energy of concrete that are widely used in engineering and scientific research.

2.5.3.1. ASTM C1074 Approach

ASTM C1074 [119] proposes a standard method for calculating the apparent activation energy of concrete by mortar strength testing. The binder content and water-cement ratio of the equivalent mortar specimens should be consistent with that of the concrete, and the fine aggregate-to-cement ratio (by weight) in the mortar specimens is mandated to align with the coarse aggregate-to-cement ratio in the concrete specimens. This stipulation ensures that, under identical curing conditions, the strength evolution of the equivalent mortar mirrors that of the concrete. The mortar specimens were subjected to curing in three distinct isothermal water baths. These three temperatures respectively represent the potential minimum and maximum temperatures attained during the concrete hydration process, as well as an intermediate temperature between the above two values.

The principle of this method involves a straightforward mathematical transformation of the Arrhenius equation, as illustrated in Eq. (2.17). This transformation elucidates a direct linear correlation between the inverse of temperature (1/T) and the natural logarithms of the rate constant (ln(K)). Consequently, the question pivots to determining the rate constant under various curing temperatures. The ASTM standard recommends employing Eq. (2.18), where the time-strength relationship of the mortar

is acquired and subsequently utilized to ascertain the value of the rate constant through data fitting. Figure 2.16 shows an example plot of ln(K) versus 1/T drawn by this procedure.

$$\ln(K) = -\frac{E_a}{RT} + lnA \tag{2.17}$$

$$S = S_u \frac{K(t - t_0)}{1 + K(t - t_0)} \tag{2.18}$$

where K is rate constant of cement hydration, S_u is the ultimate strength of concrete, the value of K and S_u. As mentioned above, the values of both K and S_u were fitted from the results of the mortar strength tests and Eq. (2.18).

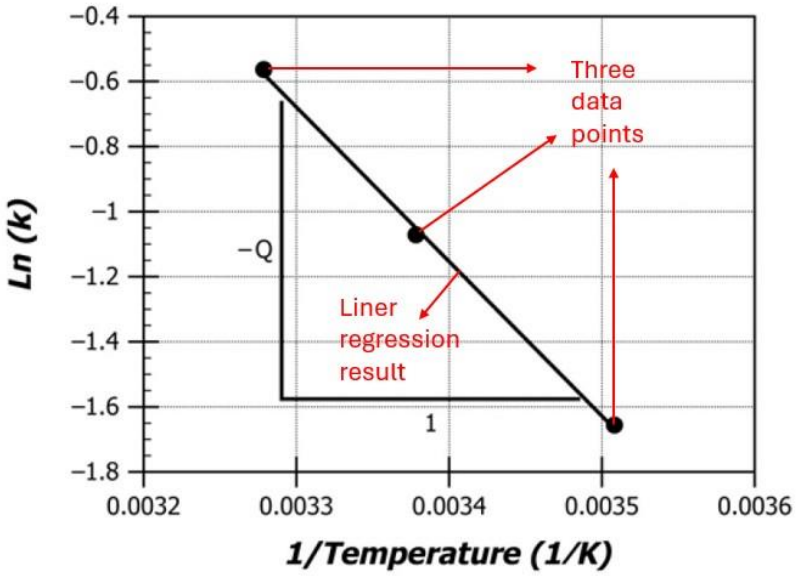

Figure 2.16. Example of plot ln(K) versus 1/T to determine E_a by ASTM C1074 method [119].

2.5.3.2. Three Parameters Equation (TPE) Model

Freiesleben Hansen and Pedersen [138] proposed a new equation to describe the relationship between concrete strength development and equivalent age maturity in 1977 (as shown in Eq. (2.19)).

$$S(t_e) = S_u \cdot e^{\left(-\left(\frac{\tau_r}{t_e}\right)^{\alpha}\right)} \tag{2.19}$$

where $S(t_e)$ is the concrete strength at equivalent age t_e, S_u is the ultimate strength of the concrete, τ_r is the concrete strength development time parameter at reference temperature, and α is the concrete strength development shape parameter.

The effect of the TPE strength-maturity correlation function on the estimation of the activation energy and the temperature sensitivity of the strength development is worth investigating. The equivalent age t_e is calculated by using the age conversion factor f (T), which can be obtained by a simple mathematical transformation of Eq. (2.13) (as shown in Eq. (2.20)). Integrating Eq. (2.19) and Eq. (2.20), it becomes evident that the age conversion factor correlates with the characteristic time constant, denoted as τ at a specific temperature T, as illustrated in Eq. (2.21).

$$f(T) = \frac{t_e}{t} \tag{2.20}$$

$$f(T) = \frac{\tau_r}{\tau} \tag{2.21}$$

where f(T) is the "age conversion factor" as defined previously, τ_r is the concrete strength development time parameter at reference temperature, τ is the concrete strength development time parameter at a specific temperature.

By integrating Eq. (2.10), Eq. (2.13), and Eq. (2.21), the relationship can be established between the rate constant K at a specified temperature and its counterpart at the reference temperature in terms of hydration time parameters:

$$\frac{K(T)}{K(T_r)} = \frac{\tau_r}{\tau} \tag{2.22}$$

By integrating Eq. (2.10), Eq. (2.12), and Eq. (2.22), the equation for the apparent activation energy, expressed in terms of the time parameter τ, can be derived in Eq. (2.23). Converting Eq. (2.23) into the format of Eq. (2.17) gives Eq. (2.24).

$$-\frac{E_a}{R} = \frac{\ln\left(\tau/\tau_r\right)}{\left(1/T_r - 1/T\right)} \tag{2.23}$$

$$\ln(\tau) = \frac{E_a}{RT} - \frac{E_a}{RT_r} - \ln(\tau_r) \tag{2.24}$$

By conducting mortar strength tests same as those described in the above ASTM Method, the value of τ can be determined through regression analysis of Eq. (2.19). Subsequently, by comparing the natural logarithm of τ values with the inverse of the temperature T in Eq. (2.24), the value of E_a/R is then equal to the slope of the best-fit line for a linear fit of ln(τ) to 1/T.

The TPE Strength-Maturity Equation Eq. (2.19), while employing the same experimental approach as the ASTM C1074 Method, adopts a distinct Strength-

Maturity correlation. This highlights the versatility in correlating strength and maturity, even when the foundational methodologies remain consistent. Cudowska and Haustein [107] evaluated the apparent activation energy values for OPC and OPC-FA blended mixtures using the TPE Strength-Maturity Equation and the ASTM Method. The findings suggest that the values derived from the TPE Strength-Maturity Equation are slightly higher than those from the ASTM Method, with a maximum deviation of approximately 4 KJ/mol. Cudowska and Haustein refrained from commenting on the accuracy of the two methods, which may be because current testing techniques might not yield an unequivocally precise value. In a parallel study, Hatzitheodorou [22] conducted similar tests on a broader range of concrete mixes, including those with GGBS and FA additions. His conclusions aligned with Aleksandra *et al.*'s [107] conclusions, noting a slight elevation in values from the TPE Strength-Maturity Equation. The apparent activation energy values obtained from both testing procedures were consistent with literature values for similar concrete mixes, underscoring the reliability of both methodologies.

2.5.3.3. Determining Activation Energy from Calorimetry Data

By conducting isothermal calorimetry tests on samples of the same mix at varying constant temperatures, the resultant data can be utilized to compute the apparent activation energy of the specimen. Analogous to the above two mortar strength test methods, isothermal calorimetry allows for applying the same experimental procedure, followed by using two distinct cement hydration heat-maturity correlation formulas to estimate the apparent activation energy. A fundamental assumption underpinning this approach is that the progression of cumulative cement hydration heat is directly proportional to concrete strength development and hydration degree [135, 139]. Consequently, the fundamental assumption of concrete maturity can be extended to hydration heat and hydration degree. For a concrete mix of the same composition, possessing an equivalent maturity level will invariably result in consistent strength, cumulative hydration heat, and hydration degree, irrespective of its temperature and time history.

Reinhardt *et al.* [140] proposed a mathematical relationship between the rate of cement hydration heat (Q) and the degree of cement hydration (α). The degree of cement hydration is the ratio of the evolved hydration heat to the theoretical maximum hydration heat (Eq. (2.25)), which will be elaborated upon in subsequent sections. By differentiating (with time) both sides of this equation, they derived a normalized heat generation rate f(α), which equals the hydration rate at a specific time Q(t) divided by the hydration peak value Q_{peak}, which relates the degree of cement hydration to the rate of cement hydration (see Eq. (2.26)). When they plotted the hydration curve from the isothermal calorimetry test with α as the x-axis and f(α) as the y-axis, it was observed that the f(α)-α curves at different temperatures nearly coincide (as shown in Figure 2.17).

$$\alpha(t) = \frac{H\,(t)}{H_u} \tag{2.25}$$

$$f(\alpha) = \alpha\dot{(t)} = \frac{H\,\dot{(t)}}{H_u} = \frac{Q(t)}{Q_{peak}} \tag{2.26}$$

where H(t) is the cumulative hydration at time t, H_u is the theoretical maximum heat of hydration of the cement (Ultimate Heat of Hydration), representing the heat of hydration resulting from the complete hydration of the mineral constituents of the cement, which can be determined via chemical analysis for cement, will be specifically discussed in subsequent sections. Q(t) is the hydration rate at time t, Q_{peak} is the hydration peak during the isothermal calorimetry test, f(α) is the normalized hydration heat rate function, which equals the hydration rate at a specific time Q(t) divided by the hydration peak value Q_{peak}.

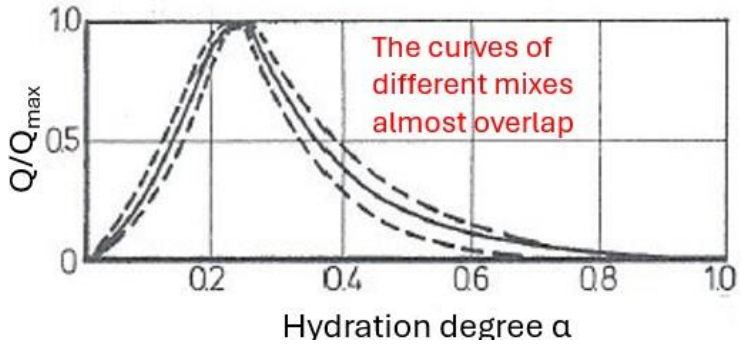

Figure 2.17. Normalized heat generation rate f(α) versus hydration degree α at different isothermal conditions, plotted by Reinhardt *et al.* [140] (Different curves represent f(α)-α curves at different temperatures).

The mathematical model introduced by Reinhardt *et al.* [140] is grounded on a fundamental premise, as supported by the analysis above, the rate of heat production can be represented as the multiplication of two distinct functions. One function, f(α), accounts for the extent of heat evolution. At the same time, the other, g(T), captures the impact of temperature, which can be characterized using the Arrhenius equation (Eq. (2.11)) as discussed in Section 2.5.2. Thus, the rate of hydration heat of cement can be expressed as [19, 20]:

$$Q = f(\alpha) \cdot g(T) = f(\alpha) \cdot Ae^{\left(\frac{-E_a}{R \cdot T}\right)} \tag{2.27}$$

This procedure is a variant of the ASTM C1074 method, wherein the mortar strength test is substituted with an isothermal calorimetry experiment. By following a similar logarithmic transformation as in the ASTM C1074 method, it can be deduced that:

$$\ln(Q) = \ln\left(f(\alpha) \cdot Ae^{\left(\frac{-E_a}{R \cdot T}\right)}\right) \tag{2.28}$$

It becomes evident that within Eq. (2.28), the presence of two multiplicative functions complicates its logarithmic form, potentially increasing the computational complexity in subsequent applications. To simplify, one can consider the peak hydration rate at each constant temperature for subsequent calculations. At this juncture, f(α) is set to 1, transforming Eq. (2.27) and Eq. (2.28) into the forms of Eq. (2.29) and Eq. (2.30), respectively. Consequently, the natural logarithm of the hydration rate, $\ln(Q_{peak})$, exhibits a linear relationship with the apparent activation energy E_a. By conducting isothermal calorimetry experiments at a minimum of three temperatures, the negative slope of the linear regression curve between $\ln(Q_{peak})$ and $1/T_{abs}$ directly corresponds to the value of E_a/R.

$$Q = Ae^{\left(\frac{-E_a}{R \cdot T}\right)} \tag{2.29}$$

$$\ln\left(Q_{peak}\right) = -\frac{E_a}{RT} + lnA \tag{2.30}$$

The TPE equation can also represent the evolution of cement hydration heat. Once again, under the assumption that the cumulative heat development from cement hydration is directly proportional to both the degree of hydration and the development of concrete strength [135], the strength term in Eq. (2.19) can be substituted with cumulative hydration heat:

$$H(t_e) = H_u \cdot e^{\left(-\left(\frac{\tau}{t_e}\right)^{\beta}\right)} \tag{2.31}$$

where $H(t_e)$ is the cumulative hydration heat at equivalent age t_e, H_u is the ultimate heat of hydration of the cement, τ is the hydration heat time parameter, and β is the hydration heat development shape parameter. The two hydration parameters can be obtained through non-linear regression analysis of the results from isothermal calorimetry experiments.

Following the same derivation process as in Eq. (2.20) to Eq. (2.23), a linear relationship between the time parameter τ and E_a can be established:

$$\ln(\tau) = \frac{E_a}{RT} - \frac{E_a}{RT_r} - \ln(\tau_r) \tag{2.32}$$

Therefore, the natural logarithm of the hydration heat time parameter is directly proportional to the inverse of the temperature. A linear relationship graph between ln(t) and 1/T can be plotted using results from the isothermal calorimetry tests and the hydration time parameter fitted from Eq. (2.31). The slope of this straight line represents

the value of E_a/R.

2.5.3.4. Factors Influencing Apparent Activation Energy

To encapsulate the variations in the apparent activation energy of concrete with different mixes, as well as the experimental methodologies employed to ascertain the apparent activation energy, Malhotra and Carino [137] presented a comprehensive table (as shown in Table 2.2). This table summarizes the values of apparent activation energy determined for various concrete mixes across different studies, each employing unique experimental techniques. The values range between 41 KJ/mol and 67 KJ/mol, conspicuously exceeding the values calculated by Freiesleben-Hansen and Pedersen activation energy equations (Eq. (2.15) and Eq. (2.16)). From Table 2.2, it is evident that variations in cement type, the incorporation of Supplementary Cementitious Materials (SCMs), or the employment of different experimental methodologies can lead to significant alterations in the derived values of apparent activation energy. Specifically, the table indicates that adding GGBS results in an increase in the apparent activation energy for concrete. Among all the experimental methods, the values derived from the chemical shrinkage method consistently yield the highest apparent activation energy. Contrary to the FHP activation energy equations, the apparent activation energy obtained from Table 2.2 are constant values and not affected by temperature, aligning with the definition of E_a in Eq. (2.11). Furthermore, most experimental methods/standards produce a consistent and fixed value for the apparent activation energy. In practical applications, especially in predicting concrete temperature and strength development, utilizing a constant value for the apparent activation energy simplifies computational processes. Numerous existing studies corroborate that employing a constant value for this energy does not compromise the accuracy of predictive outcomes.

Table 2.2. Apparent activation energy values for various concrete mixes by various test methods summarized by Malhotra and Carino [137].

Cementitious Material	Type of Test	Activation Energy (kJ/mol)	Reference
Type I (mortar)	Compressive Strength	42	Carino N.J. [141]
Type I (mortar)	Compressive Strength	44	Carino N.J. [142]
Type I (concrete)	Compressive Strength	41	Carino N.J. [142]
PC (paste)	Heat of Hydration	42 – 47	Regourd M. [143] and Gauthier E. *et al*. [144]

PC + 70% GGBS (paste)	Heat of Hydration	56	Regourd M. [143] and Gauthier E. *et al*. [144]
PC (paste)	Chemical Shrinkage	61	Geiker *et al.* [145]
RHC (paste)	Chemical Shrinkage	57	Geiker *et al.* [145]
PC (paste)	Chemical Shrinkage	67	Geiker *et al.* [146]
Type I/II (paste)	Heat of Hydration	44	Roy D. M. *et al.* [147]
Type I/II + 50% GGBS (paste)	Heat of Hydration	49	Roy D. M. *et al.* [147]

Note: Type I = CEM I Cement; PC = Portland Cement; RHC = Rapid Hardening Cement; Type II = CEM II Cement.

Barnett *et al.* [148] determined the apparent activation energy of equivalent mortar specimens with varying GGBS content (replacement of part of PC) and water-cement ratios using the Compressive Strength Method, as presented in Table 2.3. Their findings suggest that the addition of GGBS increases the value of the apparent activation energy, indicating that the hydration reaction of GGBS is more temperature-sensitive than that of cement. Furthermore, Barnett *et al.* observed that altering the water-cement ratio of the specimens seemed to have little impact on the apparent activation energy. Contrarily, Tank's [149] experimental results (Compressive Strength Method), outlined in Table 2.4, demonstrate that this conclusion is only valid for specific mixes. In Table 2.4, except for Type III cement and Type I with added FA, significant changes in the apparent activation energy values were noted for other mixes when the water-cement ratio was varied. The activation energy values are higher for the low water-cement ratio mixtures when using Type I and Type II cements. However, the opposite trend is observed for the mortar mixture with Type I cement plus 50% GGBF slag, which has a higher activation energy value when it has a high water-cement ratio. Table 2.4 concluded that adding admixtures can change the activation energy for a specific cement type. The differences in activation energy based on cement type, slag content, water-cement ratio, and admixtures demonstrate the complex interactions between these factors in concrete mixtures.

Table 2.3. Apparent activation energy determined by Barnett *et al.* [148].

%GGBS	E_a (KJ/mol)		
	High w/b (0.52-0.62)	Medium w/b (0.36-0.40)	Low w/b (0.25-0.26)
0	34.8	35.1	32.9
20	36.6	35.2	36.8
35	47.1	47.0	46.8
50	54.6	48.0	52.6
70	58.8	62.1	57.9

Table 2.4. Apparent activation energy determined by Tank [149].

Cement Type	E_a (KJ/mol)			
	w/c ratio = 0.45		w/c ratio = 0.60	
	Concrete	Mortar	Concrete	Mortar
Type I	61	62	46	44
Type II	51	55	43	42
Type III	44	40	43	42
Type I + 20% Fly Ash	30	32	31	36
Type I + 50% Slag	46	44	44	51
Type I + Accelerator	46	54	49	51
Type I + Retarder	39	42	39	34

2.5.4 Ultimate Heat of Hydration

Section 2.5.3 delineates the concept of apparent activation energy for concrete and its computational methodology. Given the author's primary research focus on the heat of cement hydration and the predictive modelling of concrete hydration temperature, there is a compelling need to elucidate critical parameters within the procedure of determining the apparent activation energy via isothermal calorimetry. Such a detailed exploration aims to enhance the applicability and precision of predicting concrete temperature development.

Eq. (2.25) defines the degree of hydration of cement by the ratio of the heat of hydration, where the Ultimate Heat of Hydration H_u represents the total heat of hydration released when the cement is fully hydrated. In practical experimentation, achieving complete cement hydration necessitates an extended duration. Da Silva *et al.* [150] suggest that the ultimate heat of hydration refers to the cumulative heat emitted by a finely-milled binder over an approximate duration of three years in saturated conditions. Consequently, obtaining the ultimate heat of hydration for cement through calorimetry methods poses challenges. A three-year timeframe is typically deemed impractical for calorimetry tests. Additionally, there is the inherent challenge of maintaining consistent, error-free operation of the calorimeter over such an extended timeframe.

In Section 2.2.1, the hydration process of cement is elaborated upon, with C_3A and C_3S playing pivotal roles in generating most of the heat during hydration. Each of the four primary mineral components exhibits unique thermal characteristics. The "ultimate heat of hydration" encapsulates the total heat liberated when every cement particle reaches complete hydration. This can be determined by summing the total heat per unit mass released by each individual component of the cement when fully hydrated, which can be expressed as the following equation:

$$H_{cem} = \sum (H_i \cdot p_i) \tag{2.33}$$

where H_{cem} is the ultimate hydration heat of the cement (J/g), H_i is the ultimate hydration heat of the i-th component (J/g), and p_i is the proportion of the i-th component to total cement by mass.

According to Eq. (2.33), the calculation result of the ultimate heat of hydration of cement depends on the accuracy of the unit mass ultimate heat of hydration of each mineral component in the cement and the accuracy of the obtained mineral composition content results of the cement. For the ultimate heat of hydration of each mineral component, several previous studies have suggested their values. Schindler *et al.* [113] summarized them in a table, as shown in Table 2.5. The suggested values given by Bogue are the most widely applied because this considers the effects of Free Lime, MgO, and SO_3 rather than just the four main mineral components of cement.

Table 2.5. Ultimate hydration heat of cement compounds summarized by Schindler *et al.* [113].

Mineral component	Heat of hydration of individual component (J/g)			
	Mindess and Young [60]	SHRP-C-321 [151]	Bogue [152]	Kishi and Maekawa [153]
C_3S	490	500	500	502
C_2S	225	256	260	260
C_3A	1160	721	866	865
C_4AF	375	302	420	419
Free Lime	-	-	1165	-
MgO	-	-	850	-
SO_3	-	-	624	-

The four primary mineral composition of cement can be obtained by X-ray diffraction (XRD) or X-ray fluorescence (XRF) experiments. XRD and XRF are powerful techniques for analysing the composition of cement. XRD offers detailed insights into the crystallography of samples, identifying and quantifying mineral phases, but requires well-prepared samples and cannot detect amorphous phases [154]. On the other hand,

XRF provides rapid and reliable elemental analysis with minimal sample preparation, making it suitable for laboratory and field applications [155, 156]. However, XRF is limited to elemental (oxide component) analysis and may require additional laboratory confirmation. The introduction of the Bogue calculation has addressed this limitation. The Bogue calculation facilitates the estimation of the content of the four primary mineral components of cement based on the results of the oxide determination by XRF test. The mathematical equations for the Bogue calculation are shown in Eqs. (2.34)-(2.37). This calculation procedure is recommended by ASTM C150 [37] and has garnered widespread acceptance and application in academic research and industrial practice .

$$p_{C_3S} = 4.071p_{CaO} - 7.600p_{SiO_2} - 6.718p_{Al_2O_3} - 1.430p_{Fe_2O_3} \quad (2.34)$$

$$p_{C_2S} = 2.867p_{SiO_2} - 0.7544p_{C_3S} \quad (2.35)$$

$$p_{C_3A} = 2.650p_{Al_2O_3} - 1.692p_{Fe_2O_3} \quad (2.36)$$

$$p_{C_4AF} = 3.043p_{Fe_2O_3} \quad (2.37)$$

where P_i represents the percentage of component i in the total cement (by weight).

Based on the definition of the ultimate heat of hydration for cement as presented in Eq. (2.33), the recommended values for the ultimate heat of hydration per unit mass of individual cement components as listed in Table 2.5 by Bogue, and the calculation procedure delineated in Eqs. (2.34)-(2.37) for quantifying the four main mineral components in cement, Schindler and Folliard [37] have formulated an equation for calculating the ultimate heat of hydration. This equation also incorporates the thermal effects of SO_3, Free Lime, and MgO, as illustrated in Eq. (2.38).

$$H_{cem} = 500p_{C_3S} + 260p_{C_2S} + 866p_{C_3A} + 420p_{C_4AF} + 624p_{so_3} + 1186p_{Free\ Lime} + 850p_{MgO} \quad (2.38)$$

where p_i represents the percentage of component i in the total cement (by weight).

The incorporation of Supplementary Cementitious Materials (SCMs) can alter the ultimate heat of hydration of cement. This modification primarily stems from the distinct compositional differences between SCMs and traditional cement. Schindler and Folliard [37] have also provided an equation for calculating the ultimate heat of hydration for binders containing slag and FA:

$$H_u = H_{cem} \cdot p_{cem} + 461p_{slag} + 1800p_{FA-CaO} \cdot p_{FA} \quad (2.39)$$

where p_{slag} is the percentage of slag in the total cementitious materials (by weight), p_{FA} is the percentage of FA in the total cementitious materials (by weight), $p_{FA\text{-}CaO}$ is the percentage of mass of CaO in fly ash to total mass of fly ash.

It is imperative to note that the contributions of slag and FA to the ultimate heat of hydration of the cementitious base material, as presented in Eq. (2.39), are approximate empirical values derived from experimental data and previous observations. In reality, the chemical composition and heat of hydration of slag and FA can vary significantly based on their type, fineness, origin, and even between different batches from the same manufacturing facility.

A practical challenge is that not every laboratory is equipped with XRD or XRF instruments, nor do they always have skilled operators. Particularly with XRD, the substantial equipment costs and the high proficiency required of the operators further accentuate this issue. In response to this dilemma, Azenha [157, 158] proposed a mathematical approach that employs the least squares method to determine the asymptotic value of H(1/t) as 1/t approaches zero, thereby approximating the value of H_u. H(1/t) can be expressed by the following equation:

$$H\left(\frac{1}{t}\right) = a \cdot e^{\left(b \cdot \frac{1}{t}\right)} \tag{2.40}$$

where a and b are fit parameters that can be derived from regression analysis. Azenha emphasized that the asymptotic value of H_u should be only considered for $1/t<0.02$, which corresponds to the cumulative heat of hydration observed in experiments lasting more than 50 hours. When $1/t \sim 0$, then $H(\sim 0) = H_u$.

2.5.5 Degree of Hydration

To elucidate the relationship of f(α)-α proposed by Reinhardt *et al.* [140] discussed in Section 2.5.3, Azenha [157] conducted isothermal calorimetry tests on cement at three distinct temperatures: 20°C, 30°C, and 40°C. The hydration heat rate curves, as depicted in Figure 2.18, reveal significant disparities in the peak hydration values, the time to reach these peaks, and the hydration rates at various stages under different temperatures. In in-situ concrete structures, the external ambient temperature and the internal inherent temperature are in constant flux, diverging considerably from laboratory data and presenting intricate complexities. Building on the premise in Section 2.5.3, which extends the fundamental assumption of concrete maturity to hydration heat and degree of hydration, Azenha plotted the hydration heat rate Q against the degree of hydration α for different temperatures, as illustrated in Figure 2.19. While the hydration curves at different temperatures still exhibit notable differences, the primary distinction lies in the hydration rates and peak values corresponding to different hydration degrees. The overall trend and shape of the curves have become markedly

analogous. Subsequently, Azenha crafted a graph showcasing the normalized heat generation rate f(α) against the degree of hydration α, as presented in Figure 2.20. At this juncture, the f(α)-α curves across different temperatures nearly coincide.

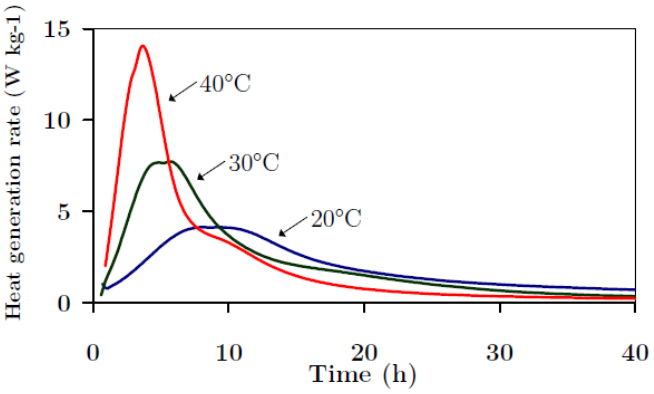

Figure 2.18. Cement hydration heat rate at different temperatures via isothermal calorimetry tests conducted by Azenha [157].

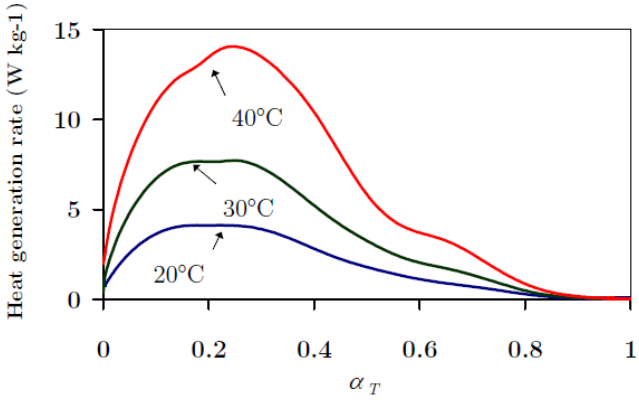

Figure 2.19. Cement hydration heat rate Q versus hydration degree α plot curves at different constant temperatures conducted by Azenha [157].

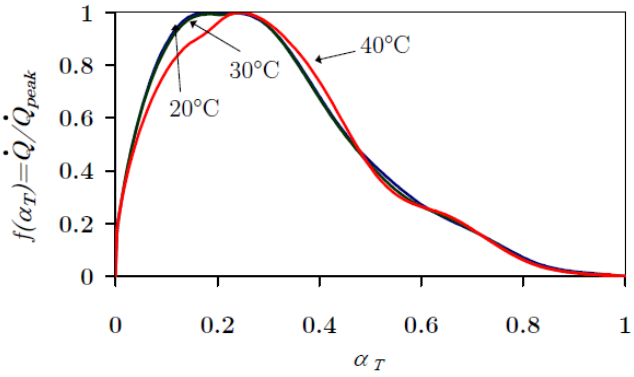

Figure 2.20. Normalized heat generation rate f(α) versus hydration degree α curves at different constant temperatures conducted by Azenha [157].

The above derivation process holds paramount significance for predicting concrete hydration heat. The f(α)−α curve in Figure 2.20 addresses the challenge of significant discrepancies in the hydration heat curves at varying temperatures, which allows

measuring the extent of hydration for a specific concrete mixture, thereby laying a theoretical foundation for the future accurate prediction of the development of concrete hydration temperatures. However, it is imperative to note that the f(α)−α curve cannot be directly employed for predicting cement hydration heat. This limitation arises because calorimetry tests and subsequent computational simulation define the independent variable concerning cement hydration heat solely in terms of time. In other words, calorimetry test is currently almost impossible to directly measuring the degree of hydration of cement [159]. Consequently, the f(α)−α curve herein serves as a "bridge" to link cement hydration heat with concrete maturity, facilitating the definition of a time-dependent relationship that quantifies the impact of temperature on the rate of cement hydration heat over time.

The degree of hydration, often denoted as α, is a pivotal parameter in cement chemistry, offering insights into the progression of cement hydration reactions. The degree of hydration is originally defined as the fraction of the cement that has reacted with water at any given time relative to the total amount of cement present (by mass). Mathematically, α can be expressed as in Eq. (2.41). Figure 2.21 elucidates the physical significance of the hydration degree of cement.

$$\alpha = \frac{m_h}{m_{tot}} \tag{2.41}$$

where m_h is the mass of hydrated cement, m_{tot} is the total mass of cement.

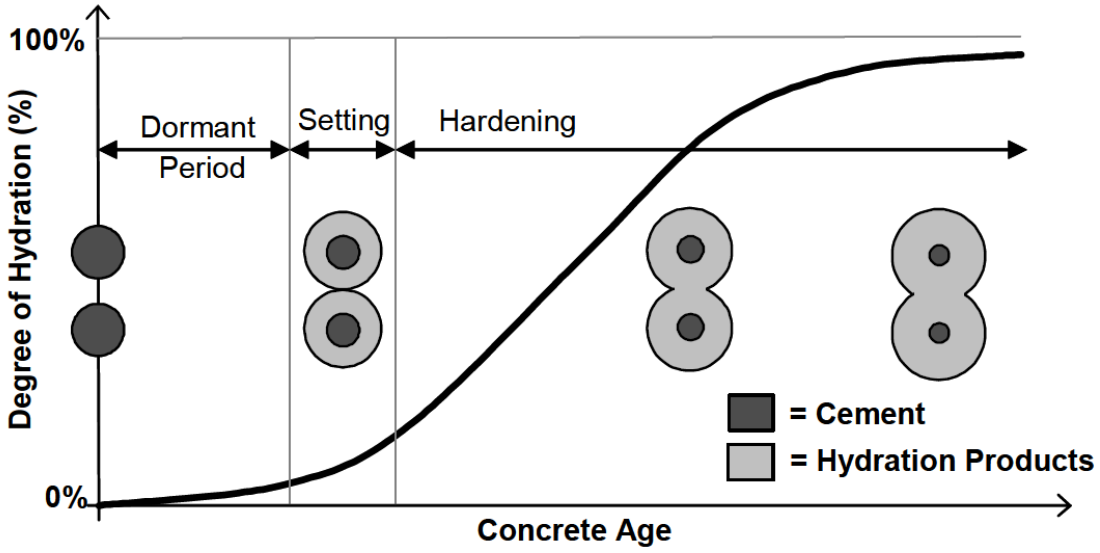

Figure 2.21. Physical significance of the hydration degree of cement [113].

As discussed in Section 2.2.1, the hydration of cement is a complex process, encompassing a series of exothermic reactions between cement particles and water. These reactions form various hydration products, such as calcium silicate hydrate (C-S-H), calcium hydroxide (CH), and ettringite, which collectively contribute to the

setting and hardening of the cementitious matrix. During the hydration process of cement, the timely separation of reaction products from the unhydrated cement is virtually unattainable. This inherent complexity underscores the infrequent adoption of the mass ratio formula in defining the degree of hydration in practical applications.

As elucidated in Section 2.4, calorimetry, which measures the heat released during the hydration process, offers a more direct and efficient method for quantifying the degree of hydration, denoted as α. Given the exothermic nature of the hydration reaction, the cumulative heat released can be correlated with the extent of hydration, presenting a more pragmatic approach in real-life applications. In practice, the heat of hydration frequently serves as an alternative metric for the degree of hydration. This preference stems from the inherent exothermic character of the hydration reaction, which, during its course, emits quantifiable heat. By monitoring the cumulative heat released over a specific duration, one can indirectly gauge the progression of cement hydration. The relationship between the heat of hydration and α is typically established through calorimetry experiments, providing a tangible methodology to bridge the two parameters. The degree of hydration in cement, α, can be represented by the ratio of the heat already released from the hydration reaction to the ultimate heat of hydration. This relationship is expressed as in Eq. (2.25), which can be determined via calorimetry tests in Section 2.4. The degree of cement hydration can be determined by measuring heat release and various experimental methods, such as the assessment of chemically bound water, chemical shrinkage, Ca(OH) content, and the specific surface of cement paste. Among them, the heat of hydration and the chemically bound water are the two most commonly used methods to determine the degree of hydration of cement.

In Section 2.5.3, the TPE equation, as proposed by Freiesleben Hansen and Pedersen [138], was highlighted to elucidate the relationship between the development of concrete strength and the heat of hydration in terms of equivalent age (referenced in Eq. (2.19) and Eq. (2.31)). This is based on the assumption that the cumulative heat of hydration of cement directly correlates with the progression of concrete strength and the degree of hydration. Based on this assumption, it becomes rational to represent the degree of hydration of cement through the TPE equation:

$$\alpha(t_e) = \alpha_u \cdot e^{\left(-\left(\frac{\tau}{t_e}\right)^{\beta}\right)} \tag{2.42}$$

where $\alpha(t_e)$ is the hydration degree at equivalent age t_e, α_u is the ultimate hydration degree that the hydration reaction can be attend, which is a parameter specific to the material, a higher α_u leads to a higher final degree of hydration, and more total heat is available for hydration. τ is the hydration heat time parameter, a higher value of τ indicates a more pronounced delay in the hydration process. β is the hydration heat development shape parameter, which characterizes the shape of the hydration-time curve, predominantly dictating the gradient of its primary linear segment. An increased β value suggests a more rapid hydration rate during this linear phase, but a slower rate

at the onset of the hydration period [99, 113]. Schindler *et al.* [113] summarized the physical significance of these three hydration parameters, which can be represented by the three graphs in Figure 2.22 to Figure 2.24. The parameters α_u, τ, and β are hydration parameters of cement hydration. The best-fit hydration parameters can be obtained by performing non-linear regression analysis on the results of the calorimetry test and the hydration degree defined in Eqs. (2.25) and (2.42).

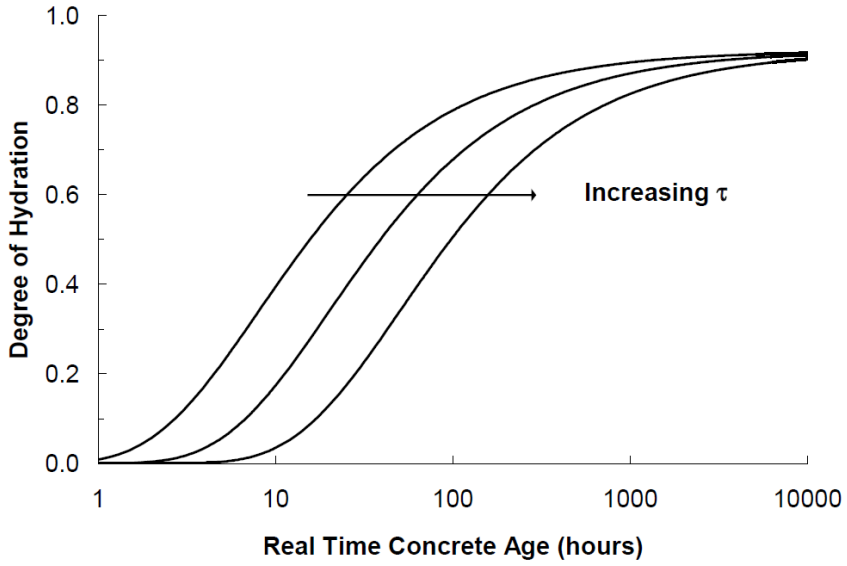

Figure 2.22. Effect of hydration time parameter τ on the cement hydration degree development [113].

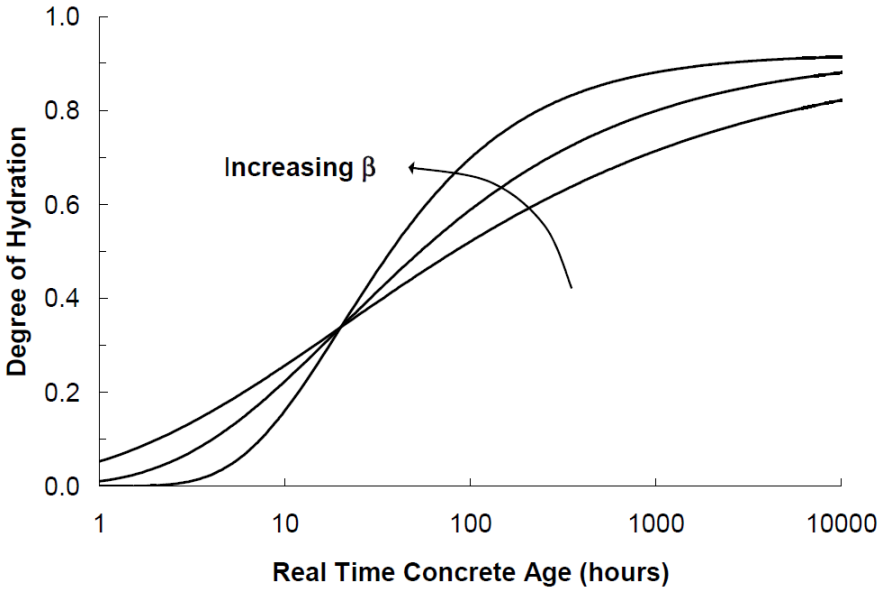

Figure 2.23. Effect of hydration shape parameter β on the cement hydration degree development [113].

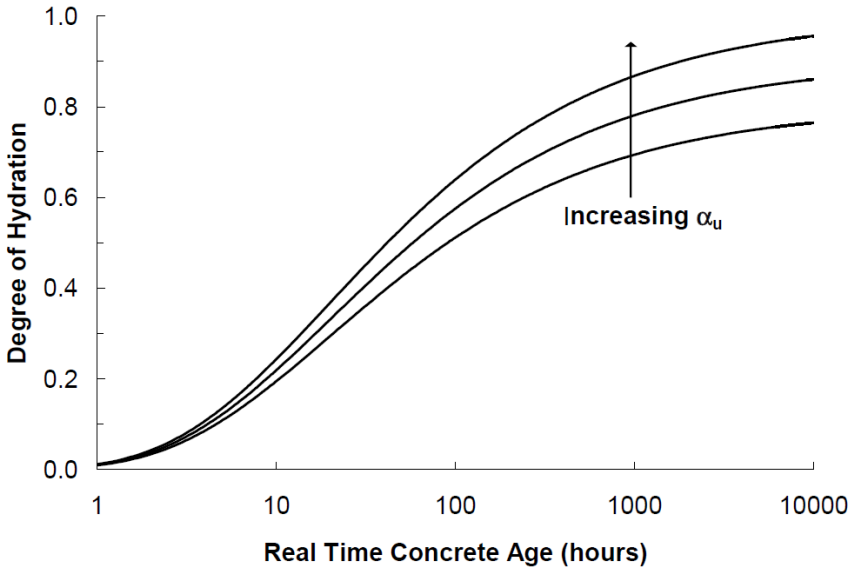

Figure 2.24. Effect of ultimate hydration degree α_u on the cement hydration degree development [113].

2.5.6 Ultimate Degree of Hydration

In practical experiments and engineering, it is almost impossible for cement to reach a 100% degree of hydration. Ge [128] indicated that the degree of hydration that could be achieved by concrete in the field after 28 days was often between 0.6 and 0.8. Roy *et al.* [147] found that the degree of hydration of a cement paste specimen aged for ten years was only 70%.

Section 2.2.3 discusses many factors that affect cement hydration. As a chemical reaction between cement and water, whether the reactants are sufficient largely impacts the hydration reaction. As the hydration of cement is a series of chemical reactions between cement and water, the availability of free water largely influences the hydration reaction. As mentioned in Section 2.2.3.3, Van Breugel [59] suggested a minimum water-cement (w/c) ratio of 0.4, while Mindess and Young [60] suggested a value of 0.42. The hydration reaction can only continue when the w/c ratio exceeds the limit value, meaning the water content reaches a certain level. Otherwise, the hydration reaction will stop. Moreover, the hydration reaction will eventually stop as the accumulating hydration products occupy the spaces initially filled with mixing water. The continuation and extent of the hydration of cement directly determine the ultimate degree of hydration that the hydration reaction can achieve. Therefore, the two main factors that affect the ultimate degree of hydration are the availability of free water to participate in the hydration reaction and space availability to accommodate the hydration products.

Assuming that the minimum required w/c ratio is 0.42. If there is sufficient free water, Hansen [160] proposed an equation to estimate the final degree of hydration:

$$\alpha_u = \frac{w/c}{0.42} \leq 1.0 \tag{2.43}$$

As the hydration process progresses, the products of hydration progressively occupy the spaces initially filled by the mixed water. Once the capillary voids are saturated, the hydration reaction stops. This suggests that a reduced water-to-cementitious ratio results in lesser water per volume unit, decreasing the ultimate degree of hydration. Hansen [160] provided a quantification of this relationship as follows:

$$\alpha_u = \frac{w/c}{0.36} \leq 1.0 \tag{2.44}$$

To account for the above limitations on cement hydration, Mills [161] conducted extensive experiments to determine the quantity of chemically bound water upon the completion of the hydration reaction. Subsequently, Mills proposed the following formula to compute the ultimate degree of hydration for saturated concrete contains FA and GGBS [112]:

$$\alpha_u = \frac{1.013\, w/c}{0.194 + w/c} + 0.50 p_{FA} + 0.30 p_{GGBS} \tag{2.45}$$

However, it is essential to highlight that these equation does not account for the influence of cement type and fineness. The finer the cement, the greater its ultimate degree of hydration [128].

2.5.7 Maturity-Based Hydration Heat Models

A primary challenge in predicting the rate of heat evolution from cement hydration in in-situ concrete is the continuously fluctuating external environmental temperature and the inherent temperature variations within the concrete itself. These lead to intricate heat dissipation and temperature development profiles, markedly different from laboratory conditions. The maturity concept defines the development of concrete strength, heat of hydration, and degree of hydration as parameters determined by concrete temperature and age. Consequently, this offers the potential to predict the hydration heat evolution of concrete under varying conditions, provided the real-time temperature and age of the concrete are known. Eq. (2.27) has presented one equation for the cement hydration rate as a function of hydration degree α and temperature T, as derived by Reinhardt *et al.* [140] and Azenha [157]. The isothermal calorimetry method can determine the function f(α) representing the hydration degree. Except for Eq. (2.27), this section will present several mathematical models for calculating the hydration heat rate of cement based on the maturity method:

2.5.7.1. TPE-based Hydration Heat Prediction

Eq. (2.25) presents the equation for the degree of hydration defined by the heat of hydration, while Eq. (2.42) introduces the TPE hydration degree equation. By combining these two equations, an expression for cumulative heat of hydration based on the equivalent age can be derived:

$$H(t_e) = \alpha(t_e) \cdot H_u = \alpha_u \cdot e^{\left(-\left(\frac{\tau}{t_e}\right)^{\beta}\right)} \cdot H_u \tag{2.46}$$

Thus, the hydration heat generation rate of cement can then be expressed by differentiating the cumulative heat of hydration with respect to equivalent age:

$$Q(t_e) = \frac{dH(t_e)}{dt_e} = H_u \cdot \alpha_u \cdot e^{\left(-\left(\frac{\tau}{t_e}\right)^{\beta}\right)} \cdot \left(\frac{\tau}{t_e}\right)^{\beta} \cdot \left(\frac{\beta}{t_e}\right) \tag{2.47}$$

The hydration heat generation rate of cement at actual age can be expressed as:

$$Q(t) = \frac{dH(t_e)}{dt} = \frac{dH(t_e)}{dt_e} \cdot \frac{dt_e}{dt} \tag{2.48}$$

By performing a straightforward mathematical transformation on the Arrhenius equivalent age equation (Eq. (2.12)), the following can be derived:

$$\frac{dt_e}{dt} = e^{\frac{-E_a}{R}\left(\frac{1}{T}-\frac{1}{T_r}\right)} \tag{2.49}$$

Through the derivation process encompassed by Eqs. (2.46)-(2.49), the heat generation rate from cement hydration at a given actual age can be expressed as the function of the concrete maturity (Arrhenius equivalent age) and the degree of cement hydration:

$$Q(t) = H_u \cdot \alpha_u \cdot e^{\left(-\left(\frac{\tau}{t_e}\right)^{\beta}\right)} \cdot \left(\frac{\tau}{t_e}\right)^{\beta} \cdot \left(\frac{\beta}{t_e}\right) \cdot e^{\frac{-E_a}{R}\left(\frac{1}{T}-\frac{1}{T_r}\right)} \tag{2.50}$$

The above derivation was conducted by Schindler and Folliard [37]. This is an iterative process. The heat release rate for each time step is determined by the degree of hydration and equivalent age (temperature and time) from the previous time step. A fundamental assumption inherent to this approach is that the initial temperature of the concrete for each time step is equivalent to the temperature of the concrete at the end of the previous time step.

The hydration parameters in Eq. (2.42) can be determined through calorimetry experiments coupled with nonlinear regression analysis. The adiabatic calorimetry, the semi-adiabatic calorimetry, and the isothermal calorimetry mentioned in Section 2.4

can all achieve this process. However, it is imperative to note that results from the semi-adiabatic calorimetry method cannot be directly employed for regression analysis. This limitation arises due to the experimental characteristic of this method that permits heat loss, resulting in an incomplete hydration heat curve. Nevertheless, this challenge can be addressed by employing a heat loss compensation process to infer the specimen's adiabatic hydration curve as discussed in Section 2.4.2. Xu *et al.* [99] computed the hydration parameters using results from both semi-adiabatic and isothermal calorimetry experiments. Their findings indicated that the value of τ derived from the semi-adiabatic calorimetry was higher than that from the isothermal calorimetry, while the β value was lower than isothermal calorimetry. This discrepancy might be attributed to coarse aggregates "delayed" effect in the semi-adiabatic calorimetry specimens. This further underscores the potential inaccuracies that traditional isothermal calorimetry experiments, which cannot include coarse aggregates, might introduce in the study of concrete thermodynamics.

2.5.7.2. Arrhenius-based Hydration Heat Prediction

Martinelli *et al.* [139] proposed a procedure to calculate the hydration heat rate of concrete under non-adiabatic conditions using data from adiabatic calorimetry, based on the Arrhenius equation. As described in Section 2.4.1, while adiabatic calorimetry experiments necessitate a specialized and complex system to maintain the specimen's adiabatic condition, they indeed offer an ideal approach to obtain a complete hydration curve for cement, given that the specimen is assumed to experience no heat loss throughout the hydration process. As mentioned in Section 2.5.2, the reaction rate of cement, being a series of chemical reactions, can be expressed through the Arrhenius equation (Eq. (2.11)). Consequently, the hydration rates for concrete under adiabatic and non-adiabatic conditions can be respectively represented as:

$$Q_a(T_a) = Ae^{\left(\frac{-E_a}{R \cdot T_a}\right)} \tag{2.51}$$

$$Q_n(T) = Ae^{\left(\frac{-E_a}{R \cdot T}\right)} \tag{2.52}$$

where Q_a and Q_n are hydration heat rates of adiabatic specimen and non-adiabatic specimen separately, T_a and T are specimen temperature of adiabatic specimen and non-adiabatic specimen separately. Based on the definition of maturity method, the cumulative heat of hydration released by concrete under non-adiabatic conditions at time t is equivalent to that released by adiabatic concrete at an equivalent age t_e. However, at this juncture, while the two concrete specimens have the same cumulative heat of hydration, the heat dissipation characteristics of the non-adiabatic specimen result in differing temperatures between the two. Consequently, the heat of hydration rates for the two specimens are different. The relationship between the hydration heat rates of the two specimens can thus be expressed as:

$$\frac{Q_a(T_a(t_e))}{Q_n(T(t))} = \frac{e^{\left(\frac{-E_a}{R \cdot T_a(t_e)}\right)}}{e^{\left(\frac{-E_a}{R \cdot T(t)}\right)}} = e^{-\frac{E_a}{R}\left(\frac{1}{T_a(t_e)} - \frac{1}{T(t)}\right)} \tag{2.53}$$

In Eq. (2.53), the term on the far right is essentially the "age conversion factor" f(T) as presented in Eq. (2.13). Therefore, the hydration rate of the non-adiabatic specimen at time t can be expressed as the product of the hydration rate of the adiabatic specimen at the equivalent age t_e and the age conversion factor f(T):

$$Q_n(t) = Q_a(t_e) \cdot e^{-\frac{E_a}{R}\left(\frac{1}{T(t)} - \frac{1}{T_a(t_e)}\right)} \tag{2.54}$$

This methodology is derived based on the foundational principles of the Arrhenius equation and the definition of equivalent age. Under conditions where ideal adiabatic conditions can be achieved, the mathematical representation of Eq. (2.54) is considerably more straightforward than that of Eq. (2.50). This simplicity might be advantageous in subsequent numerical simulations of concrete temperature, potentially reducing computational efforts.

2.5.7.3. Affinity Hydration Model

Based on the works of Cervera *et al.* [162], Da Silva *et al.* [150] developed a mathematical model to represent the cement hydration rate using the Affinity hydration model. In this model, the reference temperature is set at 25℃. The rate of cement hydration (chemical affinity form) can be expressed as the derivative of hydration with respect to time:

$$\frac{d\alpha}{dt} = \widetilde{A_{25}(\alpha)} \tag{2.55}$$

where the dimension of the cement hydration chemical affinity is 1/time, which can be obtained via isothermal calorimetry test and semi-adiabatic calorimetry test.

The analytical form of normalized affinity can be expressed as:

$$\widetilde{A_{25}(\alpha)} = B_1\left(\frac{B_2}{\alpha_u} + \alpha\right) \cdot (\alpha_u - \alpha) \cdot e^{-\bar{\eta}\frac{\alpha}{\alpha_u}} \tag{2.56}$$

where B_1 and B_2 serve as adjustable coefficients, α_u is the ultimate hydration degree. The term η denotes the micro-diffusion of free water through the hydrates that are formed. These parameters can be obtained by isothermal calorimetry tests at 25°C. When the internal temperature of the hydration reaction is in a state of continuous fluctuation, as is often the case in real-life concrete scenarios (e.g., in-situ concrete), the chemical affinity at any given temperature can be expressed in terms of the

equivalent age, following a derivation process analogous to that of Eqs. (2.51)-(2.54):

$$\widetilde{A_T} = \widetilde{A_{25}} \cdot e^{-\frac{E_a}{R}\left(\frac{1}{T}-\frac{1}{273.15+25}\right)} \tag{2.57}$$

For instance, when the concrete temperature is at 35°C, one would adjust chemical affinity at 25°C by a multiplier of 1.651 for a specific duration. This implies that a concrete hydration period of 10 hours at 35°C would produce the same heat release as concrete undergoing hydration for 16.51 hours at 25°C. The experimental findings by Da Silva *et al.* [150] indicate that the Affinity hydration model provides robust simulations for all OPC binders.

In addition to fitting data from calorimetry experiments, Da Silva and Smilauer [163] introduced an open-source Python-based application named CEMHapp. This tool calculates the parameters in Eq. (2.56) by allowing users to input the percentage content of the four primary mineral constituents of the binder. However, it is crucial to note that CEMHapp sets the ultimate degree of hydration α_u to 0.85 for all binders, which may introduce potential simulation inaccuracies. For a more precise determination of the ultimate degree of hydration, it is advisable to rely on specific calorimetry tests or the binder's composition, utilizing either Eq. (2.42) or Eq. (2.45) for computation.

2.5.7.4. NordTest Method

Wadsö [15] proposed an iterative mathematical procedure to predict the hydration curve of concrete specimens in the semi-adiabatic calorimetry method via the isothermal calorimetry test data at different temperatures in the NordTest Report. The semi-adiabatic concrete specimen, due to its allowance for heat loss and the exothermic nature of the hydration reaction, experiences continuous temperature variations, thereby rendering its hydration heat curve notably complex and challenging to predict. Initially, Wadsö conducted isothermal calorimetry experiments on specimens at different temperatures (within his project, specifically at 20, 30, 40, and 50°C). Subsequently, the calorimetry experimental results were represented by the function Q(H), expressed as a tenth-order polynomial through data fitting:

$$Q(H) = \sum_{n=0}^{10} a_n H^n \tag{2.58}$$

where the coefficient a_n in the polynomial represents the factor by which the variable term H^n is multiplied. In the context of a tenth-degree polynomial, a_n is determined through data fitting procedures, ensuring that the polynomial approximates the experimental data as closely as possible. The value and sign of an influence the magnitude and direction of the term H^n, thereby affecting the shape and properties of the polynomial function. The function Q(H) is equivalent to Q(α) in Figure 2.19, as the

cumulative heat of hydration H at a particular moment is essentially the product of the ultimate heat of hydration H_u and the degree of hydration α at that moment.

This step yields the relationships of Q(H) at four distinct temperatures: 20°C, 30°C, 40°C, and 50°C, implying that, given the cumulative heat of hydration and temperature at the end of the previous time step, the heat generation rate (thermal power) at the beginning of the next time step can be computed. However, in semi-adiabatic calorimetry specimens or in-situ concrete, the temperature is unlikely to coincide with one of these four values precisely. It is highly probable to reside between or beyond these temperatures, for which the polynomial expressions for Q(H) have not been derived. Addressing this issue, Wadsö recommends employing an interpolation method to ascertain the Q(H) relationship at a specific temperature and cumulative heat of hydration. This interpolation procedure utilizes a second-order polynomial to derive the Q(H) relationship at a particular temperature and cumulative heat of hydration, thereby determining the heat generation rate at the beginning of a given time step.

Hatzitheodorou [22] and Tang *et al.* [1] employed the above procedure to simulate the hydration heat rate and the temperature of in-situ concrete. The outcomes demonstrated that the method exhibited commendable performance when applied to mixes involving only CEM I as the binder. However, a discernible decline in simulation accuracy was observed when GGBS was utilized as a partial replacement for cement. This can be attributed to the inability of the initial tenth-order polynomial Q(H) to accurately replicate the "second-peak" phenomenon evident in the hydration curve of GGBS-CEM blended mixes. Consequently, this implies that the method harbours inherent limitations when simulating the hydration rate of concrete that incorporates SCMs.

It is imperative to underscore again that another potential source of error, as discussed in Section 2.4.3, may arise from using cement paste or mortar as specimens in isothermal calorimetry experiments, excluding the presence of coarse aggregates, which could potentially impact both thermal conductivity and the hydration rate. While Wadsö [16] posits that the hydration curve of an equivalent mortar can wholly represent that of concrete, it is pivotal to note that Wadsö's experiments solely validated the equivalency of hydration curves between cement paste and mortar, without further verification regarding the role of coarse aggregates. Moreover, with the progressive research into isothermal calorimetry, numerous research [23, 24, 99] have presented viewpoints that contrast Wadsö's, in which they believe the role of coarse aggregate on the cement hydration heat rate is not negligible.

2.6 Numerical Modelling of Early-Age Concrete Temperature Development

The hydration heat curves derived through the mathematical procedures in Section 2.5 necessitate further processing, incorporating the thermal properties of concrete (thermal conductivity and specific heat) and its boundary conditions (ambient temperature and heat dissipation) to yield the concrete temperature at each age. The complete

temperature curve thus obtained represents the anticipated development of concrete temperature. However, for in-situ concrete, its permissive heat dissipation characteristics and the continuously varying environmental temperature render the processes of temperature variation and heat dissipation highly complex.

Addressing such intricate engineering dilemmas, the Finite Element Method (FEM) emerges as a potent tool. Present-day commercial FEM software packages often encompass various modules, enabling simulation and modelling across diverse domains such as mechanics, thermodynamics, and electromagnetism, et al. The FEM is now extensively utilized within both academic and industrial spheres, as well-modelled FEM models can significantly mitigate time and financial expenditures while ensuring simulation accuracy. Within the realm of concrete temperature field prediction, boundary conditions like environmental temperature can be incorporated into the FEM model by inputting monitored environmental temperature data. The FEM software can autonomously compute the heat loss of the concrete through mathematical formulas in its specific modules while also performing iterative calculations step by step through the heat source derived in Section 2.5, thereby obtaining the complete temperature development curve of the concrete.

This section will initially delineate the fundamental principles of the concrete temperature modelling work. Subsequent discussions will elucidate pivotal material properties within this specific physical module, namely, the thermal conductivity and specific heat capacity of concrete. The influences shaping these material properties, especially the evolving trends during the early stages of concrete hardening, will be explored. Following this, a review of existing models for predicting concrete temperature will be undertaken, wherein each model's respective merits and limitations will be meticulously analysed.

2.6.1 Fundamentals of FEM Heat Transfer Models

Heat is defined in thermodynamics as a form of energy transferred in different systems or regions of the same system due to temperature gradients. This phenomenon occurs by three main modes: conduction, which is the transfer of heat through and between matter by direct contact; convection, which is the transfer of heat by the movement of a fluid (liquid or gas); and radiation, which is the transfer of heat by electromagnetic waves. Each type of heat transfer has different mechanisms and is influenced by various factors such as the properties of the materials, temperature differences and the presence or absence of a medium to facilitate energy transfer [164].

Bamforth [165] devised a one-dimensional heat transfer model to predict and mitigate thermal cracking in concrete, capable of calculating the impacts of ambient temperature and formwork removal on the surface temperature of the concrete, which can be established through a straightforward spreadsheet. However, for in-situ concrete, where boundary conditions (such as on-site temperature) are notably more complex and

variable, FEM modelling emerges as a superior choice. FEM can efficiently compute the influence of on-site temperature variations and other factors, such as geometry and materials, on the thermal development of concrete at each time step based on inputted parameters. Through iterative calculations, the FEM model facilitates the acquisition of the temperature curve of the concrete within a specified time frame.

The propagation of heat within concrete is determined by its thermal conductivity and the temperature gradient across adjacent regions, which can be defined through the Fourier heat transfer equation:

$$q = -k \cdot \Delta T \tag{2.59}$$

where q is the heat transfer per unit time and per unit area (W/m^2), k is the thermal conductivity of the concrete ($W/(m \cdot K)$), ΔT is the temperature gradient (K/m^2). A salient characteristic of in-situ concrete, as iteratively underscored in preceding sections, is its permissibility for thermal loss. The thermal dissipation from concrete is attributed to the temperature gradient between the concrete surface and its surrounding environment. This heat loss from the concrete surface culminates in a surface temperature lower than its internal temperature, thereby instigating a temperature gradient within the concrete itself. This phenomenon underpins the rationale behind Eq. (2.59).

The heat balance of concrete under the conditions of internal thermal gradient and heat exchange with the external environment can be expressed by a three-dimensional heat diffusion equation based on Fourier heat transfer principle:

$$k \cdot \left(\frac{\partial^2 T}{\partial X^2} + \frac{\partial^2 T}{\partial Y^2} + \frac{\partial^2 T}{\partial Z^2} \right) + Q = \rho \cdot C_p \cdot \frac{\partial T}{\partial t} \tag{2.60}$$

where Q is the heat generation rate of the cement (W/m^3), which have been reviewed in Section 2.5.7, X, Y, Z represent three different axes in the concrete, T is the concrete temperature (°C), ρ is the density of the concrete (kg/m^3), and C_p is the heat capacity of concrete ($J/kg \cdot K$). With known initial conditions (initial temperature of concrete), Eq. (2.60) can be solved. This mathematical formulation is a crucial framework for understanding the thermodynamic behaviour of concrete. Eq. (2.60) shows that the speed of the thermal change at a specific spatial location is proportional to the second spatial derivative, which is essentially the rate of change of the spatial gradient of the temperature at that location. In other words, heat diffusion occurs from areas of high temperature to low temperature, and the rate of temperature change is highest where the thermal gradient is sharpest.

Riding *et al.* [166] elucidated the primary modalities of heat exchange between large-

volume in-situ concrete structures and their surrounding environment and boundary conditions, using a concrete bridge column as an example. In-situ concrete structures are frequently exposed to air and sunlight upon formwork removal, engendering boundary conditions conducive to heat exchange. This encompasses thermal conduction, thermal convection, solar absorption, and irradiation. The sketch presented in Figure 2.25 of the concrete bridge column illustrates the three modes of thermal boundary conditions from the external environment—thermal convection, solar absorption, and irradiation. Thermal conduction pertains to the heat exchange phenomenon within the concrete, instigated by internal temperature gradients, which will be discussed in detail subsequently. Subsequent discussions will delineate the four heat transmission mechanisms, utilizing the in-situ concrete column depicted in Figure 2.25 as a template for elucidation:

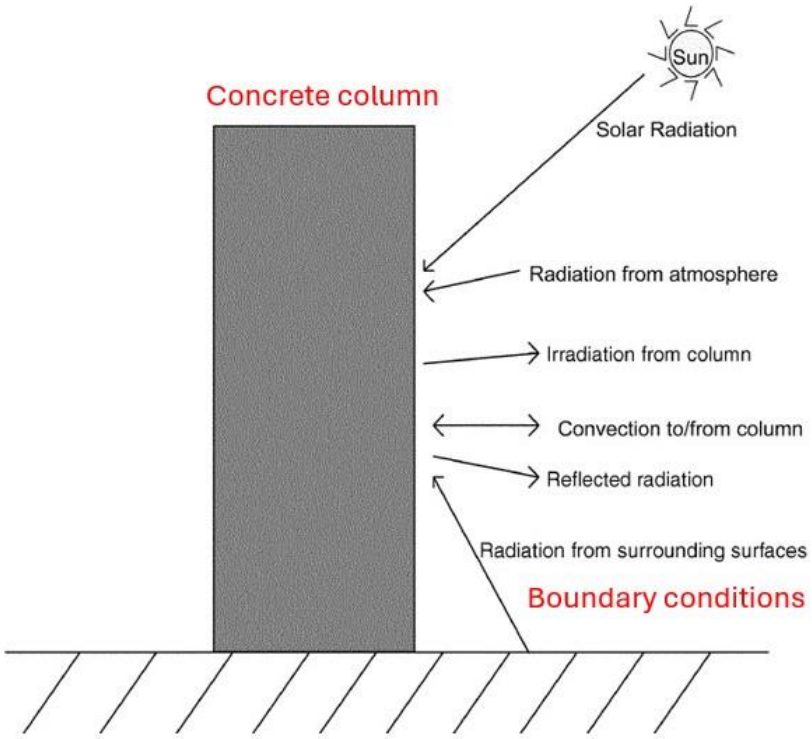

Figure 2.25. Boundary conditions of concrete bridge column [166].

Thermal Conduction: Thermal conduction refers to the transfer of heat within a material from regions of higher temperature to lower temperature. In concrete, this process is essential for understanding temperature gradients between the core and surface of mass concrete structures. The governing equation for heat conduction is expressed through the Fourier equation, as depicted in Eq. (2.59).

Figure 2.25 illustrates the thermal conduction occurring within adjacent regions of a concrete column exhibiting a temperature gradient. The core of mass concrete, due to its difficulty in dissipating heat, retains a higher temperature than its surface. This temperature gradient is critical for simulating adiabatic temperature rise in FEM models.

Thermal Convection: Thermal convection involves the transfer of heat from the concrete surface to the surrounding fluid or gas through movement. Two primary forms of convection exist [167]:

- **Natural Convection:** Driven by temperature-induced density differences.
- **Forced Convection:** Driven by external factors like wind.

For horizontal structures like in-situ concrete top surfaces, the type of convection, whether forced or natural, is dictated by the wind speed over the concrete surface [157]. In natural convection, heat movement stems from temperature differentials between the entity (concrete surfaces) and the air. The natural thermal convective is represented using the Newton's law of cooling equation [168]:

$$q_c = h_c \cdot (T_s - T_a) \tag{2.61}$$

where q_c is the heat flux at the concrete or insulation layer surfaces (W/m^2), h_c is the convection coefficient, which represents the heat transfer capacity between solids and air ($W/m^2 \cdot °C$), T_s is the temperature of the concrete or insulation layer surfaces (°C), and T_a is the ambient (air) temperature (°C).

Despite numerous previous theoretical attempts to formulate predictive equations for the heat convection coefficient, precise predictions have been confined to simplistic geometries and well-controlled environments. Most of the widely used equations for heat convection are based on wind speeds. The equation for the thermal convection coefficient proposed by Duffie and Beckman [169] is shown below:

$$h_c = 5.7 + 3.8V \tag{2.62}$$

where V is the wind speed (m/s). It is imperative to note that this formula only applies to slabs with an area less than 0.5m^2. For slabs of larger dimensions, the convective heat transfer coefficient can be determined using the equation developed by Nevander and Elmarsson [170]:

$$h_c = 6 + 4V \quad if\ V \leq 5m/s \tag{2.63}$$

$$h_c = 7.4V^{0.78} \quad if\ V > 5\ m/s \tag{2.64}$$

Schindler *et al.* [113] proposed an equation that considers the positive or negative temperature gradients between a solid horizontal surface and air (which side has the higher temperature), as illustrated below:

$$h_c = 3.727 \cdot C \cdot (0.9(T_s + T_a) + 32)^{-0.181} \cdot (T_s - T_a)^{0.266} \cdot \sqrt{1 + 2.587 \cdot V} \quad (2.65)$$

where T_s is the temperature of the concrete or insulation layer surfaces (°C), and T_a is the ambient (air) temperature (°C), C=1.79 when surface is warmer than air, C=0.89 when air is warmer than surface, and V is the wind speed (m/s).

For the early-age in-situ concrete, a prevalent issue often considered when calculating the heat convection coefficient pertains to the formwork, situated externally to the concrete surface, utilized for temporary structural support and insulation. An equivalent convection coefficient can be calculated via Eq. (2.66) [20, 22].

$$h_{eq} = \left(\frac{1}{h_c} + \sum_{1}^{n} \frac{L_i}{k_i} \right)^{-1} \quad (2.66)$$

where h_{eq} is the equivalent convection coefficient (W/m^2 ·°C), h_c is the convection coefficient between the concrete surface and air (W/m^2 ·°C), L_i is the i-th insulation layer's thickness (mm), and k_i is the i-th insulation layer's thermal conductivity (W/m·°C).

Solar Absorption: Solar absorption pertains to the assimilation of solar radiation by concrete surfaces when subjected to incident solar radiation. McCullough and Rasmussen [171] introduced an equation to encapsulate the phenomenon of solar absorption within mass concrete surfaces:

$$q_{sol} = \gamma_{abs} \cdot I_f \cdot q_{solar} \quad (2.67)$$

where q_{sol} is the solar absorption heat flux of concrete surface (W/m^2). γ_{abs} is the concrete's solar absorptivity, which is 0.1-0.35 for white curing compound concrete surfaces. I_f is the intensity factor to consider the sunlight angle during a day, and q_{solar} is the instantaneous solar radiation (W/m^2). McCullough and Rasmussen summarised the solar radiation values for different weather conditions, as shown in Table 2.6.

Table 2.6. Solar radiation values summarised by McCullough and Rasmussen [171].

Weather Conditions	Solar Radiation (W/m^2)
Sunny	1000
Partly Cloudy	700
Cloudy (Overcast)	300

Irradiation: Irradiation plays a pivotal role in the occurrence of frost on a clear night, even when the atmospheric temperature is notably above freezing [172]. The heat transfer due to irradiation influences the boundary of concrete surfaces and is realized

through electromagnetic waves interacting between a surface and its environment. The Stefan-Boltzmann law, typically utilized for this mode of heat transfer, is articulated as follows [173]:

$$q_r = -\sigma \cdot \varepsilon \cdot \left({T_s}^4 - {T_a}^4\right) \tag{2.68}$$

where q_r is the heat flux from concrete surfaces (W/m^2), σ is the Stefan-Boltzmann radiation constant (= 5.67e-8 W/ m^2·°C), ε is the concrete surface emissivity (= 0.94 for rough concrete surfaces), T_s is the temperature of concrete surfaces (°C), and T_a is the surrounding ambient temperature (°C).

2.6.2 Thermal Properties of Hardening Concrete

The thermal properties of concrete play a crucial role in FEM modelling for predicting concrete temperature development, particularly in engineering applications. These thermal attributes, including thermal conductivity, specific heat capacity, and thermal diffusivity, govern the distribution of heat within the concrete structure and influence its temperature profile over time. The thermal diffusion can be calculated from the ratio of thermal conductivity to specific heat capacity as in the following equation:

$$\delta = \frac{k}{\rho \cdot C_p} \tag{2.69}$$

where δ is the thermal diffusion of concrete (m^2/s), k is the thermal conductivity of concrete (W/(m·K)), ρ is the density of concrete (kg/m^3), and C_p is the specific heat of concrete (J/(kg·K)).

Thermal conductivity dictates the rate at which heat energy is transmitted through the concrete, impacting the speed and extent of temperature changes throughout the structure. On the other hand, specific heat capacity influences the material's ability to store thermal energy, affecting the amplitude and duration of temperature fluctuations. Furthermore, thermal diffusivity, which encapsulates both conductivity and heat capacity, plays a pivotal role in determining the rate at which thermal gradients equilibrate within the material. For instance, a concrete structure with high thermal conductivity will transfer heat more quickly and evenly than a structure with low thermal conductivity, resulting in smaller temperature differences within the material. Conversely, a concrete structure with a high specific heat capacity will store more thermal energy than a structure with a low specific heat capacity, resulting in larger temperature fluctuations within the material.

Moreover, In the early stages of concrete, the hydration heat and strength are progressively evolving, not fully realizing their hydration and hardening potential. The

concrete transitions from a semi-fluid to a solid state throughout the hardening process, experiencing a series of hydration reactions and generating various hydration products. This dynamic process inherently alters the thermal properties of the material as it progresses through concrete early stages [174]. Incorporating precise values and relationships of these thermal properties into finite element models is imperative to accurately simulate scenarios such as heat generation during hydration, heat dissipation to the surroundings, and the resultant temperature gradients within the concrete structure.

2.6.2.1 Thermal Conductivity

Thermal conductivity is a measure used to quantify a material's capacity to transfer heat. It is calculated by dividing the amount of heat that flows through a unit area by the temperature difference across a unit thickness of the material. The SI unit of thermal conductivity is watts per meter per degree Kelvin (W/(m·K)). The values of thermal conductivity of ordinary concrete are approximately between 1.4 and 3.6 [34, 175].

The thermal conductivity of concrete is predominantly influenced by various factors, including its composition, curing temperature, moisture content, and age. Kim *et al.* [114] explored the factors influencing the thermal conductivity of concrete, mortar, and cement paste. Their research emphasized that the thermal conductivity of concrete is primarily governed by the inclusion of coarse aggregate and the moisture status of the sample. Simultaneously, the kinds of cementitious materials and admixtures employed in the mortar or cement paste markedly influence their thermal characteristics. Furthermore, Kim accentuated that additional factors, such as the proportion of fine aggregate, the water-cement ratio, and the temperature during curing, also play a pivotal role in determining the thermal conductivity of concrete. While the density of concrete does not directly impact its thermal conductivity, it is noteworthy that, in the context of lightweight concrete, the presence of air, possessing a low thermal conductivity, can alter the overall thermal conductivity of the lightweight concrete [34].

The volume of aggregate constitutes approximately 60%-80% of the overall volume of concrete [176], so the content and type of aggregates are critical to the thermal conductivity of concrete. Zhang *et al.*'s [177] test results indicated that, while maintaining a constant fine aggregate content, an increase in the content of coarse aggregate leads to a rise in the thermal conductivity of concrete. This finding supports the potential discrepancies in the heat of hydration between mortar specimens and concrete specimens discussed in previous sections of the isothermal calorimetry experiments; that is, specimens with differing thermal conductivity coefficients can result in variations in the heat of hydration. Neville [34] have summarized the thermal conductivity of concrete comprising various types of aggregates, as delineated in the table below:

Table 2.7. Concrete thermal conductivity comprising various types of aggregates [34].

Type of Aggregate	Concrete Wet Density (kg/m3)	Thermal Conductivity (W/(m·K))
Quartzite	2440	3.5
Dolomite	2550	3.3
Limestone	2450	3.2
Sandstone	2400	2.9
Granite	2420	2.6
Basalt	2520	2
Barytes	3040	2
Expanded Shale	1590	0.85

Demirboga [178] investigated the impact of Supplementary Cementitious Materials (SCMs) content on the thermal conductivity coefficient of concrete. By substituting a portion of cement with silica fume, Fly Ash (FA), and Ground Granulated Blast Furnace Slag (GGBS), respectively, the findings revealed that Portland cement-only concrete exhibited the highest thermal conductivity coefficient, registering at 1.233 W/m·K. A decline in the thermal conductivity coefficient was observed with an escalation in the content of SCMs.

Neville [34] pointed out that the variation in the thermal conductivity of concrete can be disregarded when it is cured at room temperature. However, the fluctuation in the thermal conductivity becomes intricate when the concrete is cured at elevated temperatures. A slowly enhancement is observed with a temperature rise, reaching a peak approximately between 50 and 60 °C. Conversely, a precipitous decline in thermal conductivity is observed when the temperature reaches 120°C, a phenomenon attributed to the moisture loss in the concrete induced by the elevated temperature. The thermal conductivity of concrete approximately stabilizes between 120-140°C. When the temperature escalates to 800°C, the thermal conductivity is roughly half what it is at 20°C.

During the early stages of concrete setting, a transition from a semi-fluid to a progressively hardening solid state occurs. In this phase, cement undergoes continuous hydration reactions with water, consuming water and generating a lot of hydration products, thereby bestowing strength upon the concrete. Concurrently, the thermal conductivity of the concrete undergoes alterations. Mikulić *et al.* [179] monitored the variations in thermal properties of cement paste in the initial four days following the commencement of hydration reactions, utilizing the ultrasonic pulse velocity (UPV) test. Their findings delineate a three-phase alteration in thermal conductivity. The first phase spans from the onset of hydration reactions to approximately four hours, during which the thermal conductivity gradually declines. The second phase, extending from 4 to 12 hours, witnesses a deceleration in the rate of thermal conductivity decline, eventually stabilizing. Post the 12-hour mark, the third phase ensues, characterized by an exceedingly gradual decline in thermal conductivity. After this, the thermal conductivity values exhibit negligible variations. Their conclusion indicates a 20%

reduction in the thermal conductivity of the cement paste within these four days. However, their experiments were confined to cement paste, potentially overlooking the role of aggregates. The thermal conductivity curve, as monitored by Mikulić *et al.* for the cement paste over the initial four days, is illustrated below:

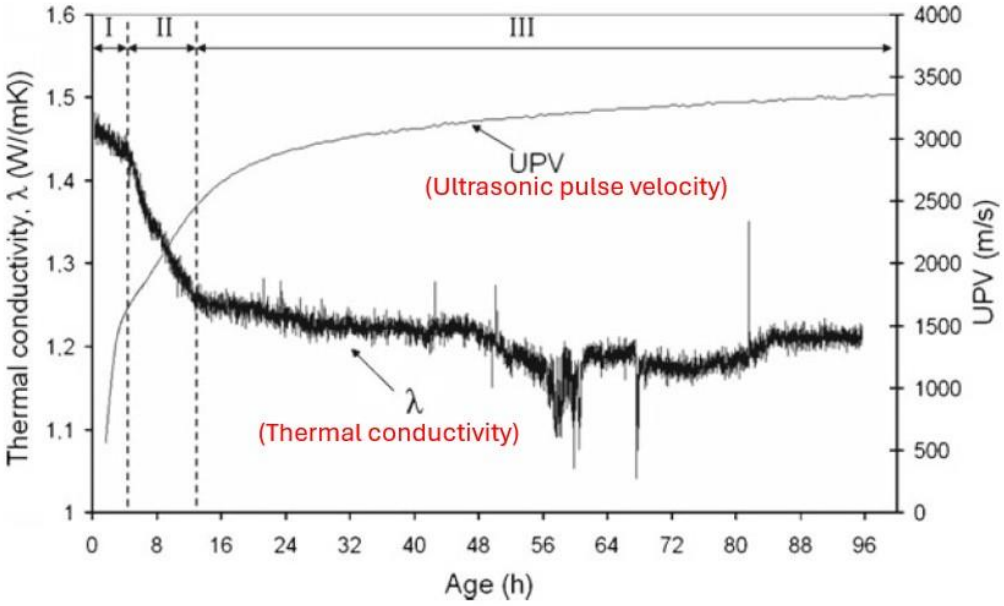

Figure 2.26. Thermal conductivity monitoring results (λ in the figure) of cement paste by Mikulić *et al.* [179].

Similarly, Brown and Javaid [180]evaluated the thermal conductivity of early-age concrete, possessing a water/cement ratio of 0.65, spanning from 6 hours to 7 days. The initial thermal conductivity of the concrete, measured at 6 hours, was recorded as 2.176 W/(m·°C). When it reached seven days, it experienced an approximate 30% reduction at 1.515 W/(m·°C). The experiments conducted by De Schutter and Taerwe [181] demonstrated that the thermal diffusivity of cement paste exhibits a linear decrease in conjunction with the hydration degree. According to Eq. (2.69), it is discernible that the thermal diffusivity is directly proportional to the thermal conductivity, thereby leading to the conclusion that the thermal conductivity will also linearly decrease with the progression of the degree of hydration. Schindler [182] suggested that the thermal conductivity of concrete linearly diminishes with the degree of hydration, transitioning from 1.33 times the ultimate thermal conductivity to the ultimate thermal conductivity itself, as illustrated in the following equation:

$$k_c(\alpha) = k_u \cdot (1.33 - 0.33\alpha) \tag{2.70}$$

where $k_c(\alpha)$ is the thermal conductivity of concrete at hydration degree α, k_u is the thermal conductivity of concrete when fully hardened.

2.6.2.2 Specific Heat Capacity

Specific heat capacity is a physical quantity in thermodynamics that represents the ability of an object to absorb heat. It refers to the amount of heat that a unit mass of an object needs to absorb or release to raise or lower its temperature by one unit. Specific heat capacity is expressed in the International System of Units as the amount of heat required for 1 kilogram of an object to increase its temperature by 1 kelvin; therefore its SI unit is J/(kg · K). The specific heat capacity of ordinary concrete typically ranges between 800 and 1200 J//(kg · ℃), as documented by the RILEM Committee 42 [183].

Concrete is formulated from cement, water, aggregates, and potential supplementary materials, amalgamated in specific proportions. The specific heat capacity of concrete can be ascertained through a weighted average approach, considering the mix proportions and the specific heat capacities of each individual components. The computational equation is as follows:

$$C_p = \sum (C_i \cdot x_i) \tag{2.71}$$

where C_p is the specific heat capacity of concrete, C_i is the specific heat capacity of the i-th component, and x_i is the mass fraction of the i-th component.

The determinants influencing the specific heat capacity of concrete are similar to those that impact its thermal conductivity. Neville [34] stated that the specific heat capacity of concrete diminishes with an escalation in density, attributing this to the fact that denser concrete encompasses a greater proportion of solid components (primarily aggregates) and fewer voids, thereby reducing the content of gases and pore water. Given that the specific heat capacities of gases and liquids typically exceed those of solids, and in accordance with Eq. (2.71), concrete with a higher density will exhibit a reduced specific heat capacity. Bamforth [165] suggested that, owing to the substantial volumetric fraction of aggregates within the concrete, the type of aggregates exerts a significant impact on its specific heat capacity. The specific heat capacity of the rocks tested by Bamforth ranged from 800 to 1000 J/(kg·K). Bamforth *et al.* [184] recommend using the range of specific heat capacities of concrete suggested in Eurocode 2 [185]. Neville [34], however, posited that the mineralogical characteristics of the aggregates minimally influence the specific heat capacity of concrete.

The elevation in the moisture content of concrete amplifies its specific heat capacity, attributed to the fact that the specific heat capacity of water (4.2e3 J/(kg·℃) at 25 ℃) substantially surpasses that of conventional concrete. This assertion was validated by Khan *et al.* [186], who conducted experiments utilizing oven-dried aggregate and saturated aggregate, respectively, as the aggregate component for concrete of identical strength. The outcomes revealed that the concrete composed of oven-dried aggregate manifested a lower specific heat capacity than the concrete formulated with saturated

aggregate.

Whiting *et al.* [187] pointed out that elevating the temperature leads to an augmentation in the specific heat capacity of concrete of normal density. This assertion was empirically corroborated by Khan *et al.* [186], who discerned through experimentation that as the temperature ascended from 30°C to 70°C, the specific heat capacity experienced an elevation from 650 to 2700 J/(kg·K).

The distinctiveness of the early stages of concrete, characterized by the ongoing hydration reactions resulting in the consumption of water and generation of hydration products, as well as the gradual transition of concrete from a semi-fluid state to a hardened state, has been reiterated throughout this section. Inevitably, its specific heat capacity also undergoes alterations during this period. Mikulić *et al.* [179] also monitored the developmental trend of the specific heat capacity of cement paste over the initial four days through experimentation. The results delineate that the variations in specific heat capacity can be segmented into three phases. The first phase transpires within the initial four hours, during which the numerical value of specific heat capacity remains constant. The second phase, occurring between four to fifteen hours, exhibits a comparatively rapid increase in specific heat capacity relative to other stages. The remaining time frame constitutes the third phase, where the specific heat capacity demonstrates a gradual and stable augmentation. In the experiment conducted by Mikulić *et al.*, the variation in the specific heat capacity of the cement paste was minimal, hovering around 916-920 J/(kg·K). Consequently, they posited that the variation in the specific heat capacity of cement paste with age can be deemed negligible. The specific heat capacity development curves of the cement paste they monitored are shown below:

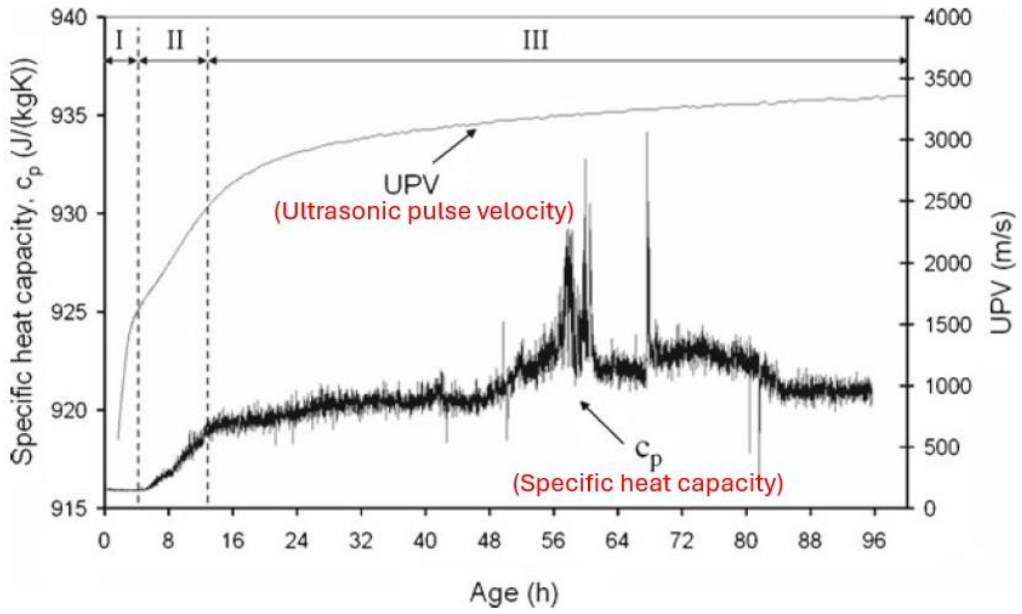

Figure 2.27. Specific heat capacity monitoring results of cement paste by Mikulić *et al.* [179].

Van Breugel [188] recommended the utilization of the subsequent formula to characterize the variation in the specific heat capacity of concrete with alterations in the concrete mix, degree of hydration, and temperature:

$$C_p = \frac{1}{\rho} \cdot \left(W_c \cdot \alpha \cdot C_{ref} + W_c \cdot (1 - \alpha) \cdot C_c + W_a \cdot C_a + W_w \cdot C_w \right) \quad (2.72)$$

where C_p is the specific heat of concrete (J/(kg·K)), ρ is the density of concrete (kg/m3), C_{ref} is the specific heat of hardened concrete (J/(kg·K)) (refer to Eq. (2.73)), W_c, W_a, W_w are the percentage of cement, aggregate, water in the total concrete (by weight), separately, and C_c, C_a, C_w are the specific heat of cement, aggregate, water, separately (J/(kg·K)).

$$C_{ref} = 8.4 \cdot T_c + 339 \quad (2.73)$$

where T_c is the concrete temperature (°C).

2.6.3 Existing FEM Models for Concrete Temperature Prediction

The exploration of Finite Element Models (FEM) in predicting and analysing the temperature variations within concrete structures has garnered significant attention and application in both academia and industry. The intrinsic complexity of in-situ concrete's thermal behaviour, especially during its early age, necessitates deploying robust, accurate, and reliable models to comprehend and predict the thermal gradients and potential risk of thermal cracking. Existing FEM models, developed and refined over the years, offer various mathematical and computational frameworks that allows researchers and engineers to simulate the heat transfer phenomena within concrete, considering various influencing factors such as cement hydration, external temperature, and material properties. This section will examine some representative existing finite element models for concrete temperature development, exploring their fundamentals, accuracy, practical applicability, and potential limitations.

2.6.3.1. COST TU1404 Benchmark Study

Jedrzejewska *et al.* [21] posited that the challenges in modelling the early thermal and mechanical behaviours of cement-based materials (CBMs) do not stem from a lack of knowledge in the domain. Instead, the true challenge lies in its vast breadth. To elucidate, many models are currently available for simulating the early-stage behaviour of CBMs. Jedrzejewska *et al.* embarked on the COST TU1404 benchmark study to comprehend and evaluate these concrete models. Specifically, Task 2 of this initiative was dedicated to models focusing on the hydration temperature of concrete. The primary objective was to assess the capability of various models in simulating the non-

linear and non-stationary temperature evolution in concrete specimens. It is imperative to note that the study's aim was not to compare heat transfer models per se but rather to discern the impact of different hydration heat output models on the ultimate prediction of concrete temperature. All models adopted material thermal properties and boundary conditions consistent with the originating experimental setup [20] to ensure a congruent comparison of simulation outcomes with analogous assumptions.

The work of Jedrzejewska *et al.* actually adopts different heat release rates from hydration, Q, in the heat diffusion equation in Eq. (2.60) for comparing the solutions of the equation. As revisited in Section 2.5.7, several distinct yet maturity-based hydration heat rate equations elucidate that the hydration rate of concrete under variable temperatures is a function of both hydration degree and temperature. Jedrzejewska *et al.* incorporated five diverse models of hydration heat rates [140, 189-192] to serve as the heat source in the concrete heat transfer model. Predominantly, these models factor in the role of concrete maturity, or the equivalent age, wherein the temperature and age of the concrete from the preceding timestep are utilized as independent variables for the hydration heat rate of the subsequent timestep. These models manifest in varied mathematical formulations and encompass distinct influencing parameters, such as chemical affinity, water content, and the porosity of the paste, among others.

One of the hydration heat rate models employed a time-dependent heat generation equation [191], which notably omits the consideration of concrete maturity. In essence, this model overlooks the dynamic influence of the evolving concrete temperature on its hydration heat rate. The expression of this model is shown below:

$$H(t) = H_{max} \cdot (1 - exp(-k \cdot t^n)) \tag{2.74}$$

where H(t) is the cumulative hydration heat at time t, H_{max} is the ultimate hydration heat, t is the concrete age, and k, n are fitting parameters.

Due to the model's disregard for temperature effects, significant discrepancies were observed in the cumulative hydration heat and the simulated concrete temperature outcomes. Specifically, when simulating the cumulative hydration heat from isothermal calorimetry experiments at varying temperatures, the model yielded identical results across all the temperatures under consideration, as depicted in Figure 2.28 This underscores the model's inability to capture the variations in cement hydration rates at different temperatures.

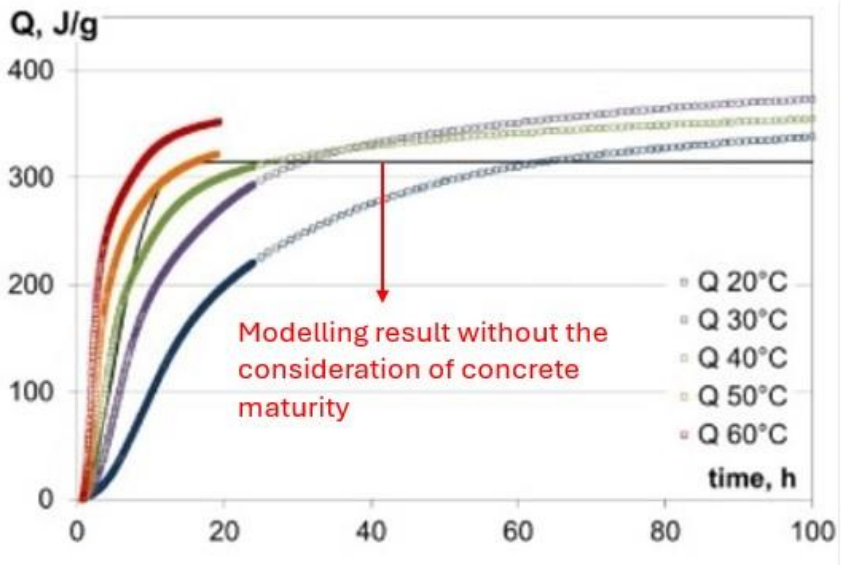

Figure 2.28. Cumulative hydration heat simulation results based on a time-dependent heat generation equation [21].

The other hydration heat rate models that incorporate equivalent age, despite minor variations in accuracy, achieved commendable precision. These results were characterized by Jedrzejewska *et al.* as being notably consistent. This observation naturally leads to another pertinent consideration: the user-friendliness of the models. In the realm of modelling, while achieving a significant degree of accuracy is paramount, the elegance and simplicity of the model are equally crucial. Overly intricate models might compromise computational efficiency and lead to convergence issues in subsequent Finite Element Method (FEM) computations. Moreover, while some highly complex models account for a plethora of influencing factors—such as the model based on Buffo-Lacarrière *et al.* [190], which considers chemical affinity, water content, porosity, initial cement content, and the volume of hydration product formation—many of these parameters require meticulous experimental determination. Such parameters are often unfeasible in standard engineering contexts and are superfluous for macroscopic thermal behaviour simulations of concrete. Furthermore, despite the inclusion of such an extensive array of parameters, the precision of Lacarrière *et al.*-based model does not necessarily surpass that of their more streamlined counterparts [21].

In their study, Jedrzejewska et al. [21] built upon the experimental framework established by Azenha *et al.* [20], employing a range of hydration heat rate models to simulate the temperature progression in concrete. Their comparative analysis of the results from different models highlighted a significant limitation in Eq. (2.74), which neglects the role of concrete maturity. Consequently, its simulation outcomes are deemed unsuitable for in-situ concrete applications. This revelation underscores two critical observations: 1). The influence of temperature on cement's hydration heat rate is an essential consideration in the simulation of in-situ concrete temperature dynamics; 2). The concept of concrete maturity serves as an effective metric to quantify this

influence. This aligns with the discourse in Section 2.54, which advocates for extending the foundational assumption of concrete maturity (that concrete with identical mix and maturity manifests consistent strength) to encompass the cumulative hydration heat and the hydration degree in concrete.

While Jedrzejewska *et al.* [21] critically evaluated the accuracy of various cement hydration heat models in predicting the temperature evolution of concrete, emphasizing the pivotal role of concrete maturity in the process, it is imperative to note that their study was predicated on the concrete temperature monitoring experiments of Azenha *et al.* [20]. In the latter's experimental setup, concrete specimens were placed within an environmental chamber, with the curing temperature meticulously maintained around 20°C. Such a curing temperature starkly contrasts with the conditions typically encountered by in-situ concrete. Consequently, in subsequent concrete temperature modelling works, the mathematical representation of heat loss from the concrete surface to the ambient air through thermal convection might be overly simplistic, failing to capture the nuanced effects of fluctuating environmental temperatures on cement hydration rates and the temperature development of in-situ concrete. Therefore, a closer approximation to the curing environment of real in-situ concrete is expected to be implemented for modelling in-situ concrete temperature development.

2.6.3.2. Calorimetry-Based Temperature Modelling

Xu *et al.* [99] evaluated the accuracy of different calorimetry tests for characterizing the cement hydration properties and predicting the concrete temperature development. They obtained the cement hydration parameters (based on Eq. (2.42)) from the results of semi-adiabatic calorimetry tests and isothermal calorimetry tests, respectively. Subsequently, these parameters were incorporated into a finite difference method model they established, aiming to simulate the temperature development within concrete pavements.

The derivation process for the heat source component (Q in Eq. (2.60)) of the concrete temperature model is similar to the approach delineated in Section 2.5.7 under "Based on TPE Hydration Degree". As elucidated in Eq. (2.42), the three hydration parameters, α_u, τ, and β, have been substantiated to possess tangible physical implications. They respectively signify the ultimate hydration degree attainable by the cement, the latency of the hydration reaction, and the rate of hydration reaction. The calorimetry outcomes presented in Section 2.4 can be harnessed in the curve-fitting procedure to deduce these hydration parameters. However, a pivotal consideration is that the experimental results suitable for the fitting process must encapsulate the complete hydration curve of the cement. Evidently, the heat loss characteristics inherent to the semi-adiabatic calorimetry experiments impede their direct applicability for curve-fitting. While adiabatic calorimetry experiments necessitate specialized systems to maintain an adiabatic condition for the specimens, such apparatus often incurs significant costs. Consequently, Xu *et al.* opted for a Heat Loss Compensation approach, converting the

hydration curve from semi-adiabatic calorimetry into an adiabatic hydration curve, thereby validating the feasibility of employing semi-adiabatic calorimetry in the curve-fitting of hydration parameters. Concurrently, they conducted isothermal calorimetry experiments on mortar specimens at multiple temperatures, with the results being able in the curve-fitting of hydration parameters.

The curve-fitting results for the hydration parameters revealed that those derived from semi-adiabatic calorimetry experiments exhibited a larger hydration time parameter τ and a smaller hydration shape parameter β compared to those based on isothermal calorimetry experiments. In light of the physical interpretations of the hydration parameters presented in Figure 2.22 to Figure 2.24, it can be inferred that the hydration degree simulations based on semi-adiabatic calorimetry would manifest a more pronounced hydration delay, coupled with an lower early-stage hydration degree, relative to those based on isothermal calorimetry. Figure 2.29 illustrates the hydration degree simulation results for one test mix, with other simulations echoing a similar trend. Xu *et al.* [99] posited that this discrepancy arises from the absence of coarse aggregates in the mortar specimens used in the isothermal calorimetry experiments, leading to an oversight of the "delaying effect" imparted by the coarse aggregates. This distinction in the curve-fitting of hydration parameters and the consequent hydration degree simulations was also reflected in the final temperature simulations for the concrete pavement. Specifically, the temperature simulations based on semi-adiabatic calorimetry displayed a more pronounced delay and lower temperatures in the early stages compared to those based on isothermal calorimetry, aligning with the trends observed in the hydration degree simulations. One such temperature simulation result is depicted in Figure 2.30. In summation, the temperature simulations rooted in semi-adiabatic calorimetry experiments demonstrated superior accuracy, potentially attributable to including coarse aggregates in the specimens, mirroring the mix composition of actual concrete pavements.

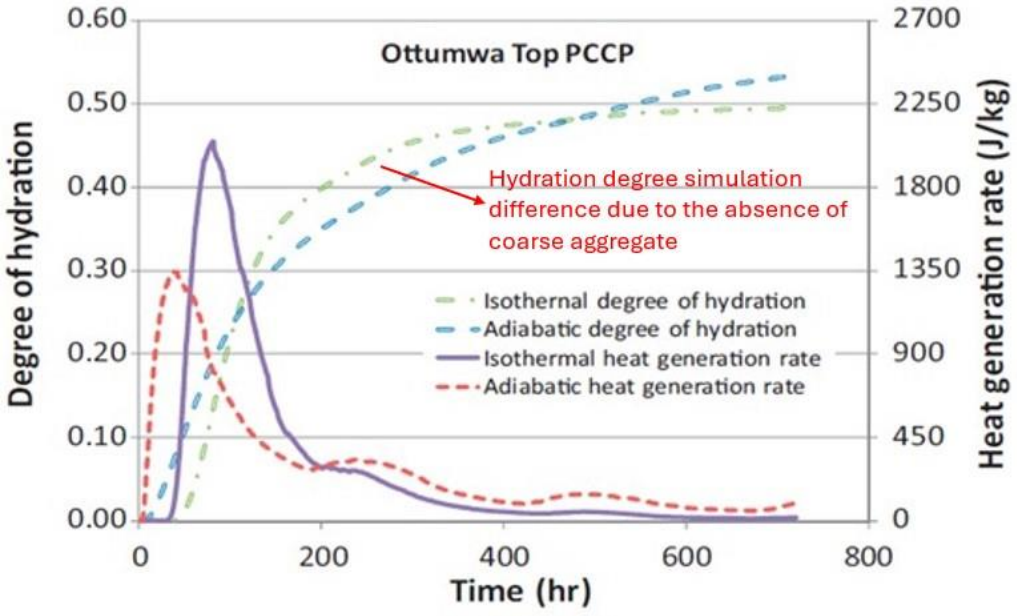

Figure 2.29. Hydration degree simulation results by Xu *et al.* [99].

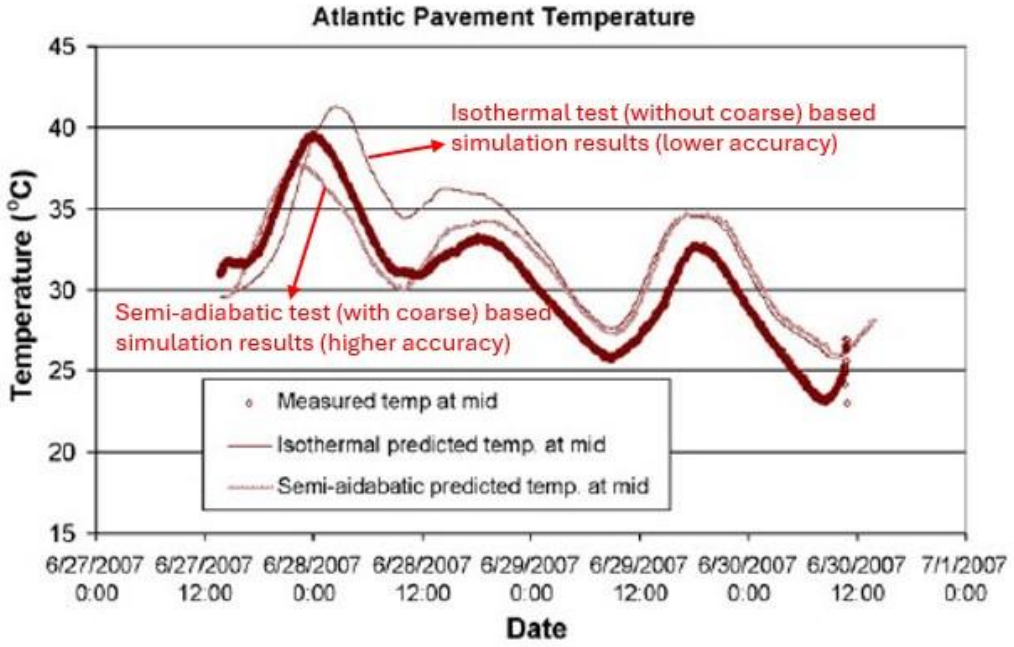

Figure 2.30. Concrete pavement temperature simulation results by Xu *et al.* [99].

By comparing the concrete temperature simulations based on semi-adiabatic calorimetry with those based on isothermal calorimetry, Xu *et al.* discerned potential inaccuracies stemming from the absence of coarse aggregates in the isothermal calorimetry experiments. This contrasts Wadsö's [16] proposition that the hydration curves of equivalent cement paste and mortar can represent concrete. These divergent perspectives were previously deliberated upon in Sections 2.4.3 and 2.5.7. While Wadsö's experiments substantiated the interchangeability of hydration curves between cement paste and mortar, the extrapolation of this equivalence to concrete remains speculative and unverified, primarily due to the volumetric constraints of isothermal calorimetry channels precluding the inclusion of coarse aggregates. Indirectly, the temperature simulations by Xu *et al.* underscored the consequential inaccuracies introduced by the omission of coarse aggregates in isothermal calorimetry specimens. Xu *et al.*'s simulation work suggested the imperative to investigate the influence of coarse aggregates in concrete on the evolution of hydration heat, aiming to enhance the precision in forecasting the temperature progression in concrete.

2.6.3.3. Influence of GGBS on FEM Modelling Accuracy

As delineated in Section 2.2.2, Ground Granulated Blast-furnace Slag (GGBS) is a by-product of the steel industry which can be used as a supplementary cementitious material in concrete, substituting a portion of cement. Owing to its sustainability, eco-friendliness (low carbon footprint), and capacity to enhance concrete properties (such as improved workability, reduced permeability, and augmented resistance to sulphate attack), GGBS has been extensively incorporated in construction to replace part of

cement. In addressing the issue of thermal cracking in concrete, the inclusion of GGBS significantly mitigates this concern, attributed to its inherently lower heat of hydration compared to CEM I cement, thereby diminishing the risk of thermal cracking. However, substituting GGBS for a portion of cement in concrete can compromise its early-age strength, potentially introducing safety vulnerabilities. To strike a "balance" between the heat-reducing benefits of GGBS and its detrimental effect on early-age strength, Tang *et al.* [1, 5] devised a FEM model to predict the early hydration temperature evolution of in-situ concrete containing GGBS.

Tang *et al.*'s FEM model was based on the results of isothermal calorimetry tests conducted at varying temperatures. To transpose the hydration curves from the isothermal calorimetry tests to actual hydration curves for in-situ concrete, they employed the NordTest Method developed by Wadsö [15], as referenced in Section 2.5.7. This method hinges on multiple curve-fitting and interpolation processes to ascertain the hydration rate at specific temperatures and specific cumulative heats of hydration (or degrees of hydration), facilitating the simulation of concrete's hydration temperature evolution over the initial three days. This computational approach encompasses two pivotal stages: initially, a tenth-degree polynomial is utilized to express the hydration rate, Q, as a function of the cumulative heat of hydration, H. Subsequently, a quadratic polynomial is employed to articulate the hydration rate, Q, at a designated temperature and specific cumulative heat of hydration. The simulation outcomes presented by Tang *et al.* revealed a high accuracy for the CEM I-only mix. However, for concrete with a high GGBS content (where 70% of CEM I is supplanted by GGBS), the simulations manifested considerable discrepancies. Figure 2.31 and Figure 2.32, respectively, depict the tenth-degree polynomial and temperature simulation results for the 70% GGBS mix.

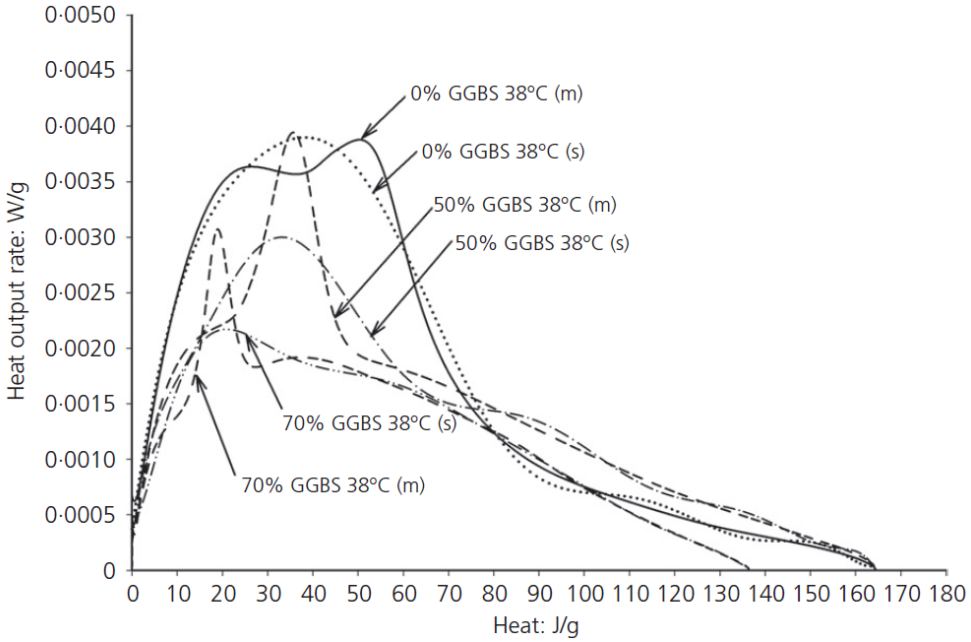

Figure 2.31. Tenth-degree polynomial regression results by Tang *et al.* [1] (m:

measurement; s: simulation).

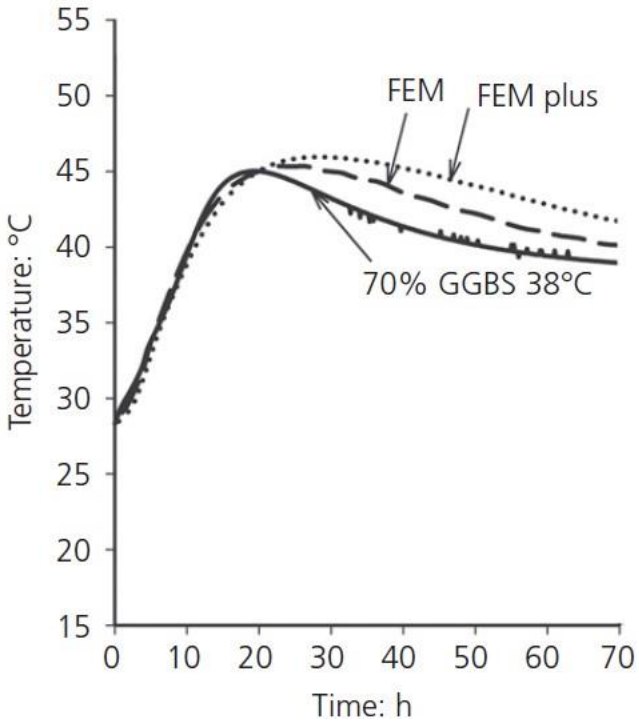

Figure 2.32. 70% GGBS concrete temperature modelling results by Tang *et al.* [1].

As discernible from Figure 2.31, the diminished accuracy in the temperature simulation of GGBS concrete can be attributed to the inability of the tenth-degree polynomial regression analysis to capture the "second peak" arising from the hydration delay effect of GGBS. This subsequently led to deviations in the subsequent predictions of hydration rate and concrete temperature evolution. Other studies [22, 23] have also reported the declining precision of traditional maturity method-based concrete hydration heat models with the incorporation of GGBS. Although these studies are predicated on different hydration heat rate models, the underlying reasons for the discrepancies appear congruent. Addressing this issue, De Schutter [65] and Zheng *et al.* [66] had previously posited that the hydration process of GGBS-CEM blended should not be perceived as a singular hydration akin to CEM-I. Instead, it necessitates consideration of the inherent hydration of GGBS and the co-reactivity effect of CEM I and GGBS, as elaborated upon in Section 2.2.3.4. However, despite the existence of theoretical solutions to this quandary, no dedicated FEM program has been developed in recent years specifically tailored for the temperature simulation of GGBS concrete. With the escalating ubiquity of GGBS, research into its hydration characteristics, followed by establishing a dedicated GGBS concrete temperature simulation program, becomes imperative.

2.7 Conclusion

Chapter 2 reviews the fundamental concepts, mechanisms, and methodologies relevant

to early-age temperature development in in-situ concrete and the associated risks of thermal cracking. It begins by examining the hydration process of cementitious materials, particularly the key chemical reactions that drive heat generation during cement hydration and highlights the significance of understanding the hydration stages to predict temperature development and mitigate potential thermal issues in mass and large-span concrete structures.

The chapter then discusses factors influencing hydration heat and temperature development, including cement type, water-cement ratio, binder fineness, supplementary cementitious materials (SCMs) such as GGBS, environmental conditions, and specimen size. These factors are critical in determining the rate of hydration, the peak temperature achieved, and the thermal gradients within concrete structures. The importance of optimizing these variables to reduce the risk of thermal cracking is emphasized.

The chapter also explores the causes and mechanisms of early-age thermal cracking in in-situ concrete, identifying internal constraints, external constraints, and environmental factors as primary contributors to thermal stress development. Mass concrete structures are particularly susceptible due to their large volume and low thermal conductivity, which can result in significant temperature differences between the core and surface. The chapter addresses thermal loading and cracking risks in long-span and thin-slab concrete structures and highlights the distinct challenges posed by these configurations.

The chapter reviews various engineering strategies to mitigate thermal cracking, including material selection, temperature gradient management through cooling water pipes and formwork insulation and reducing hydration heat by incorporating SCMs or optimizing cement content. These mitigation techniques aim to minimize thermal stresses while maintaining the required strength and durability of concrete structures.

The chapter proceeds to outline methods for measuring cement hydration and concrete temperature, focusing on calorimetry techniques. It evaluates adiabatic, semi-adiabatic, and isothermal calorimetry methods, describing their operational principles, advantages, and limitations. While adiabatic and semi-adiabatic calorimetry simulates real-world conditions by accounting for heat loss, isothermal calorimetry offers direct heat flow measurements under controlled temperature conditions. The chapter compares these techniques to provide insights into selecting the appropriate method for specific research and construction applications.

Lastly, the chapter addresses the application of numerical modelling techniques, particularly the finite element method (FEM), for predicting early-age hydration temperatures in concrete structures. It discusses the integration of heat transfer mechanisms, such as thermal conduction, convection, and radiation, into FEM models. The chapter emphasizes the importance of accurate input parameters, including the

thermal properties of materials and boundary conditions, to ensure reliable predictions.

In summary, Chapter 2 outlines key concepts, influencing factors, measurement techniques, and modelling approaches related to early-age hydration temperature development in concrete. It identifies critical knowledge gaps and emphasizes integrating material selection, construction practices, and advanced modelling techniques to achieve sustainable and durable concrete structures. The findings and insights from this literature review form the basis for the subsequent chapters, which will address the identified gaps and develop more effective strategies for managing thermal behaviour in concrete structures.

CHAPTER 3 MATERIALS AND CONCRETE MIX DESIGN

3.1 Introduction

This chapter presents the materials used in this study, detailing their physical and chemical properties and the associated testing methods. It also outlines the trial mix design process of the concrete, ensuring compliance with European and British standards, including workability and 28-day compressive strength.

3.2 Materials

3.2.1 Cement

In this research, the cement used is CEM-I 52.5N, a high-strength cement produced by CEMEX UK Cement Ltd. This cement conforms to the standards outlined in BS EN 197-1:2011 [28]. The oxide composition of the cement was determined through X-ray fluorescence (XRF) testing via a Rigaku NEX CG II XRF Analyzer in the Experimental Techniques Centre of Brunel University London. The detailed composition of the cement is presented in Table 3.1, which adheres to the BS EN 196-2: 2013 [193]. The selection of CEM-I 52.5N for this research was based on its high-strength properties, making it particularly suitable for the study's focus on early-age concrete behaviour and thermal development.

3.2.2 GGBS

As outlined in Chapter 3, this research employs Ground Granulated Blast-Furnace Slag (GGBS) as a partial replacement for cement to investigate its suppressive effect on cement hydration heat and the early-age hydration temperature rise in concrete. The GGBS used in this research is TEES SF REGEN GGBS, produced by Hanson UK. This GGBS complies with the standards of BS EN 15167-1:2006 [43]. According to technical information available on this product's website [194], using REGEN GGBS in concrete as a replacement for one tonne of Portland cement can reduce CO_2 emissions by approximately 900 kg while enhancing the concrete's durability. The oxide composition of this GGBS, alongside the previously mentioned CEM I, was measured via XRF testing, with the results presented in Table 3.1. The oxide compositions of CEM I and GGBS will be used to calculate the ultimate heat of hydration H_u of the binder in concrete, which has been discussed in detail in Section 2.5.4 (Eq. (2.39)).

Table 3.1. Oxide Compound of cement and GGBS detected via XRF tests.

Oxide Compound	Content (%)	
	CEM-I 52.5N	REGEN GGBS
CaO	60.79	37.85
SiO_2	21.32	35.49
Al_2O_3	4.06	13.76
Fe_2O_3	3.23	1.32
K_2O	0.45	0.36
MgO	2.40	5.19
SO_3	4.57	1.72
P_2O_5	1.47	1.45
TiO_2	0.26	0.77
SrO	0.11	0.06
MnO	0.06	0.29

3.2.3 Coarse Aggregate

The coarse aggregate employed in this study is locally sourced crushed riverbed stone. Adhering to the procedures outlined in BS EN 933-1:2012 [195] and BS EN 12620: 2013 [196], the aggregate was sieved using a sieving machine to obtain a uniform grading of 10 mm. Essential for the subsequent design of the concrete mix, the aggregate's density (Saturated Surface Dry (SSD) Specific Gravity and Specific Gravity) and water absorption rate were determined following the testing steps specified in AASHTO T 85 [197]. The results of these measurements are shown in Table 3.2.

3.2.4 Fine Aggregate

This study employed medium sand, with a typical size range of 0.25-0.5mm, as defined in BS EN 12620:2013 [196]. Following a procedure analogous to the coarse aggregate sieving, the sand was graded using a sieving machine using the experimental steps required by BS EN 933-1:2012 [195] and BS EN 12620: 2013 [196] to achieve the desired particle size distribution. 55.6% of the sand passed through a 600 μm sieve. Subsequently, the density and water absorption rate of the fine aggregate were measured following the procedures outlined in AASHTO T 84 [198], with the results detailed in Table 3.2.

Table 3.2. Physical properties of aggregates.

	SSD specific gravity (kg/m^3)	Water absorption (%)	Specific gravity (kg/m^3)
Coarse aggregate	2550	0.78	2530
Fine aggregate	2476	1.86	2430

3.2.5 Mixing Water

The quality of mixing water in concrete production is paramount; it must be free from harmful organic substances and inorganic compounds exceeding permissible levels. In the context of the UK, the standards for water utilized in concrete mixing are governed by BS EN 1008 [199]. In alignment with this standard, tap water was consistently employed for the concrete's mixing and water curing processes.

3.3 Concrete Mix Design and Testing

This section details the concrete trial mix process to develop a concrete mix suitable for structural applications, specifically focusing on achieving the workability and strength required for reinforced concrete (RC) beams and slabs. The mix design followed the guidelines outlined in the "Design of Normal Concrete Mixes" by the Building Research Establishment (BRE), ensuring compliance with British standards. The trial mix process included adjustments based on workability and compressive strength tests to finalize a mix that meets industry requirements. Through a series of slump tests and 28-day compressive strength tests, three variations of the concrete mix were evaluated to identify the most suitable formulation for this study.

3.3.1 Initial Mix Design and Adjustments

To ensure the concrete mix applied in this study adhered to construction standards, a design process was undertaken based on the design textbook "Design of normal concrete mixes" [63] authored by the Building Research Establishment (BRE) in the UK. It is therefore referred to as "BRE mix design" in this thesis. This manual has been crafted in alignment with British standards about the workability, strength, and durability requirements of concrete. It encompasses fundamental principles and procedures for designing concrete mixes, including performance requirements, material selection, water-cement ratio determination, aggregate content calculation, incorporation of admixtures and additives, and concrete workability and strength considerations.

Furthermore, the manual offers a range of practical tables and charts for determining design parameters, along with examples of typical concrete mix proportions. The core design philosophy of this guide is to design a concrete mix, which meets the desired workability and strength criteria based on the limited data typically available during the mix design phase. Subsequent laboratory work (trial mix) aims to adjust this initial mix to ensure the final concrete mix meets the actual production requirements.

In this research, the designed concrete aimed to achieve the strength grade of C30/37 (Characteristic strength). The initial concrete mix, formulated in accordance with the guidelines provided in "BRE mix design", is presented in the following table:

Table 3.3. Initial concrete mix design

	Total binder content (kg/m^3)	Free water-cement ratio	10 mm Coarse aggregate (kg/m^3)	Medium sand (kg/m^3)
Initial concrete mix	409	0.55	1017	696

The initial concrete mix designed for this study was subsequently adjusted based on workability and 28-day compressive strength tests to ensure it met the relevant British standards and actual production requirements. During the trial mix phase, the water-to-cement (w/c) ratio was reduced by augmenting the binder content. Two additional adjusted mixes, with w/c ratios of 0.53 and 0.5, respectively, were experimented with the initial mix, culminating in the evaluation of three concrete mix variations. The objective was to identify a mix that satisfies the workability and strength criteria for this research. The specific details of these three tested concrete mixes, including the initial concrete mix, are as follows:

Table 3.4. Concrete mixes tested in trial mix

Free water-cement ratio	Total binder content (kg/m^3)	Total water content (kg/m^3)	10 mm Coarse aggregate (kg/m^3)	Medium sand (kg/m^3)
0.55 (initial mix in Table 3.3)	409	246	1017	696
0.53	426	246	1017	696
0.50	450	246	1017	696

3.3.2 Workability Test

The workability of the concrete in this study was assessed using the slump test, a key measure of concrete's consistency and flowability. As per the slump class specifications of BS 8500-1:2015 [200], the target concrete was classified under the S3 class, with the intended slump value ranging between 80-170mm. The slump test was conducted following the procedure required by BS EN 12350-2:2019 [201]. The results from the slump tests for all three mixes conformed to the specified requirements, and the results are summarised in the following Table:

Table 3.5. Slump test results

	0.55 w/b specimen	0.53 w/b specimen	0.50 w/b specimen
Slump (mm)	120	109	94

3.3.3 Specimen Preparation and Curing

The trial mix for concrete strength was evaluated through the 28-day compressive strength testing of cylindrical concrete specimens with dimensions of 10 × 20 cm (base diameter of 10 cm, height of 20 cm). These dimensions align with one of the standard sizes recommended in BS EN 12390-1:2021 [202]. The 28-day characteristic strength of these specimens was expected to be 30 MPa. The target mean strength of the specimens can be calculated using the following formula:

$$f_{tm} = f_{ck} + k \cdot s \tag{3.1}$$

where f_{tm} is the target mean strength of the specimens (MPa), f_{ck} is the characteristic strength of the specimens (MPa), k is a statistical coefficient that depends on the reliability level of the concrete strength and is generally taken as 1.64, and s is the standard deviation, can be determined via the "BRE mix design", take 8 N/mm^2 for this study. The calculated target mean strength is 44 N/ mm^2 (MPa).

The concrete mixing works were conducted following the procedures recommended in BS 1881-125:2013 [203]. Mixing was carried out using a batch mixer with a capacity of 160 litters. As the concrete mix design was based on dry raw materials, and the "Free w/c" in the mix accounted for the aggregate's water absorption, it was necessary to pre-dry the aggregates in an oven for 24 hours prior to mixing and allow them to cool to room temperature before mixing commenced.

The procedure for the mixing process was as follows: Initially, approximately half of the coarse aggregates were introduced into the mixer, followed by adding all the fine aggregates and then the remaining coarse aggregates. The mixer was then activated and run for approximately 30 seconds. At the 15-second mark, about half of the water was poured in, and the mixer was allowed to continue operating for three minutes. The machine was then paused, and the lid closed for a five-minute resting period. Subsequently, cement was added and mixed for 30 seconds, followed by adding the remaining water. Once all materials were incorporated into the mixer, it was run for three more minutes to complete mixing. Sampling and casting should be performed promptly after the mixing process.

The casting and curing of concrete specimens were carried out according to the recommended procedures in BS EN 12390-2:2019 [201]. To prevent the adhesion of concrete to the moulds, a release oil was applied to the inner surfaces of the moulds prior to casting. In order to ensure adequate compaction of the concrete, the moulds were placed on a level surface. When the concrete was filled to approximately half of the mould's height, it was vibrated using a compaction rod at least 25 times, taking care to avoid forceful contact with the bottom of the mould. The casting was continued until the moulds were filled, and the same rodding procedure was repeated, avoiding penetrating the top surface of the previous layer. Concurrently, the sides of the moulds were gently tapped with a hammer to ensure the elimination of air bubbles and the

filling of any depressions. Five specimens were made for each mix to obtain the average compressive strength at 28 days.

Immediately after casting, the surface of the specimens was covered with cling film to prevent moisture evaporation. The specimens were transferred to an air-conditioned curing room and left for 16 hours until they hardened enough to be demoulded. After demoulding, each specimen was marked with a marker pen for identification, noting details, including the concrete mix and casting time. The specimens were then immediately placed into a water bath with a constant temperature of 20 °C for continuous curing over 28 days. Figure 3.1 shows a photograph of the cylindrical concrete specimens in the water bath.

Figure 3.1. Cylinder specimens in the 20°C-water bath (Photograph taken on 29 April 2022).

3.3.4 28-Day Compressive Strength Testing

The 28-day compressive strength testing of the concrete cylinder specimens was conducted in accordance with the procedures outlined in BS EN 12390-3:2019 [204] and BS EN 12390-4:2019 [205]. The compressive strength test utilized an Autocon concrete compressive strength machine produced by VJ Tech. This equipment allows for the input of specimen dimensions, customizing the loading rate, and features an automatic detection of specimen failure. Upon failure, the machine ceases pressure application and records the failure load.

Before testing, a capping process was employed to ensure the upper and lower surfaces

of the cylinder specimens were perpendicular to the compression axis. This capping process utilized Cylinder Capping Equipment from the CONTROLS group and a mixture of sulphur and mineral filler as capping material, known for its smoothness and performance. The capped specimens were then centrally placed on the compression axis, and the machine was set to apply a load of 5 KN/s until it stopped due to specimen failure. The line chart in Figure 3.2 shows the results of 28-day compressive strength experiments on concrete cylindrical specimens. It was observed that only specimens with a w/c ratio of 0.5 achieved the target mean strength. Consequently, all concrete specimens in this study were mixed according to the final row in Table 3.4.

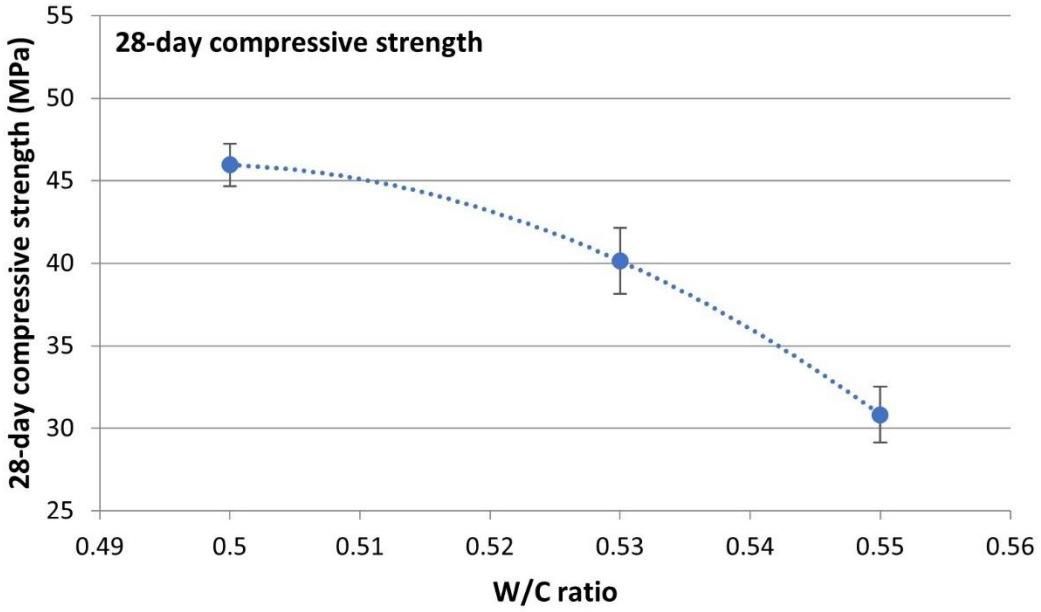

Figure 3.2. Concrete cylinder 28-day compressive strength test results

CHAPTER 4 SEMI-ADIABATIC CALORIMETRY TEST PROCEDURE, RESULTS, AND ANALYSIS

4.1 Experimental Procedure for Semi-Adiabatic Calorimetry

Semi-adiabatic calorimetry tests were conducted to simulate the early-age hydration temperature development of in-situ concrete. To investigate the effect of GGBS on reducing the hydration temperature of concrete, GGBS was used to replace 10%, 20%, 30%, 40%, and 50% of CEM I (by weight) in the concrete mix, resulting in six different concrete mixes, including the mix without GGBS determined in the trial mix process. The detailed compositions of these six concrete mixes are presented in Table 4.1. Each mix variation was designed to assess the impact of varying GGBS content on the temperature development during the concrete's early-age hydration phase (first three days). Including a control mix without GGBS provides a baseline for comparison, enabling a clear understanding of the thermal behaviour alterations induced by the GGBS. This comparative analysis is crucial for determining the effectiveness of GGBS in controlling the hydration temperature.

Table 4.1. Semi-adiabatic concrete mixes

	CEM I (kg/m^3)	GGBS (kg/m^3)	Water (kg/m^3)	Coarse aggregate (kg/m^3)	Fine aggregate (kg/m^3)
0% GGBS concrete	450	0	246	1017	696
10% GGBS concrete	405	45	246	1017	696
20% GGBS concrete	360	90	246	1017	696
30% GGBS concrete	315	135	246	1017	696
40% GGBS concrete	270	180	246	1017	696
50% GGBS concrete	225	225	246	1017	696

The semi-adiabatic concrete specimen was mixed using the same procedure as the trial mix and subsequently cast into specially designed moulds. These moulds comprised two layers of insulating materials: inner expanded polystyrene sheets and outer timber boards, with their tops left open to facilitate heat dissipation from the concrete. The expanded polystyrene had a thickness of 2 cm on the four sides and 3 cm at the base, with an internal cavity measuring 15 cm in length, width, and height, and the outer length and width are 19 cm, and the height is 18 cm. The dimensions of the outer timber

board were slightly larger, with a thickness of 1.5 cm and internal dimensions of 20 cm in length, width, and height, resulting in external dimensions of 23 cm in length and width and 21.5 cm in height. The expanded polystyrene was placed within the timber board, and the concrete was poured into the expanded polystyrene, leaving the concrete's top surface in direct contact with the air. This arrangement created a semi-adiabatic specimen composed of expanded polystyrene and timber board, emulating the temperature development of in-situ concrete. Figure 4.1 and Figure 4.2 show the insulation moulds and the semi-adiabatic insulation system.

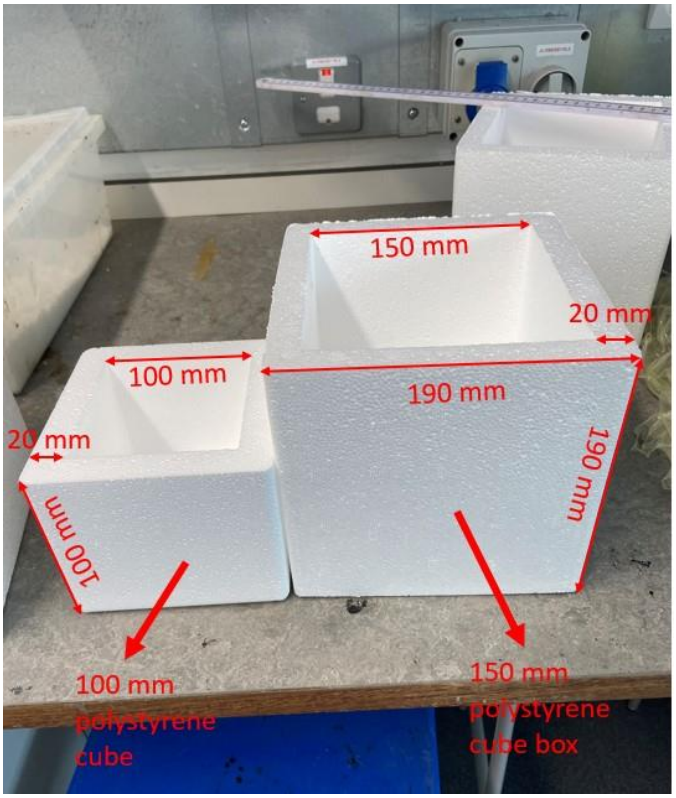

Figure 4.1. Expanded polystyrene mould (right hand one) (Photograph taken on 10 November 2022).

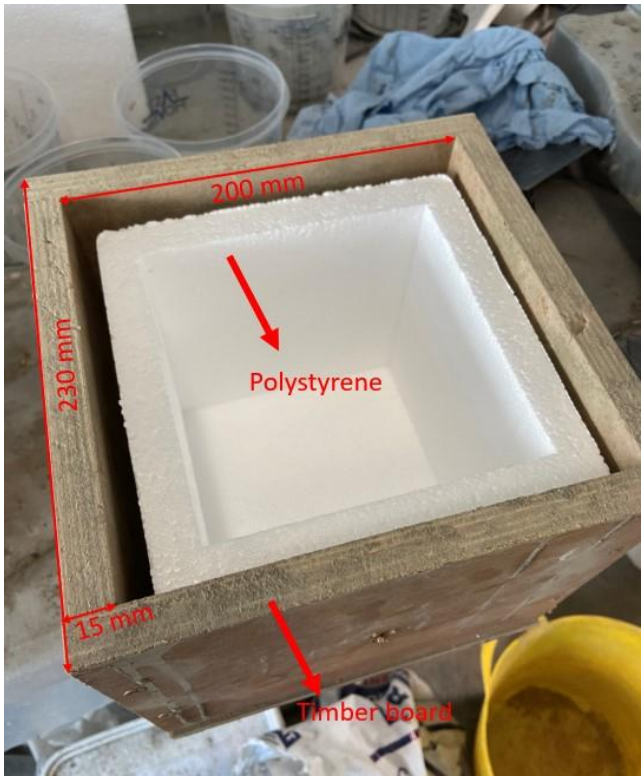

Figure 4.2. Semi-adiabatic test insulation layers (Photograph taken on 10 November 2022).

During the concrete casting process in the semi-adiabatic calorimetry tests, a type-K thermocouple was embedded at the core of each specimen to monitor temperature development. Thermocouples were connected to a 4-channel Thermocouple Data Logger capable of measuring temperatures ranging from -200°C to +1372°C with a precision of 0.1°C, more than adequate for monitoring the temperature of concrete specimens. The thermocouple was positioned at the centre of the specimen once the concrete was cast to half its height. After casting, the top of the concrete specimen was covered with cling film to prevent moisture loss (the cling film is considered as no thermal insulation). The specimens were then placed in an air-conditioned laboratory environment for curing. It is important to note that, unlike an environmental chamber that can maintain a nearly constant temperature, the air-conditioning system can only keep the room temperature within a relatively narrow fluctuation range. Additionally, the room ambient temperature may be influenced by the movement of personnel entering and leaving the laboratory. This fluctuating environmental temperature is intended to simulate the typical variable temperature conditions of in-situ concrete. For each mix, two identical specimens were cast to obtain an average value of temperature development. In addition to monitoring the temperature within the specimens, an additional thermocouple was placed near the specimens to record ambient temperature changes. It is important to note that the thermocouple for monitoring ambient temperature should not be placed on the ground or attached to the mould to avoid measurement inaccuracies. Figure 4.3 shows a photograph of the semi-adiabatic calorimetry test setup. The Thermocouple Data Logger was programmed to record the

temperature in each channel at ten-minute intervals over 72 hours (three days), representing the early-stage temperature development of the concrete.

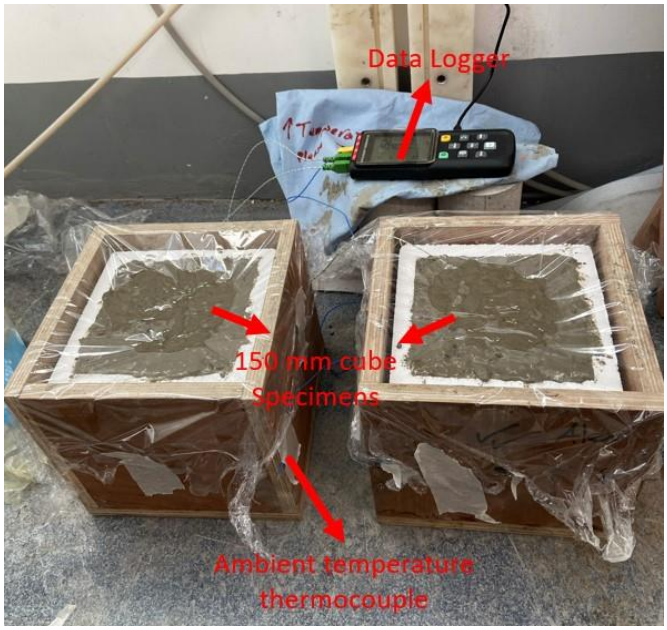

Figure 4.3. Semi-adiabatic calorimetry insulation test setup (Photograph taken on 21 November 2022).

4.2 Effect of GGBS on Hydration Concrete Temperature

Figure 4.4 to Figure 4.9 illustrate the semi-adiabatic temperature results for concrete mixes with different GGBS contents, along with the ambient temperature fluctuations represented by the grey curves. To simulate the curing conditions of in-situ concrete, the specimens were placed in an air-conditioned curing room rather than an environmental chamber. The stability of the temperature control by the air conditioning system is relatively lower compared to an environmental chamber, leading to fluctuations in the curing temperature due to the operational status of the air conditioning system. This method effectively simulates the temperature variations experienced under actual site conditions. Taking Figure 4.7 as an example, the grey curve in the figure represents the fluctuations in ambient temperature. The compact, small-range fluctuations (e.g., 0-15h, 22-38h) are attributed to the normal operational variations of the air conditioning system. Although the system is nominally set to maintain a constant temperature (20°C) for the entire laboratory, the actual temperature control by the air conditioning system is limited to its immediate vicinity due to the built-in thermometer located inside the air conditioner. Since the specimens are placed some distance away from the air conditioner to prevent being blown directly by the air conditioner, it takes time for the temperature changes around the specimens to be detected by the air conditioner. The system only adjusts its operational power after detecting these fluctuations to bring the ambient temperature back to the set value, resulting in continuous small-range real-time fluctuations in the ambient temperature around the specimens. The larger-scale fluctuations observed (e.g., 15-22h in Figure

4.7) could be due to the significant temperature changes caused by the entry and exit of personnel in the laboratory. A detailed description and analysis of each figure are provided below:

- **Figure 4.4 (0% GGBS)**: The control mix exhibited the highest peak temperature (~29.65 °C) due to the absence of GGBS, which allowed for a rapid and intense exothermic reaction. The curve is steep during the initial hydration phase, indicating a high early heat generation rate.
- **Figure 4.5 (10% GGBS)**: The peak temperature (29.40 °C) is slightly reduced compared to the control mix, reflecting the moderating influence of GGBS. The hydration curve remains steep initially but begins to diverge from the 0% GGBS curve after approximately 8 hours.
- **Figure 4.6 (20% GGBS)**: The peak temperature drops further to 26.65 °C, with a noticeable reduction in the slope of the curve during the early hydration phase. The time to peak temperature is slightly delayed compared to the 10% GGBS mix.
- **Figure 4.7 (30% GGBS)**: Despite having the highest initial temperature among all mixes (20.05 °C), the peak temperature reaches only 26.10 °C. The curve exhibits a more gradual ascent, indicating a further reduction in the early hydration rate.
- **Figure 4.8 (40% GGBS)**: The peak temperature decreases to 24.65 °C, and the curve shows a prolonged rise, suggesting that higher GGBS content extends the hydration process.
- **Figure 4.9 (50% GGBS)**: This mix demonstrates the lowest peak temperature (23.05 °C) and the most gradual temperature rise, highlighting the significant thermal mitigation effect of GGBS.

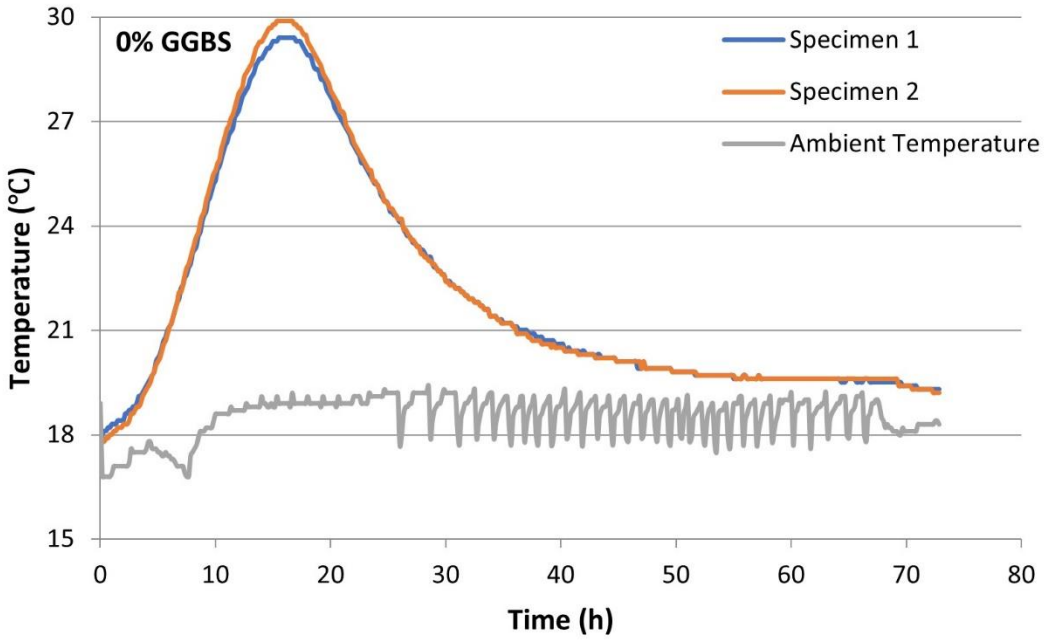

Figure 4.4. Semi-adiabatic temperature results for 0% GGBS concrete

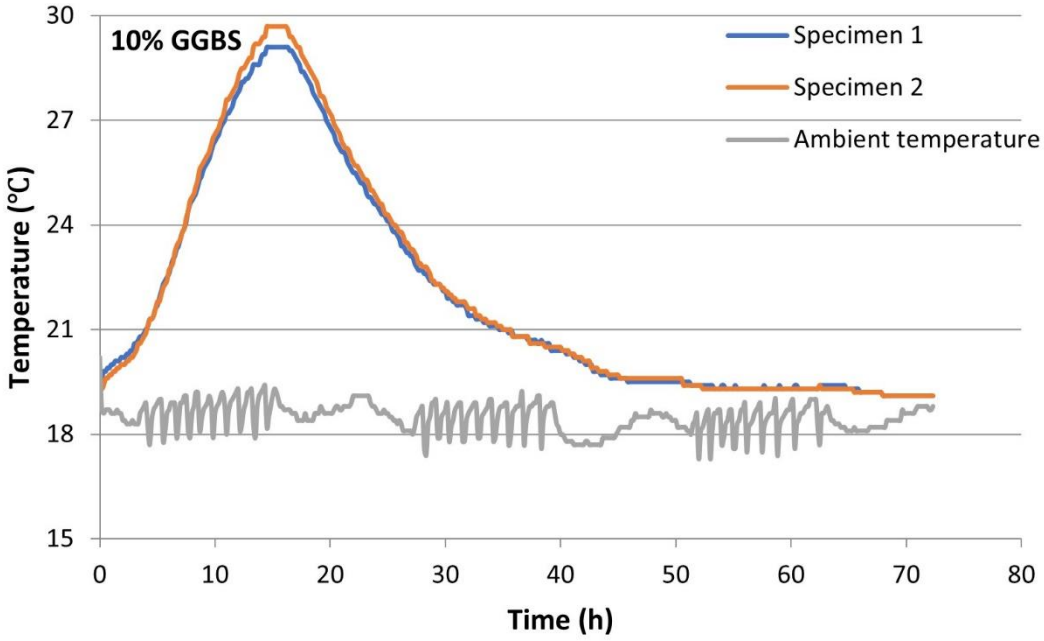

Figure 4.5. Semi-adiabatic temperature results for 10% GGBS concrete

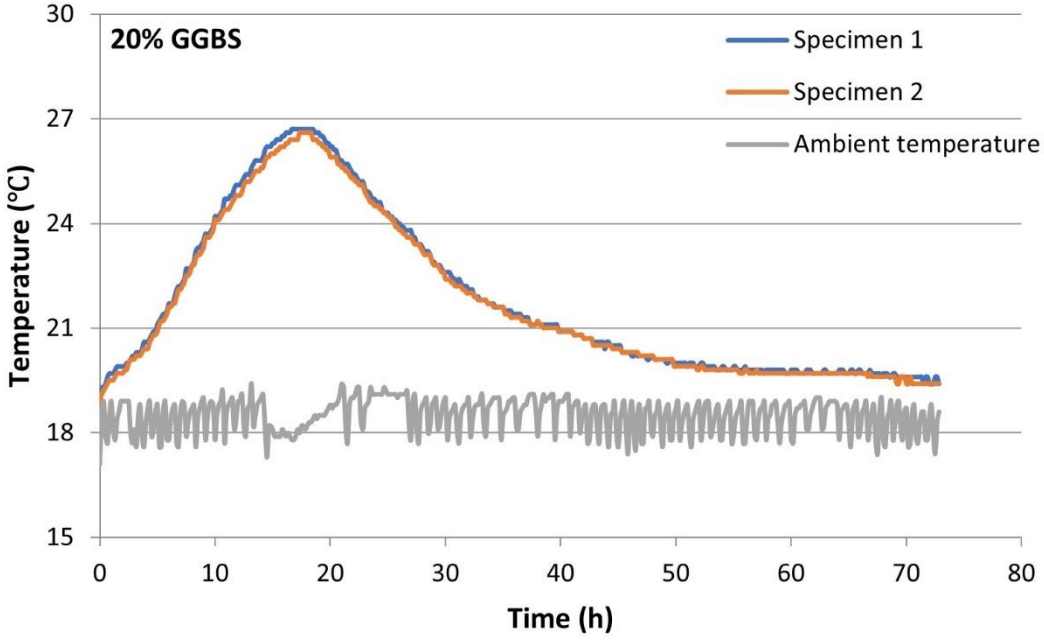

Figure 4.6. Semi-adiabatic temperature results for 20% GGBS concrete

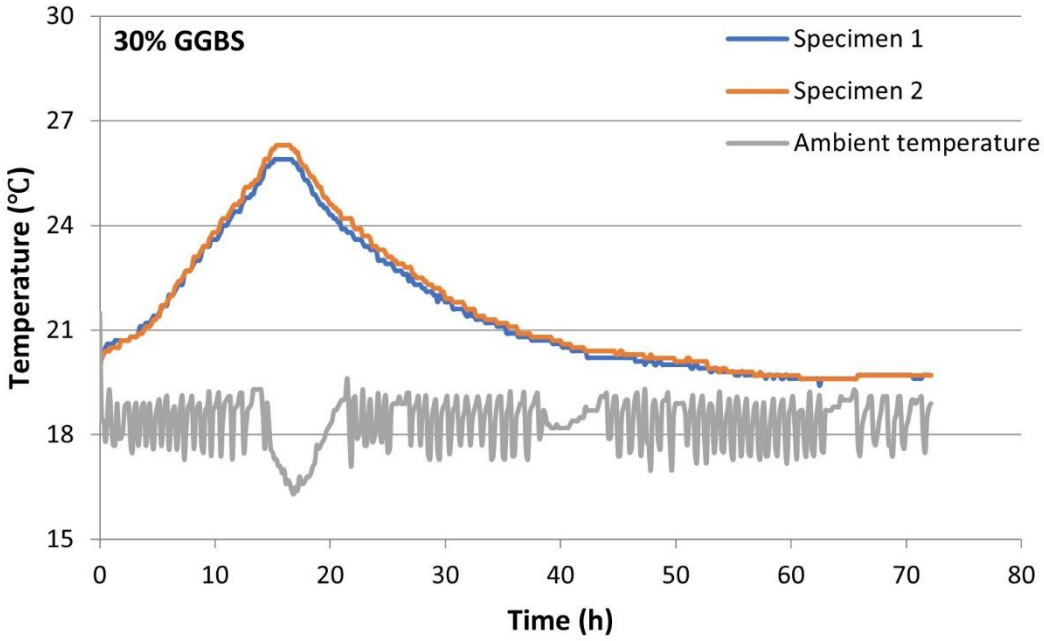

Figure 4.7. Semi-adiabatic temperature results for 30% GGBS concrete

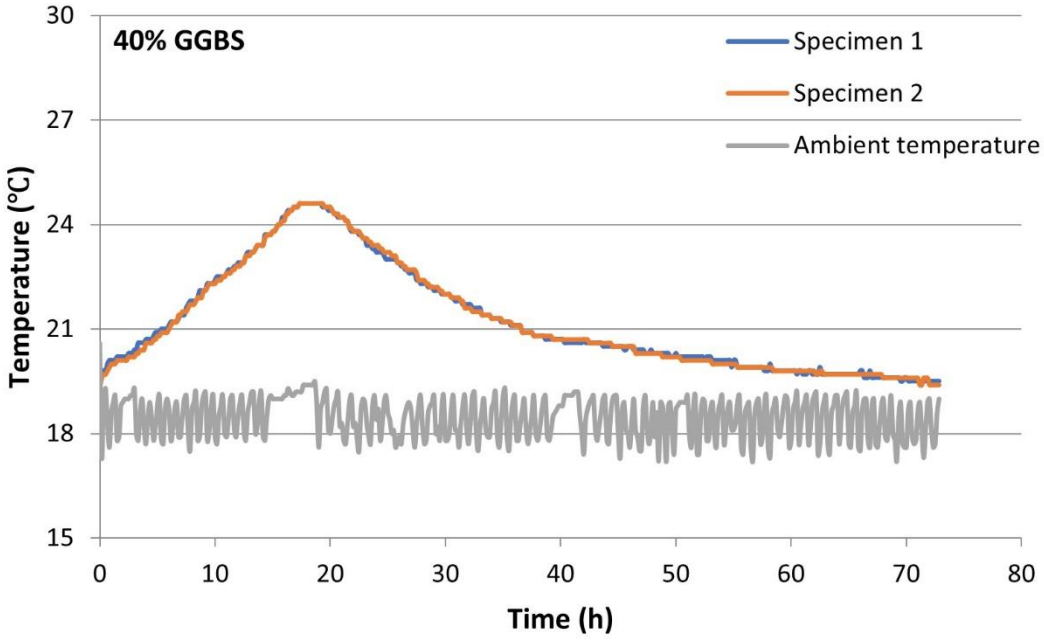

Figure 4.8. Semi-adiabatic temperature results for 40% GGBS concrete

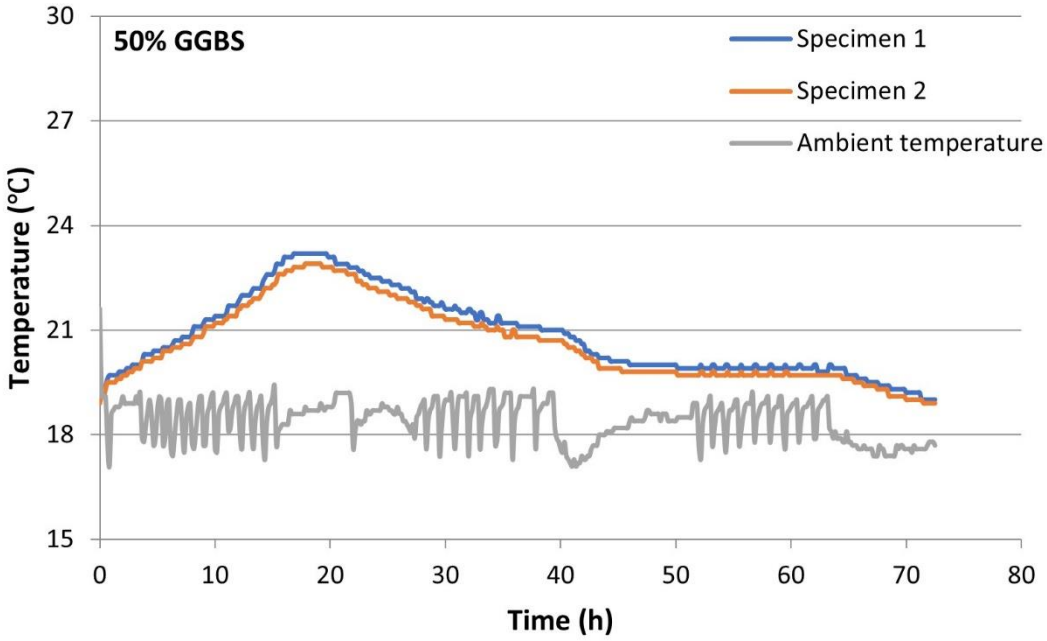

Figure 4.9. Semi-adiabatic temperature results for 50% GGBS concrete

Figure 4.10 (a) summarizes the temperature monitoring results of all specimens into a comparative graph. However, due to differences in the initial casting temperatures of the specimens, a direct comparison of the raw data may not fully represent the relative thermal behaviour of each mix.

To address this issue, the temperature data for each specimen was normalized by adjusting the initial temperatures (T_{ini}) to a common baseline of 0°C, producing a Normalized Temperature Rise curve for each mix. The Normalized Temperature Rise (T_{norm}) is calculated by subtracting the initial temperature (T_{ini}) of each specimen from its recorded temperature (T(t)) at a given time step (t). The formula is expressed as:

$$T_{norm}(t) = T(t) - T_{ini} \tag{4.1}$$

where $T_{norm}(t)$ is the normalized temperature rise at time t (°C), T(t) is the recorded temperature of the specimen at time t (°C), and T_{ini} is the initial temperature of the specimen (°C).

This normalization adjusts the starting point of all curves to 0°C, effectively eliminating the influence of initial temperature differences among the specimens. The Normalized Temperature Rise curves for all mixes are presented in Figure 4.10 (b). These curves provide additional insights into the influence of GGBS on hydration-induced thermal behaviour by focusing on the relative temperature rise from a standardized starting point.

The Normalized Temperature Rise curves (Figure 4.10 (b)) reveal distinct differences in the thermal behaviour of concrete mixes with varying GGBS contents. Concrete with higher GGBS substitution levels exhibits slower temperature rise rates and lower normalized peak temperatures, indicating a reduced rate of heat generation and a more extended hydration process. These trends align with the delayed pozzolanic reaction and reduced heat release of GGBS, which are well-documented in the literature.

Additionally, the shape of the normalized curves highlights the thermal behaviour differences between mixes. For instance:

- The 0% GGBS mix shows a sharp initial rise and an early peak, reflecting the rapid hydration of CEM I cement.
- As the GGBS content increases, the curves become more gradual, and the peaks are delayed, demonstrating the effectiveness of GGBS in moderating early-age thermal behaviour.
- The 50% GGBS mix exhibits the lowest normalized peak temperature and the flattest curve, signifying a significant reduction in hydration heat and a prolonged reaction process.

By normalizing the temperature rise data, the influence of GGBS on the hydration process becomes clearer, allowing for a more intuitive comparison of the thermal behaviour of different mixes.

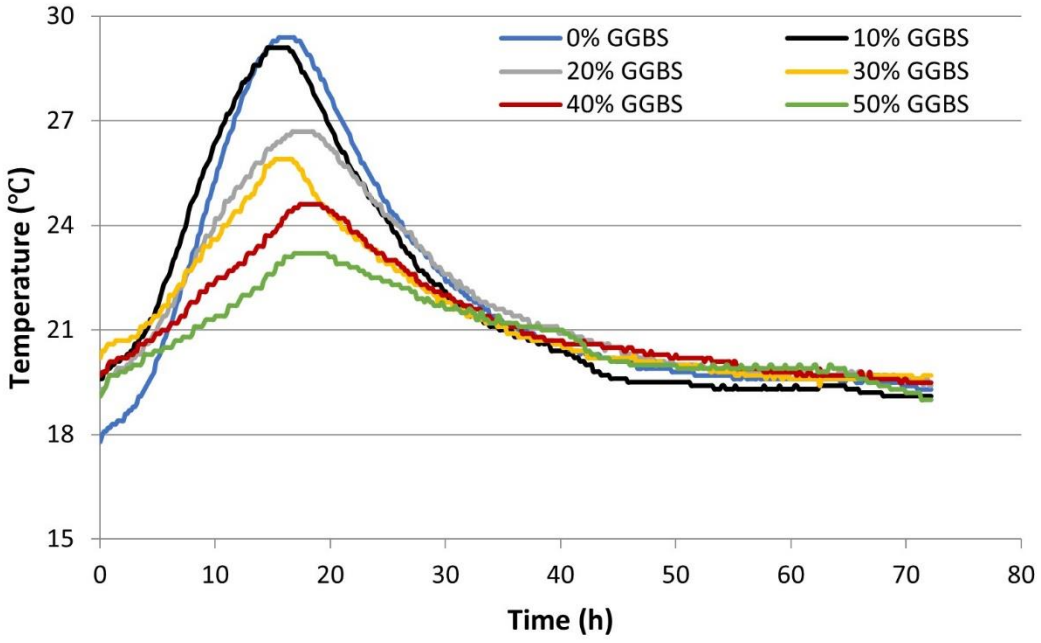

(a)

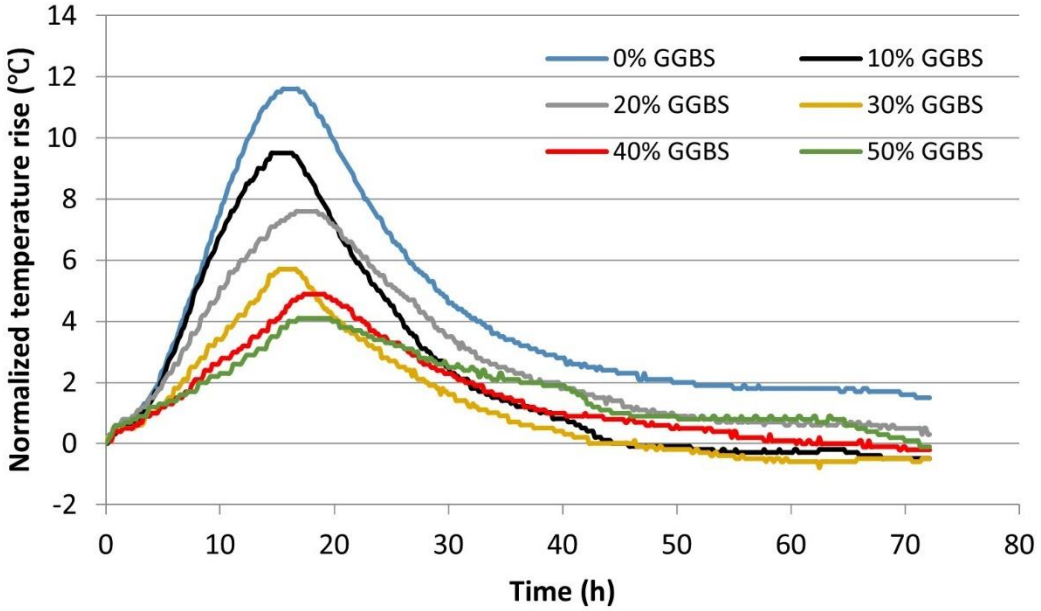

(b)

Figure 4.10. (a) Summary of the semi-adiabatic temperature results; (b) Normalized temperature rise curves.

Table 4.2. Summary of the concrete hydration temperature development

GGBS content (%)	Initial temperature T_{ini} (°C)	Peak temperature T_{peak} (°C)	Normalized peak temperature T_{normal} (°C)	Temperature rise value T_r (°C)	Time to reach peak temperature t_{peak} (h)	Average temperature rise rate R_a (°C/h)
0%	17.85	29.65	11.80	11.80	15.40	0.77
10%	19.50	29.40	9.90	9.90	14.60	0.69
20%	19.00	26.65	7.65	7.65	16.60	0.47
30%	20.05	26.10	6.05	6.05	15.25	0.40
40%	19.50	24.65	5.10	5.10	17.35	0.30
50%	19.00	23.05	4.05	4.05	17.30	0.23

Table 4.2 provides a summarize of key thermal parameters for each mix, including the Initial Temperature (T_{ini}), Peak Temperature (T_{peak}), Normalized Peak Temperature (T_{normal}), and Temperature Rise Value (T_r). The data reveal that T_{normal} is equivalent to T_r, as both represent the difference between the peak temperature and the initial temperature of the specimen. This equivalence arises because the normalization process effectively removes the initial temperature offset, aligning the starting point of all mixes to 0 °C. Despite this mathematical equivalence, the interpretation of T_{normal} emphasizes the relative temperature rise, independent of the initial temperature differences across mixes.

The initial temperatures of the specimens (T_{ini}) were influenced by environmental conditions during casting and minor procedural variations. As shown in Table 4.2, T_{ini}

varied slightly across mixes, ranging from 17.85 °C (0% GGBS) to 20.05 °C (30% GGBS). These variations highlight the challenges of maintaining consistent starting conditions in semi-adiabatic experiments conducted under simulated in-situ conditions. However, the results demonstrates that T_{ini} had a minimal impact on T_{peak}, as the thermal behaviour of the specimens was predominantly governed by the GGBS content (will be discussed in detailed later).

T_{peak} represents the absolute maximum temperature achieved during the hydration process, providing insights into the intensity of heat evolution in each mix. Conversely, T_{normal} focuses on the relative temperature rise by removing the influence of initial temperature differences. This distinction is useful for comparing the thermal performance of mixes under varying starting conditions. For instance: The 0% GGBS mix exhibited the highest T_{peak} (29.65 °C) and T_{normal} (11.80 °C), reflecting the rapid and intense hydration of CEM I. The 50% GGBS mix had the lowest T_{peak} (23.05 °C) and T_{normal} (4.05 °C), highlighting the significant thermal mitigation effect of GGBS.

The close alignment of T_{normal} across mixes underscores the reliability of normalization in isolating the effect of GGBS content. This alignment also confirms that differences in initial temperatures did not significantly distort the comparative analysis of hydration-induced thermal behaviour.

The temperature development curves of concrete with varying GGBS contents reveal a clear trend. As the ratio of GGBS substituting for CEM I increases, the peak temperature of the concrete correspondingly decreases and exhibits a linear relationship (as illustrated in Figure 4.11). Substituting 50% of CEM I with GGBS reduces the peak temperature by approximately 21.1%. However, the time taken to reach the peak temperature does not have a direct and noticeable correlation with the GGBS content. This observation can be attributed to the variable temperature environment where the specimens were placed, as discussed in grey curves in Figure 4.4 to Figure 4.9. Instead of an environment chamber, the specimens were in an air-conditioned curing room to better simulate in-situ concrete conditions. Additionally, the casting and initial temperatures of the concrete were influenced by the weather conditions on the day of the experiment, resulting in variations among different mixes, as indicated by the initial temperatures at 0 hours in Figure 4.10 (a). The ambient temperatures for each mix monitored in Figure 4.4 to Figure 4.9, although there were slight differences across specimens, the variations were minimal. However, the initial temperatures showed more significant discrepancies (as shown in Figure 4.10 (a)). Therefore, even though the relationship between peak temperature and GGBS content in Figure 4.11 is linear, the variability in initial temperature values and curing temperatures reduces the referential value of this linear correlation.

As discussed above in Table 4.2, It was observed that the 0% GGBS concrete had the lowest initial temperature but the highest peak temperature. Conversely, the 30% GGBS concrete, despite having the highest initial temperature, still exhibited a peak

temperature lower than the 0%, 10%, and 20% GGBS concretes. This indicates that the differences in initial temperatures and minor variations in ambient temperatures were insufficient to affect the influence of GGBS content on peak temperatures. However, they significantly impacted the time to reach peak temperature.

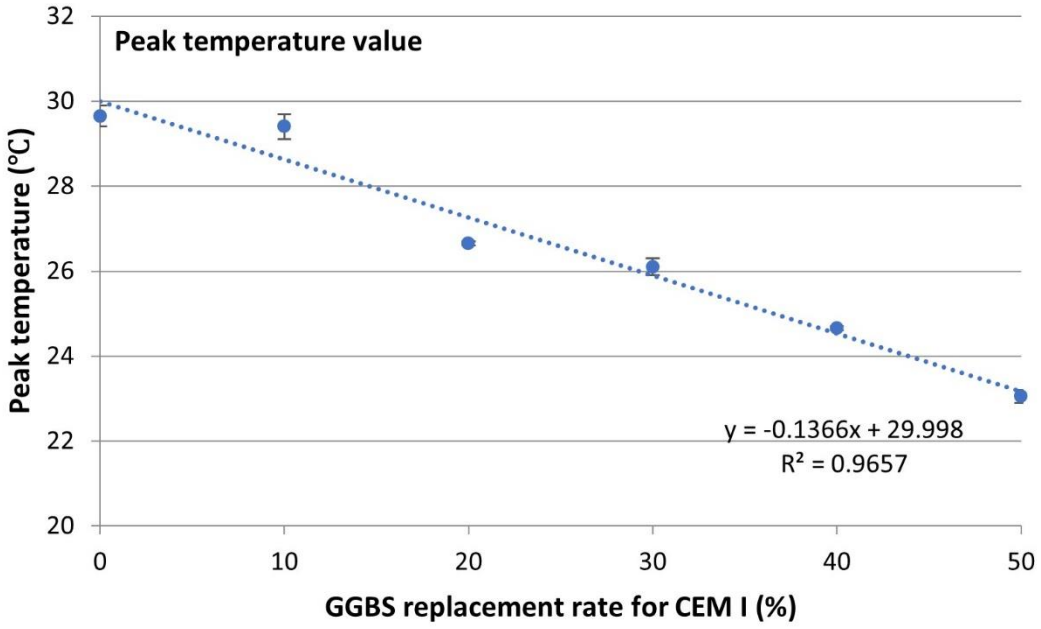

Figure 4.11. Variation of peak temperature value with GGBS content

To facilitate a clearer understanding of the influence of GGBS content on the hydration temperature of concrete, this study introduces two additional indictors: Temperature rise value (T_r) and Average temperature rise rate (R_a) to elucidate the impact of GGBS addition on concrete temperature development. The Temperature rise value (T_r) is defined as the difference between the initial and peak temperatures of the concrete (as shown in Eq. (4.2)), representing the maximum temperature increase during the hydration process. The Average temperature rise rate (R_a) is calculated as the ratio of the Temperature rise value (T_r) to the time taken to reach the peak temperature (as shown in Eq. (4.3)), thereby depicting the average rate of temperature rise during the heating phase. The results of both new indictors are also summarized in Table 4.2.

$$T_r = T_{peak} - T_{ini} \tag{4.2}$$

$$R_a = \frac{T_r}{t_{peak}} \tag{4.3}$$

where T_r is the maximum temperature increase during the hydration process (°C), R_a is the average temperature rise rate of the concrete specimen (°C/h), T_{ini} is the initial temperature of the concrete specimen (°C), T_{peak} is the peak temperature of the concrete

specimen (°C), and t_{peak} is the time to reach peak temperature (h).

Both T_r and R_a demonstrate a linear correlation with the GGBS content, as depicted in Figure 4.12 and Figure 4.13, respectively. The findings indicate that substituting 50% of CEM I with GGBS reduces approximately 63.4% in the maximum temperature rise value and a 70.1% decrease in the average temperature rise rate. This significant reduction in both T_r and R_a underscores the effective temperature control afforded by GGBS, offering promising prospects for mitigating the risk of thermal cracking in concrete structures.

The introduced new indictors Temperature rise value (T_r) and Average temperature rise rate (R_a)" incorporate the impact of the initial temperature of the specimens and the ambient temperature during the curing process, thereby providing a more accurately description of the concrete's thermal behaviour. Including initial and ambient temperature conditions makes T_r and R_a more reliable and relevant than the peak temperature fitting results depicted in Figure 4.11.

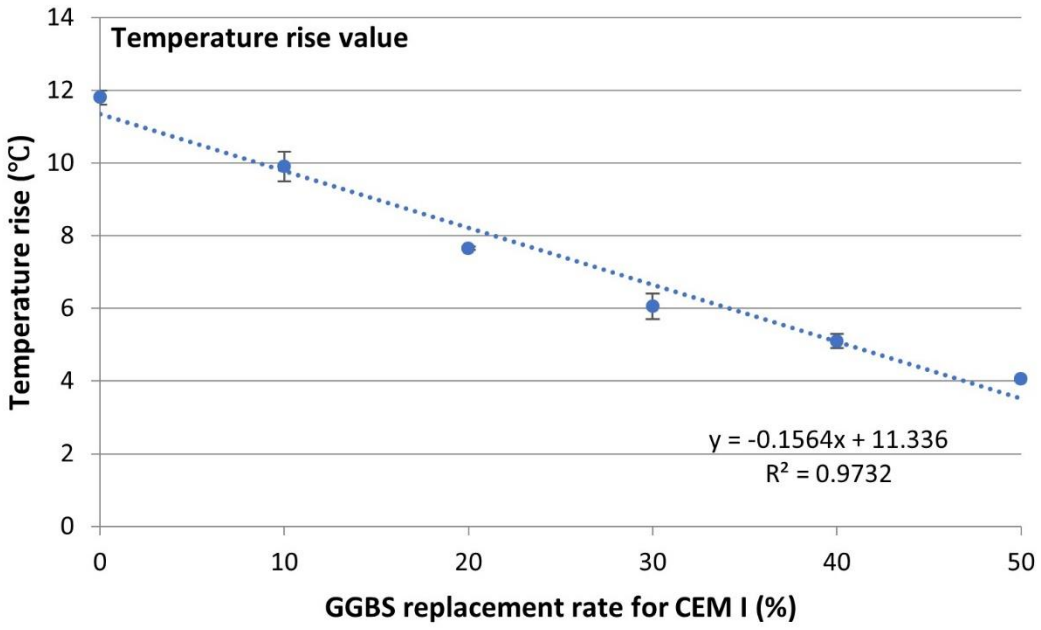

Figure 4.12. Variation of temperature rise value with GGBS content

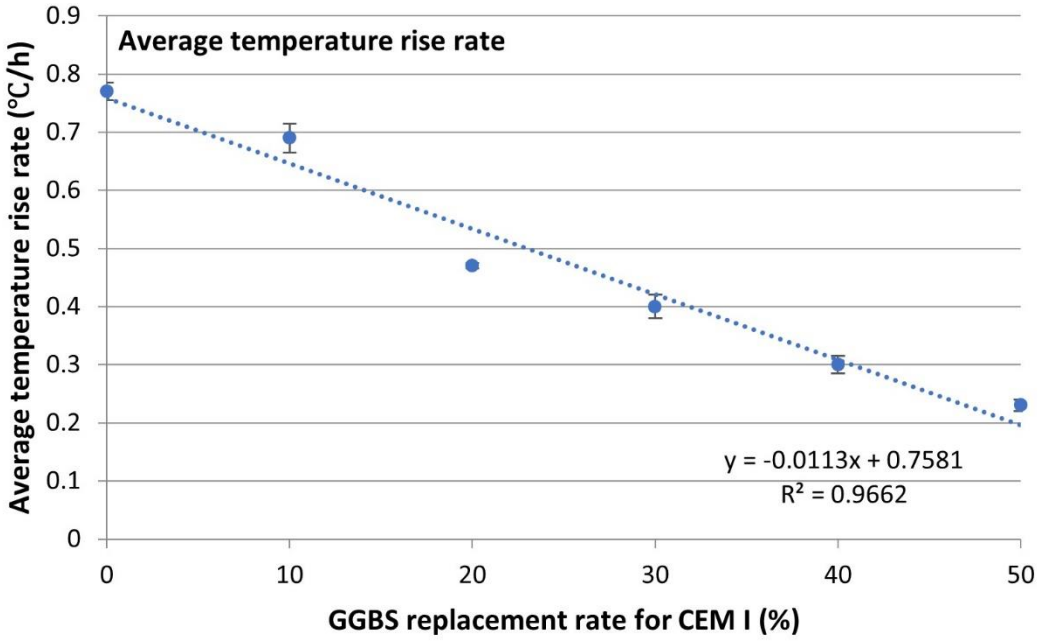

Figure 4.13. Variation of average temperature rise rate with GGBS content

4.3 Conclusion

This chapter presented the results and analysis of semi-adiabatic calorimetry tests conducted on concrete mixes with varying GGBS content, focusing on the impact of GGBS substitution on hydration-induced temperature development. The findings confirm the significant thermal mitigation effect of GGBS, highlighting its potential to reduce peak hydration temperatures and delay the temperature rise in concrete structures.

The study introduced Normalized Temperature Rise as an analytical approach to eliminate variations in initial casting temperatures, allowing for a more intuitive comparison of the thermal behaviour of different mixes. The analysis revealed that concrete with higher GGBS content exhibited a slower temperature rise and lower normalized peak temperatures. This trend underscores the effectiveness of GGBS in moderating early-age thermal behaviour by reducing hydration heat and prolonging the reaction process.

Additionally, Table 4.2 provided a detailed comparison of key thermal parameters, including Initial Temperature (T_{ini}), Peak Temperature (T_{peak}), Normalized Peak Temperature (T_{normal}), and Temperature Rise Value (T_r). The distinction between T_{peak} and T_{normal} was particularly insightful, as it highlighted the relative thermal performance of each mix while isolating the influence of starting conditions. Despite variations in Tini, the relationship between T_{peak} and T_{normal} remained consistent, underscoring the dominant role of GGBS content in controlling thermal dynamics.

Furthermore, two analytical indicators, the Temperature Rise Value (T_r) and Average Temperature Rise Rate (R_a)**,** were introduced to quantify the thermal behaviour of the mixes. These indicators account for variations in initial and curing temperatures, providing a consistent basis for comparison. Both T_r and R_a exhibited linear correlations with GGBS content. A 50% GGBS substitution led to a 63.4% reduction in T_r and a 70.1% decrease in R_a, underscoring the effectiveness of GGBS in reducing the heat generated during hydration and slowing the temperature rise.

CHAPTER 5 ISOTHERMAL CALORIMETRY TEST PROCEDURE, RESULTS, AND ANALYSIS

5.1 Experimental Procedure for Isothermal Calorimetry

Isothermal calorimetry tests were conducted to measure samples' early-age hydration heat development with varying GGBS contents at different temperatures. A key objective of this study was to evaluate the impact of coarse aggregates on the samples' hydration heat curves and hydration parameters. To accommodate coarse aggregates, a 3-channel TAM Air isothermal calorimeter from TA Instruments [106] was employed, equipped with ampoules of 125 mL volume suitable for containing the 10 mm coarse aggregates used in this study. Figure 5.1 shows the isothermal calorimeter, and Figure 5.2 shows the glass ampoule comprising an ampoule body, a metal lid, and a screw cap. The sample's hydration heat was transmitted to the machine's heat flow sensor from the ampoule's bottom. A detailed explanation of the calorimeter's running principles has been discussed in Section 2.4.3.

To explore the influence of coarse aggregates on hydration heat, or more specifically, the differences in hydration heat curves between mortar and concrete specimens, simultaneous measurements of the hydration heat development in both micro-concrete and equivalent mortar specimens are necessary. Isothermal calorimetry test will measure simultaneously micro-concrete sample and one equivalent mortar sample (as shown in Figure 5.3). The micro-concrete mix mirrored that of the semi-adiabatic calorimetry tests (as shown in Table 4.1) to obtain the same hydration heat as the semi-adiabatic calorimetry test specimen, while the equivalent mortar samples were prepared following the definition of equivalent mortar in ASTM C1074 [119]: the fine aggregate-to-cement ratio (by weight) in the equivalent mortar equated to the coarse aggregate-to-cement ratio in the concrete. It should be noted that ASTM C1074 is not a standard specific to isothermal calorimetry but a standard for predicting concrete strength development based on the maturity method. Although widely recognized isothermal calorimetry standards (such as BS EN 196-11:2018 [104], ASTM C1702 [105], and ASTM C1679 [206]) recommend cement paste or mortar samples, they do not specifically define micro-concrete or equivalent mortar. However, equivalent mortar, as defined in ASTM C1074, has been proven to exhibit similar strength development with concrete. Based on the fundamental assumption of concrete maturity, this study posits that equivalent mortar should exhibit similar hydration heat development to concrete.

Figure 5.1. TAM Air 3-channel isothermal calorimeter (Photograph taken on 02 February 2023).

Figure 5.2. 125 mL glass ampoule (Photograph taken on 15 December 2023).

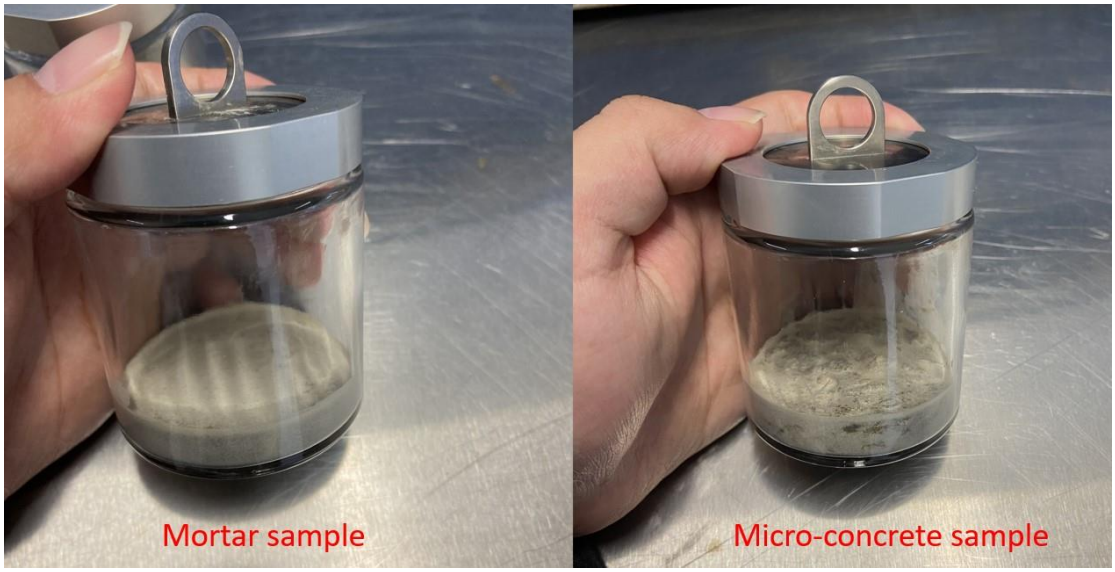

Figure 5.3. Hardened mortar sample and micro-concrete sample entirely concentrated at the ampoule's base (Photograph taken on 15 December 2023).

In the isothermal calorimetry tests, GGBS was utilized to replace a portion (10%, 20%, 30% 40%, 50%, separately) of the cement by weight to study its impact on the development of cement hydration heat, with the GGBS replacement ratios being the same as those used in the semi-adiabatic calorimetry tests. However, in contrast to the semi-adiabatic tests, the samples used in isothermal calorimetry were significantly smaller in quantity (not exceeding 50g), substantially reducing the cost involved in sample preparation. Furthermore, it is essential to note the high precision of the isothermal calorimetry equipment used in this study, which boasts an accuracy of ±8μW for the heat flow sensor and an accuracy of ±0.02°C for the thermostat. The high precision of the thermostat ensures that the isothermal calorimetry tests maintain stable isothermal curing conditions, avoiding the influence of environmental temperature fluctuations or hydration temperature rises on the hydration reaction. The high accuracy of the heat flow sensor is crucial for detecting subtle changes in heat flow, which is particularly important in this study. As mentioned above, part of this study investigates the differences in hydration heat development between concrete and equivalent mortar samples to evaluate the influence of coarse aggregates on the hydration reaction. Since the hydration heat development of equivalent mortar is quite similar to that of concrete, this is why previous studies often used mortar hydration heat as a proxy for concrete. Therefore, the high precision of the calorimeter's heat flow sensor helps accurately detect differences in the hydration heat of the two types of samples, facilitating a thorough evaluation of the effect of coarse aggregates on the hydration process. To preclude any potential influences of minerals present in ordinary tap water on the hydration reaction, all water used in the isothermal calorimetry tests in this study was deionized water. The specific mix information for the samples is detailed in Table 5.1 (the binder consists of both cement and GGBS, with the same substitution ratio as in Table 4.1 and a total of 6 mixes). As previously mentioned, each test measured a micro-concrete sample and a corresponding equivalent mortar sample. Each sample was tested

at four different temperatures: 20°C, 30°C, 40°C, and 50°C, to assess the impact of temperature on hydration heat development and to provide thermal source data for the development of the FEM model for concrete temperature (which will be discussed in detail in Section 4.6.2).

Table 5.1. Isothermal calorimetry sample mixes and reference sample

	Binder (g)	Deionized water (g)	Coarse aggregate (g)	Fine aggregate (g)	Total weight (g)	Reference sample (sand) (g)
Mortar sample	9	4.92	0	20.34	34.26	48.50
Micro-concrete sample	9	4.92	20.34	13.92	48.18	62.40

As described in Section 2.4.3, each sample in the isothermal calorimetry tests requires a corresponding reference sample. The calorimeter's output signal is determined based on the differential heat output rate between the sample and its reference sample. The selection of the reference sample adheres to two fundamental principles: 1). The material should be inert, and 2). Its specific heat capacity should be approximately the same as the corresponding sample's (the specific heat capacity equilibrium can be calculated via Eq. (5.1)). The equipment manufacturer (TAM Air), existing researches [1, 17, 18, 207, 208], and relevant standards (BS EN 196-11:2018 [104]) recommend using either water or sand as the reference material. However, considering the larger volume (125 mL) of the ampoules used in this study and the relatively small height of the filled samples compared to the ampoule's height, using water as a reference sample could lead to partial evaporation and subsequent condensation on the sides of the ampoule, thus affecting heat transfer at the base. Therefore, the same medium sand used in calorimetry experiments of this study was chosen as the reference sample. The calculated mass of the reference sample required for each test is listed in Table 5.1. The specific heat capacities of the individual components of the concrete were adopted based on the recommendations provided by the equipment manufacturer, as presented in Table 5.2. To determine the overall specific heat capacity of the concrete, a weighted average method was employed, as elaborated in Section 2.6.2.2. This method, detailed in Eq. (2.71), involves multiplying the specific heat capacity of each component by its respective mass. The sum of these products is then divided by the total mass of the concrete mix to obtain the overall specific heat capacity.

$$m_r = \frac{m_t c_t}{c_r} \tag{5.1}$$

where m_r is the mass of the reference sample, m_t is the mass of the test sample, c_t is the specific heat capacity of the test sample, and c_r is the specific heat capacity of the reference sample.

Table 5.2. Specific heat capacities of concrete components.

Component	Specific heat capacities (J/(kg·K))
CEM I cement	750
GGBS	750
Coarse aggregate	800
Fine aggregate	800
Water	4200

After adjusting the operating temperature of the calorimeter, it is imperative to allow the calorimeter to reach a stable, constant temperature state internally. This requires the calorimeter to operate continuously for at least 8 hours at the new temperature setting. Although the thermostat may attain the target temperature within approximately 20 minutes, this does not necessarily indicate that the entire internal environment of the calorimeter has stabilized at the desired temperature. Once the calorimeter has been stably operating at the new temperature, recalibration of all channels is required to ensure the accuracy and consistency of the equipment's measurements. This recalibration process is crucial for maintaining the precision of the calorimeter, as it compensates for any potential internal temperature variations or discrepancies that might arise from the temperature change.

The operational procedures for the isothermal calorimetry tests were conducted following the steps recommended in BS EN 196-11:2018 [104]. The aggregates were completely dried (by oven drying, at 100 ℃ for 24 hours) before the experiment. The materials were precisely weighed using an electronic balance with a 0.01 g accuracy, and subsequently stored in sealed containers. The containers were placed in an environmental chamber, and the chamber's temperature was adjusted to the operating temperature of the isothermal calorimeter. The materials were placed in the environment chamber for one day in advance. This was to ensure that the temperature of the materials was consistent with the operating temperature of the calorimeter.

Before initiating the test, all solid components (binder and aggregate) were mixed in a container. The solids were initially mixed with a stirring rod before the addition of deionized water to ensure uniform contact between the binder and water. The mixing of the sample was conducted using an overhead stirrer with a maximum speed of 2000 r/min. According to the research recommendations of Wang et al. [117], each sample was stirred at 2,000 r/min for 75 seconds. This recommendation, based on their studies on mixing samples for isothermal calorimetry tests, is discussed in detail in Section 2.4.3.

After mixing, the sample was transferred to an ampoule and weighted using an electronic balance with a 0.01 g accuracy. Considering that hydration heat is conducted from the bottom of the ampoule to the calorimeter, it was necessary to vibrate the sample to ensure it was entirely concentrated at the ampoule's base, avoiding the

formation of a “mound”. The ampoule was then completely sealed with a metal lid and screw cap and placed into the corresponding channel of the calorimeter. The calorimetry test started recording from then on and stop each test after 72 hours. Figure 5.4 describes the operating procedure for the isothermal calorimetry test

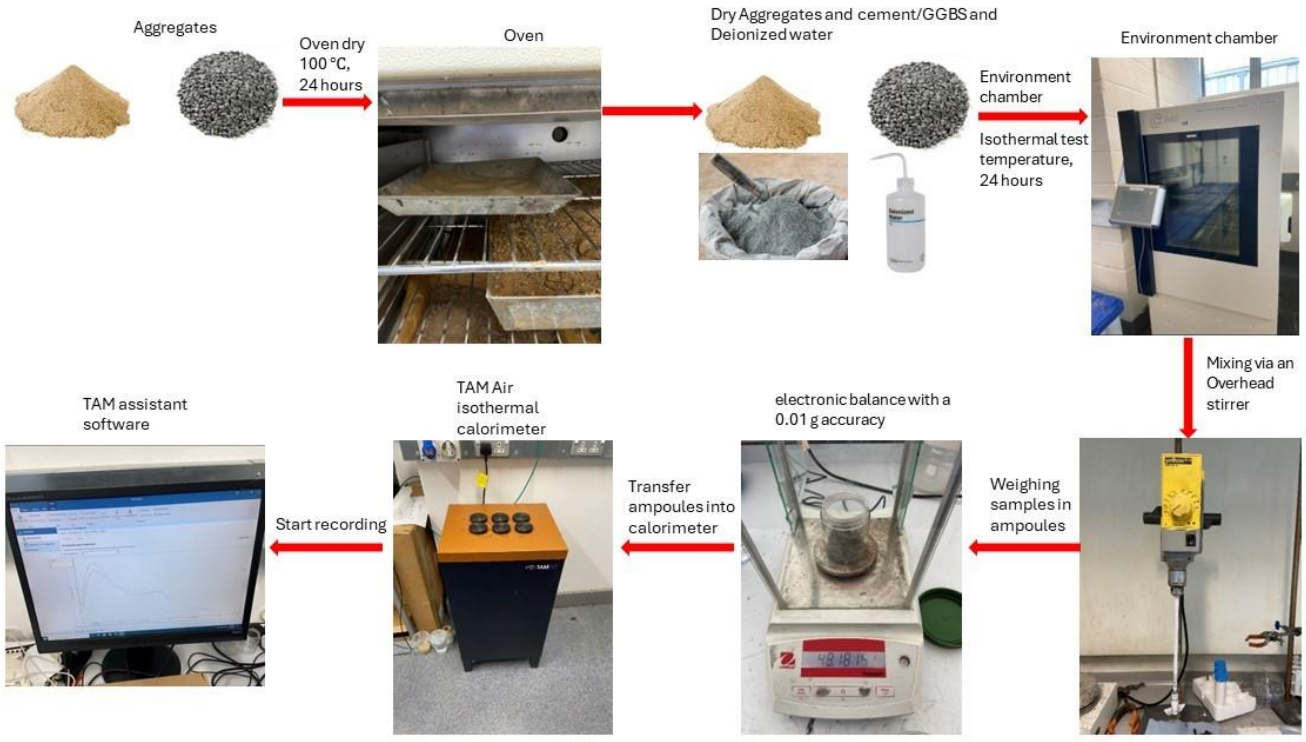

Figure 5.4. Isothermal calorimetry test procedure.

The isothermal calorimetry experiments direct results in the form of heat release power (heat flow) of the specimens, measured in watts. This study employed a normalization process to compare the equivalent mortar and micro-concrete samples among different mix compositions. This process involved dividing the measured heat flow of each specimen by the mass of the binder present in the sample. This step is based on the assumption that only the binder component participates in the hydration reactions. As a result, the “Normalized heat flow” was obtained, with units in watts per gram (W/g).

The “Normalized heat flow” of the sample’s hydration reaction, when integrated over the reaction time, results in the “Cumulative hydration heat” (Normalized heat) of the sample, expressed in joules per gram (J/g). This integration process can be mathematically represented by the following formula:

$$H = \int Q\, dt \tag{5.2}$$

where H is the Normalized heat of the sample (J/g), Q is the Normalized heat flow of the sample (W/g), and t is the hydration reaction time (h).

The varying environmental temperatures and internal temperature development of in-situ concrete complicate the hydration heat rate, adding to the challenge of predicting the hydration temperature development of in-situ concrete. Isothermal calorimetry tests at different temperatures offer valuable insights into the hydration heat rates under different constant temperatures. When applied to mathematical models based on concrete maturity theory (will be discussed in Chapter 6), the data obtained from these tests can be used to extrapolate the hydration heat rates for in-situ concrete. This information is vital for predicting concrete hydration temperature development through FEM modelling. To support subsequent modelling of concrete temperatures, the results of the isothermal calorimetry tests will also be used to determine critical parameters required for FEM modelling, including apparent activation energy and hydration parameters.

5.2 Influence of Curing Temperature on Hydration Heat

This section introduces and interprets the measurement results from the micro-concrete samples used in the study. Each experimental setup involved the simultaneous measurement of two identical micro-concrete samples, with results averaged to minimize potential discrepancies arising from individual sample variations. The isothermal calorimetry normalized heat flow data for the micro-concrete samples of the same mix at different temperatures and the cumulative hydration heat curves derived through integration via Eq. (5.2) are depicted in Figure 5.5 to Figure 5.10. The normalized hydration heat flow and normalized cumulative hydration heat represent hydration heat flow rate and cumulative heat release, which have been adjusted to eliminate minor variations in sample mass. Since the isothermal calorimeter used in this study has a high precision of ±8 μW, even slight differences in sample mass could introduce unwanted variability in the raw heat measurements. To ensure accuracy and comparability, all hydration heat data were normalized by the total mass of the binder (CEM I + GGBS) in each sample. The normalization was performed using the following equations:

$$Q = \frac{Q_t}{m_b} \tag{5.3}$$

$$H = \frac{H_t}{m_b} \tag{5.4}$$

where Q is the normalized hydration heat flow rate (W/g), H is the normalized cumulative hydration heat (J/g), Q_t is the measured hydration heat flow rate (W), H_t is the cumulative hydration heat release (J), and m_b is the total mass of cementitious binder (CEM I + GGBS) in the tested sample (g).

Although the binder mass was kept constant at 9 g across all samples, minor weighing variations (accurate to 0.01 g) were inevitable. Given the high sensitivity of the calorimeter, even these small variations could lead to differences in measured heat values. Normalizing the data ensures that the results reflect the intrinsic hydration behaviour rather than minor inconsistencies in sample mass. Furthermore, the high precision of the calorimeter means that even negligible differences in mass or placement could introduce measurement variations. By normalizing the heat data per unit binder mass, these potential discrepancies are minimized, allowing clearer trend analysis.

Another key benefit of normalization is that it ensures consistency in data processing, particularly for comparing hydration kinetics and total heat release across different GGBS replacement levels. Since all samples contained the same total binder mass, normalization allows a fair comparison of hydration behaviour without interference from mass-related variability. This approach makes it possible to accurately assess the impact of GGBS replacement on heat evolution while eliminating extraneous variability. By normalizing the hydration heat flow and cumulative heat release, the results become independent of minor weighing inconsistencies, ensuring more reliable data comparisons. Additionally, normalization reduces the influence of instrument precision on absolute heat measurements, making it easier to interpret hydration trends.

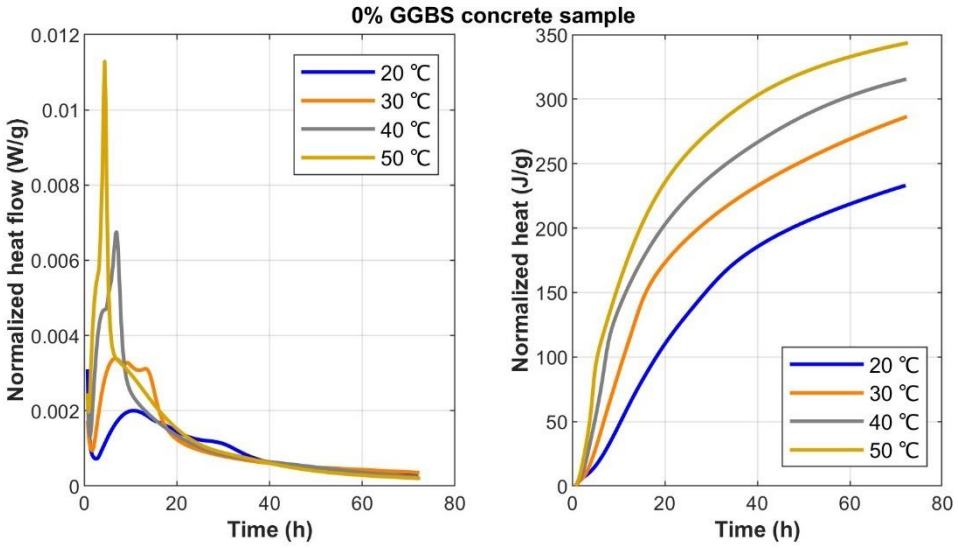

(a) (b)

Figure 5.5. Isothermal calorimetry curves for 0% GGBS micro-concrete sample at different temperatures: (a) normalized hydration heat flow; (b) normalized cumulative hydration heat.

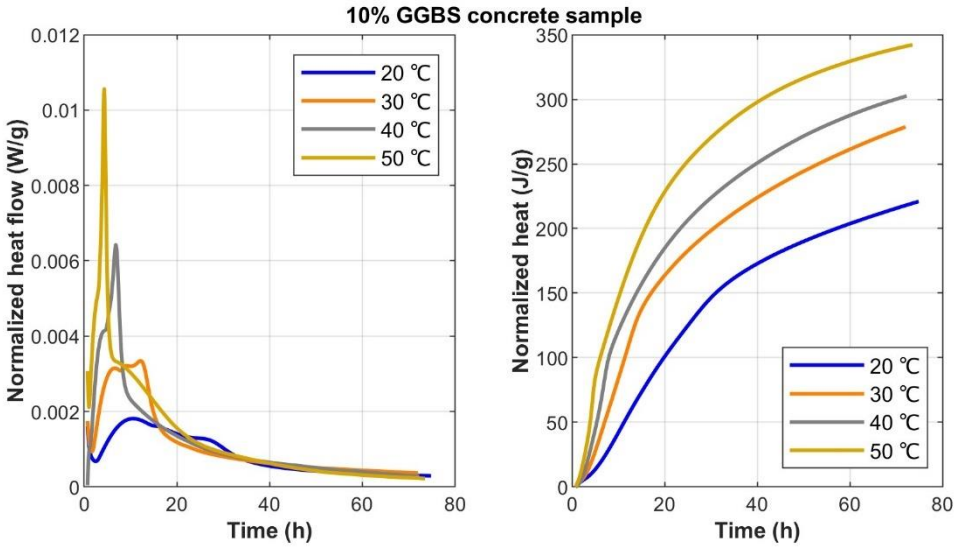

(a) (b)

Figure 5.6. Isothermal calorimetry curves for 10% GGBS micro-concrete sample at different temperatures: (a) normalized hydration heat flow; (b) normalized cumulative hydration heat.

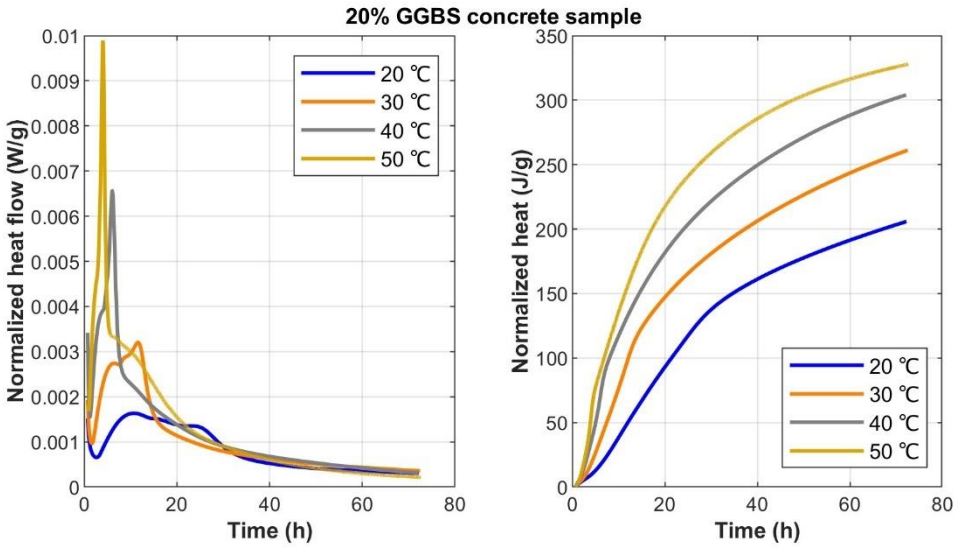

(a) (b)

Figure 5.7. Isothermal calorimetry curves for 20% GGBS micro-concrete sample at different temperatures: (a) normalized hydration heat flow; (b) normalized cumulative hydration heat.

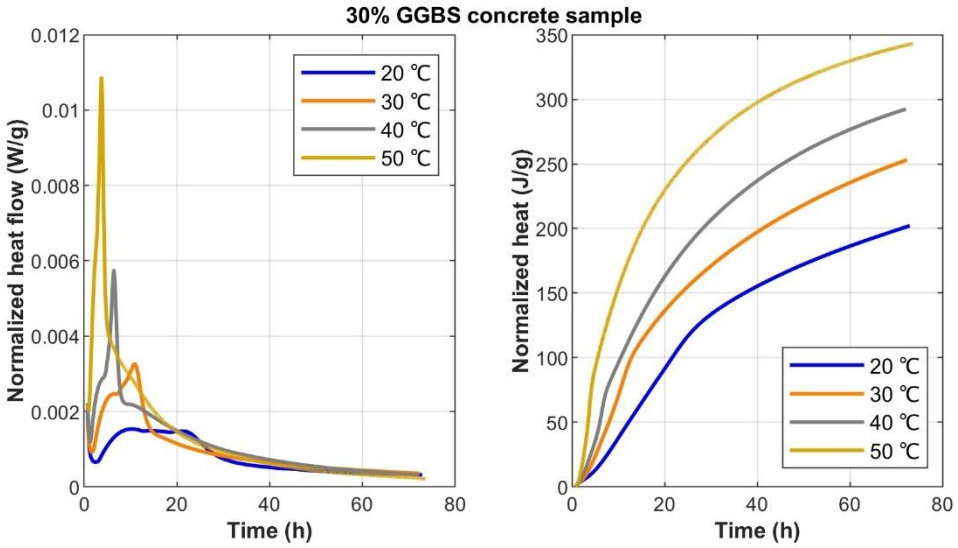

(a) (b)

Figure 5.8. Isothermal calorimetry curves for 30% GGBS micro-concrete sample at different temperatures: (a) normalized hydration heat flow; (b) normalized cumulative hydration heat.

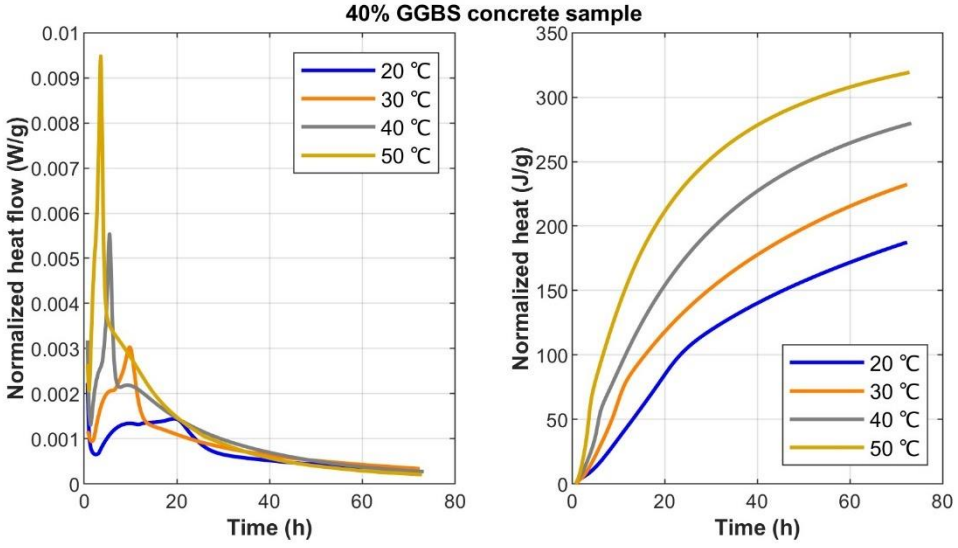

(a) (b)

Figure 5.9. Isothermal calorimetry curves for 40% GGBS micro-concrete sample at different temperatures: (a) normalized hydration heat flow; (b) normalized cumulative hydration heat.

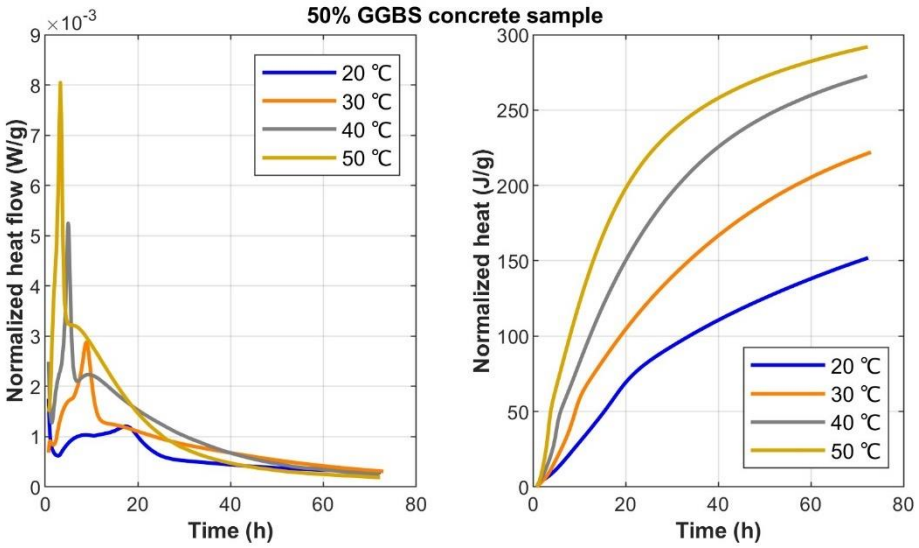

(a) (b)

Figure 5.10. Isothermal calorimetry curves for 50% GGBS micro-concrete sample at different temperatures: (a) normalized hydration heat flow; (b) normalized cumulative hydration heat.

To assess the influence of curing temperature on hydration heat development, Table 5.3 presents key hydration heat parameters for samples with varying GGBS replacement levels. These parameters include peak hydration heat, time to peak hydration, 1-day cumulative hydration heat, and 3-day cumulative hydration heat. The table provides an overview of how these critical hydration characteristics evolve with increasing curing temperature, allowing for a clearer understanding of temperature-induced variations in hydration kinetics.

Table 5.3. Summary of hydration heat development at different curing temperatures for various GGBS replacement levels.

GGBS content	Temperature	Hydration peak value (W/g)	Time to reach peak (h)	1-day cumulative hydration heat (J/g)	3-day cumulative hydration heat (J/g)
0%	20 ℃	0.0020	10.69	122.20	225.97
	30 ℃	0.0034	6.74	184.81	282.02
	40 ℃	0.0068	6.95	216.83	312.12
	50 ℃	0.0113	4.43	254.47	343.27
10%	20 ℃	0.0018	10.61	114.88	212.47
	30 ℃	0.0033	12.18	175.68	274.94
	40 ℃	0.0064	6.84	202.66	302.31
	50 ℃	0.0106	4.33	248.13	341.02
20%	20 ℃	0.0016	10.72	106.70	199.90
	30 ℃	0.0032	11.62	158.15	256.56
	40 ℃	0.0066	6.08	195.59	299.79
	50 ℃	0.0099	4.05	236.77	327.37
30%	20 ℃	0.0015	10.30	106.84	195.59
	30 ℃	0.0033	10.89	148.02	248.99
	40 ℃	0.0057	6.41	179.60	289.30
	50 ℃	0.0109	3.73	248.45	341.78
40%	20 ℃	0.0014	19.46	96.81	181.31
	30 ℃	0.0030	9.82	129.60	228.57
	40 ℃	0.0055	5.48	169.32	274.30
	50 ℃	0.0095	3.57	230.52	318.57
50%	20 ℃	0.0012	17.50	74.97	145.54
	30 ℃	0.0029	8.90	116.62	217.88
	40 ℃	0.0052	4.97	166.57	268.37
	50 ℃	0.0080	3.29	216.56	291.77

The effect of curing temperature on hydration heat development is evident across all investigated mixes. The heat flow curves (Figure 5.5 to Figure 5.10) and extracted hydration parameters (Table 5.3) illustrate clear trends in the rate, peak, and total heat release as temperature increases. These trends can be linked to fundamental hydration kinetics and phase development.

The hydration heat flow curves (Figure 5.5 to Figure 5.10) exhibit the characteristic five-stage hydration process, which undergoes significant shifts with temperature variations. The acceleration of initial hydration reactions is evident as the induction period (Stage II) shortens at higher curing temperatures, reducing the dormant phase where heat evolution remains minimal. At 50°C, the acceleration phase (Stage III) commences much earlier than at 20°C, as demonstrated by the sharp initial rise in heat

flow (Figure 5.5 to Figure 5.10). This is attributed to the fact that higher temperatures enhance the dissolution rate of cementitious compounds, expediting the onset of C_3S and C_3A hydration.

A notable increase in hydration peak value is observed with rising temperature. In CEM I-only concrete (Table 5.3), the peak hydration heat flow at 20°C is 0.0020 W/g, whereas, at 50°C, it rises to 0.0113 W/g—an increase of more than five times. This substantial increase is attributed to the temperature-driven acceleration of C_3S hydration, which intensifies heat release. Similar trends are apparent in all mixes, reinforcing that higher temperatures facilitate faster and more exothermic hydration reactions.

The time required to reach peak hydration heat flow also decreases with increasing temperature, as indicated in the hydration heat development data. In 0% GGBS concrete, for instance, the time to peak shifts from 10.69 hours at 20°C to just 4.43 hours at 50°C (Table 5.3). This trend aligns with Arrhenius' law, which states that reaction rates approximately double for every 10°C increase in temperature, leading to a more rapid attainment of peak hydration. The same pattern is observed in all mixes, further confirming the acceleration effect of elevated curing temperatures.

Higher curing temperatures also lead to increased early-age cumulative hydration heat, as evident in the 1-day cumulative hydration heat results. In the 0% GGBS concrete sample, the 1-day hydration heat rises from 122.20 J/g at 20°C to 254.47 J/g at 50°C, marking a 108% increase (Table 5.3). Similar trends are seen across all mixes, signifying that elevated temperatures significantly enhance early hydration kinetics and promote faster reaction rates.

Despite the pronounced acceleration of early hydration, long-term hydration heat evolution exhibits a different trend. While high temperatures enhance early hydration, the difference in cumulative hydration heat at 3 days is less substantial compared to the 1-day cumulative values. For example, in the 0% GGBS mix, the 3-day cumulative hydration heat at 50°C reaches 343.27 J/g, compared to 225.97 J/g at 20°C—a 52% increase, which is considerably lower than the 108% increase in 1-day hydration heat (Table 5.3). This suggests that while elevated temperatures accelerate early hydration, they do not proportionally enhance long-term hydration. This phenomenon may be due to premature consumption of reactants, where the rapid hydration at high temperatures leads to an earlier depletion of reactive phases, limiting long-term heat evolution.

Below is a detailed breakdown of the temperature effect for each mix:

0% GGBS Concrete (Figure 5.5, Table 5.3)

- The hydration peak increases from 0.0020 W/g at 20°C to 0.0113 W/g at 50°C.

- The peak occurs much earlier at higher temperatures (10.69 h at 20°C vs. 4.43 h at 50°C).
- The 1-day heat release more than doubles from 122.20 J/g to 254.47 J/g, confirming that higher temperatures significantly enhance early hydration.
- The 3-day hydration heat increase (52%) is much smaller than the 1-day increase (108%), suggesting that high-temperature curing may promote early hydration but does not proportionally improve long-term hydration.

10% GGBS Concrete (Figure 5.6, Table 5.3)

- The hydration peak increases from 0.0018 W/g at 20°C to 0.0106 W/g at 50°C, showing a similar trend to 0% GGBS concrete.
- The time to peak hydration decreases from 10.61 hours at 20°C to 4.33 hours at 50°C.
- The 1-day cumulative heat more than doubles from 114.88 J/g to 248.13 J/g, indicating that higher temperatures accelerate the hydration reaction significantly.
- The 3-day heat increase (60%) is still lower than the 1-day increase (116%), further reinforcing the observation that high-temperature curing benefits early hydration more than long-term hydration.

20% GGBS Concrete (Figure 5.7, Table 5.3)

- The hydration peak rises from 0.0016 W/g at 20 °C to 0.0099 W/g at 50 °C.
- The peak occurs at 10.72 hours at 20 °C but shifts to 4.05 hours at 50 °C.
- The 1-day cumulative heat rises by 122% (106.70 J/g → 236.77 J/g), while the 3-day increase is only 64%, suggesting accelerated early hydration but reduced impact on long-term hydration.

30% GGBS Concrete (Figure 5.8, Table 5.3)

- The peak heat flow increases from 0.0015 W/g at 20 °C to 0.0109 W/g at 50 °C.
- The peak time reduces from 10.30 hours to 3.73 hours, reinforcing the inverse relationship between curing temperature and time to peak hydration.
- Early hydration (1-day heat) is significantly affected, with a 133% increase, while the 3-day increase is 75%.
- This supports the hypothesis that high temperatures promote early-stage hydration, but their impact on later hydration is reduced.

40% GGBS Concrete (Figure 5.9, Table 5.3)

- The peak hydration rate grows from 0.0014 W/g to 0.0095 W/g, an increase of nearly 580%.
- The time to peak shifts dramatically from 19.46 hours to 3.57 hours, illustrating that high temperatures counteract the natural delay of hydration in SCM-rich systems.

- The 1-day cumulative heat increases by 138%**,** but the 3-day heat increase is 76%, confirming the trend that temperature's effect is more pronounced at early ages.

50% GGBS Concrete (Figure 5.10, Table 5.3)

- The peak hydration rate increases from 0.0012 W/g at 20°C to 0.0080 W/g at 50 °C, a 566% increase.
- The time to peak shifts from 17.50 hours to 3.29 hours, indicating that high temperatures drastically accelerate hydration in high-GGBS systems.
- The 1-day hydration heat increases by 189%, whereas the 3-day increase is only 100%, again suggesting that higher temperatures benefit early hydration more than long-term hydration.

The bar charts in Figure 5.11 to Figure 5.28 were derived from the quantitative data summarized in Table 5.3 and the hydration heat evolution curves in Figure 5.5 to Figure 5.10. These bar charts provide a visual representation of the influence of curing temperature on key hydration characteristics, including hydration peak, 1-day cumulative hydration heat, and 3-day cumulative hydration heat. The trends observed in the bar charts align with the patterns seen in the heat flow and cumulative hydration heat curves, reinforcing the positive correlation between increasing curing temperature and accelerated hydration reactions. This trend is expected, as elevated temperatures enhance the dissolution and reaction rates of cementitious phases, leading to a faster hydration process and greater early heat release. Previous studies [6, 47, 48] have similarly reported this temperature-dependent acceleration of hydration kinetics. Furthermore, the magnitude of temperature influence varies across different binder compositions, suggesting that activation energy and binder reactivity influence the extent of hydration enhancement. These findings emphasize the crucial role of temperature control in managing early-age concrete properties, particularly in mass concrete applications where excessive heat generation may contribute to thermal cracking risks.

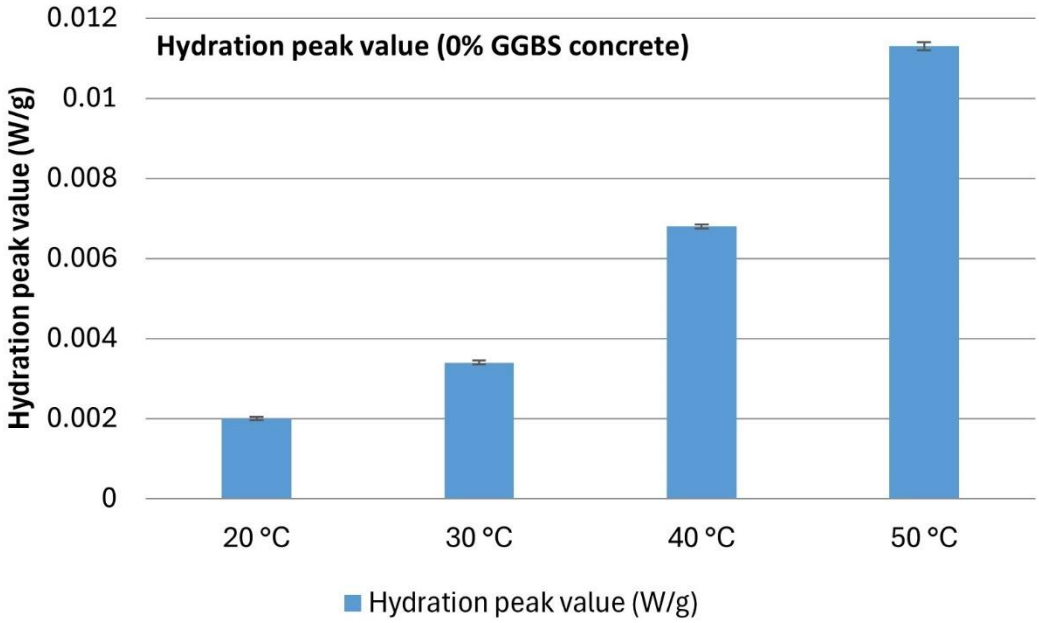

Figure 5.11. Variation of hydration peak value of 0% GGBS concrete with temperature.

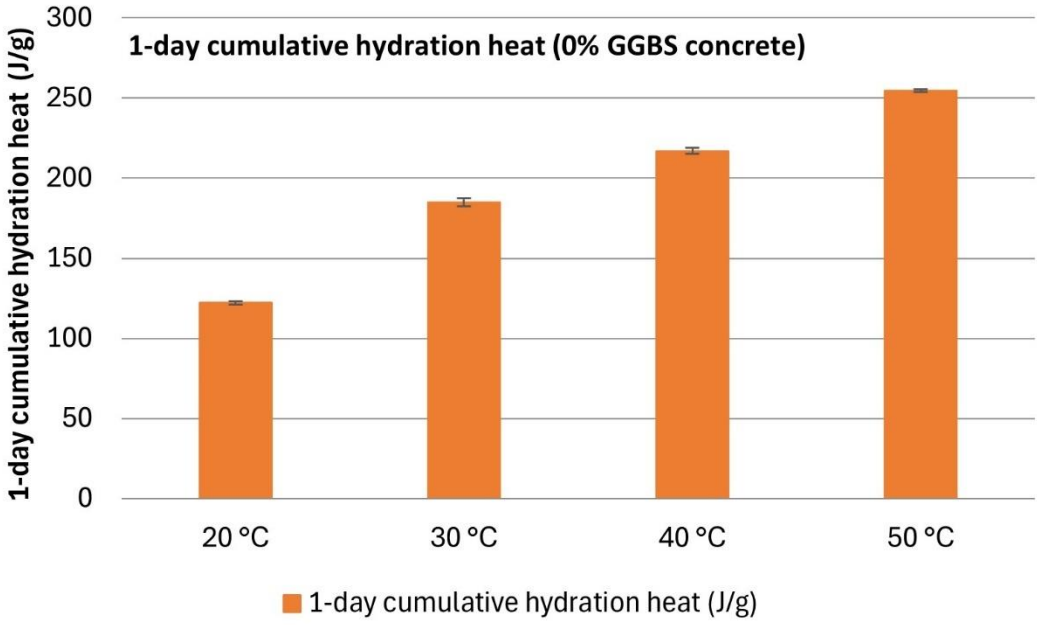

Figure 5.12. Variation of 1-day cumulative hydration heat of 0% GGBS concrete with temperature.

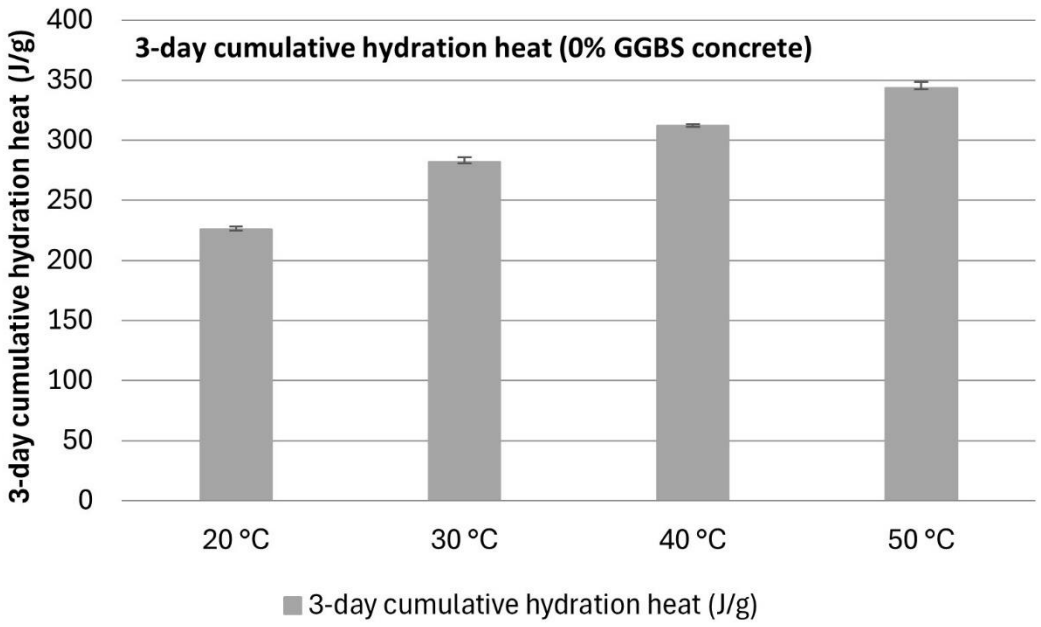

Figure 5.13. Variation of 3-day cumulative hydration heat of 0% GGBS concrete with temperature.

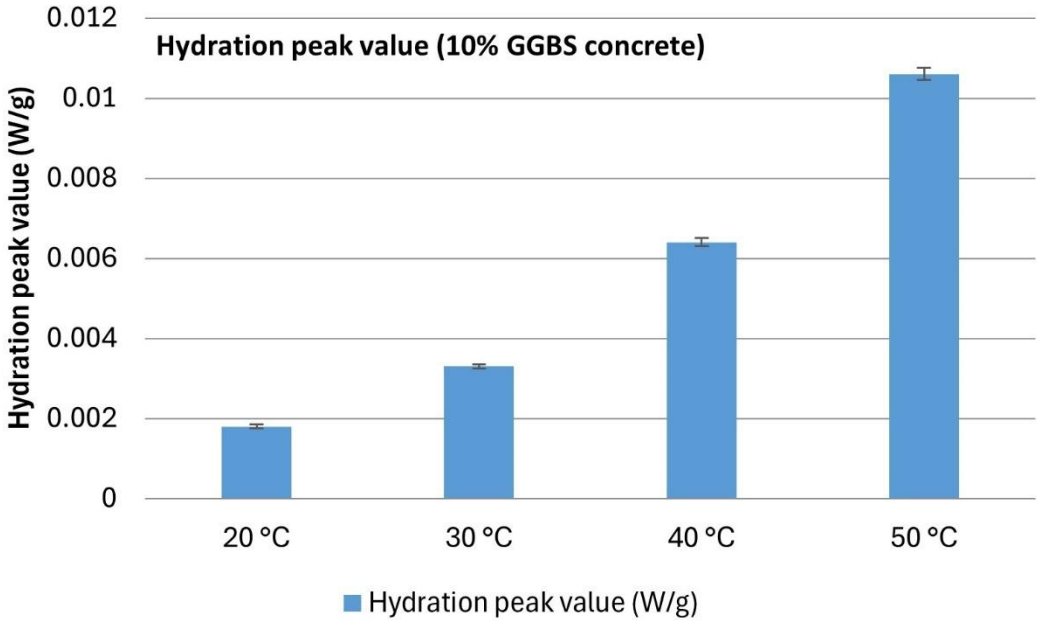

Figure 5.14. Variation of hydration peak value of 10% GGBS concrete with temperature.

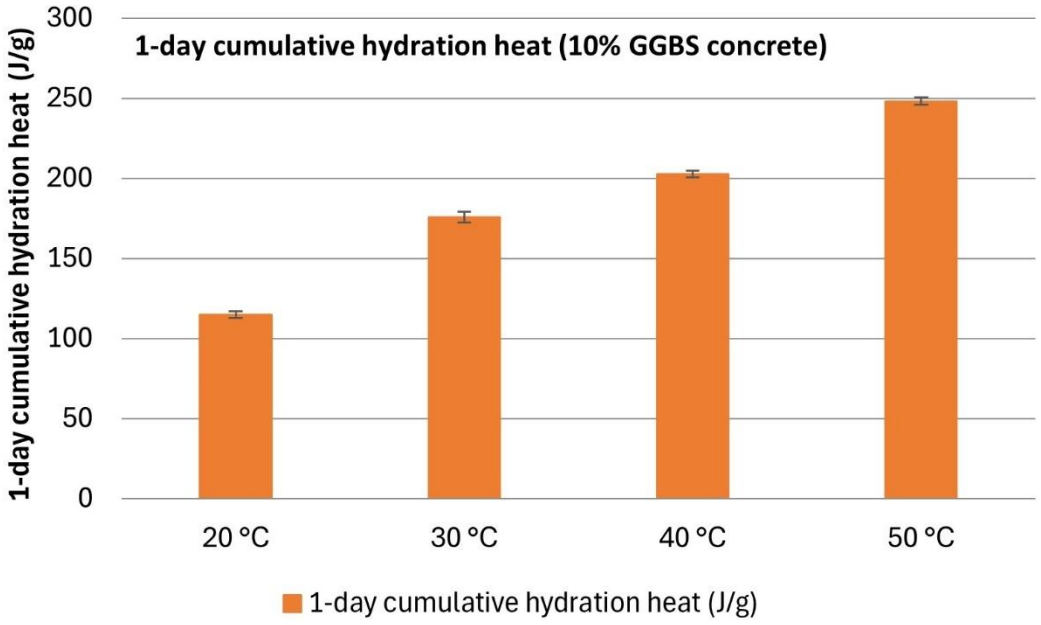

Figure 5.15. Variation of 1-day cumulative hydration heat of 10% GGBS concrete with temperature.

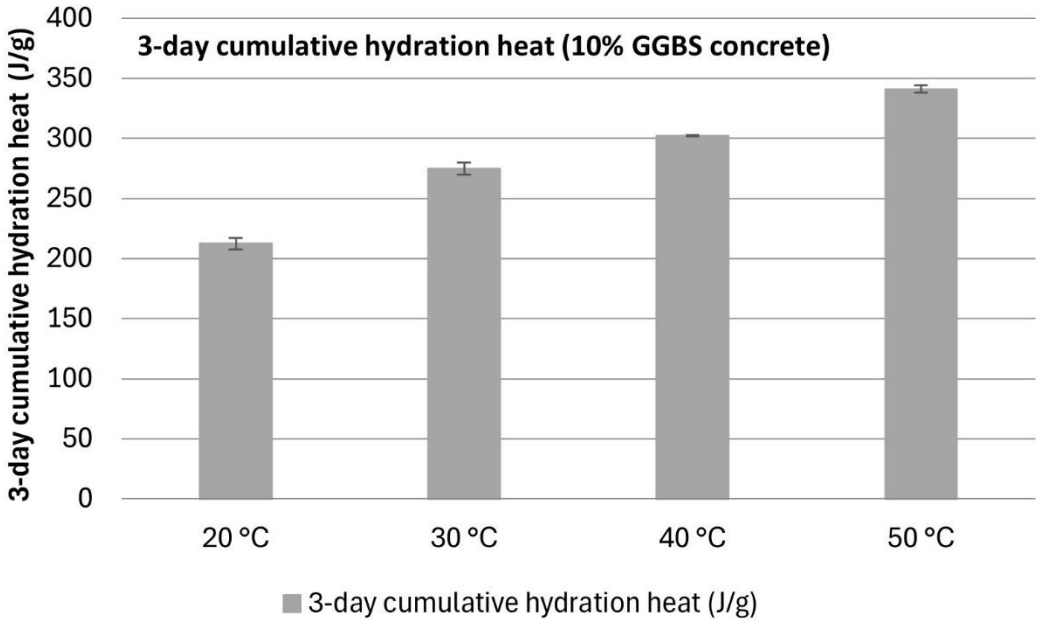

Figure 5.16. Variation of 3-day cumulative hydration heat of 10% GGBS concrete with temperature.

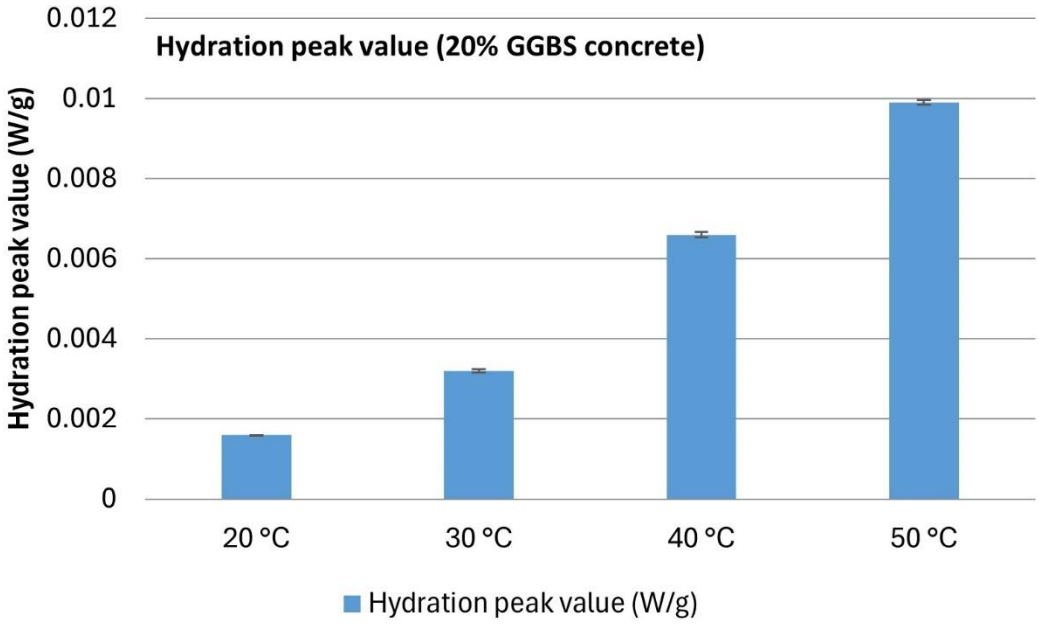

Figure 5.17. Variation of hydration peak value of 20% GGBS concrete with temperature.

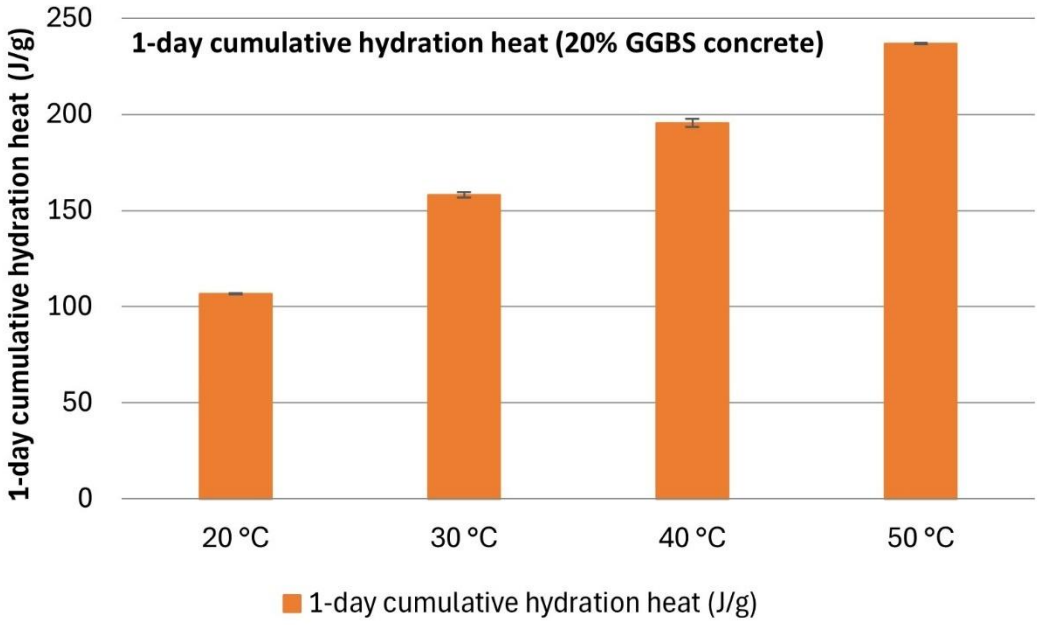

Figure 5.18. Variation of 1-day cumulative hydration heat of 20% GGBS concrete with temperature.

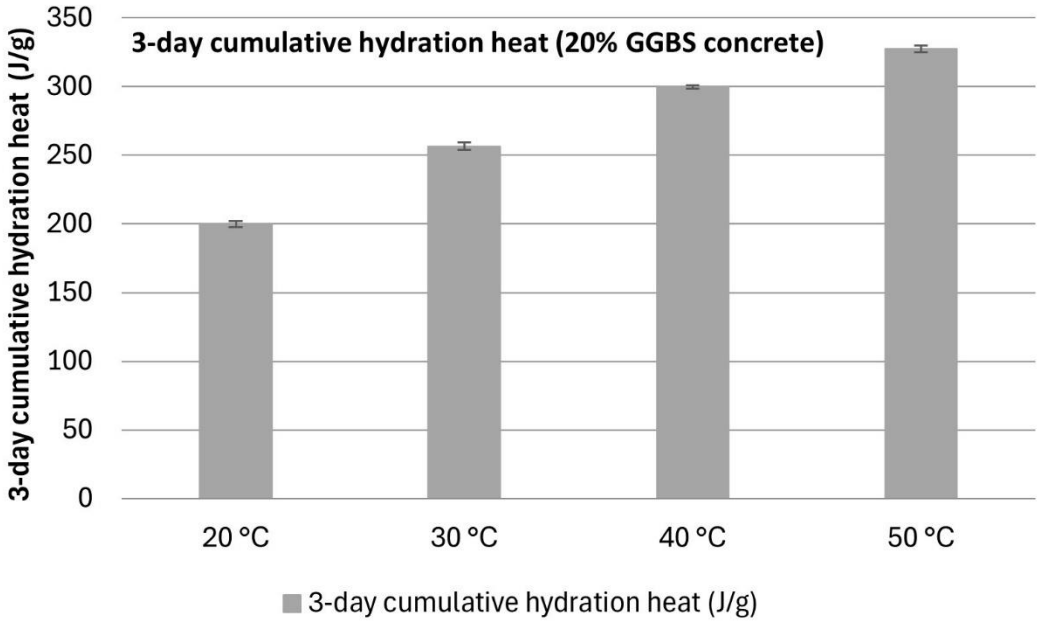

Figure 5.19. Variation of 3-day cumulative hydration heat of 20% GGBS concrete with temperature.

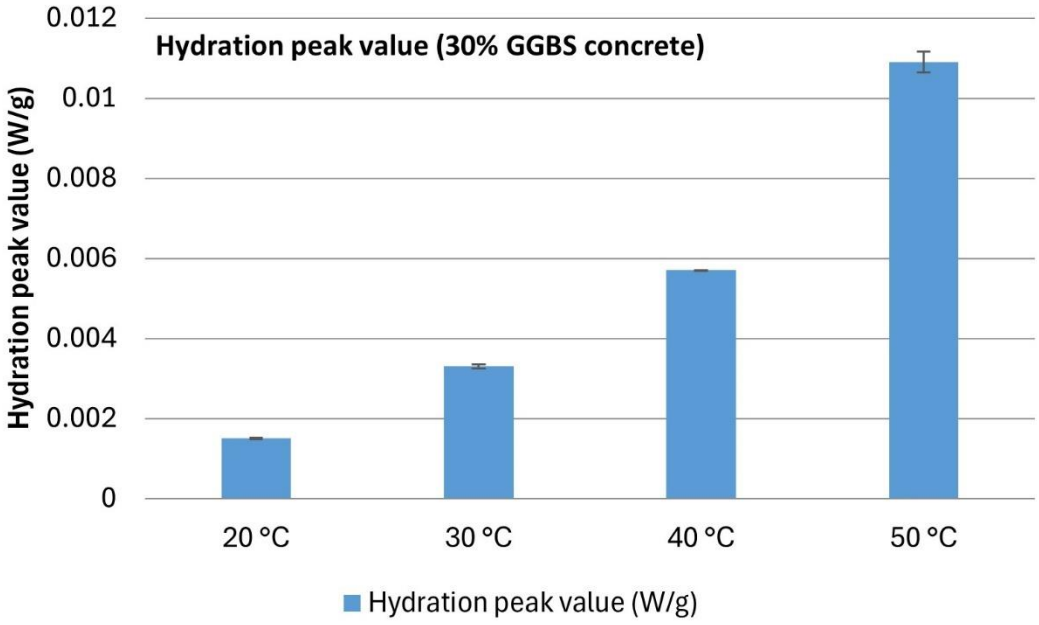

Figure 5.20. Variation of hydration peak value of 30% GGBS concrete with temperature.

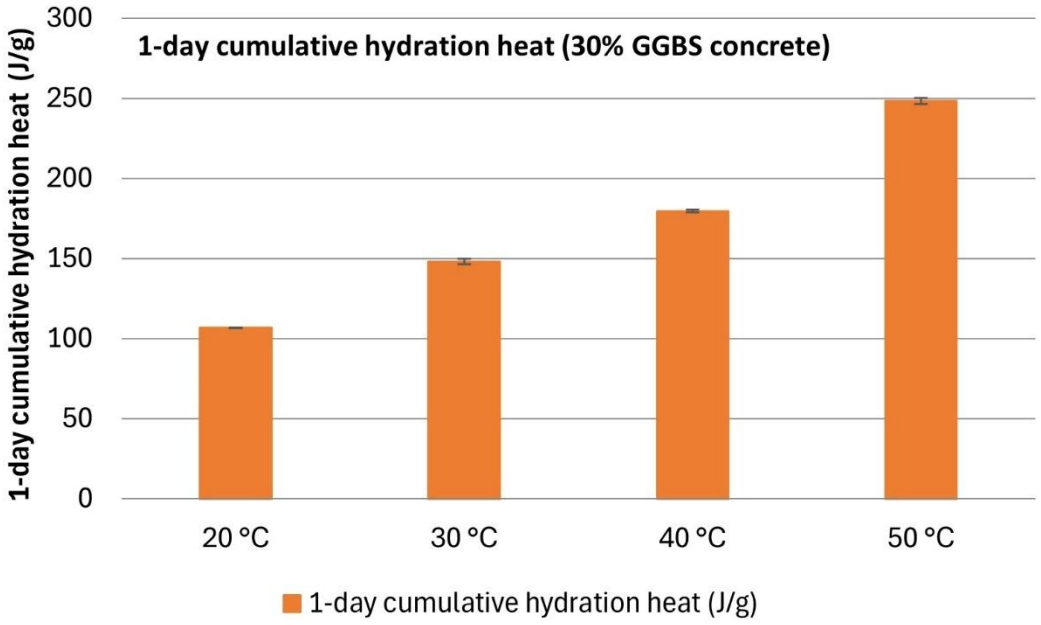

Figure 5.21. Variation of 1-day cumulative hydration heat of 30% GGBS concrete with temperature.

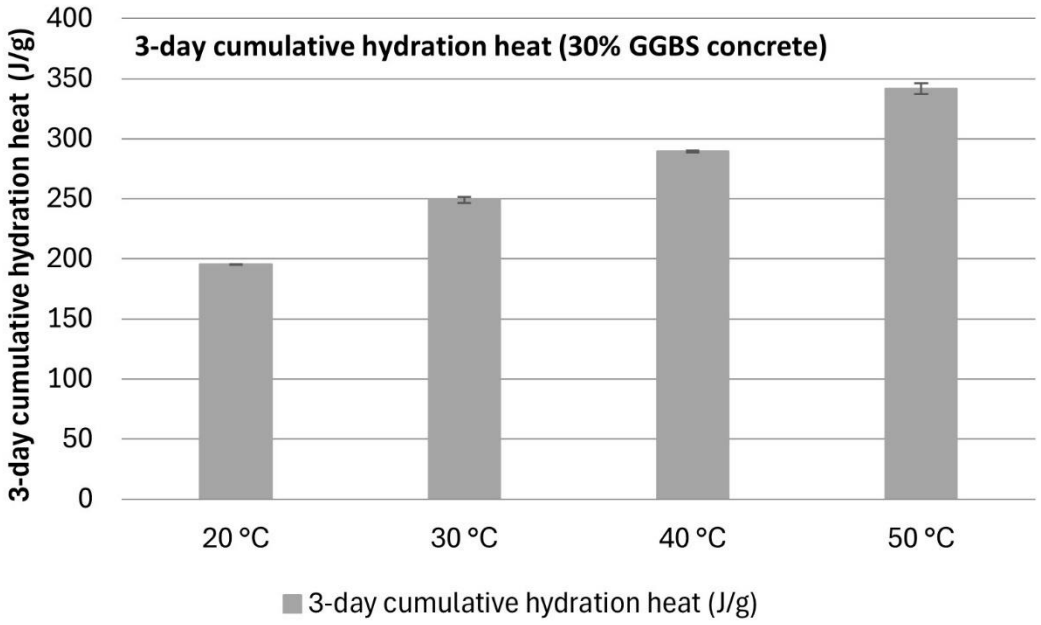

Figure 5.22. Variation of 3-day cumulative hydration heat of 30% GGBS concrete with temperature.

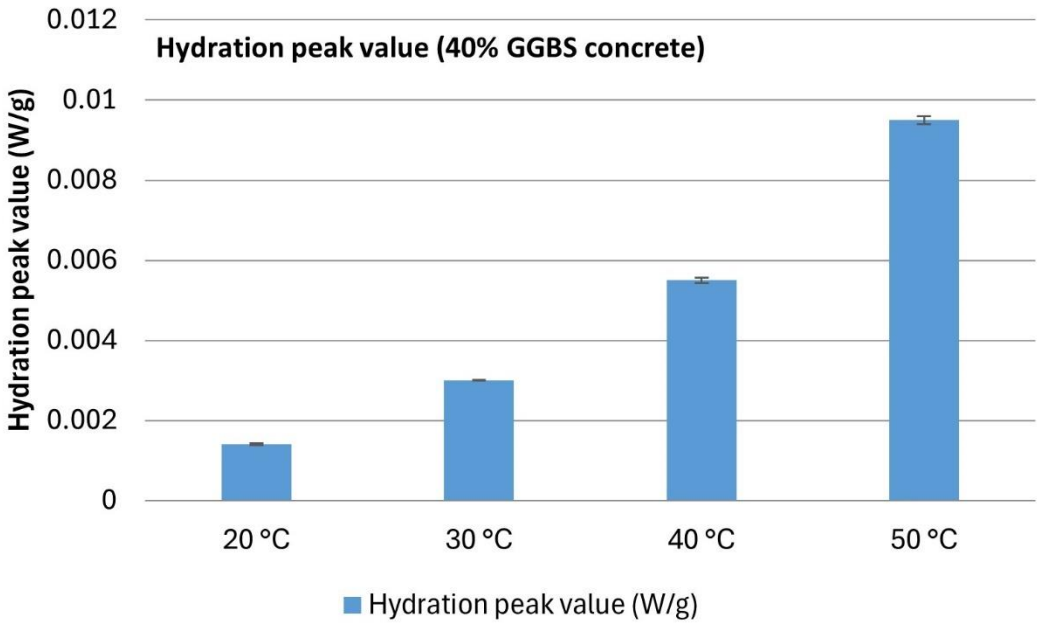

Figure 5.23. Variation of hydration peak value of 40% GGBS concrete with temperature

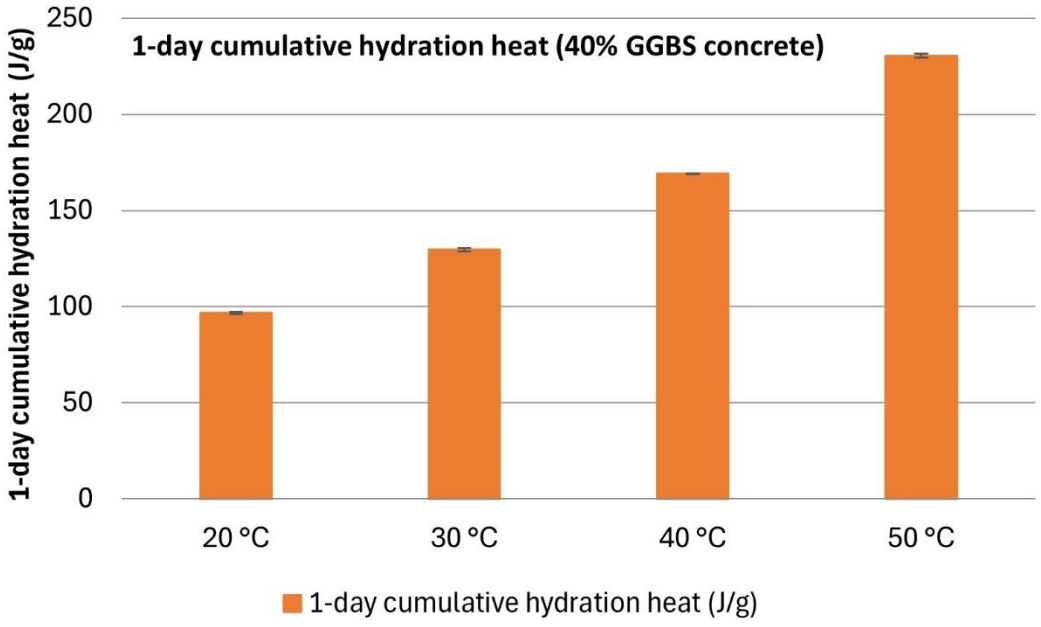

Figure 5.24. Variation of 1-day cumulative hydration heat of 40% GGBS concrete with temperature

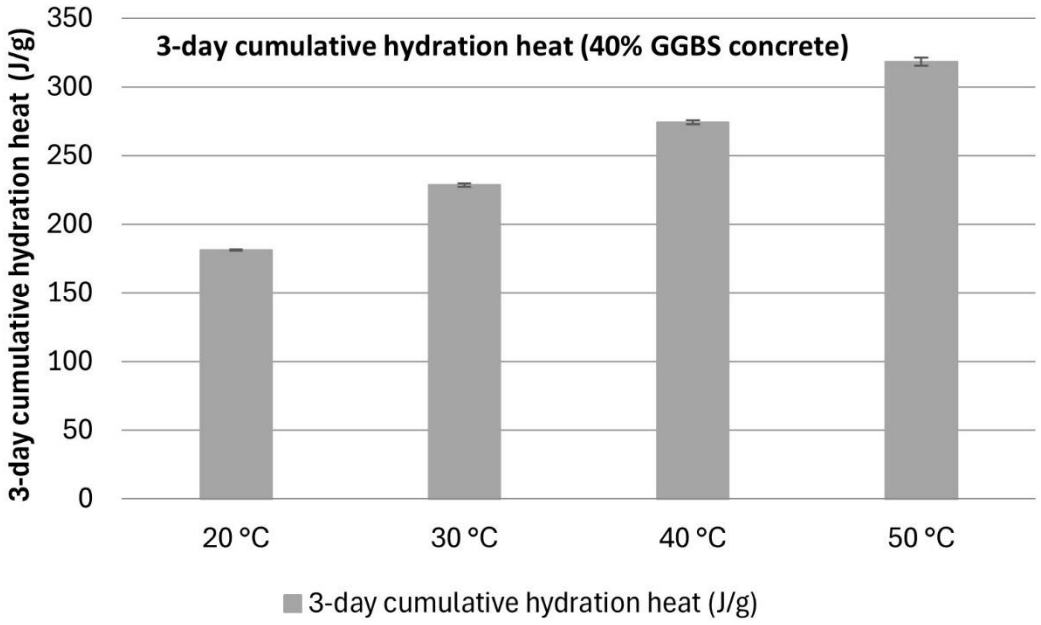

Figure 5.25. Variation of 3-day cumulative hydration heat of 40% GGBS concrete with temperature

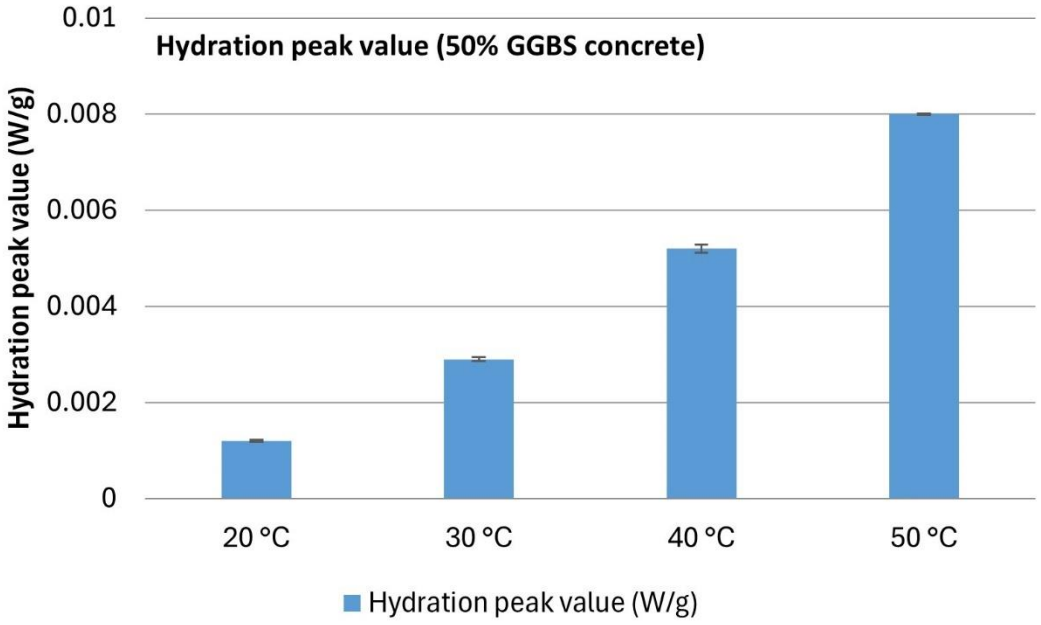

Figure 5.26. Variation of hydration peak value of 50% GGBS concrete with temperature

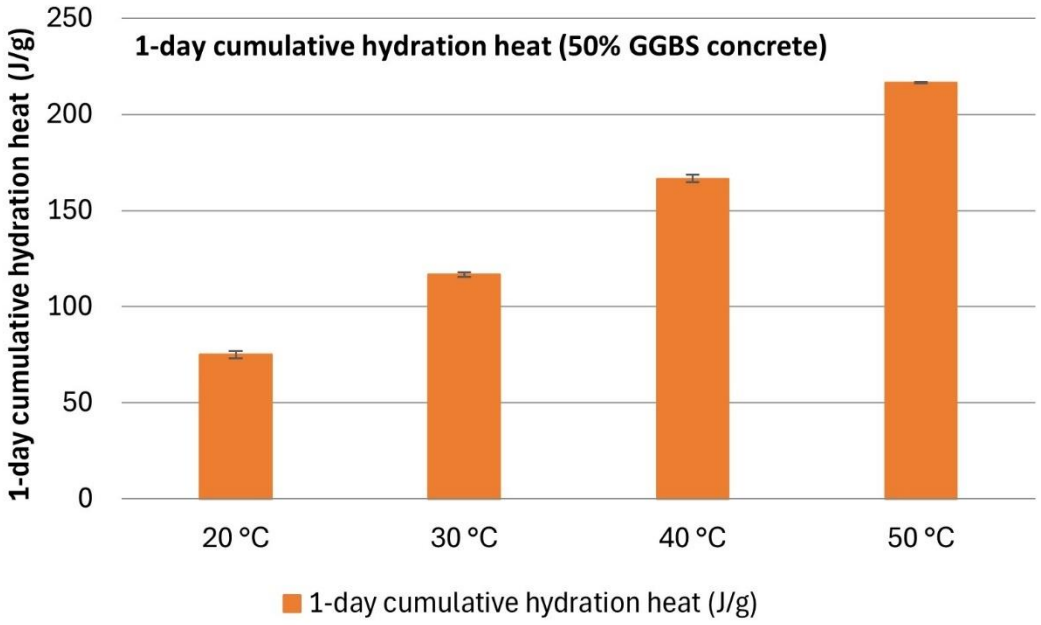

Figure 5.27. Variation of 1-day cumulative hydration heat of 50% GGBS concrete with temperature

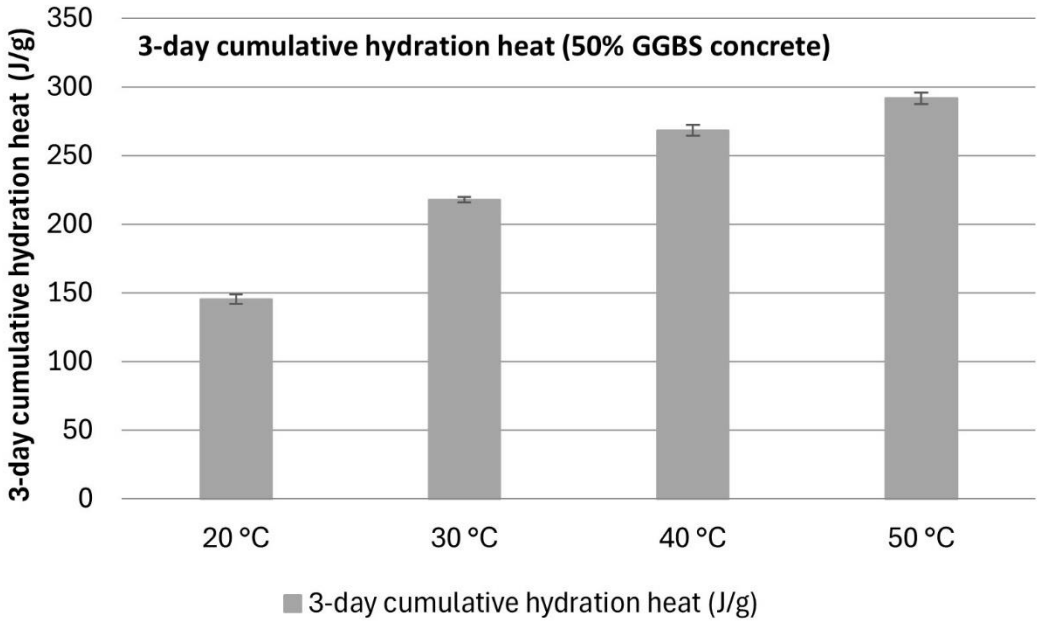

Figure 5.28. Variation of 3-day cumulative hydration heat of 50% GGBS concrete with temperature

Table 5.4 summarizes the percentage changes in these hydration heat characteristics for each mix when the temperature increases from 20°C to 50°C. Two interesting phenomena are observed. First, the percentage increase in hydration peak value and cumulative hydration heat with rising temperature increases with higher GGBS content (except for the 30% GGBS mix's hydration peak value). For example, for the CEM-

only mix, increasing temperature from 20 ℃ to 50 ℃ results in a 465% increase in peak hydration heat flow and a 51.9% increase in 3-day cumulative hydration heat (Figure 5.5). However, when GGBS replace 50% CEM I, the impact of temperature (from 20 ℃ to 50 ℃) on hydration heat development becomes more pronounced, the increase in peak hydration heat flow due to a 30 ℃ temperature increase is 566.67%, and the 3-day cumulative hydration heat increase is 100.41% (Figure 5.10). These indicates that GGBS is more temperature-sensitive than CEM I cement, suggesting that the promotion effect of elevated temperature on hydration heat is stronger for GGBS. Potential reasons for this phenomenon include: GGBS-CEM blended mixes generally have a higher apparent activation energy than CEM I, which significantly increases their reaction rate with rising temperatures (the apparent activation energy will be calculated and analysed in detail in Section 5.4.3); GGBS hydration relies on the alkaline environment produced by CEM I hydration, and the combination of GGBS and CEM I might create a synergistic effect at higher temperatures, fostering more favourable conditions for GGBS hydration. Another potential contributing factor is that GGBS hydration generally exhibits slower reaction kinetics compared to CEM I, particularly at early ages. Therefore, an increase in temperature has a disproportionate accelerating effect on GGBS hydration compared to CEM I hydration, leading to a more pronounced enhancement in heat development with temperature rise. These factors collectively result in this phenomenon, indicating that concrete with higher GGBS content exhibits more significant changes in hydration heat with temperature fluctuations, necessitating strict control and monitoring of temperature in practical applications.

Second, the percentage increase in hydration peak value due to temperature rise is much greater than that of 1-day and 3-day cumulative hydration heat. This significant difference can be attributed to several factors. The hydration peak represents the maximum rate of the exothermic reaction, which is highly sensitive to temperature changes due to the Arrhenius relationship (Eq. (2.1)), indicates an exponential relationship between reaction rate and temperature, causing a sharp increase at higher temperatures. While the hydration peak reflects the instantaneous reaction rate, cumulative hydration heat represents the integrated heat release over time. Although increasing temperature accelerates reaction kinetics, the total cumulative heat is still governed by the total amount of reactive phases in the system. Since the hydration process eventually reaches a limit dictated by stoichiometry, cumulative heat does not increase as drastically as the peak rate. Additionally, the peak value is influenced by the rapid acceleration of reactions at higher temperatures, while cumulative heat reflects the overall hydration process, constrained by stoichiometry and completeness of the reaction. Thus, the peak hydration rate is more pronounced with increasing temperature than cumulative heat, reflecting the differential sensitivity and integrated effects of the hydration process.

Isothermal calorimetry offers several advantages over semi-adiabatic calorimetry in the context of this study. First, isothermal calorimetry allows for direct measurement of the hydration heat rate, providing precise and immediate data on the heat flow during the

hydration process. Direct measurement of the hydration heat rate in isothermal calorimetry eliminates the need to determine the thermal properties of the materials, such as specific heat capacity and thermal conductivity. This avoids potential errors in the measurement process of these thermal properties. Second, the ability to maintain constant curing temperatures in isothermal calorimetry enables the study of specific factors, such as the effect of GGBS addition, without the confounding influence of temperature fluctuations. This ensures that the observed effects are primarily due to the variable of interest rather than external temperature changes. Third, the smaller sample sizes required for isothermal calorimetry (48.18 g in this study) significantly reduce the cost and complexity of sample preparation, facilitating more extensive testing and data collection. These advantages make isothermal calorimetry a valuable tool for obtaining detailed insights into the hydration heat development of concrete, particularly when assessing the impact of supplementary materials like GGBS.

Table 5.4. Increasement of hydration heat characteristics from 20 ℃ to 50 ℃.

Mix	Hydration Peak Value Increase	1-Day Cumulative Hydration Heat Increase	3-Day Cumulative Hydration Heat Increase
0% GGBS	465.00%	108.18%	51.90%
10% GGBS	488.89%	115.98%	60.52%
20% GGBS	518.75%	122.01%	63.78%
30% GGBS	626.67%	132.56%	75.75%
40% GGBS	578.57%	138.12%	75.68%
50% GGBS	566.67%	188.83%	100.41%

In summary, the analysis of hydration heat characteristics across different temperatures reveals that higher curing temperatures significantly promote hydration reactions in both CEM-only and CEM-GGBS blended mixes. The increase in hydration peak value and cumulative hydration heat is more pronounced with higher GGBS content, indicating the higher temperature sensitivity of GGBS than CEM I. This underscores the importance of strict temperature control in practical applications involving GGBS-blended concrete. Additionally, while the hydration peak value shows a sharp increase with temperature, the cumulative hydration heat exhibits a relatively moderate rise, reflecting the differential sensitivity of these hydration heat characteristics to temperature changes.

5.3 Influence of GGBS Content on Hydration Heat

This section presents the analysis of the impact of varying proportions of GGBS on the hydration heat development in micro-concrete samples. The focus is on evaluating the effect of hydration heat evolution when replacing part of CEM I with GGBS in concrete. To ensure the accuracy and reproducibility of the results, each experimental setup involved simultaneous measurements of two identical micro-concrete samples, with the outcomes averaged to mitigate potential variances due to individual sample anomalies,

in a manner analogous to the previous section. Figure 5.29-Figure 5.32 show the development of hydration heat flow and cumulative hydration heat curves of micro-concrete samples with GGBS content from 0% to 50% at 20, 30, 40, and 50°C in the first three days, respectively.

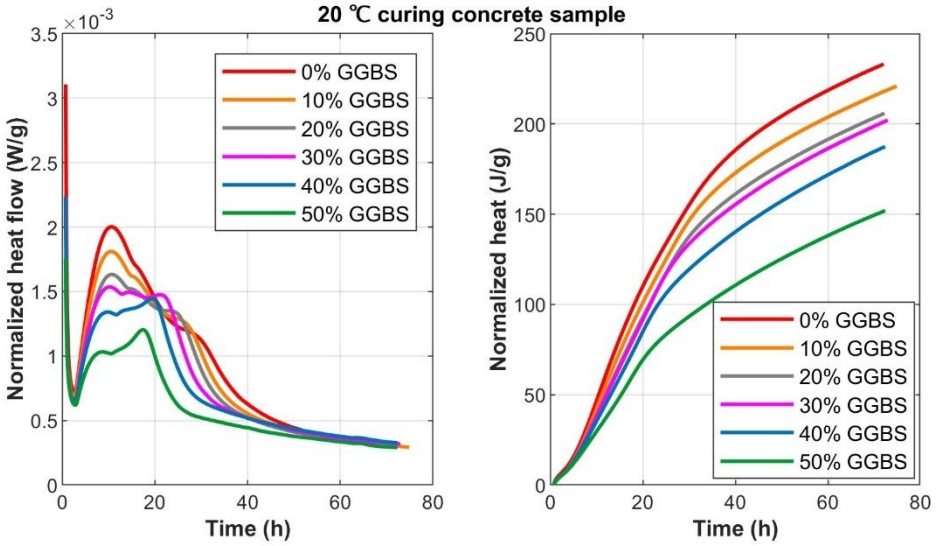

(a) (b)

Figure 5.29. Isothermal calorimetry curves for 20 ℃ curing micro-concrete sample with different GGBS contents: (a) normalized hydration heat flow; (b) normalized cumulative hydration heat.

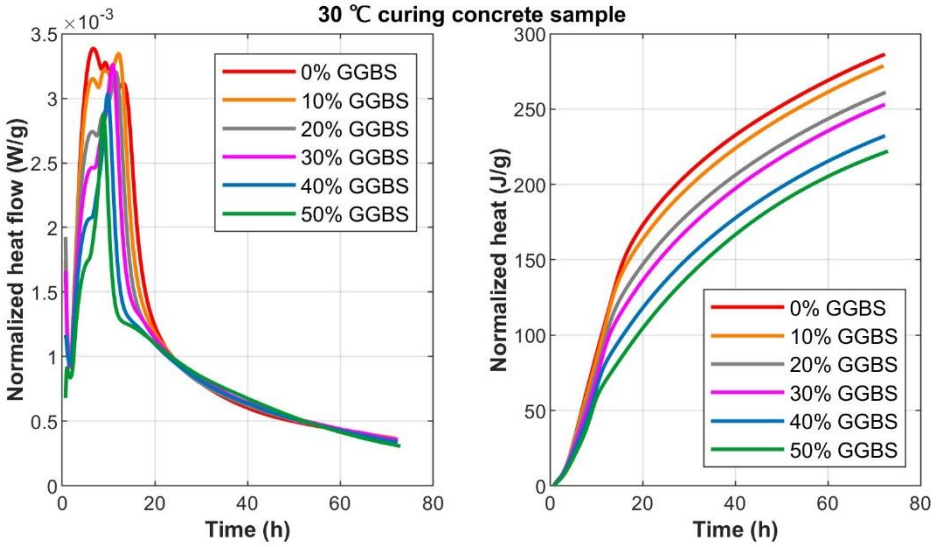

(a) (b)

Figure 5.30. Isothermal calorimetry curves for 30 ℃ curing micro-concrete sample with different GGBS contents: (a) normalized hydration heat flow; (b) normalized cumulative hydration heat.

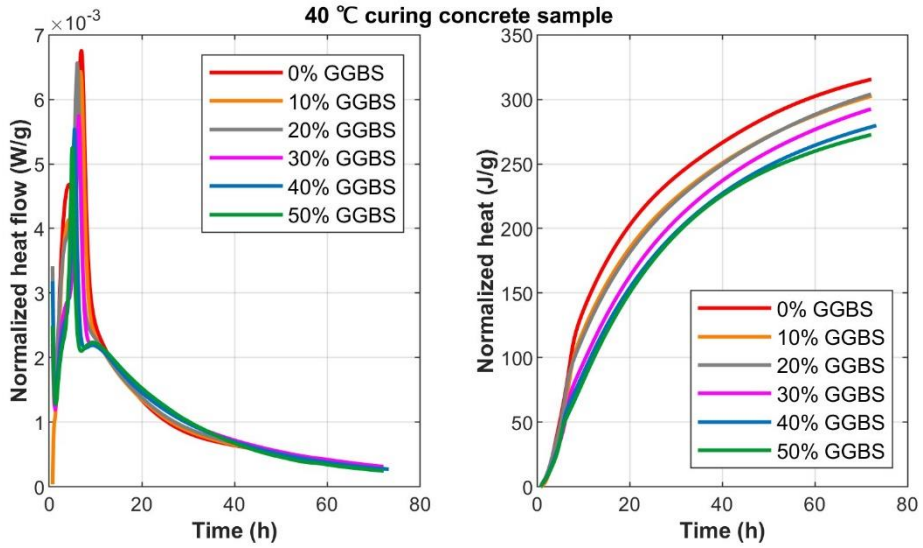

(a) (b)

Figure 5.31. Isothermal calorimetry curves for 40 ℃ curing micro-concrete sample with different GGBS contents: (a) normalized hydration heat flow; (b) normalized cumulative hydration heat.

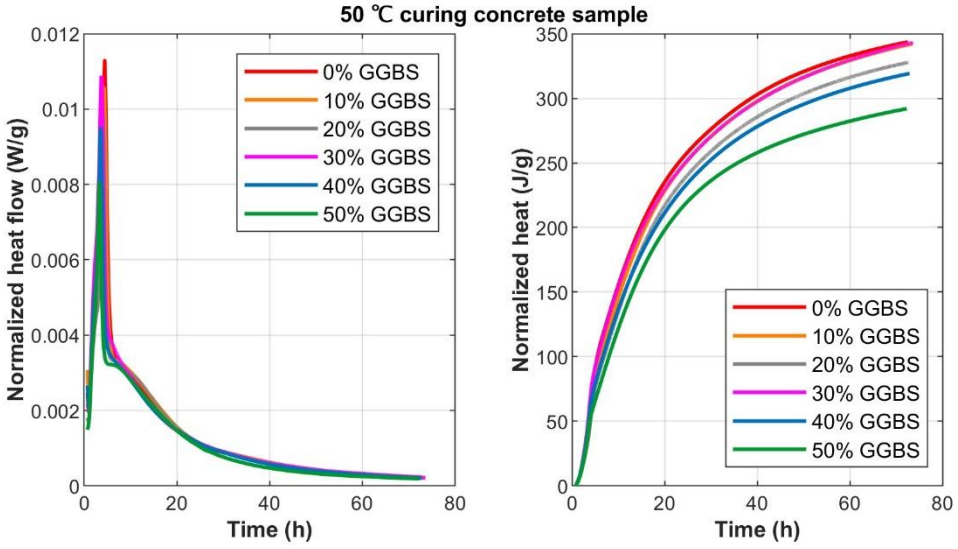

(a) (b)

Figure 5.32. Isothermal calorimetry curves for 50 ℃ curing micro-concrete sample with different GGBS contents: (a) normalized hydration heat flow; (b) normalized cumulative hydration heat.

To assess the influence of GGBS replacement part of CEM I on hydration heat development, Table 5.5 presents key hydration heat parameters for samples with varying curing temperatures. These parameters include peak hydration heat, time to peak hydration, 1-day cumulative hydration heat, and 3-day cumulative hydration heat.

The table provides an overview of how these critical hydration characteristics evolve with GGBS replacement.

Table 5.5. Summary of hydration heat development at different GGBS content for various curing temperatures.

Curing temperature	GGBS content	Hydration peak value (W/g)	Time to reach peak (h)	1-day cumulative hydration heat (J/g)	3-day cumulative hydration heat (J/g)
20 ℃	0%	0.0020	10.69	122.20	225.97
	10%	0.0018	10.61	114.88	212.47
	20%	0.0016	10.72	106.70	199.90
	30%	0.0015	10.30	106.84	195.59
	40%	0.0014	19.46	96.81	181.31
	50%	0.0012	17.50	74.97	145.54
30 ℃	0%	0.0034	6.74	184.81	282.02
	10%	0.0033	12.18	175.68	274.94
	20%	0.0032	11.62	158.15	256.56
	30%	0.0033	10.89	148.02	248.99
	40%	0.0030	9.82	129.60	228.57
	50%	0.0029	8.90	116.62	217.88
40 ℃	0%	0.0068	6.95	216.83	312.12
	10%	0.0064	6.84	202.66	302.31
	20%	0.0066	6.08	195.59	299.79
	30%	0.0057	6.41	179.60	289.30
	40%	0.0055	5.48	169.32	274.30
	50%	0.0052	4.97	166.57	268.37
50 ℃	0%	0.0113	4.43	254.47	343.27
	10%	0.0106	4.33	248.13	341.02
	20%	0.0099	4.05	236.77	327.37
	30%	0.0109	3.73	248.45	341.78
	40%	0.0095	3.57	230.52	318.57
	50%	0.0080	3.29	216.56	291.77

The hydration heat development curves displayed in this section demonstrate that an increase in GGBS content reduces both the peak hydration heat flow and the cumulative hydration heat. The hydration reaction in cementitious materials follows five distinct stages: initial dissolution, induction period, acceleration, deceleration, and long-term stabilization. The effect of GGBS content on these stages varies significantly across different curing temperatures, as observed in Figure 5.29-Figure 5.32. The hydration heat development curves illustrate that increasing GGBS content systematically alters the progression of these five stages, with the most significant differences appearing at lower curing temperatures.

During the initial dissolution phase, rapid dissolution of C_3S and C_3A occurs within the first few minutes of hydration. The impact of GGBS content on this phase is minimal since the dissolution process is primarily dictated by the immediate availability of water and the inherent solubility of cementitious compounds. However, in non-GGBS concrete (0% GGBS), a sharp initial heat flow peak is observed, which gradually diminishes as the GGBS content increases. This suggests that the presence of GGBS reduces the availability of early reactive C_3S, leading to a less pronounced initial exothermic response. At higher temperatures (40 and 50 ℃, Figure 5.31, Figure 5.32), this dissolution phase is completed more rapidly, as indicated by the steeper decline in hydration heat flow within the first few minutes in high-temperature samples.

The induction period, characterized by minimal heat flow due to the temporary passivation of cement grains, exhibits a strong dependence on GGBS content. As the GGBS replacement level increases, the induction period is prolonged, particularly at lower temperatures such as 20°C and 30°C (Figure 5.29, Figure 5.30). This is attributed to the dilution effect, where the replacement of CEM I with GGBS reduces the early availability of reactive phases responsible for hydration initiation. However, at higher temperatures (40°C and 50°C), this delay is less pronounced (Figure 5.31, Figure 5.32), as temperature accelerates dissolution and reaction kinetics, overriding the inhibitory effect of GGBS.

The acceleration phase is marked by a sharp increase in heat flow, corresponding to the peak hydration heat. The data show that increasing GGBS content leads to a reduction in both the magnitude and rate of the hydration peak. In CEM I-only mixes (0% GGBS), the hydration peak is strong and occurs earlier, whereas, in GGBS-blended mixes, the peak shifts to later times and its magnitude decreases (Table 5.5). This is due to both the dilution effect, where GGBS replaces a portion of CEM I and reduces the immediate availability of highly reactive C3S, and the delayed pozzolanic reaction of GGBS, which contributes to hydration at later stages. Interestingly, at higher temperatures (40°C and 50°C), the differences in peak heat flow among different GGBS levels become less significant (Figure 5.31, Figure 5.32). This suggests that elevated temperatures compensate for the slower reaction kinetics of GGBS-blended systems, bringing their hydration behaviour closer to that of CEM I-only concrete.

The deceleration phase follows the peak hydration period, where hydration slows due to the depletion of reactants and the formation of hydration products that hinder further dissolution. High-GGBS mixes exhibit a more gradual decrease in heat flow compared to CEM I-only concrete, particularly at lower curing temperatures (20°C and 30°C, Figure 5.29, Figure 5.30). This extended deceleration phase in GGBS-rich mixes is likely due to the continuous release of reactive silicate phases from GGBS, which sustains a lower but more prolonged heat evolution. However, at higher curing temperatures, the deceleration phase is shortened for all mixes, indicating that the hydration process is significantly accelerated, even for high-GGBS content samples.

The long-term stabilization phase, characterized by the continued slow release of hydration heat, is particularly affected by GGBS at lower temperatures. The 3-day cumulative hydration heat (Table 5.5) shows that at 20°C, the reduction in hydration heat with increasing GGBS content is much more pronounced than at higher temperatures. This suggests that at lower temperatures, the hydration of GGBS is significantly delayed, requiring extended curing durations to achieve substantial reaction completion. However, at 50°C, the differences in cumulative heat release among different GGBS contents are much smaller (Figure 5.32), indicating that high temperatures effectively accelerate both the primary hydration of CEM I and the secondary pozzolanic reaction of GGBS.

Below is a detailed breakdown of the GGBS replacement effect for each curing temperature:

20°C Hydration Heat Curves (Figure 5.29, Table 5.5)

- Increasing GGBS content significantly suppresses hydration heat.
- The first peak reduces in intensity, while the extra peak becomes increasingly pronounced.
- Time to peak increases from 10.69 hours (0% GGBS) to 17.50 hours (50% GGBS).
- Cumulative hydration heat at 3 days drops from 225.97 J/g to 145.54 J/g, highlighting a substantial long-term reduction.

30°C Hydration Heat Curves (Figure 5.30, Table 5.5)

- Higher temperatures accelerate both CEM I and GGBS hydration.
- The extra peak shifts earlier than at 20°C, reducing the difference between peaks.
- Time to peak still increases with GGBS but is less pronounced than at 20°C.
- Cumulative hydration heat at 3 days drops from 282.02 J/g (0% GGBS) to 217.88 J/g (50% GGBS), a smaller reduction compared to 20°C.

40°C Hydration Heat Curves (Figure 5.31, Table 5.5)

- The first peak is no longer distinct in high-GGBS mixes, merging with the secondary peak.
- GGBS reaction accelerates, reducing time delays observed at lower temperatures.
- The hydration peak value decreases, but the time to peak no longer increases significantly.
- Cumulative hydration heat at 3 days shows only a moderate reduction, from 312.12 J/g (0% GGBS) to 268.37 J/g (50% GGBS).

50°C Hydration Heat Curves (Figure 5.32, Table 5.5)

- The first peak is nearly undetectable in all GGBS mixes.

- Time to peak remains within a narrow range (3.29–4.43 hours) across all GGBS contents.
- The hydration peak suppression effect is weaker at 50°C than at lower temperatures.
- Cumulative heat at 3 days remains high across all mixes, with only a 15% reduction from 0% to 50% GGBS, indicating higher temperatures compensate for the slower GGBS reaction.

The impact of GGBS content on hydration heat development at a constant temperature, as shown in this section, markedly contrasts with the findings discussed in Section 5.2 (Figure 5.5 to Figure 5.10). In Section 5.2, irrespective of the GGBS content, the effect of temperature increase on the hydration curve shape and trend was remarkably consistent across samples, indicating a similar degree of influence across the same mix. However, in the current section, the influence of GGBS content on hydration heat development varies significantly at different curing temperatures.

For instance, at lower temperatures (20°C), there are substantial differences in the hydration heat curves of samples with varying GGBS contents. However, as the temperature increases, the impact of GGBS content on hydration heat becomes less pronounced. It becomes evident that at higher temperatures, the differences in hydration heat curves for various GGBS contents diminish, culminating in almost overlapping curves at 50 °C, making it challenging to distinguish between them. This suggests that the inhibitory effect of GGBS on cement hydration heat is mitigated at higher curing temperatures. If based on one of the fundamental assumptions of this study (as mentioned several times in Section 2.5.3), i.e., the maturity of concrete with the same mix is directly proportional to the strength, cumulative heat of hydration, and hydration degree. The finding above is consistent with Tang *et al.*'s [1]conclusion that the early-age strength insufficient problem in GGBS concrete can be mitigated through high-temperature curing.

The hydration heat flow curves presented in this section, derived from samples with varying GGBS contents under the same curing temperature, offer a clear observation of the "extra peak" phenomenon resulting from the addition of GGBS. A horizontal comparison of hydration heat flow charts at different temperatures reveals a significant temperature impact on the "extra peak" phenomenon. The lower the temperature, the more pronounced the "extra peak", making it easier to observe.

At 20°C, the "extra peak" emergence becomes increasingly apparent with the addition of GGBS. For samples with lower GGBS contents, the first peak in the hydration heat flow curve is greater than the second. However, as the GGBS content increases, the disparity between the first and final peaks gradually diminishes. At 30% GGBS content, the sizes of the first and final peaks are almost equal. Above 30% GGBS, the final peak surpasses the first, with the difference becoming more significant as the GGBS content increases.

The “extra peak” phenomenon becomes more distinct as the temperature rises. This is evident in several aspects, such as at 30°C, where the final peak in the 10% GGBS sample already exceeds the first. Additionally, at higher temperatures, the time gap between the first and second peaks narrows, indicating that an increase in temperature accelerates CEM I hydration and GGBS hydration. When the temperature reaches 40°C, the first peak in samples with more than 30% GGBS is barely noticeable. At 50°C, the first peaks in all samples are almost undetectable. In such cases, the so-called “first peak” is more accurately described as a “sudden change point” in the rate of hydration rather than a peak because, from a numerical point of view, it is not the maximum value in a small range. After that, the hydration rate increases until it reaches the so-called “extra peak value”.

Upon analysing the variation of the “extra peak” phenomenon with GGBS content and temperature, it becomes evident why the “Time to reach peak” parameter in the tables of this section (Table 5.5) and Section 5.2 (Table 5.3) appears irregular. As the GGBS content increases and the temperature rises, the dominance of the first peak over the final peak; thus, the “Time to reach peak”, which is used to describe the time to reach the maximum hydration peak in the process, depends on whether this peak is the first or final.

The hydration heat development curves presented in this section reveal the effects of varying GGBS content on the hydration heat development of concrete at constant temperatures. It is evident that increasing the GGBS content in the concrete mix results in a reduction of both peak hydration heat flow and cumulative hydration heat. To more precisely observe the influence of GGBS content on hydration heat development at different temperatures, Table 5.5 summarize key hydration heat characteristics for samples with varying GGBS contents at constant temperatures. These characteristics include peak hydration heat, time to reach peak hydration, 1-day cumulative hydration heat, and 3-day cumulative hydration heat, outlining the trends of these critical hydration characteristics as a function of curing temperature variation.

Analysis of these hydration heat characteristics indicates that, for most concrete mixes, the peak hydration heat, 1-day cumulative hydration heat, and 3-day cumulative hydration heat decrease with increasing GGBS content (except the results at 50℃, which will be discussed later). This demonstrates a negative correlation between hydration heat development and GGBS substitution levels, further confirming the inhibitory effect of GGBS on hydration heat. Figure 5.33 to Figure 5.44 visually display this relationship using bar charts, illustrating the trends across different temperatures for all concrete mixes.

Table 5.6 summarizes the percentage changes in hydration heat characteristics when substituting 50% of CEM I with GGBS at different curing temperatures. The results indicate that, except for the hydration peak value at 30 °C, the reduction in hydration

heat characteristics due to GGBS substitution becomes less pronounced as temperature increases. At 20 °C, replacing 50% of CEM I with GGBS results in a 40% decrease in peak hydration heat flow and a 35.58% reduction in 3-day cumulative hydration heat (Figure 5.29). These reductions highlight the significant role of GGBS in mitigating hydration heat at lower curing temperatures. However, as the curing temperature increases, the influence of GGBS substitution diminishes. At 50 °C, the reduction in peak hydration heat flow due to 50% GGBS replacement is only 29.20%, and the 3-day cumulative hydration heat reduction is 15% (Figure 5.32), suggesting that the inhibitory effect of GGBS on cement hydration weakens as curing temperature rises.

Interestingly, at 30 °C, the peak hydration heat flow is reduced by only 14.71%, which deviates from the trend observed at other temperatures. This suggests that the effect of GGBS on hydration kinetics may not follow a strictly linear relationship with temperature. One possible explanation is that at this intermediate temperature, the activation of GGBS is still relatively moderate, whereas, at 40°C and beyond, the enhancement of GGBS reactivity due to temperature increase becomes more dominant. As temperature rises, the hydration kinetics of GGBS accelerate significantly, leading to a convergence of hydration heat between CEM-only and CEM-GGBS blended mixes. This trend can be attributed to the fact that GGBS is more temperature-sensitive than CEM I. At lower temperatures, GGBS hydration is limited by the availability of calcium hydroxide (CH) from CEM I hydration and by the slower dissolution of GGBS particles. The pozzolanic reaction of GGBS typically proceeds at a much lower rate than CEM I hydration at ambient temperatures. However, as temperature increases, the reaction rate of GGBS accelerates significantly, narrowing the gap in hydration heat between CEM-only and CEM-GGBS mixes. This suggests that, while GGBS effectively reduces hydration heat at lower temperatures, its influence diminishes at higher temperatures because the elevated temperature compensates for the otherwise slow pozzolanic reaction.

Additionally, the results highlight an important practical consideration: while high temperatures can accelerate the early hydration of GGBS-containing mixes, they may also reduce the long-term hydration benefits typically associated with GGBS. In conventional curing conditions, GGBS contributes to long-term strength development by undergoing gradual pozzolanic reactions over weeks or months. However, at elevated temperatures, the pozzolanic activity is triggered much earlier, potentially leading to a reduced long-term strength gain compared to GGBS mixes cured at lower temperatures. This finding underscores the need for careful temperature management in real-world applications to optimize both early-age and long-term performance.

In conclusion, the results indicate that GGBS substitution significantly reduces hydration heat, but the magnitude of this reduction decreases with increasing temperature. The enhanced reactivity of GGBS at higher temperatures diminishes its inhibitory effect on heat evolution, leading to a convergence in hydration heat between CEM-only and CEM-GGBS mixes. Therefore, temperature control is crucial in

practical applications to maximize the thermal benefits of GGBS while maintaining its long-term performance advantages.

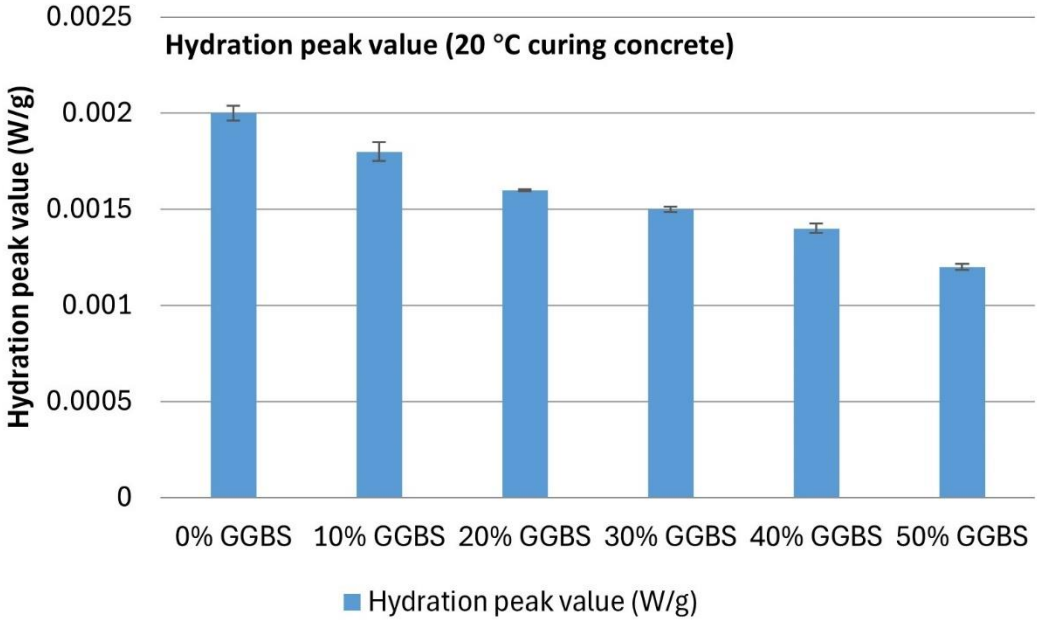

Figure 5.33. Variation of hydration peak value of 20 °C curing concrete with GGBS content.

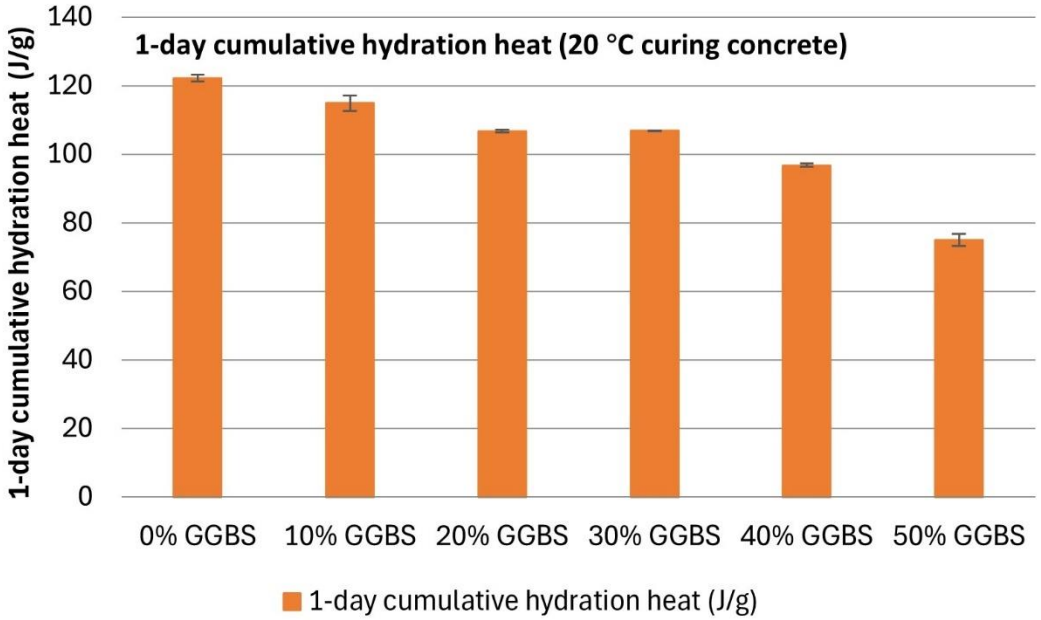

Figure 5.34. Variation of 1-day cumulative hydration heat of 20 °C curing concrete with GGBS content.

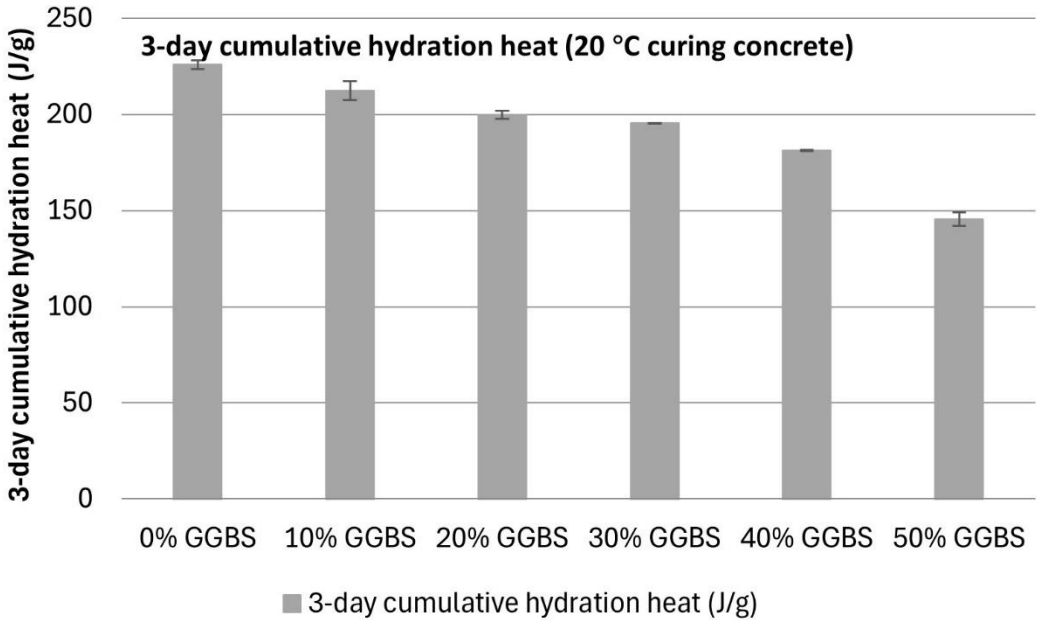

Figure 5.35. Variation of 3-day cumulative hydration heat of 20 °C curing concrete with GGBS content.

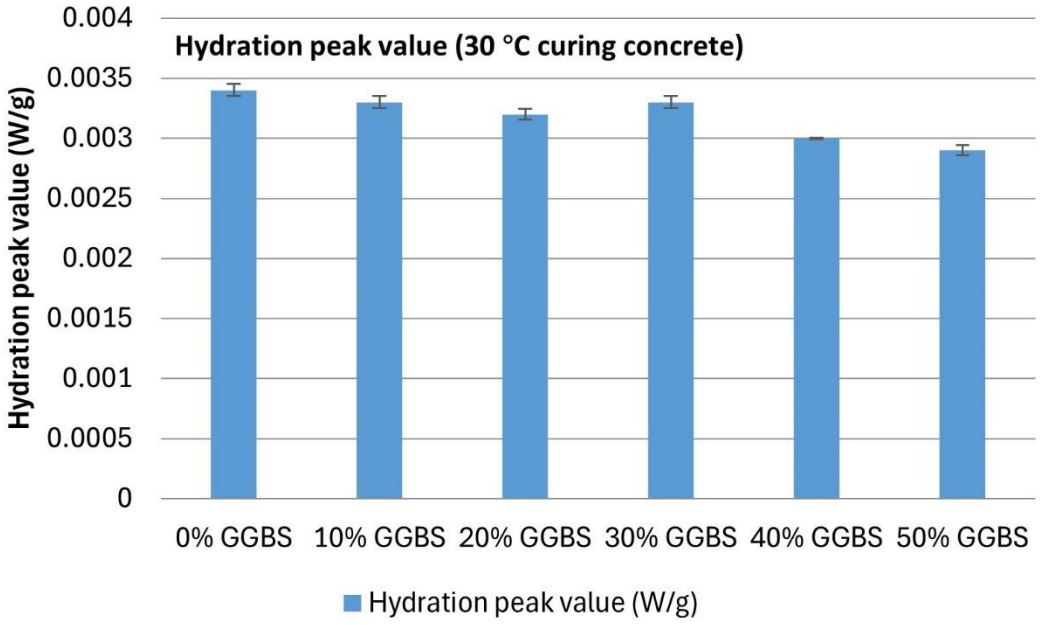

Figure 5.36. Variation of hydration peak value of 30 °C curing concrete with GGBS content.

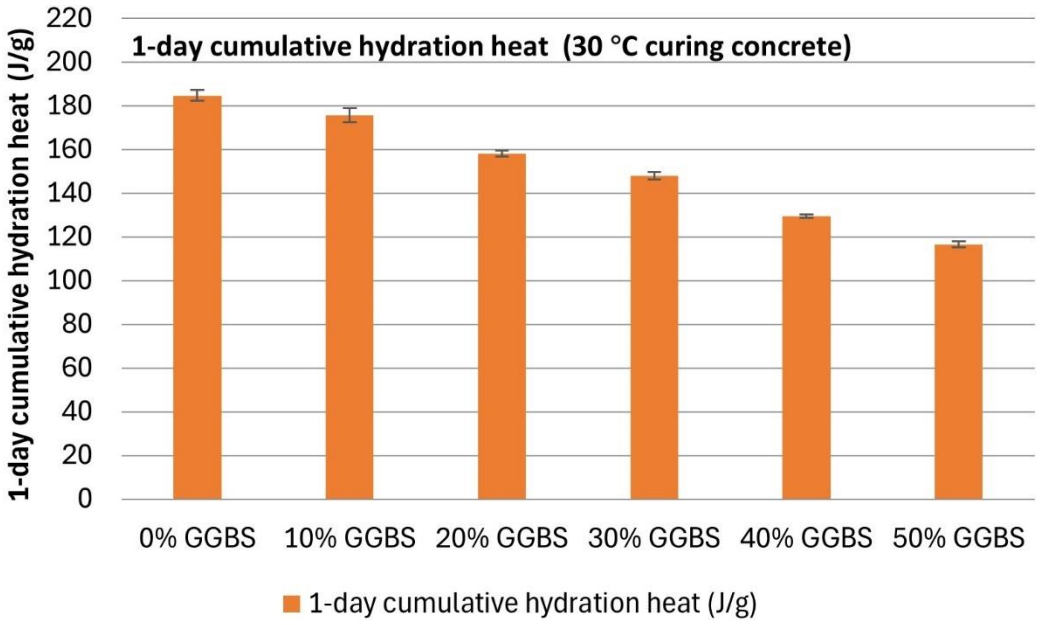

Figure 5.37. Variation of 1-day cumulative hydration heat of 30 °C curing concrete with GGBS content.

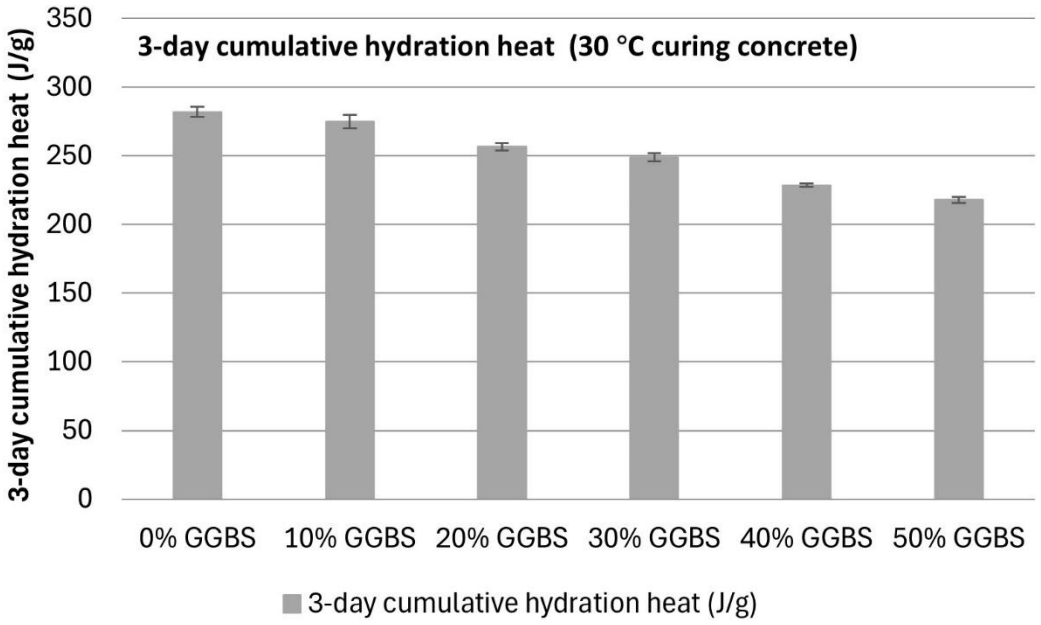

Figure 5.38. Variation of 3-day cumulative hydration heat of 30 °C curing concrete with GGBS content.

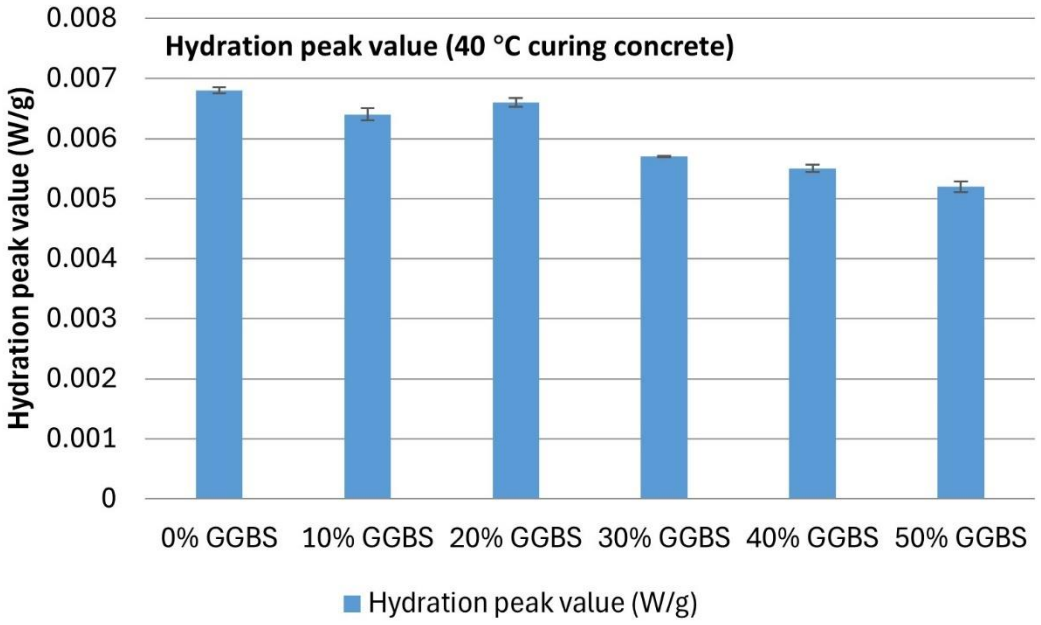

Figure 5.39. Variation of hydration peak value of 40 °C curing concrete with GGBS content.

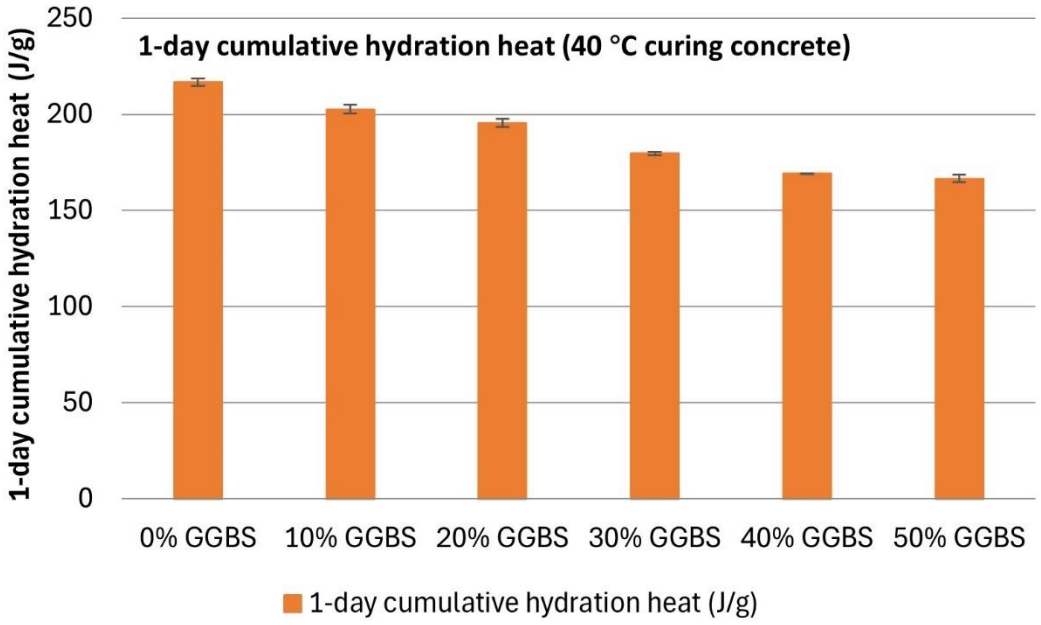

Figure 5.40. Variation of 1-day cumulative hydration heat of 40 °C curing concrete with GGBS content.

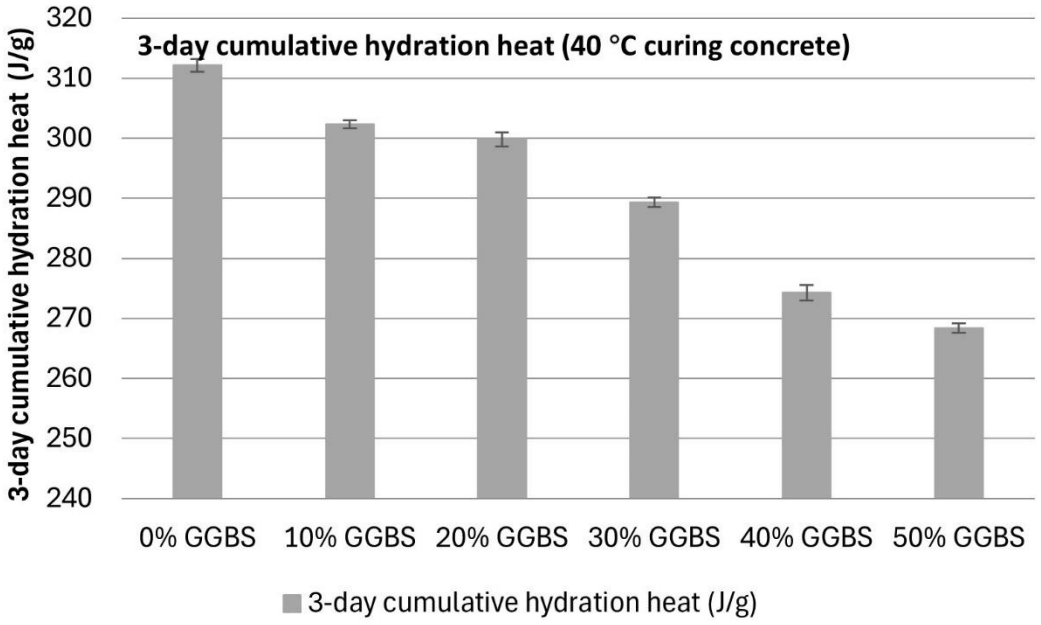

Figure 5.41. Variation of 3-day cumulative hydration heat of 40 °C curing concrete with GGBS content.

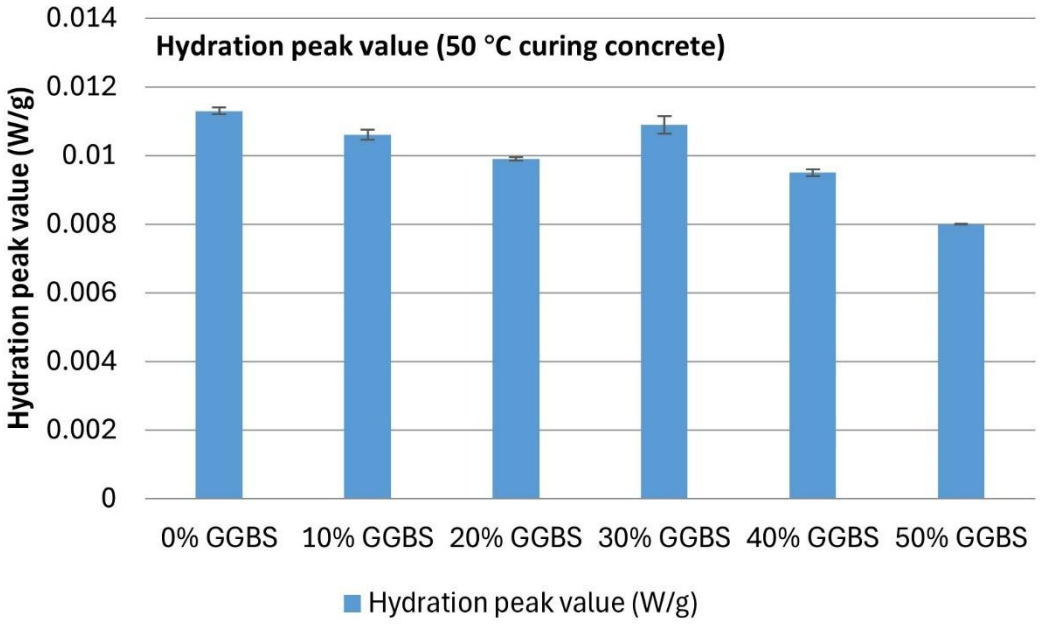

Figure 5.42. Variation of hydration peak value of 50 °C curing concrete with GGBS content.

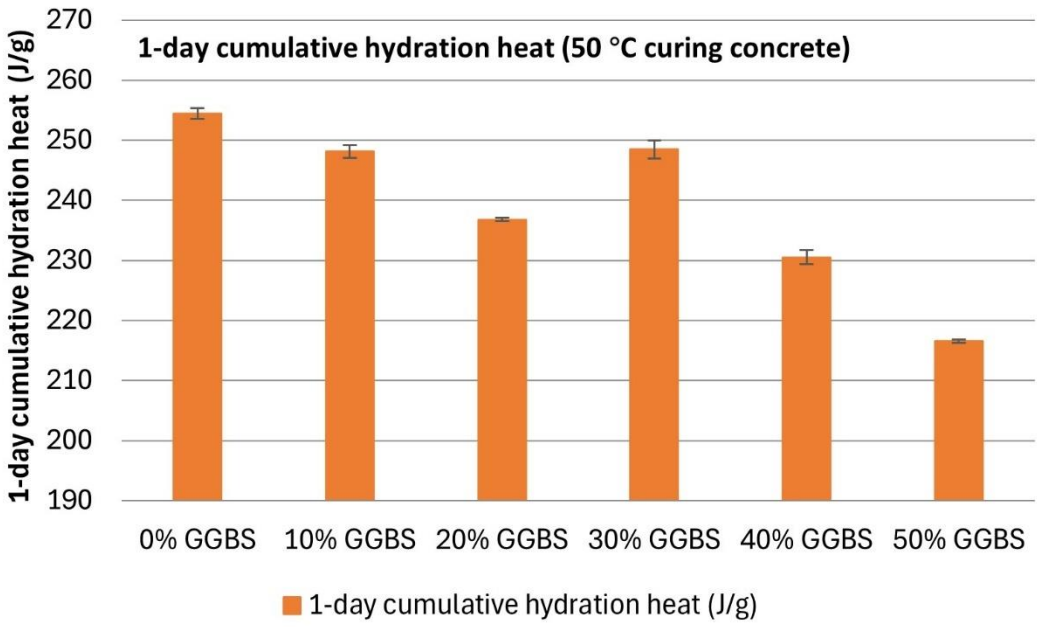

Figure 5.43. Variation of 1-day cumulative hydration heat of 50 °C curing concrete with GGBS content.

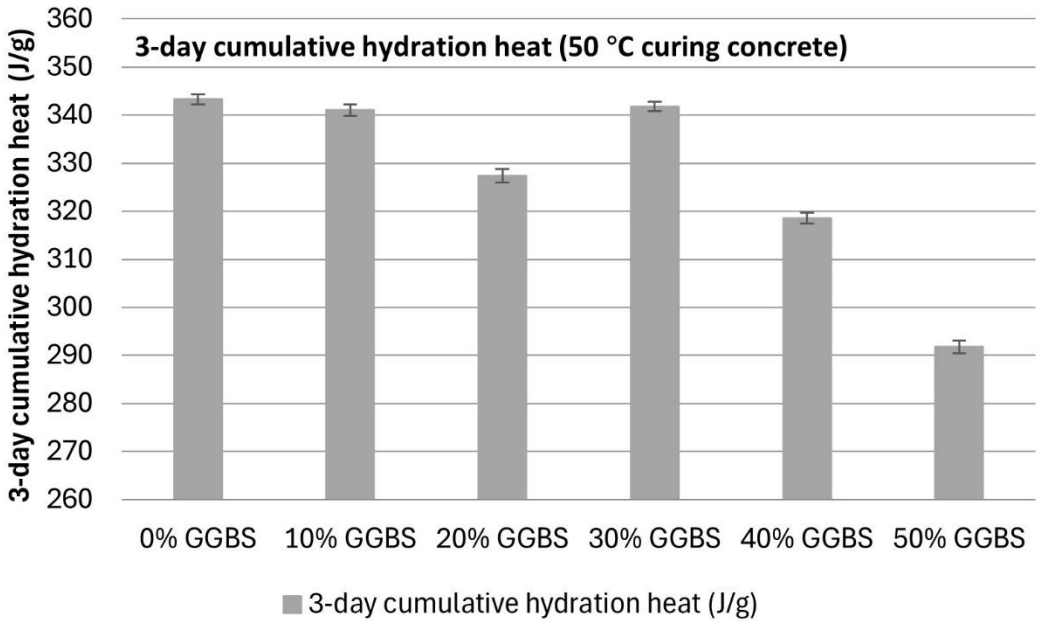

Figure 5.44. Variation of 3-day cumulative hydration heat of 50 °C curing concrete with GGBS content.

Table 5.6. Increasement of hydration heat characteristics when replace 50% CEM with GGBS.

Temperature	Hydration Peak Value Increase	1-Day Cumulative Hydration Heat Increase	3-Day Cumulative Hydration Heat Increase
20 °C	-40.00%	-38.64%	-35.58%
30 °C	-14.71%	-36.91%	-22.73%
40 °C	-23.53%	-23.21%	-14.02%
50 °C	-29.20%	-14.91%	-15.00%

In summary, this section investigates the influence of GGBS content on hydration heat development under different curing temperatures. The results indicate that increasing GGBS content leads to a reduction in peak hydration heat flow, a delayed hydration peak, and lower cumulative hydration heat, particularly at lower temperatures. The five-stage hydration process is significantly altered by GGBS replacement, with an extended induction period and the emergence of an "extra peak" in hydration heat flow. At lower temperatures (20 °C and 30 °C), GGBS has a pronounced inhibitory effect on hydration heat evolution, while at higher temperatures (40 °C and 50 °C), this effect diminishes as the reactivity of GGBS increases, leading to a convergence in hydration heat between CEM-only and CEM-GGBS mixes. The findings emphasize that while GGBS effectively mitigates early-age hydration heat, its influence is temperature-dependent, highlighting the need for careful temperature control in practical applications to optimize both early-age and long-term performance.

5.4 Influence of Coarse Aggregate on Hydration Heat

5.4.1 Introduction

In previous chapters of this study, a recurrent theme has been the limitations of conventional isothermal calorimetry equipment in accommodating coarse aggregates due to the restricted volume of their containers. This limitation led many researchers to use cement paste or mortar specimens as proxies for concrete in their hydration heat studies. A fundamental assumption of these studies is that the hydration heat development of a cement paste/mortar specimen with the same binder content and water-to-cement ratio is representative of that of concrete. However, this assumption has not been verified due to instrumental constraints, leading to contentious views in the research community.

This study employs a 3-channel TAM Air isothermal calorimeter. This calorimeter features containers with a capacity of 125 mL, which is sufficient to include the 10 mm coarse aggregates used in our concrete specimens. Each isothermal calorimetry test simultaneously measured micro-concrete samples and their equivalent mortar counterparts, allowing for a direct comparison of their hydration heat development. Tests were conducted at four different temperatures (20 °C, 30 °C, 40 °C, and 50 °C)

and with varying GGBS contents (0%, 10%, 20%, 30%, 40%, and 50%). The detailed material information and experimental procedures have been thoroughly described in Section 5.1.

Preliminary observations indicated that at 20 °C, the hydration heat flow and cumulative hydration heat of micro-concrete samples and equivalent mortar specimens were almost identical, hence their results will be detailed in APPENDIX A. For the remaining temperatures (30 °C, 40 °C, and 50 °C), a large part of results showed noticeable differences in cumulative hydration heat between the two types of samples, which will be showcased in this section. In addition to presenting the direct experimental outcomes, this section will delve deeper into the role of coarse aggregate in concrete hydration heat development by deriving key parameters such as apparent activation energy, equivalent age, hydration degree, and hydration parameters. These significant parameters in the hydration reaction will further elucidate the impact of coarse aggregate on the development of hydration heat in concrete.

5.4.2 Comparing Hydration Heat in Micro-Concrete and Mortar

The following figures (Figure 5.45 to Figure 5.62) show the heat of hydration development curves for micro-concrete and equivalent mortar samples with different GGBS contents at 30 °C, 40 °C and 50 °C:

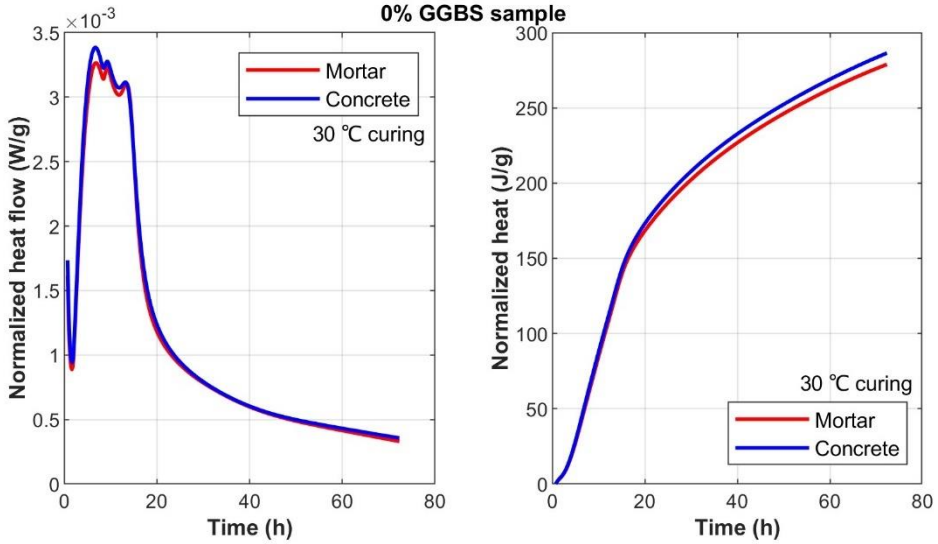

(a) (b)

Figure 5.45. Isothermal calorimetry for 0% GGBS sample at 30 °C: (a) normalized hydration heat flow; (b) normalized cumulative hydration heat.

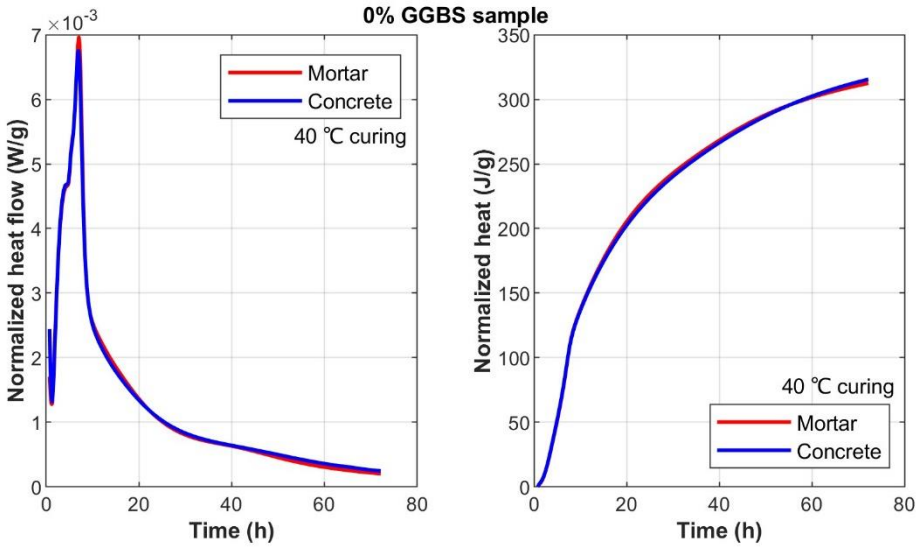

(a) (b)

Figure 5.46. Isothermal calorimetry for 0% GGBS sample at 40 °C: (a) normalized hydration heat flow; (b) normalized cumulative hydration heat.

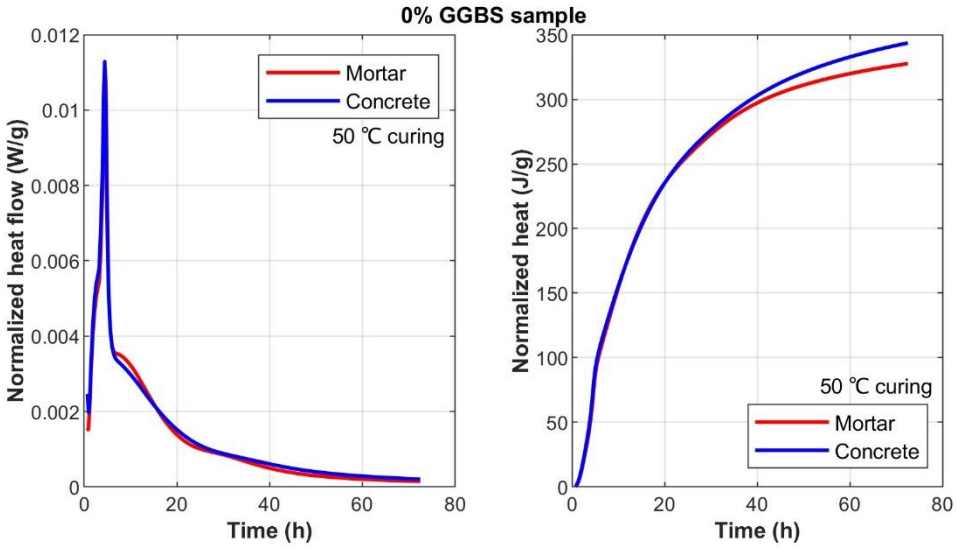

(a) (b)

Figure 5.47. Isothermal calorimetry for 0% GGBS sample at 50 °C: (a) normalized hydration heat flow; (b) normalized cumulative hydration heat.

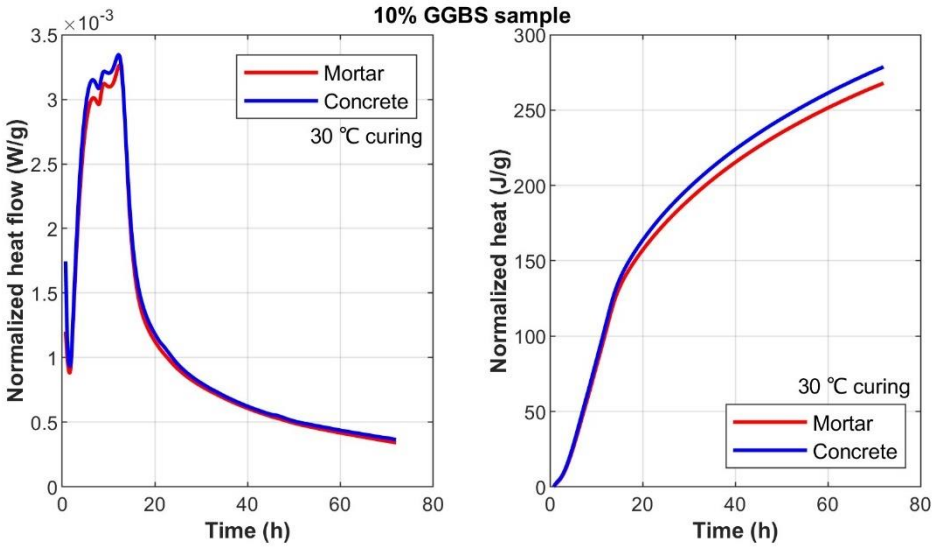

(a) (b)

Figure 5.48. Isothermal calorimetry for 10% GGBS sample at 30 °C: (a) normalized hydration heat flow; (b) normalized cumulative hydration heat.

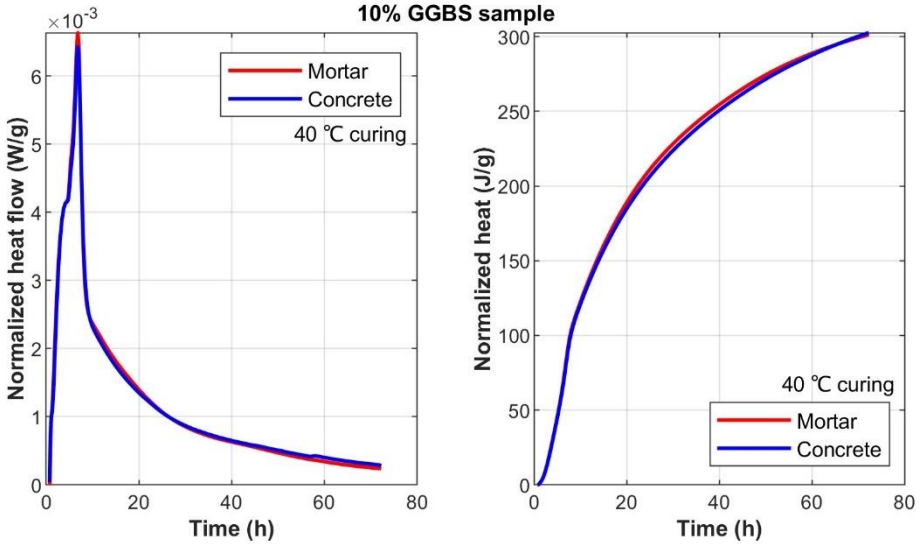

(a) (b)

Figure 5.49. Isothermal calorimetry for 10% GGBS sample at 40 °C: (a) normalized hydration heat flow; (b) normalized cumulative hydration heat.

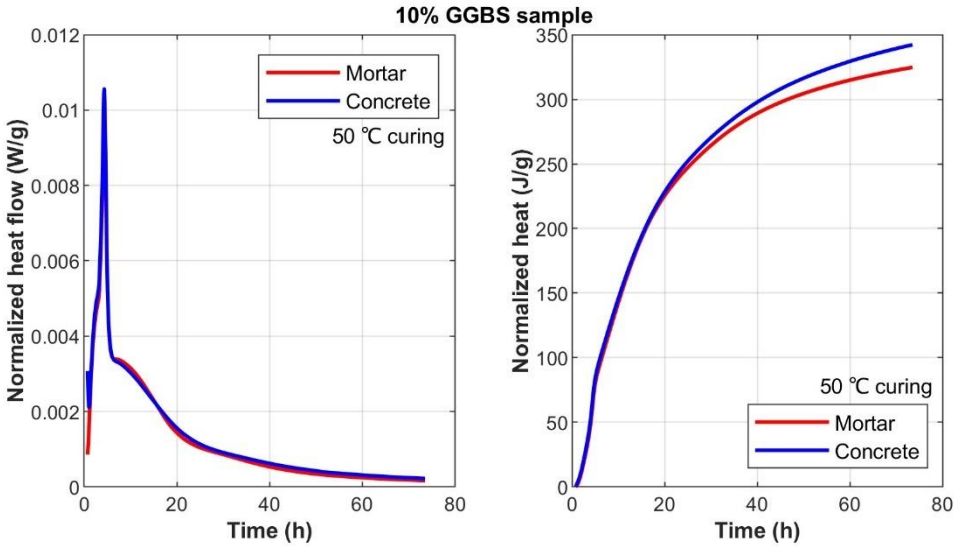

(a) (b)

Figure 5.50. Isothermal calorimetry for 10% GGBS sample at 50 °C: (a) normalized hydration heat flow; (b) normalized cumulative hydration heat.

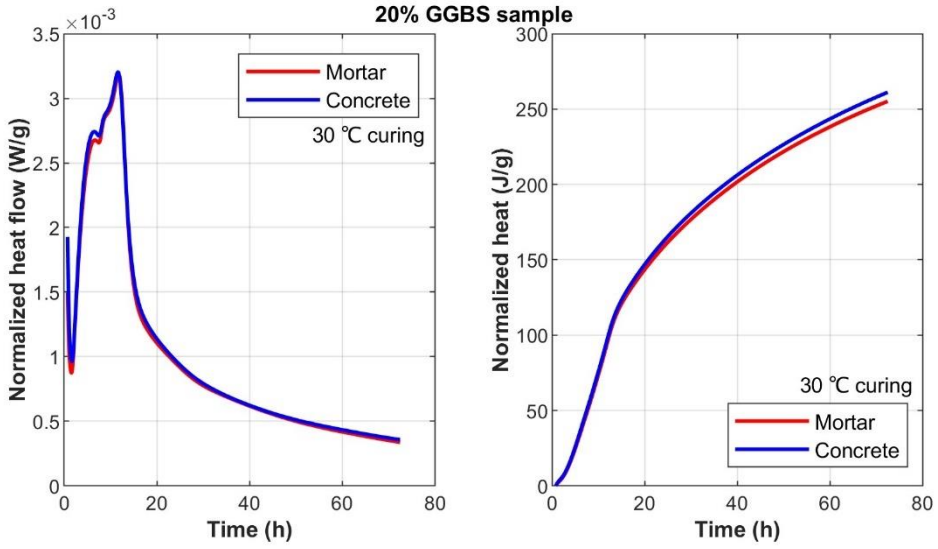

(a) (b)

Figure 5.51. Isothermal calorimetry for 20% GGBS sample at 30 °C: (a) normalized hydration heat flow; (b) normalized cumulative hydration heat.

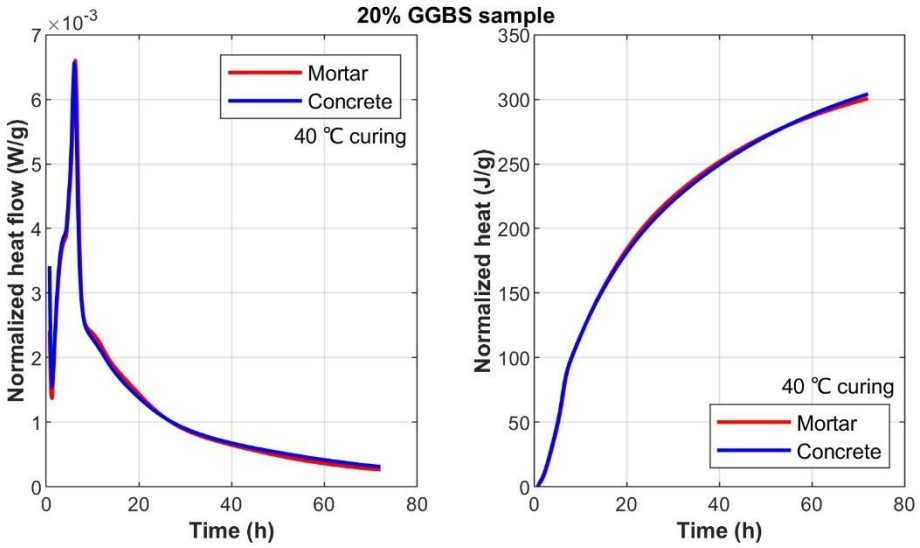

(a) (b)

Figure 5.52. Isothermal calorimetry for 20% GGBS sample at 40 °C: (a) normalized hydration heat flow; (b) normalized cumulative hydration heat.

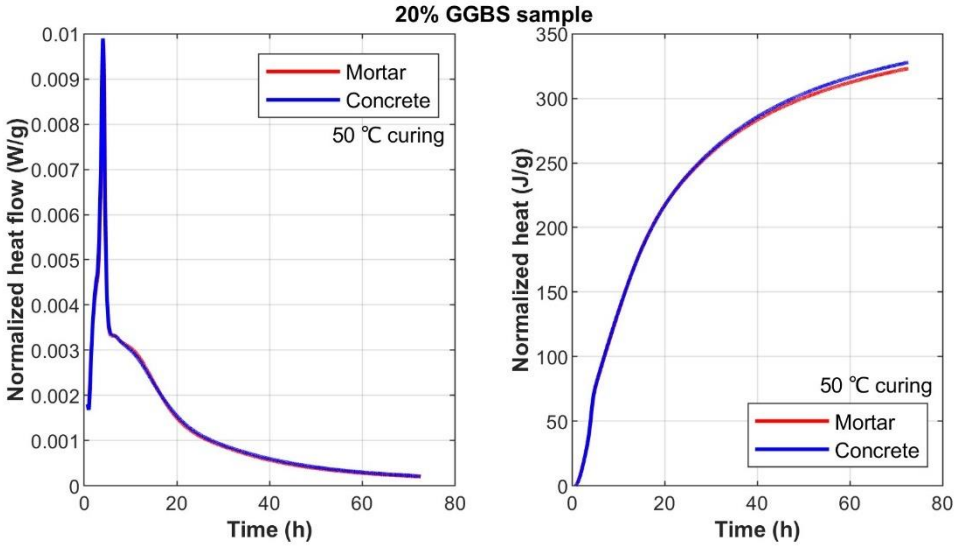

(a) (b)

Figure 5.53. Isothermal calorimetry for 20% GGBS sample at 50 °C: (a) normalized hydration heat flow; (b) normalized cumulative hydration heat.

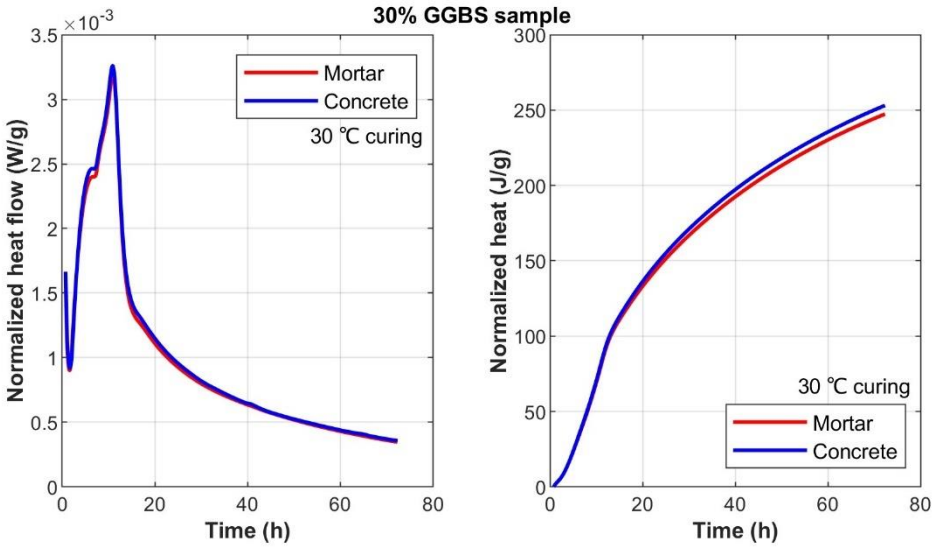

(a) (b)

Figure 5.54. Isothermal calorimetry for 30% GGBS sample at 30 °C: (a) normalized hydration heat flow; (b) normalized cumulative hydration heat.

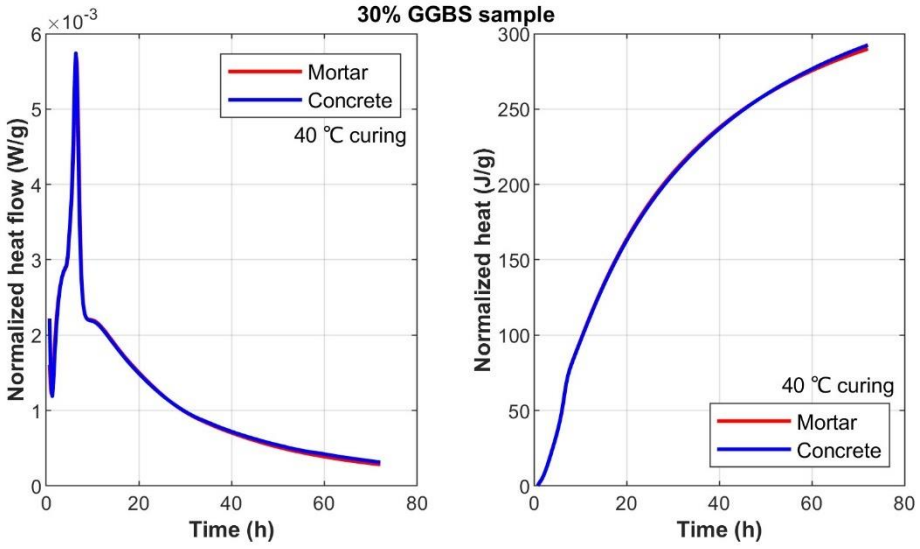

(a) (b)

Figure 5.55. Isothermal calorimetry for 30% GGBS sample at 40 °C: (a) normalized hydration heat flow; (b) normalized cumulative hydration heat.

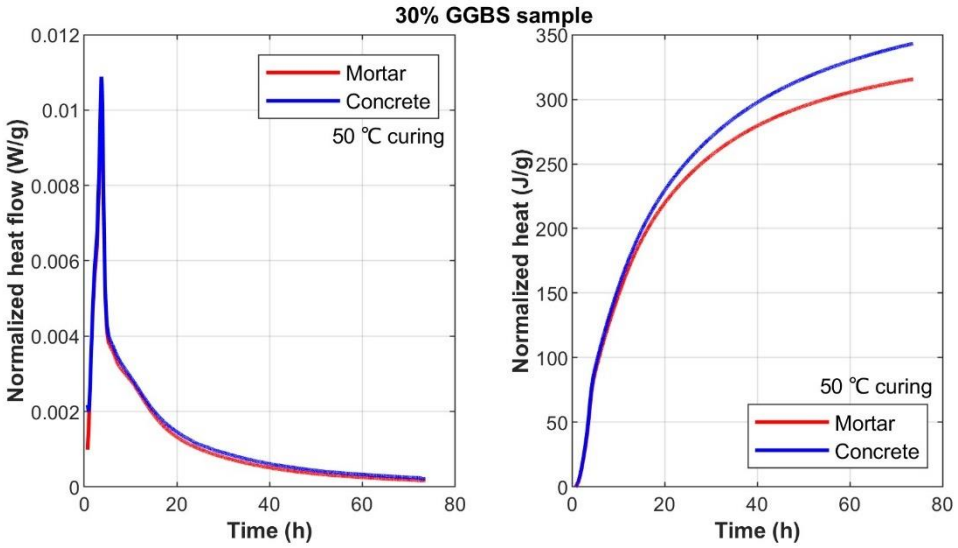

(a) (b)

Figure 5.56. Isothermal calorimetry for 30% GGBS sample at 50 °C: (a) normalized hydration heat flow; (b) normalized cumulative hydration heat.

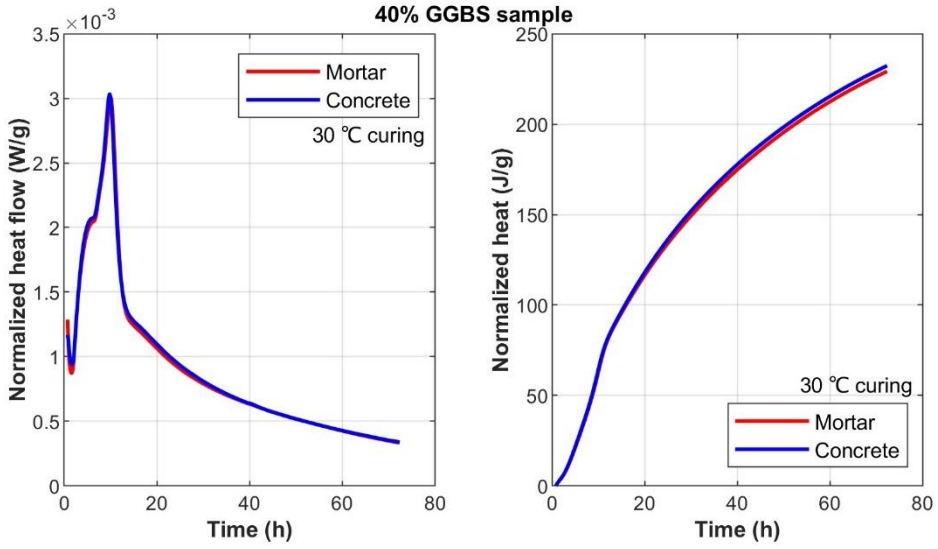

(a) (b)

Figure 5.57. Isothermal calorimetry for 40% GGBS sample at 30 °C: (a) normalized hydration heat flow; (b) normalized cumulative hydration heat.

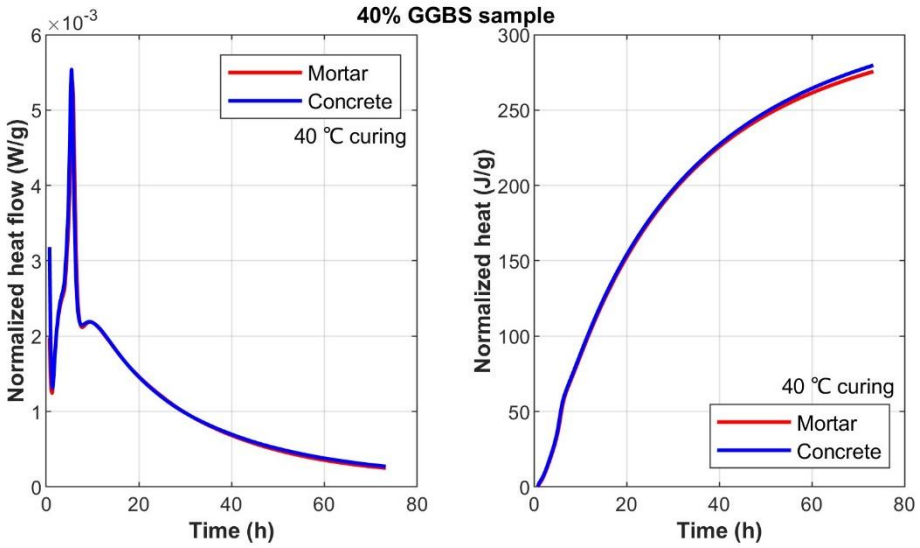

(a) (b)

Figure 5.58. Isothermal calorimetry for 40% GGBS sample at 40 °C: (a) normalized hydration heat flow; (b) normalized cumulative hydration heat.

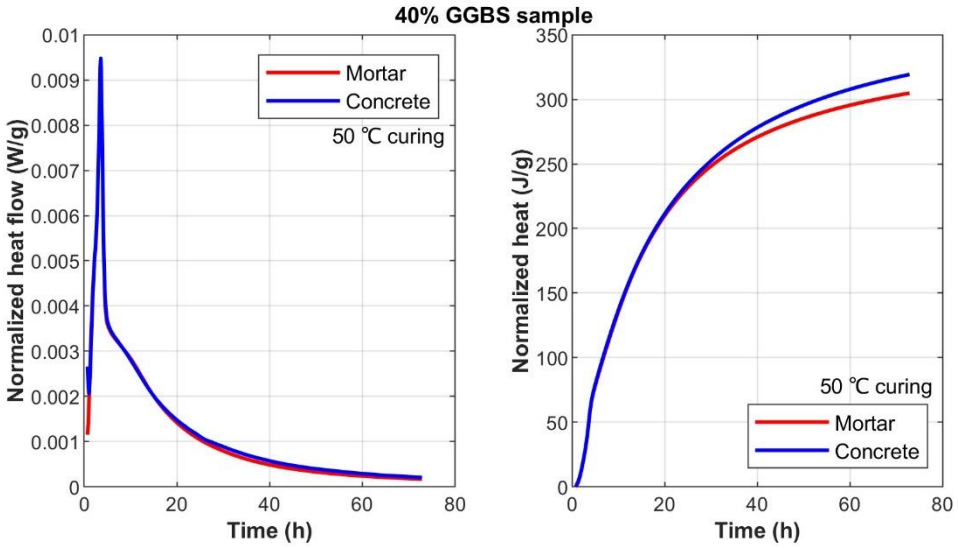

(a) (b)

Figure 5.59. Isothermal calorimetry for 40% GGBS sample at 50 °C: (a) normalized hydration heat flow; (b) normalized cumulative hydration heat.

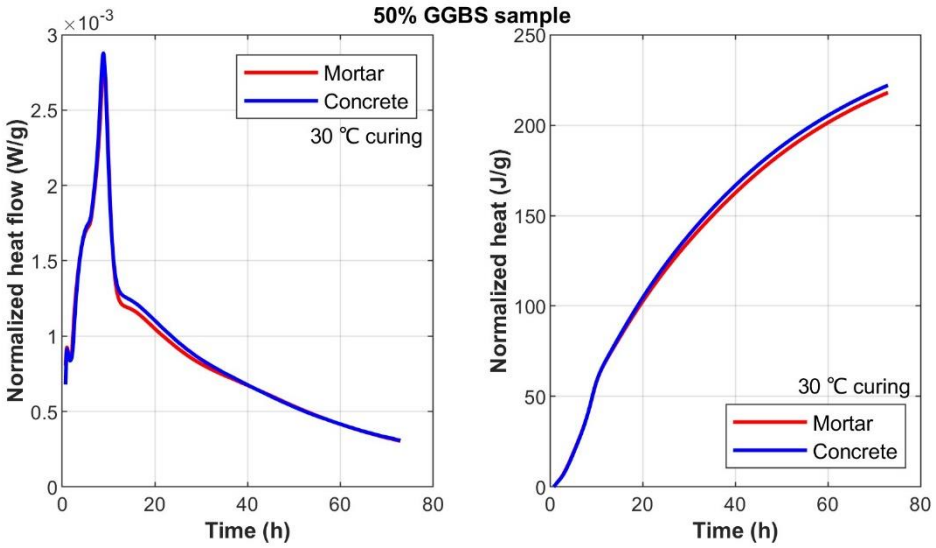

(a) (b)

Figure 5.60. Isothermal calorimetry for 50% GGBS sample at 30 °C: (a) normalized hydration heat flow; (b) normalized cumulative hydration heat.

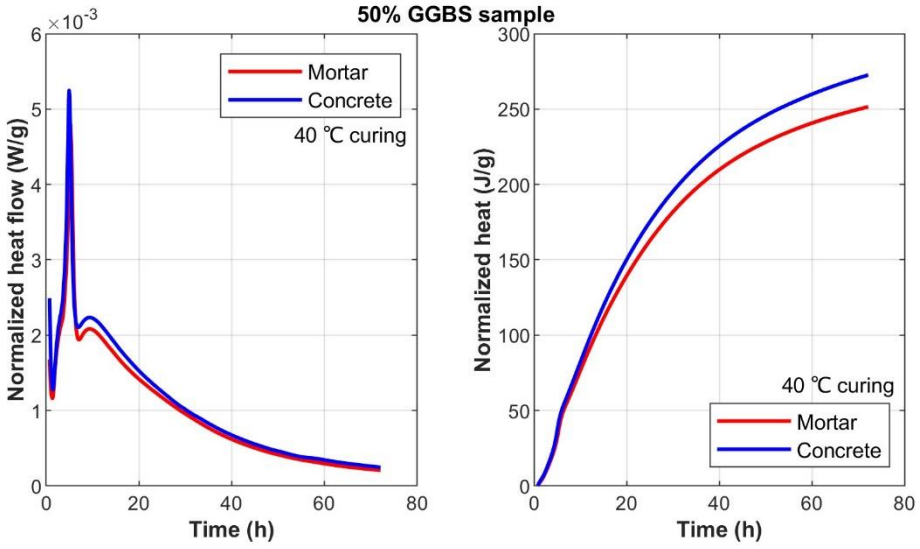

(a) (b)

Figure 5.61. Isothermal calorimetry for 50% GGBS sample at 40 °C: (a) normalized hydration heat flow; (b) normalized cumulative hydration heat.

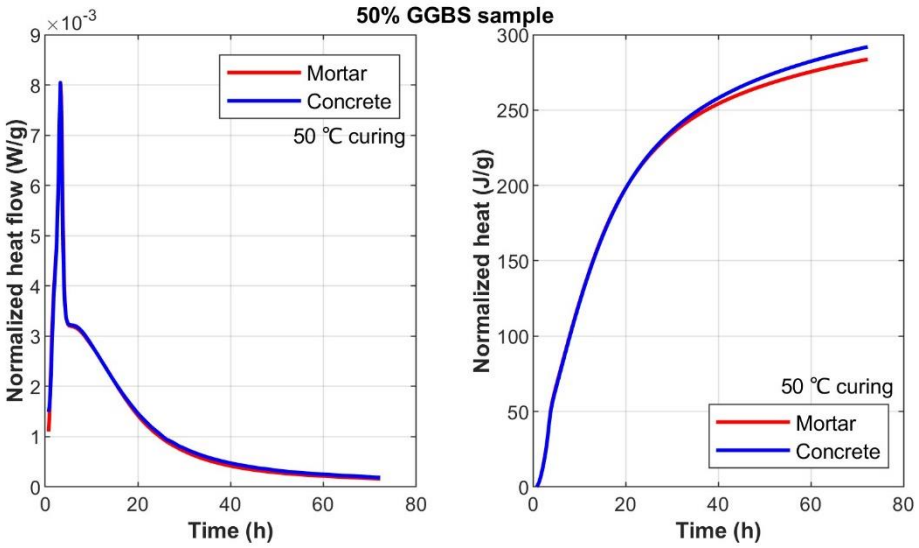

(a) (b)

Figure 5.62. Isothermal calorimetry for 50% GGBS sample at 50 °C: (a) normalized hydration heat flow; (b) normalized cumulative hydration heat.

Table 5.7. Normalized 3-day cumulative hydration heat

Sample information		Normalized 3-day cumulative hydration heat (J/g)			
GGBS content	Temperature	Mortar sample	Micro-concrete sample	Difference*	Difference in %
0% GGBS	30 °C	274.90	282.02	7.12	2.59%
	40 °C	310.03	312.12	2.09	0.67%
	50 °C	327.38	343.27	15.89	4.85%
10% GGBS	30 °C	264.80	274.94	10.14	3.83%
	40 °C	301.04	302.31	1.27	0.42%
	50 °C	323.78	341.02	17.24	5.32%
20% GGBS	30 °C	251.48	256.56	5.08	2.02%
	40 °C	297.49	299.79	2.30	0.77%
	50 °C	322.68	327.37	4.69	1.45%
30% GGBS	30 °C	243.58	248.99	5.41	2.22%
	40 °C	287.71	289.30	1.59	0.55%
	50 °C	314.60	341.78	27.18	8.64%
40% GGBS	30 °C	225.86	228.57	2.71	1.20%
	40 °C	271.74	274.30	2.56	0.94%
	50 °C	304.26	318.57	14.31	4.70%
50% GGBS	30 °C	213.86	217.88	4.02	1.88%
	40 °C	248.58	268.37	19.79	7.96%
	50 °C	283.54	291.77	8.23	2.90%

*: All differences in 3-day cumulative hydration heat values in this Table are Micro-concrete samples minus Mortar samples.

The analysis of a vast array of isothermal calorimetry test results (Figure 5.45 to Figure 5.62) across various temperatures and GGBS contents reveals a significant match in the hydration heat flow curves of micro-concrete and equivalent mortar samples. This high degree of similarity suggests a close parallel in the development of hydration heat between concrete and mortar specimens. However, the primary distinction in hydration heat development between micro-concrete and equivalent mortar samples is predominantly observed in their 3-day cumulative hydration heat values. While some mixes exhibit closely aligned values for both sample types, notable discrepancies in the 3-day cumulative hydration heat are observed in specific mixes, such as the 0% GGBS sample at 50 °C, 10% GGBS sample at 30 °C, 10% GGBS sample at 50 °C, 30% GGBS sample at 50 °C, 40% GGBS sample at 50 °C, and the 50% GGBS sample at 40 °C.

Before quantifying these observations, one clear trend can be discerned: for all micro-concrete samples at temperatures equal to or greater than 30 °C, the 3-day cumulative hydration heat is consistently higher than that of their corresponding equivalent mortar samples. This suggests that including coarse aggregate enhances the development of hydration heat, an effect that accumulates over time and becomes distinctly evident after three days. This phenomenon may be attributed to the solid coarse aggregate's higher thermal conductivity than the semi-fluid newly prepared mortar. Table 5.7 summarize the 3-day cumulative hydration heat data from the figures above, facilitating a comparative analysis of the hydration heat differences between the two sample types.

The "Difference" column in Table 5.7 represents the 3-day cumulative hydration heat disparity between the micro-concrete samples and their corresponding equivalent mortar samples for each mix. It is consistently observed that this value is positive, indicating that the 3-day cumulative hydration heat for micro-concrete samples is invariably higher than that for the equivalent mortar samples when the curing temperature is at or above 30°C. However, it must be acknowledged that the magnitude of the "Difference" does not exhibit a direct relationship with either the GGBS content or the temperature. One notable observation is that the more significant "Difference" for each GGBS content mix typically occur under higher temperature curing conditions (the maximum "Difference" for the 0%, 10%, 30%, and 40% GGBS mixes occur at 50°C, which the differences are 4.85%, 5.32%, 1.45%, 8.64%, 4.70% separately for these mixes. While for the 50% GGBS mix, it is at 40°C, which a 7.96% difference). This suggests that higher curing temperatures enhance the effect of coarse aggregate in promoting the development of hydration heat.

The largest "Difference" recorded in this study occurs in the 30% GGBS mix under 50°C curing, which has an 8.64% hydration heat difference, indicating that the promoting effect of coarse aggregate on the hydration reaction is independent of the GGBS content. However, considering the precision and sensitivity of the TAM Air isothermal calorimeter used in this study (with an accuracy of ±8μW for the heat flow sensor and ±0.02 °C for the thermostat), the lack of an explicit (linear) pattern in the

“Difference” values might be attributed to slight experimental variations (even though sample weighing was accurate to 0.01 g) and potential contaminants on the coarse aggregate.

The comparison between the hydration heat development in micro-concrete and equivalent mortar specimens reveals an overall similarity in hydration heat flow curves across different temperatures and GGBS contents. The hydration heat flow trends, presented in Figure 5.45 to Figure 5.62, exhibit a high degree of alignment between micro-concrete and mortar samples, indicating that the presence of coarse aggregate does not significantly alter the short-term hydration kinetics. This suggests that, at least during the initial hydration phases, coarse aggregates do not introduce substantial thermal resistance or significantly impact the rate of heat evolution in the system.

However, a key distinction emerges in the cumulative hydration heat values over three days. As shown in Table 5.7, for all micro-concrete samples at curing temperatures equal to or above 30 °C, the 3-day cumulative hydration heat is consistently higher than that of their corresponding mortar samples. This suggests that, while the hydration kinetics (as captured by the heat flow curves) are not significantly affected by coarse aggregate inclusion, the long-term heat release does exhibit noticeable differences.

A closer examination of the 3-day cumulative heat values reveals that the magnitude of this difference varies across mixes and temperatures. For instance, at 50 °C, the 0% GGBS mix exhibits a hydration heat difference of 4.85%, while the 10% and 40% GGBS mixes display differences of 5.32% and 4.70%, respectively. The largest recorded discrepancy is 8.64% for the 30% GGBS mix at 50 °C. While this might initially suggest that the presence of coarse aggregate enhances hydration heat development, it is crucial to recognize that these differences fall within a moderate range rather than representing a substantial deviation. The largest discrepancy of 8.64% does not necessarily indicate a fundamentally different hydration mechanism between micro-concrete and mortar; instead, it may be attributed to minor experimental variations within the precision range of the TAM Air isothermal calorimeter. The calorimeter's accuracy (±8μW for the heat flow sensor and ±0.02 °C for the thermostat) introduces a level of measurement uncertainty, which, along with potential sample mass variations (despite being controlled to ±0.01 g) and possible inconsistencies in mixing and compaction, could account for at least a portion of the observed differences.

While the hydration heat differences between micro-concrete and mortar samples are measurable, their underlying causes remain uncertain. Several possible explanations can be considered:

1. **Influence of Coarse Aggregate on Thermal Conductivity and Hydration Environment**
   One hypothesis is that the presence of coarse aggregates alters the thermal conductivity and heat distribution within the sample. Coarse aggregates

generally have a higher thermal conductivity than the surrounding cementitious paste, which might facilitate heat dissipation within the sample and lead to a more uniform hydration reaction. Additionally, the interfacial transition zone around the aggregates is known to have a different microstructure compared to the bulk paste, potentially leading to localized changes in porosity and hydration rates. These effects could result in subtle differences in heat evolution over extended hydration periods.

2. **Experimental Variability and Measurement Precision**
   Despite rigorous efforts to maintain consistency in sample preparation, minor variations in mixing, compaction, and initial temperature conditions could introduce slight differences in hydration heat measurements. Given that the observed differences do not exhibit a clear linear trend with either temperature or GGBS content, it is possible that at least part of the variation is due to measurement uncertainty rather than a systematic effect of coarse aggregates. The lack of a distinct trend across different GGBS contents and temperatures suggests that the hydration heat variations could be within the experimental margin of error.

3. **Higher Curing Temperatures and Heat Evolution Trends**
   One notable trend in Table 5.7 is that the largest hydration heat differences occur at higher temperatures, particularly at 50 °C. This could be due to the overall acceleration of hydration kinetics at elevated temperatures, making any minor differences in sample conditions more pronounced. However, the lack of a consistent correlation between temperature and the magnitude of the difference (e.g., the 50% GGBS mix shows its highest discrepancy at 40 °C instead of 50 °C) suggests that additional microstructural analyses may be needed to determine whether these variations are driven by hydration mechanisms or simply experimental variability.

To further investigate whether the presence of coarse aggregate influences hydration behaviour beyond what is captured by calorimetry, additional microstructural characterization techniques such as X-ray diffraction (XRD) and Thermogravimetric analysis (TGA) could be employed.

X-ray diffraction (XRD) could be used to analyse hydration product formation, particularly in the interfacial transition zone where coarse aggregate interfaces with the surrounding cement paste. This could help determine whether there are differences in phase composition, such as variations in portlandite (CH) crystallinity or C-S-H gel formation, which might contribute to the observed differences in cumulative hydration heat.

Thermogravimetric analysis (TGA) could provide a quantitative assessment of hydration degree by measuring bound water content and chemically combined phases

over time. If the micro-concrete samples exhibit higher degrees of hydration compared to equivalent mortar specimens, this could confirm that coarse aggregates influence hydration beyond just heat evolution.

These techniques would allow for a more detailed examination of hydration kinetics and phase development in micro-concrete versus mortar, helping to clarify whether hydration heat differences observed in calorimetry tests are associated with genuine microstructural differences or are simply artifacts of experimental variation. Additionally, performing replicate calorimetry tests under the same conditions could help assess the reproducibility of these differences. If similar trends persist across multiple repetitions, it would strengthen the argument that coarse aggregates exert a measurable influence on hydration heat development. Conversely, if variability is high across replicates, it would suggest that the differences are more likely due to random experimental fluctuations rather than a fundamental effect of coarse aggregate.

From a practical perspective, these findings suggest that using mortar specimens as a proxy for concrete in hydration heat studies remains a reasonable approximation, particularly when focusing on short-term hydration kinetics. However, the slight but consistent differences in cumulative heat at higher temperatures indicate that, for long-term hydration evolution predictions and thermal modelling in mass concrete applications, the inclusion of coarse aggregates should be considered. While mortar-based calorimetry can effectively capture early hydration behaviour, the potential thermal effects of coarse aggregates may become more relevant in larger-scale structures where temperature gradients and internal heat accumulation can lead to differential hydration rates.

Additionally, the role of coarse aggregates in modifying the hydration environment of GGBS-blended concrete remains an open question. If future XRD and TGA analyses reveal differences in hydration product formation, this could influence the optimization of concrete mix designs, particularly in high temperature curing conditions. These findings highlight the necessity for further research integrating microstructural characterization alongside calorimetric analysis to fully elucidate the impact of coarse aggregates on concrete hydration.

5.4.3 Determination of Apparent Activation Energy

The apparent activation energy (E_a) of a sample's hydration reaction is a pivotal parameter within the context of hydration processes, denoting the minimal energy required to initiate the reaction and indicating the sample's sensitivity to temperature changes. Detailed insights into E_a have already been discussed in Section 2.5.3. A higher E_a value indicates that the hydration reaction rate is more dependent on temperature, meaning that small temperature changes can significantly alter the rate of cementitious phase transformations. This section will deduce E_a from the outcomes of isothermal calorimetry tests. A fundamental assumption of this study is that the value

of the E_a is solely dependent on the material composition of the sample and independent of the curing temperature. This assumption is vital for deriving the E_a through isothermal calorimetry tests, as the procedure involves linear fitting of the maximum rate of hydration at different temperatures for the same mix of samples, producing a fixed value for that mix. Consequently, temperature, being a variable in the fitting process, cannot be considered an influencing factor on the E_a itself (for a detailed derivation process, refer to Section 2.5.3.3). Ultimately, E_a can be formulated as a linear equation incorporating the maximum hydration rate at a specified temperature and the temperature itself, as shown in Eq. (2.30). For ease of discussion, this section lists this formula again in Eq. (5.5). By conducting isothermal calorimetry experiments at a minimum of two temperatures (four temperatures in this study), the negative slope of the linear regression curve between $\ln(Q_{peak})$ and $1/T_{abs}$ directly corresponds to the value of E_a/R.

This section aims to utilize the derived values of E_a to assess the influence of coarse aggregate on the hydration reaction. Additionally, the values of E_a will serve as critical parameters in subsequent FEM models for predicting concrete temperature development. Furthermore, this section intends to evaluate the impact GGBS on the hydration process through the derived values of E_a, thereby providing the results of how material composition, including the presence of coarse aggregate and GGBS, influences the concrete's hydration reactions and temperature sensitivity.

$$\ln(Q_{peak}) = -\frac{E_a}{RT} + lnA \tag{5.5}$$

where Q_{peak} is the hydration heat flow peak value of a sample at a temperature (W/g), E_a is the apparent activation energy (J/mol), R is the universal gas constant = 8.314 (J/Kmol), T is the temperature (K), and A is a constant of proportionality.

The E_a values for micro-concrete and equivalent mortar samples with varying GGBS contents were obtained through linear regression analysis. Given that all samples' R-squared values exceeded 0.98, indicating high reliability in the fitting equations, detailed fitting curve graphs will not be presented within this section but in APPENDIX B. Instead, all results have been summarized in Table 5.8. The R-squared values of these liner regression analysis between $\ln(Q_{peak})$ and $1/T_{abs}$ are also been summarized in Table 5.8.

The results of E_a values from Table 5.8 reveals that for the majority of the mixes, the E_a values for micro-concrete samples are higher than those for the corresponding equivalent mortar samples, except the 0% and 20% GGBS mixes where the micro-concrete samples exhibit E_a values slightly lower by 54.87 and 420.69 J/mol (-0.12% and -0.86%), respectively. In the other four mixes, the smallest difference (micro-concrete minus equivalent mortar) is 692.64 J/mol (1.43%) for 40% GGBS mix, and the largest is 1270.38 J/mol (2.62%) for 50% GGBS mix. This suggests that, for most

mixes, the temperature sensitivity of concrete is higher than that of the equivalent mortar, meaning that with temperature increases, the rate of cement hydration heat release accelerates more rapidly, leading to greater heat liberation. This conclusion further corroborates the findings from Section 5.4.2 and Table 5.7, which indicated that the more significant "Differences" for each GGBS content mix typically occur under higher temperature curing conditions.

This trend suggests that coarse aggregates may influence hydration kinetics, but the mechanism is not entirely straightforward. Two possible explanations for this phenomenon include:

1. Influence of Thermal Conductivity on Hydration Environment
Coarse aggregates have a higher thermal conductivity than the cement matrix, which could facilitate localized heat transfer and dissipation. This effect may lead to a more uniform temperature distribution within the sample, slightly altering the rate of reaction initiation and shifting the measured E_a value.

2. Interfacial Transition Zone (ITZ) Effects
The ITZ between aggregates and paste exhibits different microstructural properties compared to bulk-paste, including higher porosity, increased CH content, and variations in ion diffusion rates. These factors could affect the local reaction environment, particularly regarding GGBS activation, which is highly dependent on CH availability.

It is important to note that despite the percentage difference in E_a between concrete and mortar samples being very small (as shown in the "Difference in %" column of Table 5.8), this is primarily due to the large absolute values of E_a, which often exceed 45000 J/mol. The maximum absolute difference observed was only 1270.38 J/mol, resulting in a minimal percentage difference. Given that the observed differences in E_a are small (below 3%), further experimental verification using microstructural analysis techniques such as XRD and TGA could help determine whether these differences are due to genuine changes in hydration kinetics or simply experimental variability. However, subsequent finite element simulations in this study have demonstrated that models based on mortar hydration heat exhibit significantly lower accuracy compared to those based on concrete (as will be discussed in detail in Chapter 6). This finding indicates that even small differences in E_a can lead to substantial errors in predicting concrete temperatures.

Additionally, the results in Table 5.8 also elucidate the effect of GGBS addition on Ea. Regardless of the sample type (micro-concrete or equivalent mortar), despite numerical differences, the trend of E_a variation with GGBS content remains consistent. Starting from 0% GGBS, E_a increases with the addition of GGBS until it peaks at the 30% GGBS mix, after which it begins to decrease slowly. However, the E_a values for 40% and 50% GGBS mixes remain higher than those for 0% and 10% GGBS mixes (in micro-concrete, the E_a values for 40% and 50% GGBS concrete are also higher than

that of 20% GGBS concrete). Two key conclusions can be drawn from these observations: 1) A 30% GGBS content appears to be a specific "threshold" at which the E_a value of the samples peaks, making the mix more sensitive to higher temperatures. This further explains why, in Section 5.3, the three hydration heat characteristic parameters of 30% GGBS concrete at 50°C are higher than those of 10% and 20% GGBS concrete. 2) Substituting a part of CEM I with GGBS increases the E_a value, suggesting that GGBS exhibits higher temperature sensitivity than CEM I. This reinforces the conclusions from Sections 5.2 and 5.3. However, the relationship between E_a values and GGBS content is not directly proportional. Instead, it increases with GGBS content up to a certain "threshold" before gradually decreasing, yet not falling below the E_a values for mixes without GGBS or with lower GGBS content.

Table 5.8. Apparent activation energy (E_a) calculated by linearly data fitting.

Sample information	Apparent activation energy (J/mol)				R-squared value of data fitting	
	Mortar sample	Micro-concrete sample	Difference*	Difference in %	Mortar sample	Micro-concrete sample
0% GGBS	46328.10	46273.23	-54.87	-0.12%	0.9904	0.9959
10% GGBS	45952.31	46841.91	889.60	1.94%	0.9945	0.9986
20% GGBS	48751.63	48330.94	-420.69	-0.86%	0.9902	0.9922
30% GGBS	49850.74	50765.28	914.54	1.83%	0.9988	0.9983
40% GGBS	48562.82	49255.46	692.64	1.43%	0.9983	0.9979
50% GGBS	48554.59	49824.97	1270.38	2.62%	0.9912	0.9837

*: All differences in E_a values in this Table are Micro-concrete samples minus Mortar samples.

5.4.4 Equivalent Age and Hydration Degree Analysis

Concrete maturity and its applications have been thoroughly discussed in Sections 2.5.1 and 2.5.2, where the notion of equivalent age maturity (t_e), based on the Arrhenius equation, is extensively applied in concrete technology. Equivalent age (t_e) refers to the time required for a concrete mix to attain a maturity index at a designated reference temperature analogous to that achieved under different curing temperatures. This concept is instrumental in assessing the impact of temperature on the development of concrete's strength, hydration heat, and degree of hydration and further aids in predicting concrete temperature and strength. The equivalent age based on the Arrhenius equation is expressed through Eq. (2.12), with 20 °C as the reference temperature in this study. It is restated here as Eq. (5.6) for ease of reference. Under the same mix conditions, a larger t_e for a sample at a given cumulative hydration heat indicates a longer time required to reach that cumulative hydration heat at the reference temperature.

$$t_e = \sum e^{\frac{E_a}{R}\left(\frac{1}{T_r}-\frac{1}{T}\right)} \cdot \Delta t \tag{5.6}$$

where t_e is the equivalent age (h), Δt is the curing time interval (h), T is the sample temperature (K), and T_r is the reference temperature, take 294.15 K (20 °C) in this study.

The concept of the degree of hydration (α) was elaborated in Section 2.5.5, typically defined through the hydration heat of concrete, i.e., the ratio of the heat released by concrete to its ultimate hydration heat (as shown in Eq. (5.7)). Thus, for the same mix, the evolution of a sample's α over time is essentially equivalent to its cumulative hydration heat. The maximum value of α is 1 (almost never reached), allowing for an evaluation of the extent of hydration reaction under certain conditions through the difference between the degree of hydration at the end of the test and 1.

$$\alpha(t) = \frac{H\ (t)}{H_u} \tag{5.7}$$

where α(t) is the hydration degree at time t, H(t) is the cumulative hydration at time t (J/g), H_u is the ultimate heat of hydration of the sample (J/g).

Because the evolution of the degree of hydration α yields conclusions similar to those of cumulative hydration heat, this section will present the development of the degree of hydration α over the equivalent age t_e for samples with varying GGBS contents under different curing temperatures. This study uses 20 °C as the reference temperature, it is possible not only to calculate the equivalent duration at 20 °C for samples cured at other temperatures for three days but also to observe the degree of hydration α achieved by the samples at the end of three days. This section will also juxtapose the micro-concrete samples and their corresponding equivalent mortar samples in the same graph to evaluate the effect of coarse aggregate inclusion on the equivalent age and degree of hydration. Since 20 °C serves as the reference temperature, the evolution of the degree of hydration α at 20 °C over the equivalent age t_e essentially corresponds to its real-time development; thus, only the development curves of the degree of hydration α over the equivalent age t_e at 30 °C, 40 °C, and 50 °C will be presented in this section.

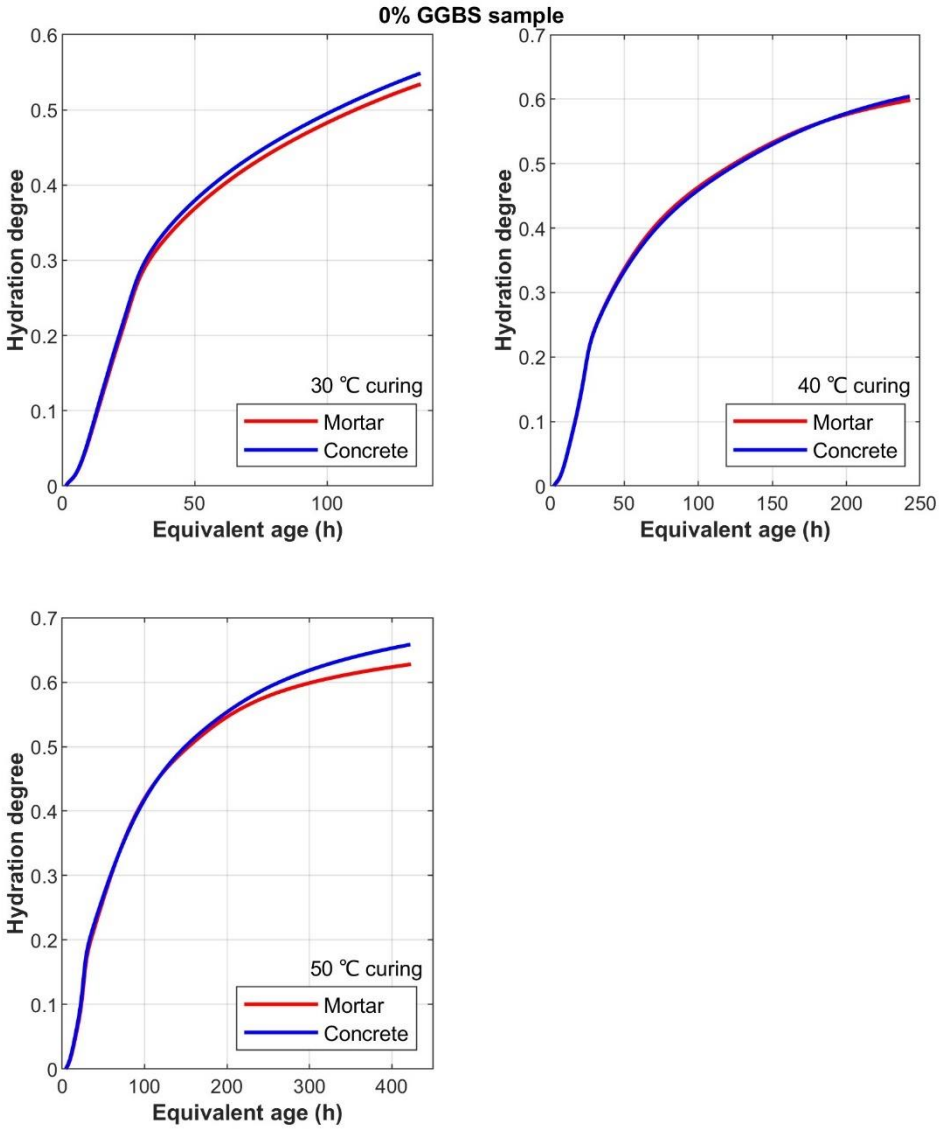

Figure 5.63. Hydration degree development of 0% GGBS sample at 30 °C, 40 °C, 50 °C.

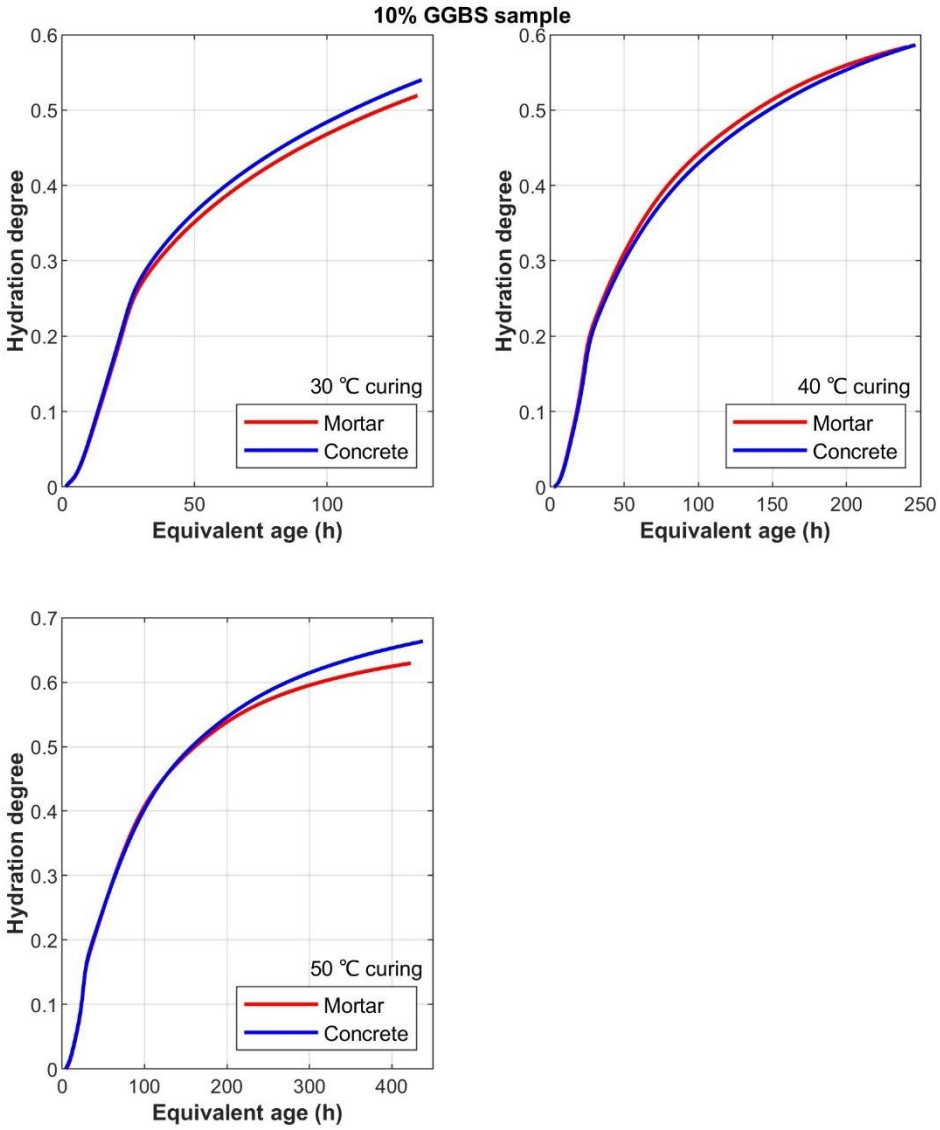

Figure 5.64. Hydration degree development of 10% GGBS sample at 30 °C, 40 °C, 50 °C.

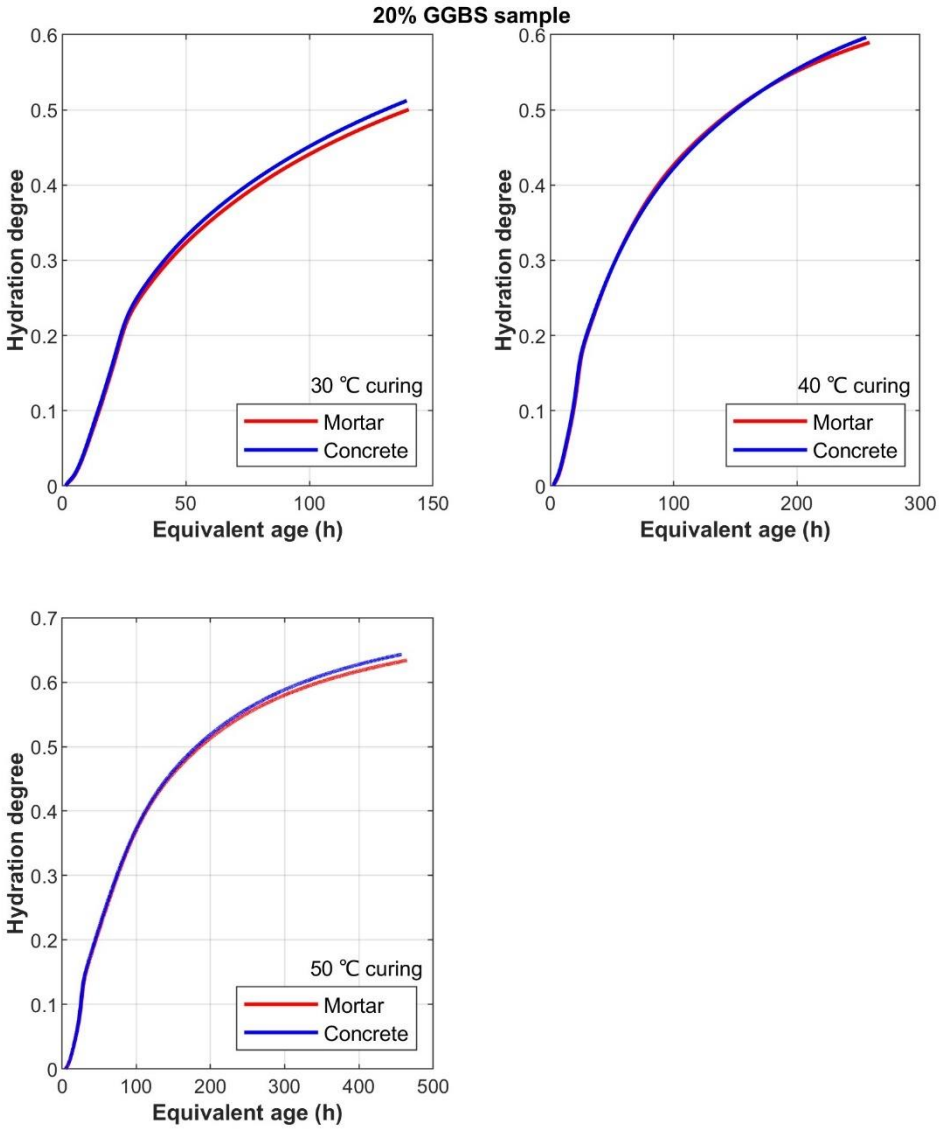

Figure 5.65. Hydration degree development of 20% GGBS sample at 30 °C, 40 °C, 50 °C.

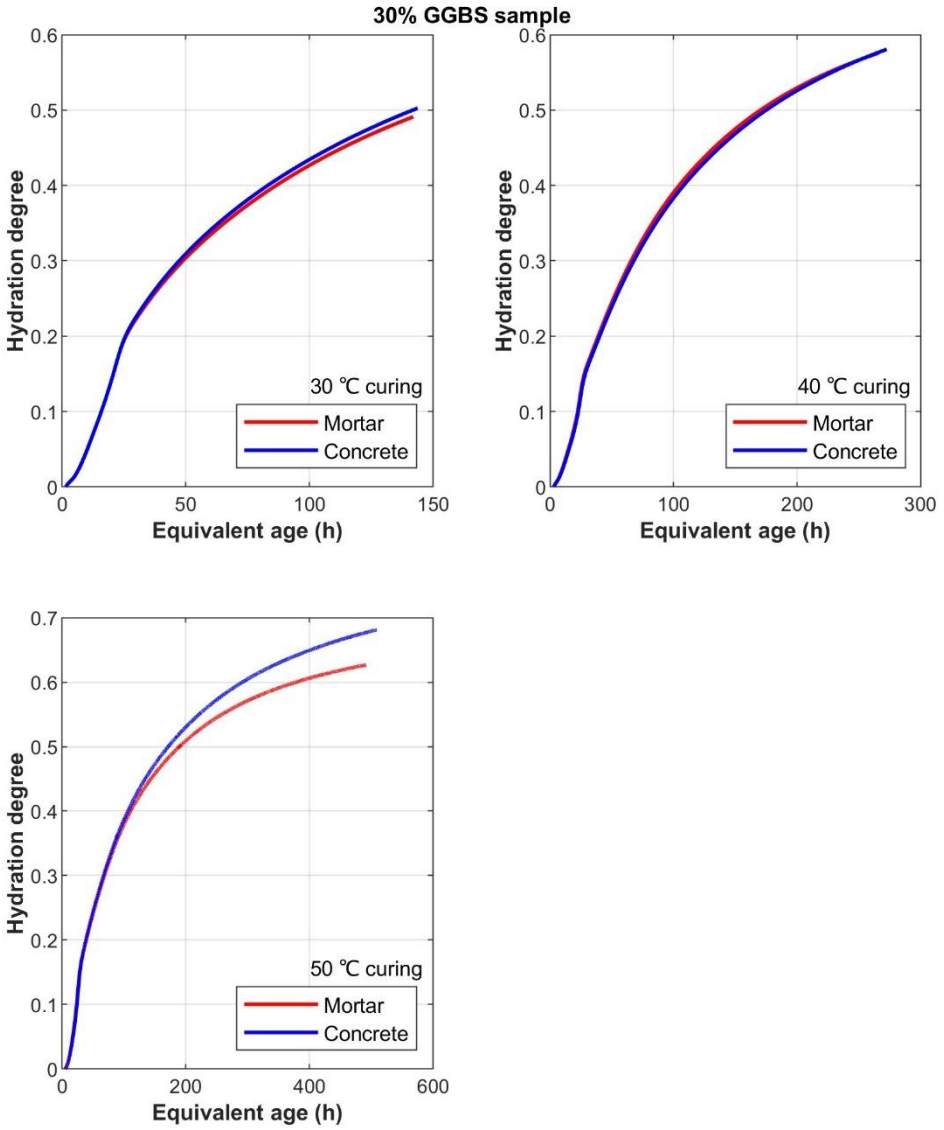

Figure 5.66. Hydration degree development of 30% GGBS sample at 30 °C, 40 °C, 50 °C.

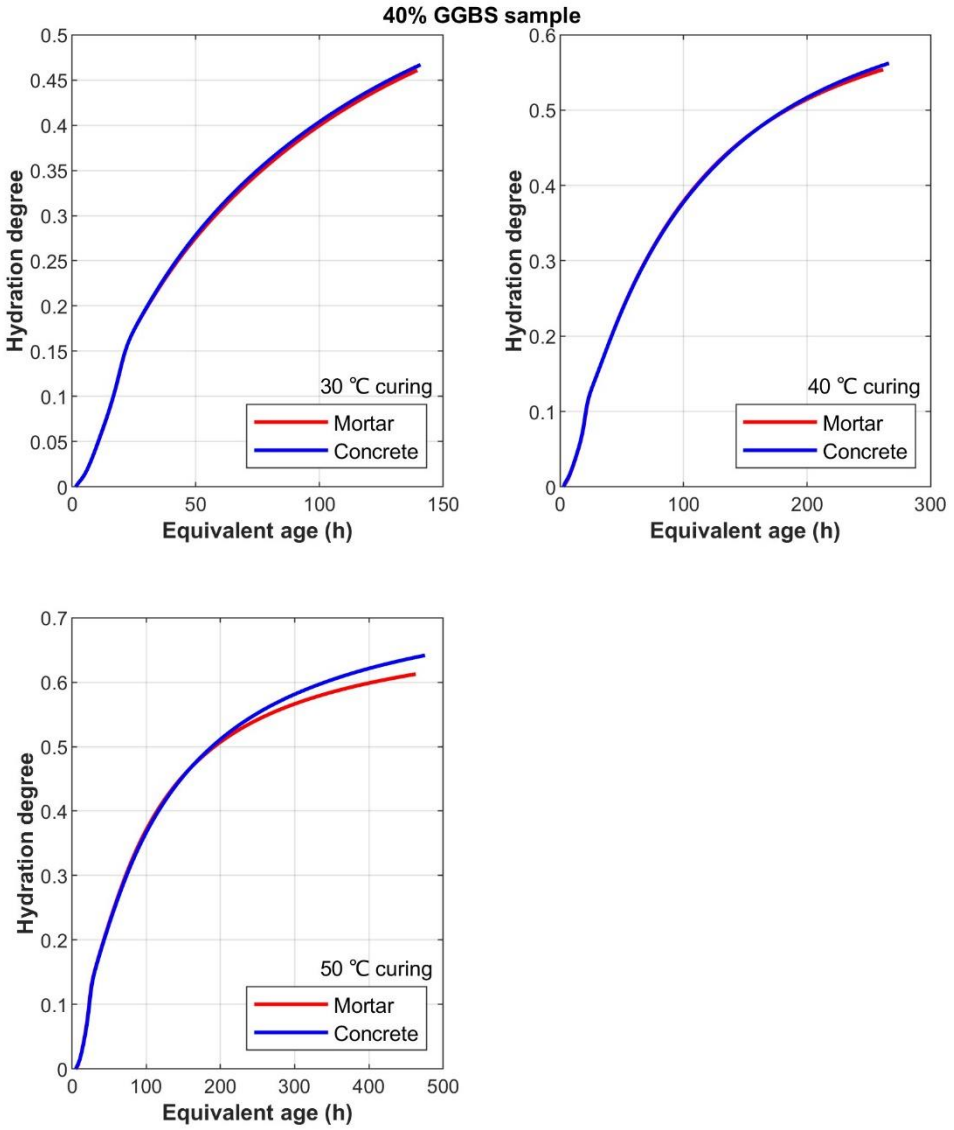

Figure 5.67. Hydration degree development of 40% GGBS sample at 30 °C, 40 °C, 50 °C.

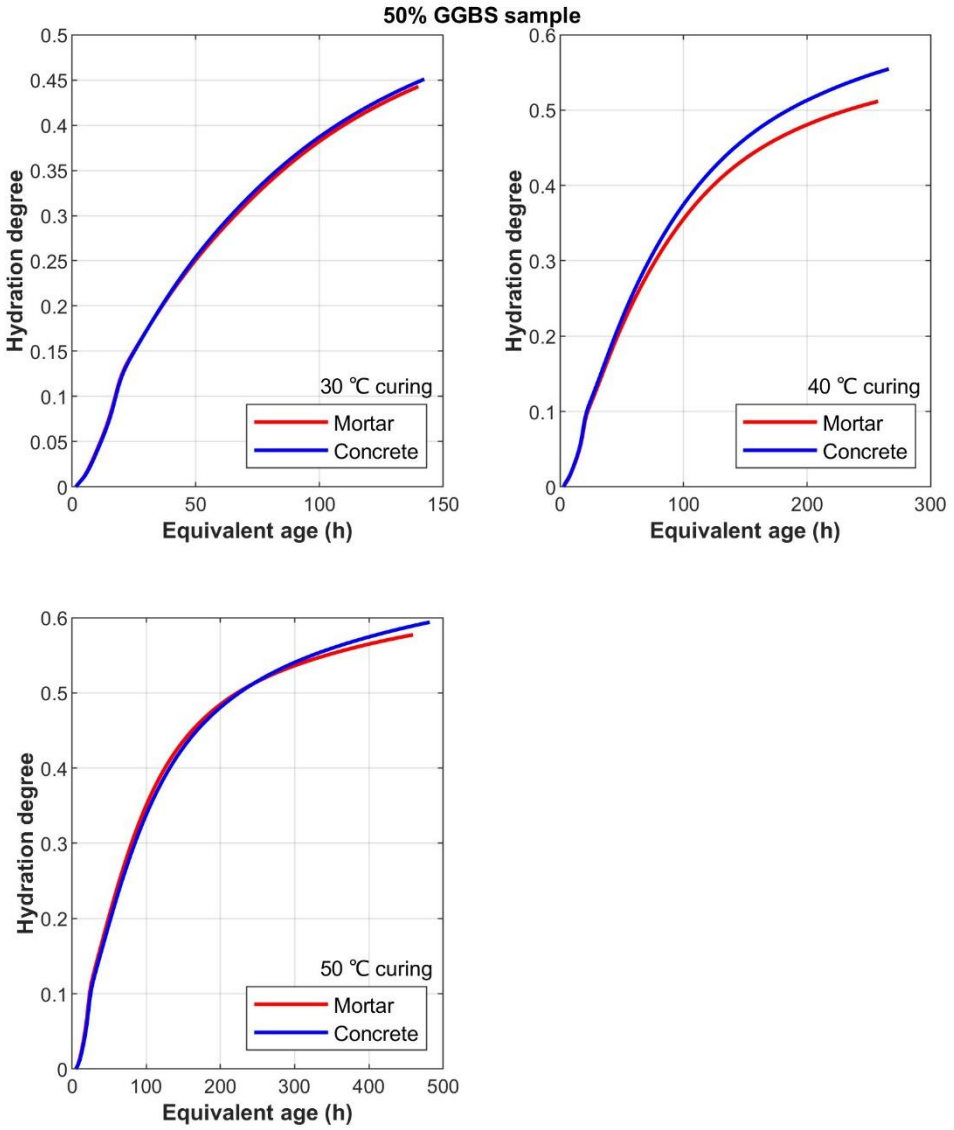

Figure 5.68. Hydration degree development of 50% GGBS sample at 30 °C, 40 °C, 50 °C.

Table 5.9 and Table 5.10 summarize the equivalent age (t_e) and degree of hydration (α) achieved by the micro-concrete and mortar samples at the end of the testing period (72 hours). These tables compare the hydration development of the two types of samples under the same curing conditions. Table 5.9 shows that temperature significantly impacts the t_e of samples across all GGBS contents. At 30°C, the t_e for all samples at 72 hours exceeds the equivalent of 130 hours of curing at the reference temperature of 20°C. At 40°C, all samples show t_e values surpassing 240 hours, with the maximum reaching 272.32 hours (for 30% GGBS concrete at 40°C). At 50°C, the t_e values for all samples range between 414.48 and 497.88 hours, indicating a substantial effect of temperature on the development of t_e. In this study, samples cured at 50°C for 72 hours are equivalent to nearly 500 hours of curing at 20°C, marking an increase of up to 591.5%. As the temperature rises, the value of t_e is expected to grow exponentially, given that t_e increases with temperature according to its defining equation Eq. (5.6),

where the mix and reference temperature are fixed, leaving the actual temperature T of the specimen as the variable. However, the relationship between t_e and GGBS content at a constant temperature appears ambiguous, possibly due to the inherent definition of t_e. Since t_e compares a sample's maturity to that of the same mix cured at 20°C, different GGBS contents imply different reference samples. This complexity in t_e is significantly greater than that observed in comparing 3-day cumulative hydration heat across sections, which essentially compares to a baseline of zero.

In comparing the t_e of micro-concrete and equivalent mortar samples cured at the same temperature within the same mix, Table 5.9 employs a "Difference" column (micro-concrete sample t_e minus equivalent mortar sample t_e to highlight disparities between the two sample types. While most micro-concrete samples exhibit higher t_e values than their mortar counterparts, about 33.3% of micro-concrete samples have lower t_e values. This discrepancy likely stems from the definition of t_e itself, where micro-concrete and equivalent mortar samples are compared to different reference samples despite having identical binder content and water-cement ratio.

Table 5.10 shows the degree of hydration (α) achieved by all samples at various temperatures after three days. As previously mentioned, since the degree of hydration is defined by the ratio of the released heat of hydration to the ultimate hydration heat, the results of three-day hydration degree can somewhat be considered equivalent to the three-day cumulative hydration heat. However, there are distinctions. Firstly, the degree of hydration, α, allows for an assessment of the completeness of hydration at three days by comparing it to the theoretical maximum value of 1, an assessment not possible through cumulative hydration heat alone. Secondly, similar to equivalent age t_e, each sample's degree of hydration, α, is defined relative to a specific reference, making the apparent lack of a straightforward mathematical relationship between α and GGBS content in Table 5.10 understandable. Unlike cumulative hydration heat, which shows a clear negative correlation with GGBS content, the degree of hydration's relationship to GGBS content is obscured by the varying ultimate hydration heats used as divisors for different mixes.

Regarding the impact of temperature on the degree of hydration α for the same mix of samples, the effect is analogous to that observed with three-day cumulative hydration heat, given the constant ultimate hydration heat within the same mix (as explained in Section 2.5.4). It is observed that as temperature increases, the value of three-day hydration also rises.

To assess the influence of coarse aggregate, the "Difference" column in Table 5.10 represents the subtraction of the three-day degree of hydration α value of the equivalent mortar from that of the micro-concrete sample. It is important to note that the data in Table 5.10 are rounded to two decimal places, equivalent to a precision of 1%, which explains the presence of zero "Difference" values. Nonetheless, similar to the three-day cumulative hydration heat statistics, all micro-concrete samples exhibit a higher degree

of hydration than their mortar counterparts. The maximum difference observed is 11.29% for the 30% GGBS sample at 50°C, consistent with the cumulative hydration heat analysis findings. Additionally, it is noted that the largest "Differences" occur under high-temperature conditions across all GGBS contents, the same as the cumulative hydration heat findings.

Table 5.9. Equivalent age of samples.

Sample information		Equivalent age t_e (h) at 3 days			
GGBS content	Temperature	Mortar sample	Micro-concrete sample	Difference*	Difference in %
0% GGBS	30 °C	134.79	134.69	-0.10	-0.074%
	40 °C	242.42	242.07	-0.35	-0.14%
	50 °C	420.46	419.58	-0.88	-0.21%
10% GGBS	30 °C	134.10	135.73	1.63	1.22%
	40 °C	240.05	245.71	5.66	2.36%
	50 °C	414.48	414.48	0	0
20% GGBS	30 °C	139.28	138.49	-0.79	-0.57%
	40 °C	258.32	255.48	-2.84	-1.10%
	50 °C	461.12	453.79	-7.33	-1.59%
30% GGBS	30 °C	141.37	143.13	1.76	1.24%
	40 °C	265.87	272.32	6.45	2.43%
	50 °C	480.83	497.88	17.05	3.55%
40% GGBS	30 °C	138.93	140.24	1.31	0.94%
	40 °C	257.04	261.75	4.71	1.83%
	50 °C	457.81	470.05	12.24	2.67%
50% GGBS	30 °C	138.91	141.32	2.41	1.73%
	40 °C	256.99	265.69	8.70	3.39%
	50 °C	457.67	480.36	22.69	4.96%

*: All differences in t_e values in this Table are Micro-concrete samples minus Mortar samples.

Table 5.10. 3-day hydration degree of samples.

Sample information		3-day hydration degree α			
GGBS content	Temperature	Mortar sample	Micro-concrete sample	Difference*	Difference in %
0% GGBS	30 °C	0.53	0.55	0.02	3.77%
	40 °C	0.60	0.60	0	0
	50 °C	0.63	0.66	0.03	4.76%
10% GGBS	30 °C	0.52	0.54	0.02	3.85%
	40 °C	0.58	0.58	0	0
	50 °C	0.63	0.66	0.03	4.76%
20% GGBS	30 °C	0.50	0.51	0.01	2.00%
	40 °C	0.59	0.60	0.01	1.69%
	50 °C	0.63	0.64	0.01	1.59%
30% GGBS	30 °C	0.49	0.50	0.01	2.04%
	40 °C	0.58	0.58	0	0
	50 °C	0.62	0.69	0.07	11.29%
40% GGBS	30 °C	0.46	0.47	0.01	2.17%
	40 °C	0.55	0.56	0.01	1.82%
	50 °C	0.61	0.64	0.03	4.92%
50% GGBS	30 °C	0.44	0.45	0.01	2.27%
	40 °C	0.51	0.55	0.04	7.84%
	50 °C	0.58	0.59	0.01	1.72%

*: All differences in α values in this Table are Micro-concrete samples minus Mortar samples.

5.4.5 Determination of Hydration Parameters

In Sections 2.2.4 to 2.5.6, the concept and application of hydration degree, defined through the heat of hydration, were reviewed. During experimental phases, the degree of hydration can be defined by the ratio of the heat of hydration released by the cement to the ultimate hydration heat (as shown in Eq. (5.7)). Isothermal calorimetry tests serve as an effective means to directly obtain specimen heat flow and cumulative hydration heat under constant temperatures, thus facilitating the easy acquisition of a sample's degree of hydration at various stages. However, the scenario for in-situ concrete is significantly more complex than that in isothermal calorimetry tests. The continuously changing internal temperature of the concrete and the varying external environmental temperatures mean that results from isothermal calorimetry experiments cannot be directly applied to predict in-situ concrete temperatures. Hence, the concept of equivalent age was introduced to normalize the effects of temperature. Section 5.4.4 summarized the development of equivalent age and degree of hydration from isothermal calorimetry tests.

This section delves into the analytical relationship between the degree of hydration and equivalent age, based on the Three Parameters Equation (TPE) introduced by Freiesleben Hansen and Pedersen [118] and mentioned in Section 2.2.5 (Eq. (2.42)), the TPE is restated here again as Eq. (5.8) for ease of reference. This formula has been extensively applied and validated, affirming the physical significance of its three hydration parameters (as illustrated in Figure 2.22 to Figure 2.24). Based on the results of different samples' equivalent age and degree of hydration development at various temperatures from Section 5.4.4, this section aims to solve for the best-fit values of the three hydration parameters of Eq. (5.8) through nonlinear fitting. The results will be analysed to assess the impact of temperature, GGBS content, and coarse aggregate on the hydration heat development.

$$\alpha(t_e) = \alpha_u \cdot e^{\left(-\left(\frac{\tau}{t_e}\right)^{\beta}\right)} \tag{5.8}$$

where $\alpha(t_e)$ is the hydration degree at equivalent age t_e, α_u is the ultimate hydration degree that the hydration reaction can be attend, a higher α_u leads to a higher final degree of hydration, and more total heat is available for hydration. β is the hydration heat development shape parameter, which characterizes the shape of the hydration-time curve, predominantly dictating the gradient of its primary linear segment. An increased β value suggests a more rapid hydration rate during this linear phase, but a slower rate at the onset of the hydration period. And τ is the hydration heat time parameter, a higher value of τ indicates a more pronounced delay in the hydration process.

The fitting results of the hydration parameters for micro-concrete and equivalent mortar samples at different temperatures and GGBS contents are summarized in Table 5.11. The final two columns of the data reflect the R-squared values of the fitting equations, rounded to three decimal places using standard rounding methods. The observation that all R-squared values exceed 0.998 underscores the high reliability of the fitted results for all hydration parameters. This excellent fit confidence indicates a strong correlation between the observed hydration behaviour and the modelled parameters across all tested conditions, reinforcing the validity of the hydration models Eq. (5.8) applied in this study. Such high R-squared values affirm the appropriateness of the models used and highlight the consistency and predictability of hydration parameters as influenced by variables like temperature and GGBS content within the tested ranges.

Given the extensive data in Table 5.11, which is not conducive to direct observation, this study utilizes three bar charts (Figure 5.69 to Figure 5.71) to summarize the variations in the three hydration parameters with changes in temperature and GGBS content.

The statistical analysis of the hydration parameters indicates that the ultimate hydration degree α_u does not correlate clearly with the GGBS content when the curing temperature remains constant. For samples with the same GGBS content, when the

GGBS content is below 20%, the value of α_u tends to increase with rising temperature. However, for GGBS contents of 20%, 30%, and 40%, the value of au first increases with temperature, peaks at 40°C, and then slightly declines at 50°C. In contrast, for a GGBS content of 50%, the value of α_u first increases, reaching a peak at 30°C, before gradually decreasing slightly at 40°C and 50°C. This suggests that curing high GGBS content concrete at excessively high temperatures may inhibit its later-stage hydration development. As observed in Figure 5.69, almost all micro-concrete samples exhibit a higher α_u than their corresponding equivalent mortar samples, indicating that the concrete specimens potentially achieve a more complete long-term hydration development than the mortar, thereby possessing a larger ultimate heat of hydration and, consequently, higher ultimate strength.

The hydration shape parameter β, when analysed under constant temperature conditions, does not display a clear correlation with the GGBS content. For samples with equal GGBS content, the value of β initially decreases with an increase in temperature and then increases. The influence of coarse aggregate on β is distinctly observed in Figure 5.70, where almost all micro-concrete samples exhibit lower β values than their corresponding equivalent mortar samples. This suggests that the rate of cumulative hydration heat development in the early stages of hydration for micro-concrete samples is slower than that of equivalent mortar samples but surpasses that of mortar samples in later stages.

When the curing temperature remains constant, the hydration time parameter τ slightly increases with the addition of GGBS, indicating that the inclusion of GGBS introduces a delay in the hydration reaction. This delay is attributed to GGBS not immediately reacting with water but waiting until CEM has reacted with water to produce enough alkaline substances to initiate GGBS hydration. For GGBS contents below 30%, the value of τ increases with rising temperature. When GGBS content exceeds 30%, the value of τ initially increases with temperature and then slightly decreases, indicating that higher temperatures introduce a more significant delay in the hydration reaction. However, as the GGBS content increases, this delay effect is mitigated at higher temperatures. It is evident from Figure 5.71 that almost all micro-concrete samples exhibit a higher τ value compared to equivalent mortar samples, and this difference enlarges with increasing temperature. This indicates that including coarse aggregate introduces a more significant delay in the hydration reaction, and this effect becomes more pronounced with rising temperature. This is particularly significant in scenarios where concrete temperatures may exceed 50°C, such as in mass concrete, where the delay induced by coarse aggregates cannot be overlooked. These results are consistent with the conclusion in Section 6.4.2 that the "Difference" in the heat of hydration between concrete and mortar may be magnified as the hydration temperature increases. This finding also corroborates Xu *et al.*'s [99] speculation that the delay effect of coarse aggregates in concrete could lead to discrepancies in predicting concrete temperature development based on isothermal calorimetry of mortar samples. It also contrasts with Wadsö's [16] assertion that the hydration heat development of cement paste and mortar

samples could substitute for concrete samples, highlighting the complex interactions within concrete systems that influence hydration heat development.

Table 5.11. Hydration parameters fitting results

Sample information		Hydration parameters							
GGBS content	Temperature	α_u		β		τ		R- squared	
		Mortar	Concrete	Mortar	Concrete	Mortar	Concrete	Mortar	Concrete
0% GGBS	20 °C	0.649	0.665	0.879	0.822	22.500	23.249	0.999	0.999
	30 °C	0.689	0.707	0.828	0.825	28.188	28.053	0.998	0.998
	40 °C	0.773	0.815	0.747	0.690	39.629	43.534	0.999	0.998
	50 °C	0.755	0.857	0.830	0.704	52.357	61.871	0.999	0.999
10% GGBS	20 °C	0.625	0.611	0.891	0.860	22.475	22.597	0.999	0.999
	30 °C	0.704	0.734	0.767	0.761	30.746	31.064	0.998	0.998
	40 °C	0.801	0.848	0.698	0.645	46.521	53.895	0.999	0.999
	50 °C	0.779	0.881	0.793	0.693	57.858	69.619	0.999	0.999
20% GGBS	20 °C	0.545	0.585	0.923	0.863	21.922	23.131	0.999	0.999
	30 °C	0.739	0.762	0.691	0.682	37.868	38.062	0.999	0.999
	40 °C	0.862	0.957	0.643	0.568	57.373	69.271	0.999	0.999
	50 °C	0.824	0.858	0.737	0.706	73.175	76.318	0.999	0.999
30% GGBS	20 °C	0.583	0.594	0.844	0.823	23.599	23.933	0.999	0.999
	30 °C	0.809	0.818	0.621	0.629	48.065	47.708	0.998	0.999
	40 °C	0.924	0.972	0.620	0.591	78.268	88.181	0.999	0.999
	50 °C	0.803	0.936	0.701	0.631	65.609	81.408	0.999	0.999
40% GGBS	20 °C	0.607	0.631	0.746	0.711	27.728	29.270	0.999	0.999
	30 °C	0.900	0.902	0.541	0.547	67.789	66.744	0.999	0.999
	40 °C	0.899	0.950	0.621	0.590	78.823	87.027	0.999	0.999
	50 °C	0.789	0.886	0.724	0.650	66.180	80.574	0.999	0.999
50% GGBS	20 °C	0.629	0.637	0.608	0.577	39.365	42.221	0.999	0.999
	30 °C	0.956	0.927	0.520	0.545	85.606	78.830	0.999	0.999
	40 °C	0.797	0.885	0.672	0.651	72.889	79.215	0.999	0.999
	50 °C	0.716	0.763	0.799	0.753	63.889	73.812	0.998	0.999

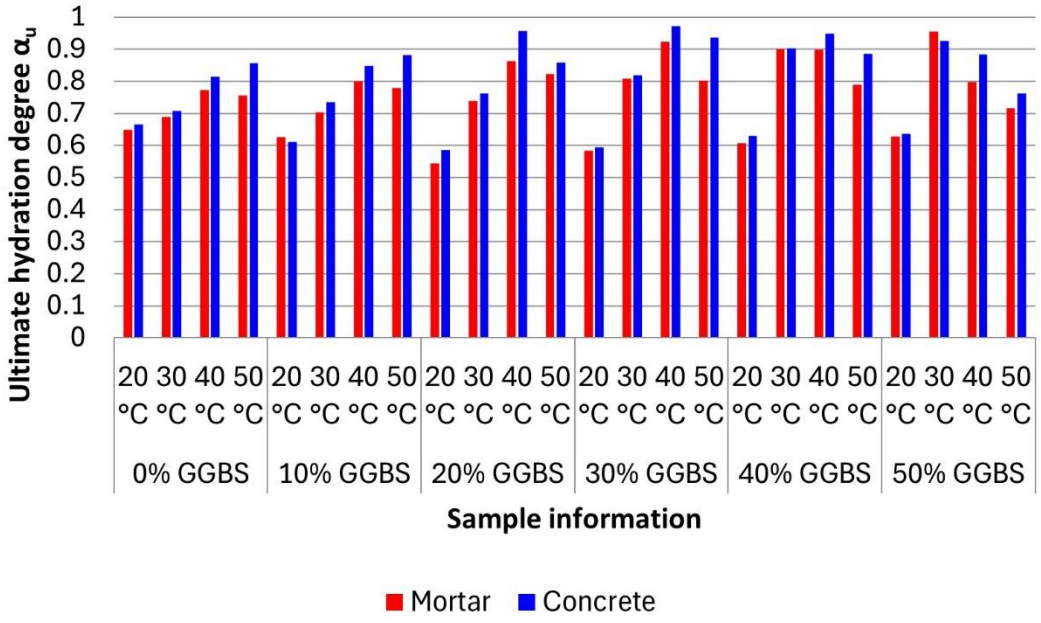

Figure 5.69. Ultimate hydration degree α_u

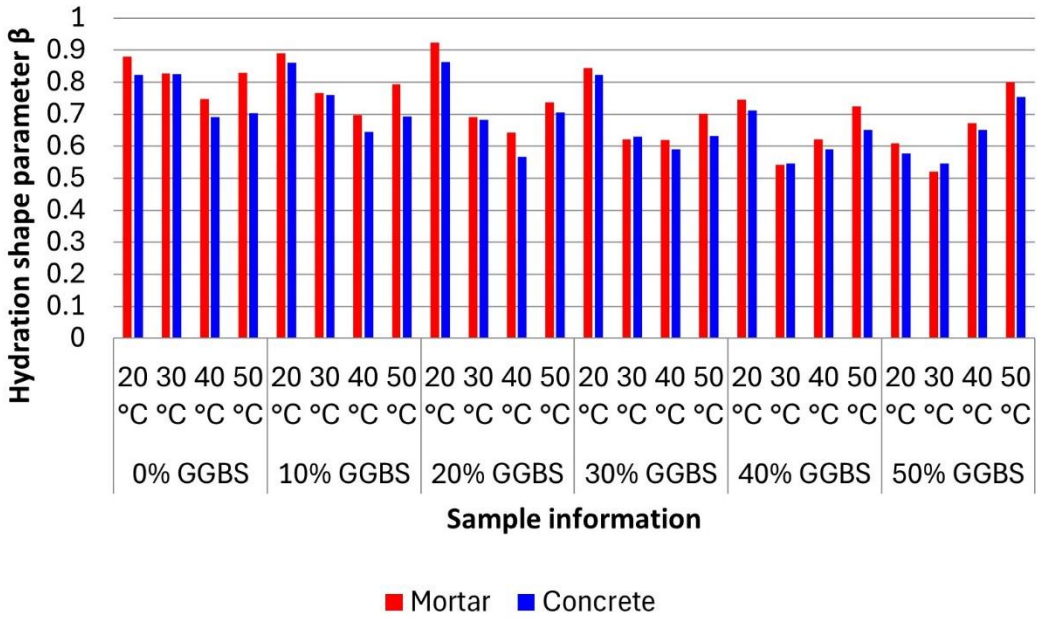

Figure 5.70. Hydration shape parameter statistics

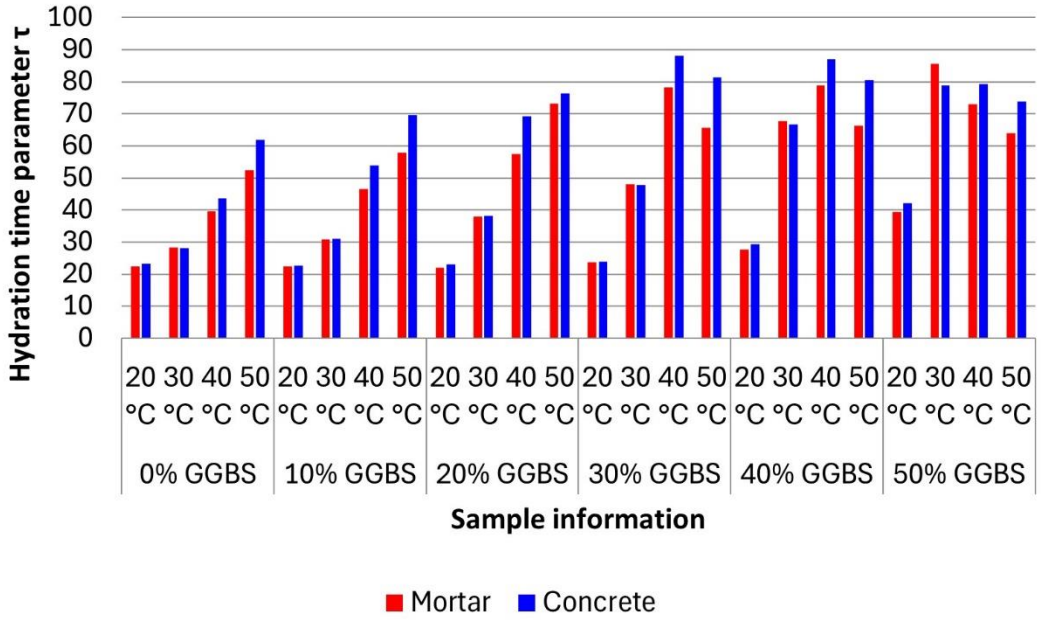

Figure 5.71. Hydration time parameter statistics

5.5 Conclusion

This chapter analysed the isothermal calorimetry test results to investigate the influence of curing temperature, GGBS content, and coarse aggregate on hydration heat development. The findings indicate that increasing curing temperature significantly accelerates early hydration reactions, leading to higher hydration heat peak values and cumulative hydration heat at one and three days. However, the acceleration effect diminishes over longer curing periods, suggesting that while higher temperatures enhance early hydration, they do not proportionally increase long-term hydration heat. The effect of GGBS content on hydration heat development was also examined. Increasing GGBS replacement reduces the hydration peak value and delays hydration, particularly at lower temperatures. The results show that while GGBS substitution effectively reduces early-age hydration heat, its influence diminishes at higher curing temperatures due to the increased reactivity of GGBS under elevated temperatures. Additionally, the emergence of the secondary hydration peak associated with GGBS hydration was observed, with its prominence increasing as the GGBS content rises and the curing temperature decreases.

The impact of coarse aggregate on hydration heat was assessed by comparing the hydration behaviour of micro-concrete and equivalent mortar samples. The results indicate that for most test conditions, micro-concrete samples exhibited slightly higher three-day cumulative hydration heat than their equivalent mortar counterparts, particularly at higher curing temperatures. However, the observed differences do not follow a clear trend with temperature or GGBS content, making it difficult to determine

whether the presence of coarse aggregate directly affects hydration heat development. It cannot be ruled out that these differences fall within the range of normal experimental variability rather than being a fundamental effect of coarse aggregate. Therefore, further validation is needed to confirm whether coarse aggregate has a measurable influence on hydration heat. Additional experiments, such as X-ray diffraction (XRD) and thermogravimetric analysis (TGA), could help clarify whether the differences in cumulative hydration heat are associated with variations in hydration product formation or are within the range of experimental error.

The apparent activation energy (E_a) of the hydration reaction was derived from isothermal calorimetry data. The results show that the activation energy generally increases with GGBS content, reaching a peak at 30% GGBS replacement before decreasing slightly. This suggests that GGBS-blended systems exhibit higher temperature sensitivity than cement-only systems, aligning with the observed acceleration of hydration at elevated temperatures. Additionally, the activation energy values for micro-concrete samples were slightly higher than those of equivalent mortar samples in most cases, which may indicate a small but measurable effect of coarse aggregate on hydration kinetics.

To further evaluate hydration kinetics, the relationship between the degree of hydration and equivalent age was analysed using a three-parameter hydration model. The fitting results show that the ultimate degree of hydration (α_u) does not exhibit a clear correlation with GGBS content when the curing temperature remains constant. However, at high GGBS contents and elevated curing temperatures, the ultimate hydration degree appears to decrease slightly, suggesting that excessive GGBS and high temperatures may inhibit later-stage hydration development. The hydration shape parameter (β) and hydration time parameter (τ) also vary with temperature and GGBS content, with coarse aggregates contributing to a delay in hydration development at higher temperatures.

Overall, the results provide insights into the effects of temperature, GGBS content, and coarse aggregate on hydration heat development. However, further experimental validation, particularly using XRD and TGA, is necessary to confirm whether the differences between micro-concrete and equivalent mortar hydration behaviour are due to fundamental material differences or experimental variability.

CHAPTER 6 CONCRETE TEMPERATURE FEM MODELLING RESULTS AND ANALYSIS

6.1 Finite Element Modelling of Early-Age Concrete Temperature

This study developed a finite element model (FEM) aimed at accurately predicting the early-age hydration temperature development of in-situ concrete containing ground granulated blast furnace slag (GGBS). The model investigates the potential influencing factors outlined in Section 1.2, the impact of variable ambient temperatures and coarse aggregates on the accuracy of the concrete temperature model. It also assesses the applicability of existing hydration heat models, initially designed for CEM-only concrete, to CEM-GGBS concrete based on the modelling results.

The temperature model was developed using commercial FEM software, COMSOL Multiphysics 6.1. Data from isothermal calorimetry tests were adjusted using an Arrhenius-based approach to simulate the hydration heat development in actual concrete, and these results were utilized to support the heat source of the model. The model's accuracy was evaluated via the temperature monitoring results of semi-adiabatic calorimetry tests (Chapter 4). The outcomes of this model are crucial for enhancing predictive models used in mass concrete and large-span structures, where temperature and related stress/cracking due to hydration are key considerations.

6.1.1 Structural Element Modelling

The developed FEM model is designed to simulate the temperature development of concrete specimens from semi-adiabatic calorimetry tests, thereby necessitating that the structural elements within the model mirror those of the concrete specimens utilized in the experiments. Specifically, the model is based on 150 mm concrete cubic specimens encased within two layers of insulation, consisting of polystyrene and timber board, with the thicknesses of these insulating layers thoroughly detailed in Section 4.1. The initial geometric model created in COMSOL (concrete specimen with insulation layers) is shown in Figure 6.1. The temperature at the core of the concrete specimens and the ambient environmental temperature were continuously monitored during the experimental phase (Section 4.2). These environmental temperatures will be integrated as the boundary condition in the FEM model, and the specimen's temperature data will be used to assess the model's accuracy.

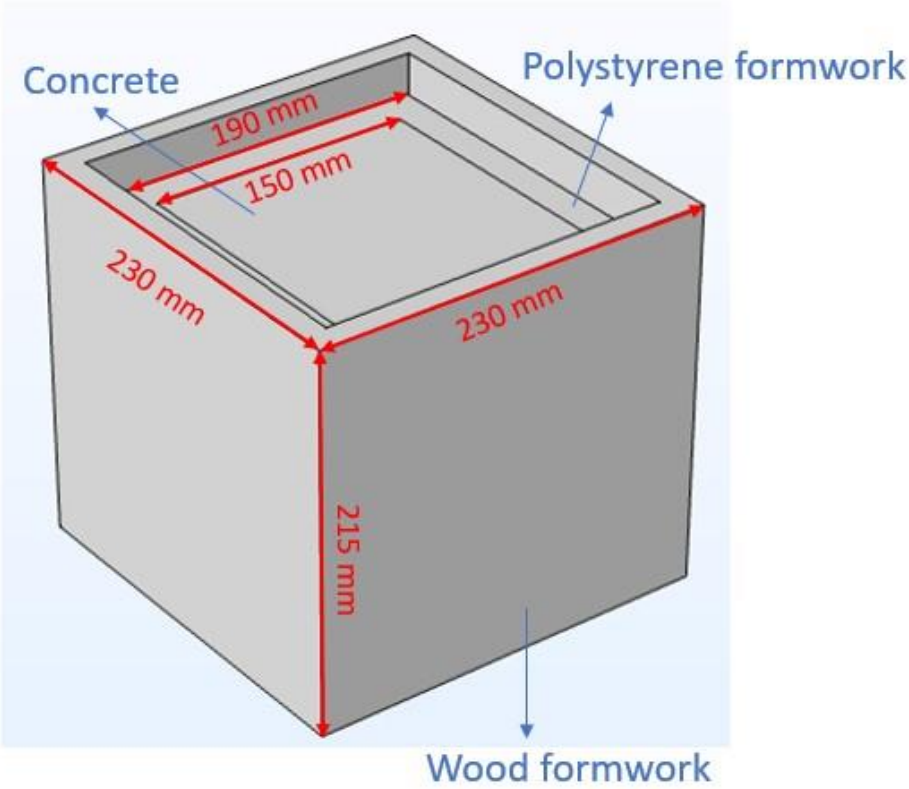

Figure 6.1. Geometrical modelling of semi-adiabatic concrete specimen.

6.1.2 FEM Modelling Process

6.1.2.1 Concrete Heat Balance

In the FEM modelling process, the development of concrete temperature is simulated through a heat transfer model. This model necessitates attaining thermal equilibrium, where the heat generated by the hydration reaction of concrete equals the sum of the heat absorbed by the rise in concrete temperature and the thermal losses. These thermal losses can be either positive or negative. For instance, when the surface temperature of the concrete exceeds the ambient temperature, heat dissipation occurs through convective heat transfer and irradiation, decreasing surface temperature, thereby constituting a positive thermal loss. Conversely, when the concrete surface is exposed to sunlight, it absorbs heat through solar absorption, increasing surface temperature, which equates to a negative thermal loss.

These thermal losses are induced by external environmental conditions such as air temperature and solar radiation, which are defined as boundary conditions within the FEM software. The thermal balance equation for concrete (Eq. (2.60)) and the equations for various boundary conditions (Eqs. (2.61)-(2.68)) have been elaborated in Section 2.6.1. However, it is crucial to note that Eq. (2.60) solely represents the internal thermal balance of concrete and does not incorporate the boundary conditions

delineated in Eqs. (2.61)-(2.68). To express the thermal equilibrium of concrete in the context of heat exchange with the external environment, it is imperative to integrate these boundary conditions into Eq. (2.60). The resultant expression is as follows:

$$\rho \cdot C_p \cdot \frac{\partial T}{\partial t} - \nabla(k \cdot \nabla T) = Q + h_c \cdot (T_s - T_a) \tag{6.1}$$

where ρ is the density of the concrete (kg/m^3), C_p is the heat capacity of concrete (J/kg·K), T is the concrete temperature (°C), k is the thermal conductivity of concrete (W/(m·K)), Q is the heat generation rate of the cement (W/m^3), h_c is the convection coefficient (W/m^2 ·°C), T_s is the temperature of the concrete or insulation layer surfaces (°C), T_a is the ambient temperature (°C).

In semi-adiabatic calorimetry experiments, concrete specimens are placed within an uncontrolled laboratory environment. Despite the fluctuating ambient temperatures over time, the specimens remain unexposed to direct solar radiation. Consequently, the model disregards the influence of solar absorption and irradiation, focusing solely on the thermal losses attributed to thermal convection.

6.1.2.2 Concrete Thermal Properties

The definition of the thermal properties of the material is essential for the subsequent computation of the heat transfer FEM model. In this concrete heat transfer model, the thermal conductivity and specific heat capacity of concrete must be defined. The variation of the thermal properties of Harding Concrete with the hydration reaction was reviewed in Section 2.6.2. Considering that this study simulates the development of the hydration temperature of the field concrete in the early stage (the first three days), the concrete gradually hardens from a semi-fluid state to a solid state during this stage. Therefore, theoretically, it is inappropriate to use fixed concrete thermal properties, although many works that simulate the early hydration temperature of concrete adopt the thermal properties of fully hardened concrete. Based on the content reviewed in Section 2.6.2 of this study, this study assumes that the thermal conductivity and specific heat capacity of the early concrete vary linearly with the degree of hydration, following Eq. (2.70) and Eq. (2.72), respectively. For ease of discussion, this section lists these two formulas again as follows:

$$k_c(\alpha) = k_u \cdot (1.33 - 0.33\alpha) \tag{6.2}$$

$$C_p = \frac{1}{\rho} \cdot \left(W_c \cdot \alpha \cdot C_{ref} + W_c \cdot (1 - \alpha) \cdot C_c + W_a \cdot C_a + W_w \cdot C_w\right) \tag{6.3}$$

where $k_c(\alpha)$ is the thermal conductivity of concrete at hydration degree α (W/(m·K)),

k_u is the thermal conductivity of concrete when fully hardened (W/(m·K)), C_p is the specific heat of concrete (J/(kg·K)), ρ is the density of concrete (kg/m^3), C_{ref} is the specific heat of hardened concrete (J/(kg·K)) (refer to Eq. (2.73)), W_c, W_a, W_w are the percentage of cement, aggregate, water in the total concrete (by weight), separately, and C_c, C_a, C_w are the specific heat of cement, aggregate, water, separately (J/(kg·K)).

The thermal conductivity of hardened concrete, k_u, is obtained from the literature data [4] and is set to 1.7 W/(m·K). The calculation of the specific heat capacity of concrete requires the specific heat capacities and percentages (by weight) of its constituent components. The detailed mix proportions of concrete are shown in Table 4.1. The specific heat capacities of cement, GGBS, coarse aggregate, fine aggregate, and water are summarized in Table 5.2.

6.1.2.3 Boundary Conditions

In this FEM model, the thermal dissipation mechanism for concrete is exclusively considered through the mode of thermal convection. This simplification is justified as the specimens are placed within a laboratory setting, shielded from direct solar irradiation. Additionally, omitting less significant boundary conditions can significantly reduce the computational demands of the model. The mechanism of thermal convection and its governing equations were thoroughly reviewed in Section 2.6.1.

Thermal convection is primarily dependent on the temperature differential between the concrete surface and the surrounding air, as well as the convective heat transfer coefficient, h_c, which can be represented by Eq. (2.61) or the leftmost term in Eq. (6.1) The value of h_c is chiefly influenced by wind velocity. Due to the absence of wind velocity data within the laboratory setting, the convective heat transfer coefficient between the concrete surface and air is adopted from literature [4], with a value of 5.6 W/m^2·°C.

It is imperative to note that only the top surface of the concrete specimen is directly exposed to the surrounding environment, while the four sides and the bottom are encapsulated by two layers of insulation materials, namely polystyrene and timber board, as depicted in Figure 4.3. Consequently, the above convective heat transfer coefficient, h_c (5.6 W/m^2·°C), applies solely to the thermal exchange between the concrete's top surface and the air. Despite the sides and bottom being enveloped by insulating materials, they are not perfectly adiabatic; thus, thermal losses through these surfaces must be considered.

The thermal loss through the sides and bottom of the concrete specimen involves heat transfer from the concrete surface to the insulating materials, primarily through conduction, followed by convective heat exchange between the outer surface of the

outer insulation layer (timber board) and the air. Therefore, the modelling process initially requires calculating the heat conduction between the concrete and polystyrene, and between polystyrene and timber board, due to their solid-state and direct contact. Subsequently, the convective heat exchange between the timber board and air must be assessed. However, this can be a complex procedure, necessitating the additional construction of an insulation layer model within the geometric modelling process and setting up appropriate contact methods to prevent computational errors. To streamline the model construction and reduce computational demands, this model adopts the concept of an equivalent convection coefficient h_{eq}, as discussed in Eq. (2.66), to represent this intricate heat transfer process. This approach has been widely used and validated [20, 22]. For ease of discussion, the formula is reiterated below to illustrate the relevant thermal parameters further:

$$h_{eq} = \left(\frac{1}{h_c} + \sum_{1}^{n} \frac{L_i}{k_i} \right)^{-1} \tag{6.4}$$

where h_{eq} is the equivalent convection coefficient (W/m^2 ·°C), h_c is the convection coefficient between the concrete surface and air (W/m^2 ·°C), L_i is the i-th insulation layer's thickness (mm), and k_i is the i-th insulation layer's thermal conductivity (W/m·°C).

As deduced from Eq. (6.4), the magnitude of the equivalent convection coefficient, h_{eq}, is determined by each insulating material layer's thermal conductivity and thickness. The thermal conductivities of polystyrene and timber board were derived from literature [4, 184] and provided a basis for this calculation. Table 6.1 presents the thermal properties of hardened concrete and the two insulating materials. The calculated value of the equivalent convection coefficient, h_{eq}, for the sides and bottom of the specimen, are 1.47 and 1.14 W/m·°C, separately. This equivalent convection coefficient encapsulates the complex heat transfer process through the insulating layers, simplifying the thermal model's representation of heat loss from the concrete to the surrounding environment. In the actual modelling process, the two layers of the concrete mould can be omitted, allowing for the creation of a geometric model of the concrete specimen alone (a 150 mm cube, as illustrated in Figure 6.2). Heat losses through the sides and bottom of the concrete specimen are defined by adjusting the heat convection coefficients for these surfaces.

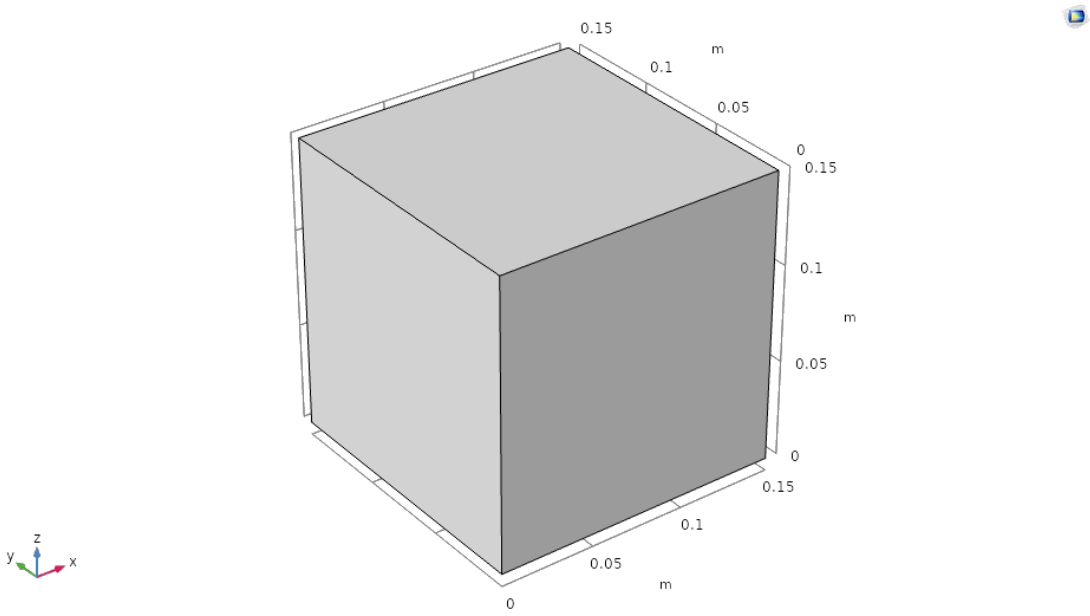

Figure 6.2. Geometric model of concrete specimen (without mould)

Table 6.1. Thermal properties of hardened concrete and insulation materials [4, 184].

	Thermal conductivity (W/m·°C)	Specific heat capacity (J/kg·°C)
Hardened concrete	1.7	1000
Polystyrene	0.0624	1040
Timber board	0.15	122

6.1.2.4 Deriving Heat Source from Isothermal Calorimetry

In the concrete heat transfer model, the only internal heat source stems from the hydration heat released during the hydration reaction between cementitious materials (CEM I and GGBS in this study) and water within the concrete. The heat source component of the FEM model in this research is derived from isothermal calorimetry tests described in Section 4.5, with experimental results presented in Chapter 6. These tests measured hydration heat curves for samples with varying GGBS contents under different constant temperature conditions, providing crucial data for describing hydration heat rates in in-situ concrete where internal temperatures continuously change. To investigate the impact of coarse aggregates on cement hydration, the isothermal calorimetry tests included measurements of both micro-concrete and equivalent mortar samples. This approach allows for evaluating how adding coarse aggregates affects the hydration reaction. The hydration heat results from both sample types will be used separately in the modelling work to assess potential errors in simulating concrete temperatures using mortar hydration heat data.

The heat source for the concrete thermal model will be based on the outcomes of these isothermal calorimetry experiments. During the modelling phase, comparisons will be made between models based on micro-concrete samples and those on equivalent mortar samples. However, given that the in-situ concrete's temperature and ambient environmental conditions vary over time, the results from isothermal calorimetry tests—which maintain samples under constant temperature conditions—cannot be directly applied as the heat source for simulating in-situ concrete temperatures. The model developed must, therefore, be time-dependent, calculating the heat source and temperature at each time step until reaching 72 hours. This study will employ a hydration heat release formula based on the Arrhenius equivalent age (Eq. (2.50)), with its derivation process elaborately described in section 2.5.7.1. A fundamental assumption of this process is that concrete samples of the same mix, when they have the same equivalent age, will exhibit the same cumulative hydration heat release, regardless of their curing conditions and historical hydration heat development. Due to the formula's complexity and the need to calculate the equivalent age t_e, the degree of hydration α, the cumulative heat of hydration H, and the heat release rate Q at each time step, the heat source component will be divided into several subdomains to express these essential parameters. To articulate the setup of the heat source section more clearly, some formulas from Chapter 2 will be re-presented herein for coherence and ease of reference.

The Domain Ordinary Differential Equations (DODE) physics interface within COMSOL Multiphysics will be utilized to define the equivalent age t_e, degree of hydration α, and cumulative hydration heat H for each time step. The hydration heat release rate Q at each timestep will be determined based on these DODE equations.

The first DODE will initially articulate the concrete's equivalent age t_e. This process will translate the age t of concrete at a specific temperature to the equivalent age t_e of the same concrete mix at a reference temperature set at 20 °C of this study. The equivalent age equation is reformulated into a differential equation as follows:

$$\frac{dt_e}{dt} = e^{\frac{-E_a}{R}\left(\frac{1}{T}-\frac{1}{T_r}\right)} \tag{6.5}$$

where t_e is the concrete equivalent age (h), t is the concrete actual age (h), E_a is the apparent activation age of the sample (J/mol), which have been calculated for all samples in section 5.4.3 (Table 5.8), R is the universal gas constant = 8.314 (J/Kmol), T is the temperature (K), and T_r is the reference temperature (293.15 K (20 °C) of this study).

The degree of hydration α of concrete will be articulated through the Three Parameters Equation (TPE) for hydration as presented in Eq. (2.42). It is critical to note that the

time variable in Eq. (2.42) is the equivalent age t_e rather than the actual age t. In the environment of FEM software, it is not feasible to output results with the equivalent age t_e as the independent variable. Moreover, in practical applications, results are typically required with the actual age t serving as the independent variable. Therefore, it becomes necessary to substitute t_e with t in Eq. (2.42). This substitution can be accomplished using the following expression:

$$\frac{d\alpha(t)}{dt} = \frac{d\alpha(te)}{dt_e} \cdot \frac{dt_e}{dt} \tag{6.6}$$

Thus, the second DODE will be employed to express the degree of hydration α of concrete at the actual temperature for a given time step. By converting Eq. (2.42) into a form of an ordinary differential equation, it is possible to obtain:

$$\frac{d\alpha(t)}{dt} = \alpha_u \cdot e^{\left(-\left(\frac{\tau}{t_e}\right)^{\beta}\right)} \cdot \left(\frac{\tau}{t_e}\right)^{\beta} \cdot \left(\frac{\beta}{t_e}\right) \cdot \frac{dt_e}{dt} \tag{6.7}$$

Incorporating Eq. (6.5) and Eq. (6.6) into Eq. (6.7) results in a differential equation for the degree of hydration α with respect to the actual age t:

$$\frac{d\alpha(t)}{dt} = \alpha_u \cdot e^{\left(-\left(\frac{\tau}{t_e}\right)^{\beta}\right)} \cdot \left(\frac{\tau}{t_e}\right)^{\beta} \cdot \left(\frac{\beta}{t_e}\right) \cdot e^{\frac{-E_a}{R}\left(\frac{1}{T}-\frac{1}{T_r}\right)} \tag{6.8}$$

In COMSOL, equations that have been previously defined can be directly invoked, the actual modelling process for describing the degree of hydration, α, does not necessitate the complex formulation as presented in Eq. (6.8). Instead, it can be simplified to the form of Eq. (6.7). This will significantly reduce the complexity of the modelling process and minimizes the potential for human error associated with overly complex formulas.

The third DODE is formulated to express the concrete's cumulative hydration heat, H, at a given time step. The value of cumulative hydration heat at a certain degree of hydration can be derived from the definition of hydration degree (Eq. (2.25)), where the hydration heat H at a specific degree of hydration is equal to the product of the degree of hydration and the ultimate hydration heat H_u (Eq. (2.46)). However, akin to Eq. (2.42), Eq. (2.46) is based on equivalent age rather than actual age, necessitating a similar transformation as detailed in Eq. (6.6). Consequently, the differential equation representing the cumulative hydration heat, H, with respect to actual age, t, can be articulated as follows:

$$\frac{dH(t)}{dt} = H_u \cdot \frac{d\alpha(t)}{dt} \tag{6.9}$$

Eqs. (6.5), (6.6), and (6.9) represent the three distinct ODEs defined within the model to characterize the heat source, thereby simplifying the complex rate equation of hydration heat as presented in Eq. (2.50). Notably, the last ODE, Eq. (6.9), defines the cumulative hydration heat. However, in practice, the time derivative of the cumulative hydration heat precisely equates to the heat release rate Q due to hydration at that specific time, which is the required form of the heat source in the COMSOL heat transfer model. Given that the ultimate hydration heat in this study is expressed in J/g, while the heat source in COMSOL is in J/m^3, the expression for the heat source Q defined under the solid heat transfer physics field is as follows:

$$Q(t) = C_b \cdot \frac{dH(t)}{dt} \tag{6.10}$$

where Q(t) is the hydration heat release rate at an actual age t (J/m^3), C_b is the binder content of concrete (g/m^3).

The actual mathematical expression for the heat source, Eq. (2.50), incorporates unknown parameters from the Three-Parameter Equation (TPE) related to cement hydration reactions, namely the ultimate hydration degree (α_u), the shape factor (β), and the time factor (τ), in addition to the apparent activation energy (E_a). The apparent activation energy and hydration parameters for samples with varying GGBS content at different temperatures have been determined in Chapter 5.

These parameters are crucial for accurately modelling the thermal behaviour of concrete during the early-age hydration process. By leveraging these fitting-derived hydration parameters and activation energy values, the proposed finite element model is equipped to predict temperature evolution within GGBS-incorporated concrete structures with enhanced precision. Incorporating concrete-specific hydration parameters into the thermal model underscores the detailed and systematic approach adopted to ensure the model's relevance and reliability in predicting early-age thermal risks in contemporary concrete engineering practices.

6.1.2.5 Concrete Initial Temperatures and Ambient Temperatures

The operation of the time-dependent model necessitates an initial value, specifically the initial temperature of the concrete, which can be considered the outcome of step 0. With this initial temperature inputted, the essential parameters required for calculating the results of step 1—namely, the equivalent age (t_e), the degree of hydration (α), and most critically, the rate of heat release (Q)—can be determined as outlined in Section 6.1.2.4.

These parameters are pivotal for solving the heat source and thus for elucidating the results of step 1, which is the temperature of the concrete at the end of this step. In a time-dependent model, the results of each time step are iterative outcomes based on all preceding time steps. Therefore, the accuracy of the initial temperature, which should realistically reflect the actual conditions, is vital for precise simulation of concrete hydration temperature development. In this study, the initial temperature of the concrete specimens is set based on the initial temperatures recorded by thermocouples immediately after the mixing of semi-adiabatic calorimetry specimen. This initial temperature, corresponding to the temperature of freshly mixed concrete, ensures that the model begins with conditions that closely mirror the real concrete specimen.

The environmental temperature surrounding the concrete specimens is fundamentally the boundary condition, as discussed in Section 6.1.2.3. The temperature difference between the environment and the concrete or insulation layer's outer surface determines the convection cooling scenario at each time step, which, in turn, dictates the thermal loss of the concrete specimen. This thermal loss is critical as it determines the residual heat available for the self-heating of the concrete, thus establishing the temperature of the concrete at the end of each time step and, consequently, influencing the rate of heat release due to hydration in the subsequent time step. Therefore, the accurate input of boundary conditions is crucial. The environmental temperatures for each semi-adiabatic calorimetry concrete specimen were also monitored via thermocouples, which have been presented in Chapter 4. These recorded environmental temperatures are imported into the FEM model to serve as boundary conditions.

This chapter presents a detailed analysis of the results obtained from the finite element modelling (FEM) of concrete temperature evolution. The process of concrete temperature modelling is thoroughly described in Section 6.1. This model simulates the temperature development of concrete specimens from the semi-adiabatic calorimetry experiments detailed in Chapter 4. Utilizing three Differential Ordinary Differential Equations (DODEs) based on the equivalent age principle, established in Section 6.1.2.4, the "Mathematics" physics field in this model transforms isothermal calorimetry data into the actual hydration heat of the modelling concrete, thus providing the heat source for the FEM model. In COMSOL, the coupling of the "mathematics" physics field with the "Heat Transfer in Solids" physics field enables the simulation of the hydration temperature development over the first three days for concrete specimens with varying GGBS contents.

To address the three objectives set out in Section 1.2—namely, the influence of variable ambient temperatures on in-situ concrete temperature evolution, the impact of coarse aggregates on the heat of cement hydration and concrete temperature changes, and the accuracy of existing mathematical heat of hydration models (initially designed for CEM-only concrete) in predicting the temperature evolution of GGBS-CEM mixed

specimens—different modelling approaches were used for each mix of specimens. During the modelling process, multiple heat sources (derived from either micro-concrete or equivalent mortar specimens) and boundary conditions (either actual monitored ambient temperatures or constant temperatures) were applied to all specimens. The applicability of the existing hydration heat model to GGBS-CEM blended mixes was evaluated by examining the effect of increasing GGBS content on the model's accuracy. The accuracy of these different modelling methods was assessed by comparing the simulation results with the semi-adiabatic calorimetry results presented in Section 4.2.

6.2 Mesh Results

To optimize computational efficiency, the model leverages the symmetry planes in the XZ and YZ directions, dividing the model into four identical parts by cutting along these planes and using only one-quarter for calculations. Figure 6.1 provides a description of the model, including the insulated mould and specimen. Figure 6.3 (a) and (b) respectively present the quarter-model schematics cut along the X-Z and Y-Z symmetry planes. This approach reduces the computational domain, significantly lowering the computational load while maintaining solution accuracy. Given the regular cubic geometry of the concrete specimen, a hexahedral meshing technique was employed. This method is selected for its efficiency in handling simple geometries and its ability to generate structured meshes, which are advantageous for the numerical stability and accuracy of finite element analysis [27]. The resulting mesh comprised 6,525 elements. The hexahedral elements, congruent with the specimen's geometry, minimize numerical errors associated with mesh distortion, making them particularly suitable for simulating heat transfer in cubic samples. Figure 6.3 (c) shows the meshed quarter-symmetry concrete specimen.

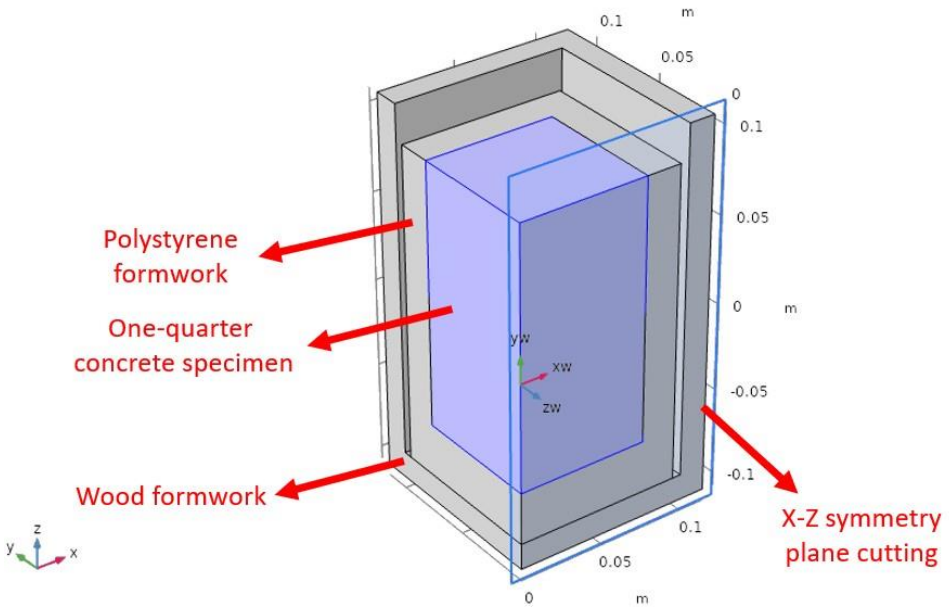
Polystyrene formwork
One-quarter concrete specimen
Wood formwork
X-Z symmetry plane cutting
0.1
m
0.05
0
0.1
0.05
0
m
-0.05
-0.1
0.1
0.05
0
m
yw
xw
zw
z
y
x

(a)

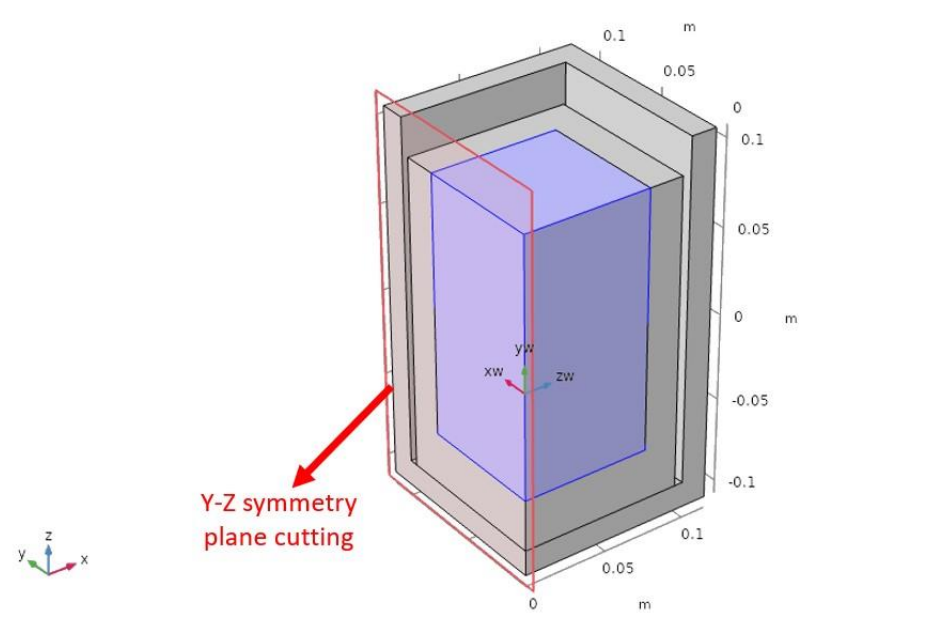
Y-Z symmetry plane cutting
0.1
m
0.05
0
0.1
0.05
0
m
-0.05
-0.1
0.1
0.05
0
m
yw
xw
zw
z
y
x

(b)

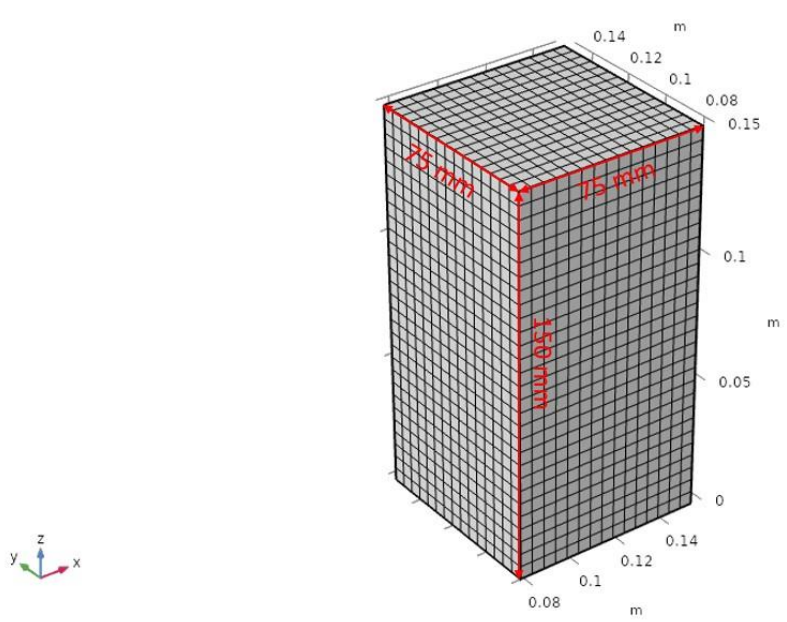

(c)

Figure 6.3. Concrete one-quarter symmetric model cutting setup and mesh results: (a) X-Z symmetry plane cutting; (b) X-Z symmetry plane cutting; (c) Concrete one-quarter symmetric model mesh results (without mould).

6.3 Concrete Temperature Modelling Results and Analysis

Section 6.1 details the procedures for establishing the concrete temperature FEM model, encompassing thermal balance, material properties, boundary conditions, heat sources, etc. The heat source, derived from the hydration reaction of CEM I/GGBS, is critical as it is the only internal heat source in the model. This model utilizes the "Mathematics" physics field in COMSOL, defined by three Domain Ordinary Differential Equations (DODEs) (Eqs. (6.5) and (6.6) into (6.7)). These DODEs calculate the equivalent age, degree of hydration, and cumulative hydration heat at each time step. The results are then coupled with the "Heat Transfer in Solids" physics field to determine the hydration heat release rate and the concrete temperature at each time step. The parameters involved in the "Mathematics" field, including apparent activation energy and hydration parameters, are derived from isothermal calorimetry results (Sections 5.4.3 and 5.4.5).

To achieve the objectives outlined in Section 1.2, the simulation process for each GGBS content in concrete employed three distinct approaches. Firstly, the heat source was derived from the isothermal calorimetry results of micro-concrete samples. Secondly, the boundary condition (ambient temperature) was set as a constant, based on the average value from the semi-adiabatic calorimetry environmental temperature monitoring results (as depicted by the grey lines in Figure 4.4 to Figure 4.9). Lastly, the heat source utilized the isothermal calorimetry results of equivalent mortar samples.

For the first and third models, where the heat sources include or exclude coarse aggregates, the boundary conditions were set using real-time environmental temperatures from the semi-adiabatic calorimetry tests, aimed at accurately assessing the impact of coarse aggregates on the accuracy of the concrete temperature models. The second model used a constant environmental temperature, with the heat source from the micro-concrete isothermal calorimetry results, to precisely evaluate how variable environmental temperatures affect the accuracy of the concrete temperature models.

The results of the concrete temperatures FEM model over three days are depicted in Figure 6.4 to Figure 6.9 for concrete mixes containing 0%, 10%, 20%, 30%, 40%, and 50% GGBS, respectively. In these figures, the blue dashed line represents the measured results from the semi-adiabatic calorimetry tests, which serve as a benchmark for evaluating the accuracy of the models. The orange curve represents the "Micro-concrete based model", which uses isothermal calorimetry data from micro-concrete samples as the heat source. Within the scope of this study, this "Micro-concrete based model" is considered to exhibit the highest accuracy. The grey curve represents the "Average ambient temperature model", which employs a constant ambient temperature as a boundary condition. This corresponds to the second type of model discussed earlier. Finally, the yellow curve represents the "Mortar based model", which uses isothermal calorimetry data from equivalent mortar samples as the heat source, representing the third type of model. Moreover, Table 6.2 and Table 6.3 summarises the peak hydration temperature and the time taken to reach it for the three models respectively, along with their errors in comparison to the temperature monitoring results of semi-adiabatic calorimetry concrete specimens.

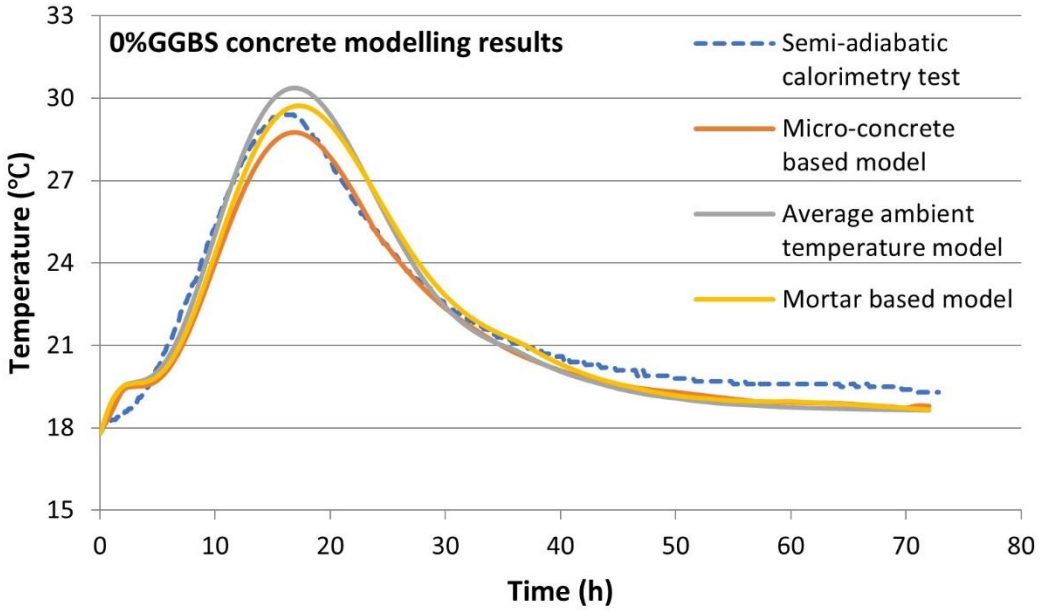

Figure 6.4. 0% GGBS concrete modelling results

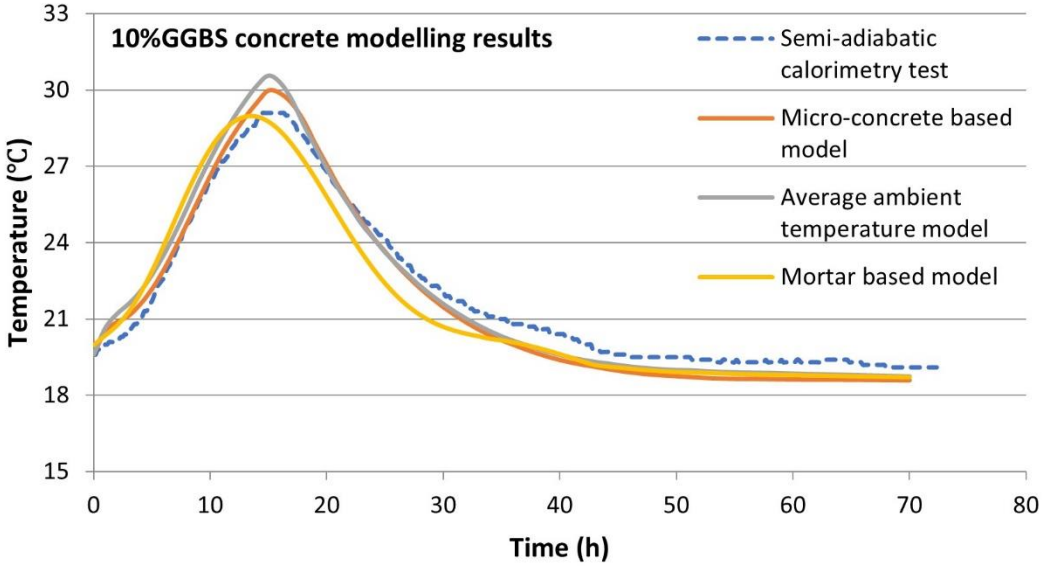

Figure 6.5. 10% GGBS concrete modelling results

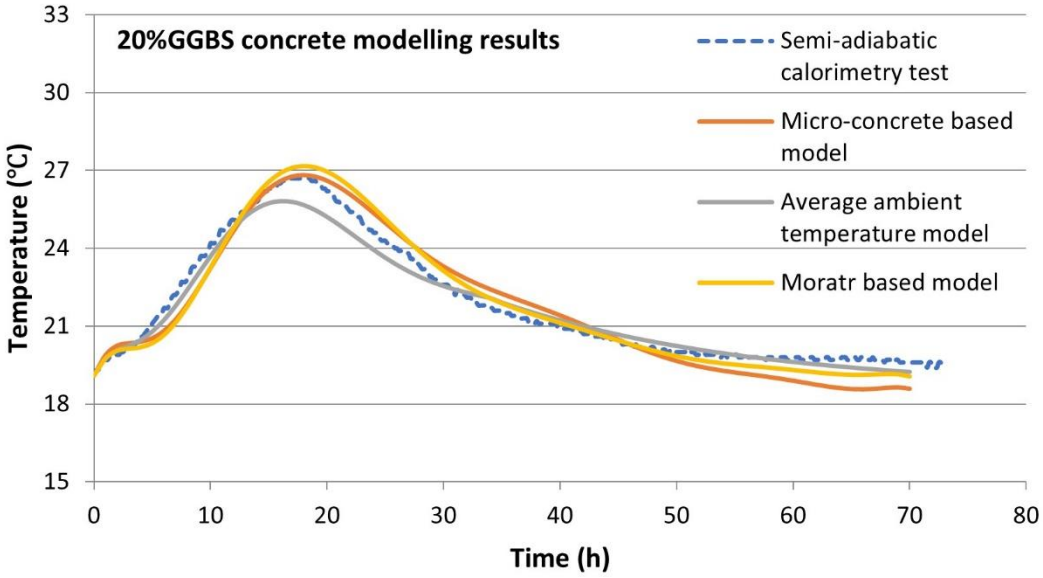

Figure 6.6. 20% GGBS concrete modelling results

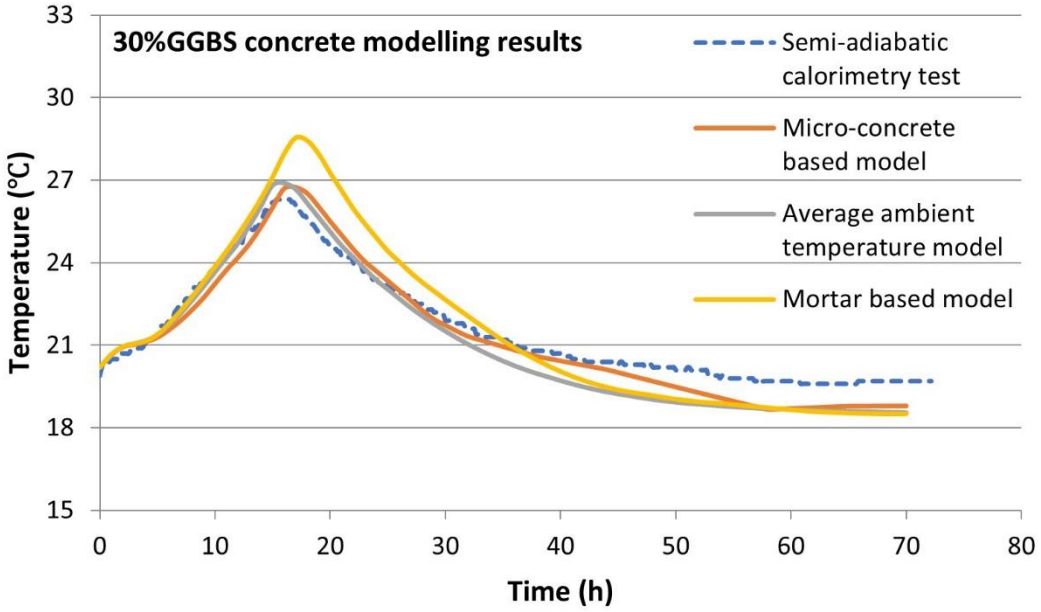

Figure 6.7. 30% GGBS concrete modelling results

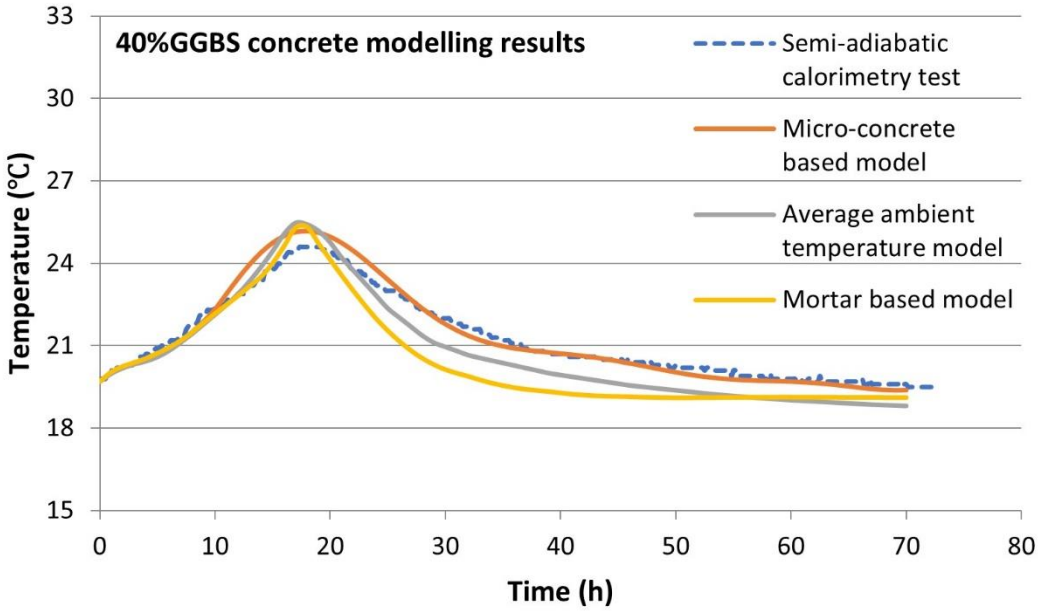

Figure 6.8. 40% GGBS concrete modelling results

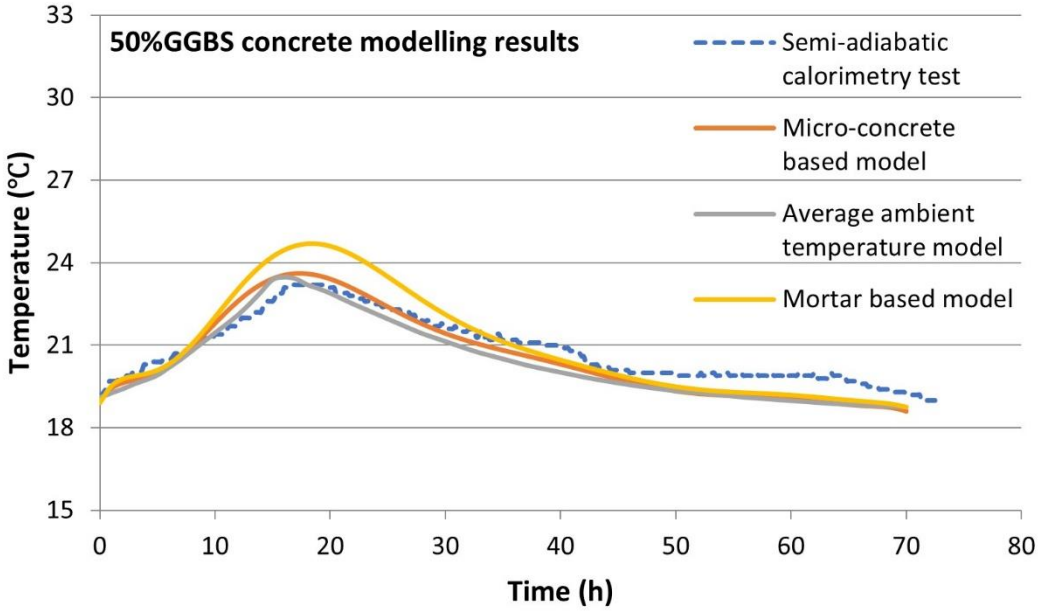

Figure 6.9. 50% GGBS concrete modelling results.

Table 6.2. Peak hydration temperature modelling results

	Concrete peak temperature (°C) modelling results and errors						
GGBS content	Test	Concrete model*	Concrete model error	AVE model*	AVE model error	Mortar model*	Mortar model error
0%	29.65	28.76	3.00%	30.38	2.45%	29.72	0.24%
10%	29.40	29.98	3.03%	30.56	5.03%	28.95	0.50%
20%	26.65	26.82	0.46%	25.82	3.30%	27.17	1.77%
30%	26.10	26.75	2.49%	26.90	3.05%	28.54	9.36%
40%	24.65	25.18	2.35%	25.48	3.56%	25.32	2.91%
50%	23.05	23.61	2.43%	23.48	1.85%	24.69	7.11%

*: Concrete model means the modelling results from the "Micro-concrete based model", AVE model means the modelling results from the" Average ambient temperature model", and Mortar model means the modelling results from the "Mortar based model".

Table 6.3. Time to reach peak hydration temperature modelling results

	Time to reach peak temperature (h) modelling results and errors						
GGBS content	Test	Concrete model	Concrete model error	AVE model	AVE model error	Mortar model	Mortar model error
0%	15.40	16.00	3.90%	15.90	3.24%	16.60	7.79%
10%	14.60	15.00	2.74%	15.00	2.74%	13.90	4.80%
20%	16.60	16.90	1.81%	15.60	6.02%	17.00	2.41%
30%	15.25	15.90	4.26%	15.30	0.33%	16.50	8.20%
40%	17.35	17.30	0.29%	17.20	0.86%	17.30	0.29%
50%	17.30	17.20	0.58%	16.00	7.51%	17.80	2.89%

Table 6.2 and Table 6.3 provide statistical summaries of the peak hydration temperatures and the times to reach these peaks, which are two critical and easily quantifiable parameters in the development of concrete temperature. However, it is important to note that relying solely on these two indictors to evaluate the modelling outcomes would be insufficiently. In this research context, the temperature evolution of the concrete is represented by a continuous curve that spans 72 hours. This curve includes not only the peak temperatures but also significant stages that are less quantifiable, such as the heating and cooling phases of the concrete. These aspects are integral to understanding the full thermal behaviour of concrete and require detailed examination through the visual analysis of the simulated temperature curves rather than through isolated data points. Thus, a holistic evaluation necessitates the consideration of the entire temperature development curve to accurately assess the performance and accuracy of the models used in this study. The following parts of this section will complete the analysis of the three objectives established in this study through three sub-sections.

The results presented in this section provide a comparison of the three FEM approaches used to simulate early-age concrete temperature development. The simulation outcomes for different GGBS content mixes highlight the variations in peak hydration temperature, time to peak, and overall temperature evolution across different modelling conditions. However, a more detailed interpretation is required to fully understand the effects of key influencing factors on the accuracy of the models.

The following subsections offer an in-depth analysis of the primary factors affecting model performance. Section 6.3.1 examines the influence of variable ambient temperatures by comparing models with constant and real-time recorded boundary conditions. Section 6.3.2 investigates the impact of coarse aggregate inclusion on hydration heat development and model accuracy. Finally, Section 6.3.3 evaluates the applicability of the TPE model to GGBS-CEM blended concrete, identifying potential limitations and areas for improvement.

6.3.1 Influence of Boundary Condition on Concrete Temperatures Predictions

In Figure 6.4 to Figure 6.9, the grey curves along with the data labelled "AVE model" in Table 6.2 and Table 6.3 represent the model where the boundary condition for the environmental temperature is not based on actual ambient conditions but is instead set to a constant value. This constant value is the average ambient temperature recorded over a 72-hour period during the semi-adiabatic calorimetry tests. The study compares the results obtained from the "AVE model" with those from the "Concrete model". The analysis aims to evaluate the influence of fluctuating ambient temperatures on the predictive accuracy of concrete temperature development models.

The simulation errors depicted in Table 6.2 and Table 6.3, under the columns labelled "Concrete model error" and "AVE model error", demonstrate that, for the critical parameters of "Peak hydration temperature" and "Time to reach peak hydration temperature", most of the "Concrete model" exhibits higher accuracy compared to the "AVE model". The exceptions are observed in the cases of 0% and 50% GGBS samples, the "AVE model" slightly outperforms the "Concrete model" in simulating the "Peak hydration temperature". Similarly, for the 0% and 30% GGBS samples, the "AVE model" demonstrates marginally better accuracy in predicting the "Time to reach peak hydration temperature". Nevertheless, the errors in the "Concrete Model" for these key parameters remain below 5%, indicating a minimal deviation from the observed values. In contrast, the "AVE model" exhibits several errors exceeding 5%, specifically in the "Peak hydration temperature" for the 10% GGBS concrete and the "Time to reach peak hydration temperature" for the 20% and 50% GGBS concretes.

Figure 6.4 to Figure 6.9 show the temperature development of concrete over 72 hours simulated by different models. The observations clearly illustrate the significant impact of setting boundary conditions to reflect actual ambient temperatures in the models. This impact extends beyond the two specific parameters represented in Table 6.2 and Table 6.3, affecting the entire process of concrete temperature development during the initial 72-hour period examined in this study. It is worth noting that, for all GGBS contents, there are minimal discrepancies between the "AVE model" and the "Concrete model" during the initial heating phase, which lasts approximately 15 hours. The primary differences become evident at the peak temperature and during the subsequent cooling phase. The divergence between the "AVE model" and the "Concrete model" can be attributed to the variability in actual ambient temperatures, as all other significant input parameters, such as heat sources and material properties, are identical. The largest discrepancies are observed in the 20% GGBS concrete and 40% GGBS concrete. In simulations of 20% GGBS concrete, the "AVE model" consistently underestimates temperatures compared to experimental results, particularly in the short period following peak temperature (approximately between 15 to 30 hours). Discrepancies in the 40% GGBS concrete are most pronounced during the cooling

phase, specifically between 20 to 72 hours. The “AVE model” consistently underperforms relative to experimental outcomes. These modelling results indicating a significant impact of environmental temperature fluctuations on the accuracy of concrete temperature models.

In the simulation results for other GGBS contents, it is observed that the accuracy of the “AVE model” consistently lags slightly behind that of the “Concrete model”, although the precision of both models is relatively similar. However, this does not imply that variable ambient temperatures have a negligible impact on the development of concrete temperature; rather, it reflects the minimal fluctuations in ambient temperature during the semi-adiabatic calorimetric tests, which remained within a small range (less than ± 5 °C). In contrast, the ambient temperatures in actual field conditions for curing concrete often vary significantly due to factors such as weather changes (e.g., sharp temperature drops caused by rain or snow and rises due to sunlight) and diurnal temperature variations. These real-world factors, which can cause wide-ranging fluctuations in ambient temperatures, undoubtedly have a significant impact on cement hydration and concrete temperature development. Accurate input of boundary conditions, particularly ambient temperature, is crucial for predicting concrete hydration temperatures within this study. It is also essential for further predictions based on maturity theory for concrete strength, as well as forecasts related to thermal stresses and potential thermal cracking in concrete. The lack of adequate boundary conditions can lead to errors in temperature predictions. The potential errors increase with greater fluctuations in actual ambient temperatures. Thus, ensuring the precise inclusion of variable environmental temperature as a boundary condition is essential for reliable predictions and safe construction practices.

6.3.2 Influence of Coarse Aggregate on Concrete Temperature Predictions

In Section 5.4, isothermal calorimetry tests were carried out on both micro-concrete and equivalent mortar specimens to obtain hydration heat curves of specimens with different GGBS contents at different curing temperatures. By comparing the derived hydration heat development curves and characteristic hydration heat parameters such as apparent activation energy, degree of hydration, and hydration parameters, the test results support the hypothesis of Xu *et al.* [99], that the inclusion of coarse aggregates induces a delay in the cement hydration heat, which becomes more pronounced at higher curing temperatures.

In Figure 6.4 to Figure 6.9, the orange curves represent the model’s heat source derived from micro-concrete sample isothermal calorimetry results, whereas the yellow curves correspond to the equivalent mortar sample-based model. In Table 6.2 and Table 6.3, the “Concrete model” and “Mortar model” refer to the simulation results for the “Peak hydration temperature” and “Time to reach peak hydration temperature”, respectively.

The columns labelled “Concrete model error” and “Mortar model error” represent the discrepancies between these simulation outcomes and the test results.

The data presented in Table 6.2 and Table 6.3 show that in the majority of cases the accuracy of the “Concrete model” is better than that of the “Mortar model” for the key parameters “Peak hydration temperature” and “Time to reach peak hydration temperature”. Exceptions to this trend occur only at 0% and 10% GGBS concentrations for “Peak hydration temperature”, where the “Mortar model” shows slightly better accuracy, although the deviations for the “Concrete model” are marginal, recorded at 3.00% and 3.03% respectively, which are acceptable discrepancies.

As mentioned earlier, focusing solely on these two points from Table 6.2 and Table 6.3 would inadequately assess the overall accuracy of the models. A closer examination of Figure 6.4 to Figure 6.9 clearly illustrates that the “Concrete model” typically offers greater precision across all simulations than the “Mortar model”. Interestingly, except for the 40% GGBS concrete, during the heating phase of the other specimens, the “Mortar model” curves are generally steeper (indicating a larger average slope), which leads to these models reaching peak temperatures earlier (as in the case of the 10% GGBS specimen) or achieving higher peak temperatures (as observed in 0%, 20%, 30%, and 50% GGBS specimens).

This pattern aligns with theoretical expectations, as the heat source part of the concrete temperature FEM modelling is based on the TPE equation (Eq. (2.42)), which includes three hydration parameters that have physical significance and dictate the shape and progression of the hydration heat curve (as detailed in Figure 2.22 to Figure 2.24). Calculations from Section 5.4.5 show that despite the influence of GGBS content and hydration temperature on hydration parameters, almost all the hydration heat time parameter τ is consistently higher for concrete samples compared to their mortar counterparts. This implies a delayed reaction due to the presence of coarse aggregates in concrete, which explains why the “Mortar model” has a steeper temperature rise curve during the heating phase than the “Concrete model”. This observation directly substantiates and supports the hypothesis posited by Xu *et al.* [99] that the delaying effect of coarse aggregates can lead to discrepancies in simulation outcomes.

Moreover, another key factor influencing the difference between the models is the hydration shape parameter β. As analysed in Section 5.4.5, almost all micro-concrete samples exhibit lower β values than their equivalent mortar counterparts. Based on previous literature (Section 2.5.5), an increased β value suggests a more rapid hydration rate during the linear phase. Therefore, equivalent mortar, with a higher β value, exhibits faster cumulative hydration heat development in the early stages compared to micro-concrete, leading to a more rapid temperature increase. This further explains why the “Mortar model” tends to reach peak hydration temperature more quickly than the

"Concrete model".

Figure 6.7 and Figure 6.9 show significant deviations in the simulation results for the "Mortar model" compared to the "Concrete model" for 30% and 50% GGBS concrete. The primary distinction between these models lies in their heat sources: the "Mortar model" derives its heat from equivalent mortar samples in isothermal calorimetry results, while the "Concrete model" utilizes results from micro-concrete samples. This difference is reflected in the hydration parameters input into the FEM models, as specified in Table 5.11 from Section 5.4.5.

As noted in the Section 4.1, the semi-adiabatic calorimetry was conducted in a laboratory environment, which had a limited effect on the hydration reaction. Moreover, the size of the specimens in these experiments (150 mm cubes) is considerably smaller than the concrete used in modern construction such as mass concrete and large-span structures. Therefore, using data derived from equivalent mortar samples to simulate temperature development in large-scale in-situ concrete can result in significantly amplified errors, potentially reaching unacceptable levels. Such inaccuracies in predicting concrete temperature can lead to substantial deviations in subsequent predictions of concrete strength, thermal stress, and potential for thermal cracking, ultimately risking insufficient concrete strength development or incorrect timing for formwork removal, which could lead to safety hazards.

Consequently, this study concludes that the delaying effect of coarse aggregates on hydration heat development in concrete is non-negligible and should be considered when using isothermal calorimetry data to predict in-situ concrete temperature development. For accurate simulation results, it is imperative to utilize micro-concrete samples that fully replicate the actual concrete mix used on site, rather than equivalent mortar or cement paste samples. This approach ensures the reliability of the model predictions, particularly in the context of large-scale concrete applications.

6.3.3 Applicability of TPE Models for GGBS-CEM Blends

This objective primarily addresses the issue of heat sources for the FEM model, focusing not on material concerns such as coarse aggregate as previously discussed, but rather on the mathematical modelling of hydration heat. As discussed in detail in Sections 2.6 and 6.3.2, isothermal calorimetry results cannot be used directly as a heat source for in-situ concrete temperature models but require mathematical transformations. These transformations adjust the data to account for the effects of environmental conditions and the inherent temperature variations of the concrete on the cement hydration rate. In this study, a three-parameter equation (TPE) based on the equivalent age (maturity) of concrete (Eq. (2.42)) was employed. Through a series of mathematical derivations, it was transformed into a formula suitable for use as a time-

dependent heat source in the concrete FEM model (the detailed derivation process is presented in Section 6.1.2.4). This process calculates the equivalent age, degree of hydration, and cumulative hydration heat for each time step using three differential ordinary differential equations (DODEs). These calculations determine the concrete temperature at the end of each time step and the hydration heat rate at the beginning of the next time step. The DODEs are defined within the COMSOL Multiphysics "Mathematics Module" and are integrated with the "Heat Transfer in Solids Module" to form a multi-physics model at the simulation level.

The TPE model used in this study accurately, originally developed for ordinary CEM I cement, may not fully capture the complexities of multi-component cementitious systems. As detailed in Sections 2.2.3.4, and 2.6.3, the hydration process of GGBS-CEM blended mixes differs significantly from that of CEM-only mixes. Initially, in GGBS-CEM mixes, the CEM cement hydrates independently, activating the GGBS only after sufficient alkaline substances are produced by the hydration of CEM. This delayed activation of the GGBS is the main reason why replacing part of the cement with GGBS results in reduced early heat of hydration and strength.

Theoretically, the hydration process of GGBS-CEM blended mixes is more complex than that of CEM-only mixes. Consequently, some researchers [23, 24, 65, 66] argue against using the TPE model to describe the hydration of GGBS-CEM blends, suggesting that its application may compromise the accuracy of the model. This contention underscores the need for cautious application and possible adaptation of the TPE model when used to predict the thermal behaviour of GGBS-CEM blended concrete in practical scenarios.

As Sections 6.3.1 and 6.3.2 have already demonstrated the importance of incorporating precise boundary conditions and heat sources containing coarse aggregates, this section will solely focus on the applicability of the TPE hydration heat model used for the micro-concrete based model. Among the established FEM models (illustrated in Figure 6.4 to Figure 6.9), all micro-concrete based models (represented by orange curves) achieved a high and acceptable level of accuracy. However, a noticeable trend among the models, except for the 0% GGBS specimen, is that the peak hydration temperatures were consistently higher than the experimental measurements. While currently challenging to explain through mathematical derivation alone, this phenomenon may be attributed to the TPE hydration heat model used in this study, which does not account for the two-stage hydration process typical in GGBS-CEM blended mixes. Instead, it is assumed that GGBS participates in hydration from the beginning, which leads to an overestimation of early-stage heat generation and, consequently, higher peak temperatures than that test observed.

A key limitation of the TPE model in this context is its assumption of a single-stage

hydration process, which does not reflect the delayed and prolonged reaction of GGBS. From the hydration parameter analysis in Section 5.4.5, it was observed that the hydration shape parameter (β) is generally smaller for micro-concrete compared to equivalent mortar, which, based on literature review findings (Section 2.5.5), suggests a slower rate of cumulative hydration heat development in the early stages for micro-concrete samples. This implies that in TPE-based FEM simulations, the early-stage heat evolution for GGBS-containing concrete is likely to be overestimated, leading to discrepancies in peak temperature predictions. Additionally, the hydration time parameter (τ) was found to be consistently higher for micro-concrete samples, indicating a more pronounced delay in hydration. These findings further highlight the need for adjustments to the TPE model to better reflect the actual kinetics of GGBS hydration.

Therefore, while the accuracy of the simulation results in this study is commendably high, it is undeniable that there is potential for further optimization. To address these challenges, further research is proposed to develop an enhanced TPE model that explicitly incorporates the two-stage hydration process typical of GGBS-CEM blends. This model will require the adjustment of hydration parameters based on empirical data specific to GGBS-CEM interactions. Additionally, modifications should consider the effects of temperature and GGBS content on the induction period and the long-term hydration rate. The development and validation of this model will require extensive experimental studies and iterative simulations to refine parameter estimates and ensure the model's robustness across a range of compositional and environmental conditions. Future work should also explore alternative mathematical models that can explicitly differentiate between the hydration stages of CEM and GGBS, allowing for a more accurate representation of the hydration heat evolution in blended cement systems.

6.4 Initial Temperature Parametric Analysis

Section 6.3 have validated the FEM model, established based on isothermal calorimetry results of micro-concrete, demonstrating its capability to accurately predict the early hydration temperature development in in-situ concrete containing GGBS. This validated model provides a foundation for further parametric studies investigating the influence of various factors on concrete hydration temperature prediction, such as cement thermal properties, concrete volume, and boundary conditions. A significant real-world phenomenon in in-situ concrete, also the subject of investigation in Section 6.3.1, is the impact of variable ambient temperature on concrete hydration heat. Section 6.3.1 examined the influence of ambient temperature as a boundary condition on the model's accuracy. Another potential impact of ambient temperature on this type of model is on the initial temperature of the concrete, specifically the temperature of fresh, newly mixed concrete, which can affect the FEM model's accuracy. In this study, the initial temperature used in the model is derived from the initial temperature of semi-

adiabatic calorimetry specimens, as described in Section 6.1.2.5. However, the variable ambient temperature conditions at the construction site often result in continuously changing initial temperatures of the fresh concrete before it is placed into the formwork. Thus, failing to accurately and promptly measure the initial temperature of the fresh concrete, and instead assuming a default value (such as a room temperature of 20℃) as the initial temperature of the concrete model, may impact the model's accuracy. Furthermore, as described in Sections 6.1.2.4 and 6.1.2.5, the model is time-dependent, meaning that the results at each time step are determined by the results of the previous time step. Consequently, the final computed results of the model are an iterative process from the initial to the final state. Inaccurate initial values in such a time-dependent model may exacerbate the model's error over time. This section utilizes COMSOL's built-in parametric analysis functionality to investigate the influence of different initial temperatures on the model's accuracy. Using 20% GGBS concrete as an example (Figure 6.6), the measured initial temperature was varied by increasing and decreasing it by 2 ℃ separately, and the model was then run based on the micro-concrete isothermal calorimetry results as the heat source. The results are presented in Figure 6.10. The blue dashed line and the orange curve represent the semi-adiabatic calorimetry test results and the simulation results under the correct initial temperature, respectively. The red and green curves represent the simulation results for initial temperatures increased and decreased by 2℃, respectively. Table 6.4 summarizes the peak hydration temperature and the time required to reach this temperature for the three different initial temperatures, as well as their errors compared to the temperature monitoring results of the concrete samples in the semi-adiabatic calorimeter.

From Figure 6.10, it is evident that increasing the initial temperature (red curve) results in a significantly higher predicted concrete temperature. This not only raises the peak temperature but also causes the peak to be reached earlier. Although the simulation results with the increased initial temperature align closely with the experimental results during part of the cooling phase (20-70h), there are substantial and noticeable discrepancies during the heating phase, at the peak temperature, and in the initial cooling phase (0-20h). Conversely, decreasing the initial temperature (green curve) results in a markedly lower predicted concrete temperature, leading to significant simulation errors. As shown in Figure 6.10, the simulation results with the decreased initial temperature are consistently lower than the experimental results, with no overlapping portions, indicating a low reliability of this simulation outcome. Table 6.4, which summarizes the peak hydration temperature and the time to reach the peak temperature for the three different initial temperatures, reveals that the simulation results with the correct initial temperature achieved the highest accuracy. Both increasing and decreasing the initial temperature led to larger simulation errors for these two hydration temperature characteristics. Notably, the simulation with the decreased initial temperature shows a peak temperature error of 9.87%, and the simulation with the increased initial temperature exhibits a time to reach peak temperature error of

8.43%.

This analysis underscores the critical importance of accurately determining the initial temperature in predictive modelling. The substantial errors observed when deviating from the correct initial temperature highlight the sensitivity of the FEM model to initial conditions, particularly in time-dependent simulations where inaccuracies can propagate and amplify over time. Ensuring accurate initial temperature measurements is therefore essential for enhancing the fidelity and reliability of such models.

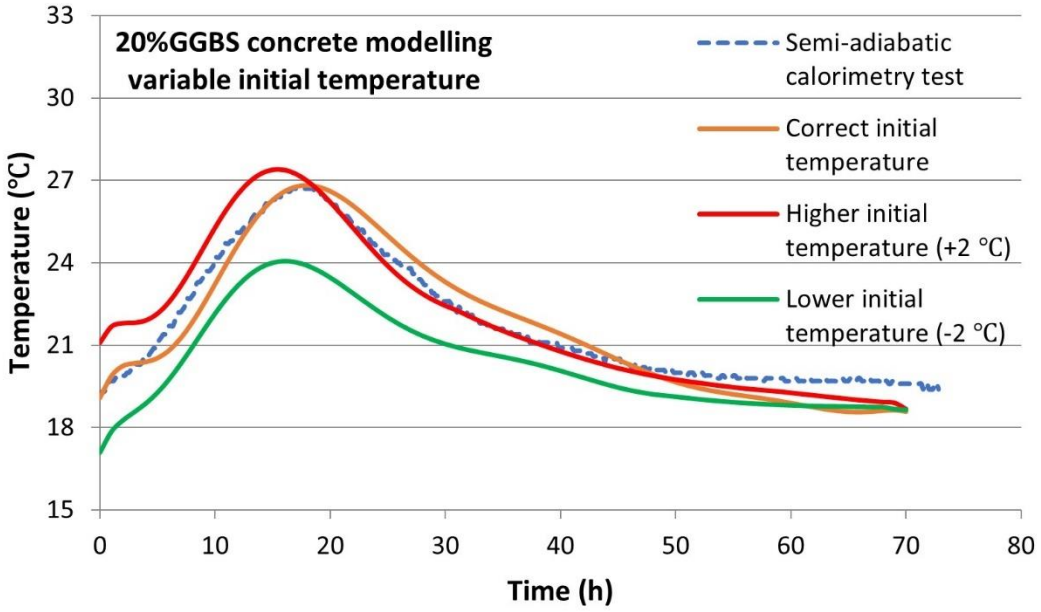

Figure 6.10. Parametric analysis for initial temperature for 20% GGBS concrete

Table 6.4. Peak hydration temperature and Time to reach peak temperature: Parametric analysis for initial temperature for 20% GGBS concrete.

Peak temperature (°C) modelling results and errors						
Test	T_{ini}*	T_{ini} _error	T_{ini} +2*	T_{ini} + 2_error	T_{ini}-2*	T_{ini}- 2_error
26.65	26.82	0.46%	27.39	2.59%	24.06	9.87%
Time to reach peak temperature (h) modelling results and errors						
Test	T_{ini}	T_{ini} _error	T_{ini}+2	T_{ini}+ 2_error	T_{ini}-2	T_{ini}- 2_error
16.60	16.90	1.81%	15.20	8.43%	16.00	3.61

*: T_{ini} represents the simulation results with the correct initial temperature, corresponding to the orange curve in Figure 6.10. T_{ini} +2 represents the simulation results with the initial temperature increased by 2 °C, corresponding to the red curve in Figure 6.10. Similarly, the notation T_{ini}-2 represents the simulation results with the initial temperature decreased by 2 °C, corresponding to the green curve in Figure 6.10.

The term xxx_error represents the error between the simulation results and the semi-adiabatic calorimetry results.

6.5 Conclusion

This study developed and validated a finite element model (FEM) to predict the early-age hydration temperature development of in-situ concrete containing ground granulated blast furnace slag (GGBS). The model incorporated key influencing factors such as variable ambient temperatures, the presence of coarse aggregates, and the applicability of existing hydration heat models originally designed for CEM-only concrete. The modelling approach was based on the isothermal calorimetry test results of micro-concrete and equivalent mortar specimens, with hydration heat data transformed using the Arrhenius equivalent age principle. The model was implemented in COMSOL Multiphysics 6.1, integrating heat transfer analysis with differential ordinary differential equations (DODEs) to simulate hydration heat evolution over time.

The results demonstrated that incorporating variable ambient temperatures as boundary conditions significantly improved the accuracy of the FEM model. While the average ambient temperature model provided reasonable predictions, discrepancies arose particularly in the cooling phase, highlighting the importance of using real-time environmental data to enhance model fidelity. These findings emphasize that ignoring fluctuations in ambient conditions can lead to errors in predicted hydration temperatures, with potential consequences for concrete strength estimation and thermal stress analysis in field applications.

The study also examined the effect of coarse aggregates on hydration heat evolution. Comparison between micro-concrete and equivalent mortar models revealed that the presence of coarse aggregates delays the hydration process, leading to lower peak hydration temperatures and longer times to reach these peaks. The micro-concrete-based model consistently outperformed the equivalent mortar-based model in accuracy, particularly for higher GGBS content specimens. Analysis of hydration parameters confirmed that the hydration shape parameter (β) was generally lower for micro-concrete, resulting in a slower initial hydration rate, while the hydration time parameter (τ) was higher, indicating a more pronounced delay in hydration. These findings underscore the necessity of using micro-concrete rather than equivalent mortar to derive hydration heat data for modelling, particularly in large-scale in-situ concrete applications where thermal cracking risks must be carefully managed.

The applicability of the three-parameter equation (TPE) hydration heat model to GGBS-CEM blended mixes was also evaluated. While the TPE model provided high accuracy in general, it was observed that peak hydration temperatures were consistently overestimated for GGBS-containing concrete. This discrepancy is likely due to the

assumption that GGBS participates in hydration from the beginning, whereas in reality, its activation is delayed due to the need for an alkaline environment generated by CEM hydration. Hydration parameter analysis further supported this conclusion, indicating that early-stage heat release rates for GGBS-CEM blends were likely overestimated by the TPE model. These findings suggest that further refinements to the TPE model are necessary to explicitly incorporate the two-stage hydration mechanism of GGBS, which could be achieved through parameter adjustments informed by empirical data and experimental validation.

A parametric analysis on the influence of initial concrete temperature further confirmed the sensitivity of the FEM model to initial conditions. Variations in initial temperature by just ±2 °C led to significant deviations in peak hydration temperature and time-to-peak predictions, demonstrating that accurate measurement of the fresh concrete temperature is critical for reliable modelling. As the model is time-dependent, errors in the initial conditions propagate over time, amplifying discrepancies in later stages of hydration. This underscores the importance of careful temperature monitoring during concrete mixing and placement to ensure accurate predictions of early-age thermal development.

In summary, this study provides a framework for predicting early-age concrete temperature evolution, integrating experimental hydration heat data with finite element simulations. The findings highlight the necessity of incorporating real-time ambient temperature conditions, using micro-concrete samples for heat source derivation, and refining hydration heat models to better represent GGBS hydration mechanisms. These insights contribute to improving predictive models for mass concrete and large-span structures, ultimately aiding in mitigating thermal cracking risks and optimizing construction practices for long-term structural performance.

CHAPTER 7 CONCLUSIONS AND RECOMMENDATIONS FOR FUTURE WORK

7.1 Summary of Research

This study investigated the early-age hydration temperature development of concrete containing Ground Granulated Blast Furnace Slag (GGBS) through a combination of experimental testing and finite element modelling (FEM). The primary objectives were to examine the influence of variable ambient temperatures, assess the role of coarse aggregates in hydration heat evolution, and evaluate the applicability of existing hydration models to GGBS-CEM blended mixes. To achieve these objectives, semi-adiabatic calorimetry tests, isothermal calorimetry tests, and numerical modelling were conducted.

The experimental works involved semi-adiabatic calorimetry tests, which simulated the hydration temperature development of in-situ concrete with varying GGBS contents (0%, 10%, 20%, 30%, 40%, 50%). The temperature development of the concrete and its surrounding environment was monitored using thermocouples to assess the mitigating effects of GGBS on the hydration temperature development of concrete. Isothermal calorimetry tests, which directly measure the heat output rate of samples under constant temperature curing, were conducted to evaluate the hydration heat development of samples with different GGBS contents at various temperatures (20, 30, 40, 50 °C). To observe the differences in hydration heat between concrete and mortar, this study employed an isothermal calorimeter with a 125 mL capacity, which can contain coarse aggregate, to simultaneously measure micro-concrete samples and equivalent mortar samples, assessing the impact of the inclusion of coarse aggregates on the hydration reaction.

The results from the isothermal calorimetry tests were used to support the heat source for the concrete temperature FEM model. Using an Arrhenius-based equivalent age model, the isothermal calorimetry hydration heat curves were converted to actual concrete hydration heat curves. The temperature monitoring results from the semi-adiabatic calorimetry tests were used to evaluate the accuracy of the concrete temperature model. The simulation work for concrete with each GGBS content employed three different approaches to assess the impacts of variable environmental temperatures, the inclusion of coarse aggregates, and the addition of GGBS on the accuracy of the concrete temperature predictions.

7.2 Summary of Experimental Findings

The experimental findings highlighted several key trends regarding the hydration temperature development of GGBS-containing concrete. The semi-adiabatic

calorimetry tests demonstrated that increasing GGBS content led to a significant reduction in peak hydration temperature and a longer induction period. This effect was particularly pronounced at higher GGBS replacement levels, where the temperature rise was considerably lower than that of CEM I-only concrete. The results confirmed the effectiveness of GGBS in reducing early-age thermal risks in concrete.

The isothermal calorimetry tests provided detailed insights into hydration heat development under different curing temperatures and mix compositions. The results showed that increasing curing temperatures significantly accelerated hydration, leading to higher peak heat release rates and larger cumulative heat at early ages. However, this acceleration effect diminished over longer hydration periods, indicating that elevated temperatures primarily enhance early-stage hydration but do not proportionally increase long-term hydration heat.

The effect of GGBS content was also examined, revealing that higher GGBS replacement ratios resulted in lower peak hydration heat and delayed hydration reactions, particularly at lower curing temperatures. The presence of extra hydration peaks was observed for GGBS-blends, with their prominence increasing as the curing temperature decreased, highlighting the delayed reactivity of GGBS in blended cement systems.

Furthermore, the comparison between micro-concrete and equivalent mortar specimens indicated that the inclusion of coarse aggregates slightly delayed hydration and increased cumulative hydration heat at later stages. The apparent activation energy (E_a) of the hydration reaction was also derived, showing a trend where E_a increased with GGBS content, peaking at 30% GGBS replacement before slightly decreasing. This suggests that GGBS-blended systems exhibit higher temperature sensitivity than cement-only systems. The study also identified variations in hydration parameters, such as hydration shape (β) and time (τ) parameters, further confirming that coarse aggregates contribute to delays in hydration.

7.3 Summary of FEM Modelling Findings

The FEM modelling, developed using isothermal calorimetry data and validated against semi-adiabatic calorimetry results, demonstrated that incorporating variable ambient temperatures as boundary conditions significantly improved the accuracy of the model. The comparison between models using real-time environmental temperature and constant temperature assumptions highlighted the necessity of accurately capturing ambient conditions to achieve reliable temperature predictions.

The influence of coarse aggregates was also assessed through FEM simulations using hydration heat data from micro-concrete and equivalent mortar samples. The results

indicated that using equivalent mortar hydration heat led to overestimated temperature rises, reinforcing the need to incorporate micro-concrete hydration heat data for accurate modelling.

Furthermore, the applicability of the three-parameter equation (TPE) model to GGBS-CEM blended mixes was evaluated. While the TPE model provided generally accurate results, it consistently overestimated peak hydration temperatures for GGBS-containing concrete. This issue likely stems from the model's assumption that GGBS hydration occurs simultaneously with CEM I hydration rather than recognizing its delayed activation. Refinements to hydration models incorporating the two-stage reaction mechanism of GGBS would improve predictive accuracy.

A parametric analysis on the influence of initial concrete temperature confirmed that minor deviations (± 2 °C) in initial temperature significantly impacted peak temperature predictions and hydration timing. This finding emphasizes the necessity of precise temperature monitoring during mixing and placement to ensure accurate FEM simulations.

7.4 Study Limitations and Potential Improvements

Despite addressing key research questions, this study has certain limitations. One major limitation is the incomplete understanding of the influence of coarse aggregates on hydration heat evolution. While micro-concrete samples captured some effects, the underlying mechanisms remain unclear. Advanced material characterization techniques, such as X-ray diffraction (XRD) and thermogravimetric analysis (TGA), could provide further insights into these interactions.

Another limitation is the reliance on the TPE hydration model, which does not fully accommodate the delayed activation of GGBS. Although the model performed well overall, further refinement is needed to incorporate the two-stage hydration mechanism characteristic of GGBS-CEM blends. Future studies should develop modified hydration models tailored to these blended cement systems.

Additionally, this study validated FEM models against laboratory-controlled semi-adiabatic calorimetry results. However, real-world concrete structures experience more complex thermal interactions. Future research should validate these models using field-scale concrete elements, accounting for external heat sources, humidity variations, and interactions with surrounding materials.

7.5 Recommendations for Future Research

Several directions for future research arise from this study's findings. First, further

investigation into the role of coarse aggregates in hydration heat evolution is needed. Techniques such as XRD, TGA, and scanning electron microscopy (SEM) may elucidate how aggregate properties influence cement hydration.

Second, improving hydration models for GGBS-CEM blended mixes should be prioritized. Future work should refine existing models or develop new formulations that explicitly account for the delayed hydration of GGBS. Empirical calibration using a broader range of mix designs and curing conditions would enhance predictive accuracy.

Third, extending FEM validation to field-scale studies is crucial. Deploying temperature sensors in large-scale concrete elements and comparing measured data with simulation results would help refine the model for real-world applications. Understanding the influence of curing methods, formwork insulation, and environmental exposure would further enhance its reliability.

Finally, integrating temperature predictions with thermal stress analysis would provide a more comprehensive assessment of early-age cracking risks. Future research could explore coupling FEM temperature simulations with stress-strain modelling to better predict cracking potential in mass concrete and large-span structures.

References

[1] K. Tang, J. Khatib, G. Beattie, Effect of partial replacement of cement with slag on the early-age strength of concrete, Proceedings of the Institution of Civil Engineers - Structures and Buildings 170(6) (2017) 451-461.
[2] ACI 207.1R-05: Guide to Mass Concrete, American Concrete Institute, Farmington Hills, 2005.
[3] ACI 207.2R-07: Report on Thermal and Volume Change Effects on Cracking of Mass Concrete, American Concrete Institute, Farmington Hills, MI, 2007.
[4] A.M. Lawrence, M. Tia, C.C. Ferraro, M. Bergin, Effect of Early Age Strength on Cracking in Mass Concrete Containing Different Supplementary Cementitious Materials: Experimental and Finite-Element Investigation, Journal of Materials in Civil Engineering 24(4) (2012) 362-372.
[5] K. Tang, S. Millard, G. Beattie, Early-age heat development in GGBS concrete structures, Proceedings of the Institution of Civil Engineers - Structures and Buildings 168(8) (2015) 541-553.
[6] K. Tang, S. Wilkinson, G. Beattie, Effects of curing temperature on the hydration of GGBS concrete and the use of electron microscope particle analysis, Advances in Cement Research 29(8) (2017) 322-335.
[7] R. Balamuralikrishnan, J. Saravanan, Effect of Alccofine and GGBS Addition on the Durability of Concrete, Civil Engineering Journal 5(6) (2019) 1273-1288.
[8] E. Rozière, A. Loukili, E. Hachem, F. Grondin, Durability of concrete exposed to leaching and external sulphate attacks, 39(12) (2009) 1188-1198.
[9] M.R. Akram, S. Raza, Effect of micro silica and ggbs on compressive strength and permeability of impervious concrete as a cement replacement, 3(7) (2015) 7456-7468.
[10] S.P. Mukherjee, G. Vesmawala, S.C. Shah, Exploring GGBS Utilization in Construction of Residential Projects & Its Contribution toward Environment, Journal of Mechanical and Civil Engineering 13(4) (2016) 01-11.
[11] M. Rajaram, A. Ravichandran, A. Muthadhi, Studies on optimum usage of GGBS in concrete, International Journal of Innovative Science and Research Technology 2 (2017) 773-778.
[12] D.J.M. Flower, J.G. Sanjayan, Green house gas emissions due to concrete manufacture, The International Journal of Life Cycle Assessment 12(5) (2007) 282-288.
[13] İ. Şanal, Fresh-state performance design of green concrete mixes with reduced carbon dioxide emissions, Greenhouse Gases: Science and Technology 8(6) (2018) 1134-1145.
[14] M. Tahersima, P. Tikalsky, Finite element modeling of hydration heat in a concrete slab-on-grade floor with limestone blended cement, Constr Build Mater 154 (2017) 44-50.
[15] L. Wadsö, An experimental comparison between isothermal calorimetry, semi-adiabatic calorimetry and solution calorimetry for the study of cement hydration, Final Report, NORDTEST Project 1534-01, 2002.
[16] L. Wadsö, Isothermal calorimetry for the study of cement hydration, Division of

Building Materials, Lund University, 2002.
[17] L. Wadsö, Applications of an eight-channel isothermal conduction calorimeter for cement hydration studies, Cement International 5(5) (2005) 94-101.
[18] Q. Xu, J. Hu, J.M. Ruiz, K. Wang, Z. Ge, Isothermal calorimetry tests and modeling of cement hydration parameters, Thermochimica Acta 499(1-2) (2010) 91-99.
[19] M. Azenha, R. Faria, D. Ferreira, Identification of early-age concrete temperatures and strains: Monitoring and numerical simulation, Cement and Concrete Composites 31(6) (2009) 369-378.
[20] M. Azenha, R. Faria, H. Figueiras, Thermography as a technique for monitoring early age temperatures of hardening concrete, Constr Build Mater 25(11) (2011) 4232-4240.
[21] A. Jedrzejewska, F. Benboudjema, L. Lacarriere, M. Azenha, D. Schlicke, S. Dal Pont, A. Delaplace, J. Granja, K. Hajkova, P.J. Heinrich, G. Sciume, E. Strieder, E. Stierschneider, V. Smilauer, V. Troyan, COST TU1404 benchmark on macroscopic modelling of concrete and concrete structures at early age: Proof-of-concept stage, Constr Build Mater 174 (2018) 173-189.
[22] A. Hatzitheodorou, In-situ strength development of concretes with supplementary cementitious materials, PhD Thesis, University of Liverpool, 2007.
[23] K.A. Riding, J. Vosahlik, K. Bartojay, C.L. Lucero, A. Sedaghat, A. Zayed, C.C. Ferraro, Methodology Comparison for Concrete Adiabatic Temperature Rise, Aci Mater J (2019).
[24] L.E. Al-Hasani, J. Park, G. Perez, H.N. Herndon, J.B. Brown, Y.K. Cho, T.R. Gentry, K.E. Kurtis, Quantifying concrete adiabatic temperature rise based on temperature-dependent isothermal calorimetry; modeling and validation, Materials and Structures 55(7) (2022) 191.
[25] P. Saranya, P. Nagarajan, A.P. Shashikala, Ecofriendly GGBS Concrete: A State-of-The-Art Review, IOP Conference Series Materials Science and Engineering 330 (2019) p. 012057.
[26] B. Li, P. Hou, H. Chen, P. Zhao, P. Du, S. Wang, X. Cheng, GGBS hydration acceleration evidence in supersulfated cement by nanoSiO2, Cement and Concrete Composites 132 (2022) 104609.
[27] COMSOL Multiphysics Reference Manual.
[28] BS EN 197-1:2011: Cement. Composition, specifications and conformity criteria for common cements, British Standards Institution, London, UK, 2011.
[29] M. Thomas, Thomas, M. Supplementary Cementing Materials in Concrete (1st ed.), CRC Press, 2013.
[30] R. Siddique, M.I. Khan, Supplementary cementing materials, Springer Science & Business Media, 2011.
[31] P.K. Mehta, P.J.M. Monteiro, Concrete: Microstructure, Properties, and Materials, 4th ed. ed., McGraw-Hill Education, New York, 2014.
[32] K.H.J. Buschow, R.W. Cahn, M.C. Flemings, B. Ilschner, E.J. Kramer, S. Mahajan, P. Veyssière, Encyclopedia of Materials: Science and Technology, Elsevier, Oxford,

2001, pp. 7768-7773.
[33] S. Mindess, J.F. Young, D. Darwin, Concrete. 2nd Edition, Prentice Hall, 2003.
[34] A.M. Neville, Properties of Concrete. 5th Edition, Longman London, 2011.
[35] P.C. Hewlett, M. Liska, Lea's chemistry of cement and concrete. 5th Edition, Butterworth-Heinemann, 2019.
[36] Z.C. Lu, M. Haist, D. Ivanov, C. Jakob, D. Jansen, S. Leinitz, J. Link, V. Mechtcherine, J. Neubauer, J. Plank, W. Schmidt, C. Schilde, C. Schröfl, T. Sowoidnich, D. Stephan, Characterization data of reference cement CEM I 42.5 R used for priority program DFG SPP 2005 "Opus Fluidum Futurum – Rheology of reactive, multiscale, multiphase construction materials", Data in Brief 27 (2019) 104699.
[37] A.K. Schindler, K.J. Folliard, Heat of hydration models for cementitious materials, Aci Mater J 102(1) (2005) 24-33.
[38] X. Pang, L. Sun, F. Sun, G. Zhang, S. Guo, Y. Bu, Cement hydration kinetics study in the temperature range from 15 °C to 95 °C, Cement and Concrete Research 148 (2021) 106552.
[39] A. De Korte, Hydration and thermal decomposition of cement/calcium sulphate based materials, PhD Thesis, Eindhoven University of Technology, 2015.
[40] D. Marchon, R.J. Flatt, 8 - Mechanisms of cement hydration, Science and Technology of Concrete Admixtures, Woodhead Publishing, 2016, pp. 129-145.
[41] S. Wang, X. Wei, Z. Fan, The Early Hydration Characteristics of Portland Cements with Superplasticizer Using Electrical Measurements, American Journal of Civil Engineering and Architecture 4(5) (2016) 153-158.
[42] I. Ustabas, Ş. Erdoğdu, I. Omur, E. Yilmaz, Pozzolanic Effect on the Hydration Heat of Cements Incorporating Fly Ash, Obsidian, and Slag Additives, Advances in Civil Engineering 2021 (2021) 1-12.
[43] BS EN 15167-1:2006: Ground granulated blast furnace slag for use in concrete, mortar and grout. Part 1–definitions, specifications and conformity criteria, British Standards Institution, London, UK, 2006.
[44] I. Journals, D. Suresh, K. Nagaraju, Ground Granulated Blast Slag (GGBS) In Concrete – A Review, Journal of mechanical civil engineering 12(4) (2015) 76-82.
[45] R. Palod, S. Deo, G.D. Ramtekkar, Review and suggestions on use of steel slag in concrete and its potential use as cementitious component combined with GGBS, International Journal of Civil Engineering and Technology 8 (2017) 1026-1035.
[46] J. Tao, X. Wei, Effect of ground granulated blast-furnace slag on the hydration and properties of cement paste, 31(6) (2019) 251-260.
[47] Q. Wang, M. Miao, J. Feng, P. Yan, The influence of high-temperature curing on the hydration characteristics of a cement–GGBS binder, Advances in Cement Research 24(1) (2012) 33-40.
[48] C. Li, L. Jiang, Utilization of limestone powder as an activator for early-age strength improvement of slag concrete, Constr Build Mater 253 (2020) 119257.
[49] Cementitious Slag Makers Association. (2023). Sustainability. UKCSMA. Retrieved 20 Dec. 2023, from from https://ukcsma.co.uk/sustainability/.

[50] F. Kelly, The Structural Engineer, Volume 101, Issue 7, 2023, Page(s) 24-27.
[51] The Institution of Structural Engineers. (2023). Retrieved 20 Dec. 2023, from https://www.istructe.org/resources/news/news-release/.
[52] American Concrete Institute. ACI 207.2R-9: Effect of Restraint, Volume Change, and Reinforcement on Cracking of Mass Concrete. Farmington Hills, MI: American Concrete Institute; 2010.
[53] S. Wang, W. Zhang, S. Zhang, L. Lu, X. Cheng, Variation of resistance to chloride penetration of iron-rich phosphoaluminate cement with admixture materials subjected to NaCl environment, Constr Build Mater 231 (2020) 117165.
[54] Y. Lee, S. Lim, H. Lee, Chloride resistance of portland cement-based mortar incorporating high aluminate cement and calcium carbonate, Materials 13(2) (2020) 359.
[55] A.K. Yasin, R. Bayuaji, T. Susanto, A review in high early strength concrete and local materials potential, IoP Conference Series: Materials Science and Engineering, IOP Publishing, 2017, p. 012004.
[56] D.P. Bentz, E.J. Garboczi, C.J. Haecker, O.M. Jensen, Effects of cement particle size distribution on performance properties of Portland cement-based materials, Cement and Concrete Research 29(10) (1999) 1663-1671.
[57] J. Byfors, Plain concrete at early ages, (1980).
[58] RILEM 42-CEA, 1981, Properties of set concrete at early ages: State of the art report, Materials and Structures, Vol.14, No. 84, 399-450.
[59] K. Van Breugel, Simulation of Hydration and Formation of Structure in Hardening Cement-based Materials, Cement and Concrete Research 25(3) (1993) 522-530.
[60] S. Mindess, J.F. Young, D. Darwin, Concrete Prentice-Hall, Englewood Cliffs, NJ, 1981.
[61] S.B. Singh, P. Munjal, N. Thammishetti, Role of water/cement ratio on strength development of cement mortar, Journal of Building Engineering 4 (2015) 94-100.
[62] S. Panda, P. Sarkar, R. Davis, Effect of Water-Cement Ratio on Mix Design and Mechanical Strength of Copper Slag Aggregate Concrete, IOP Conference Series: Materials Science and Engineering 936(1) (2020).
[63] D. Whiting, A. Litvin, S.E. Goodwin, Specific Heat of Selected Concretes, ACI Journal Proceedings 75(7) (1978) 299-305.
[64] S. Liu, W. Han, Q. Li, Hydration Properties of Ground Granulated Blast-Furnace Slag (GGBS) Under Different Hydration Environments, Materials Science 23(1) (2017) 70-77.
[65] G. De Schutter, Hydration and temperature development of concrete made with blast-furnace slag cement, Cement and Concrete Research 29(1) (1999) 143-149.
[66] L. Zheng, K. Paine, R. Dhir, Heat evolution and hydration modelling of GGBS cement, International Symposium on Role of Cement Science in Sustainable Development, University of Dundee, Scotland, UK, 2003.
[67] Y. Tan, K. Tang, Modelling In Situ Concrete Temperature Development: The

Impact of Ambient Temperature and GGBS Replacement, CivilEng 5(3) (2024) 694-716.
[68] T.A. Yikici, H.-L. Chen, Use of maturity method to estimate compressive strength of mass concrete, Constr Build Mater 95 (2015) 802-812.
[69] M. Soutsos, A. Hatzitheodorou, J. Kwasny, F. Kanavaris, Effect of in situ temperature on the early age strength development of concretes with supplementary cementitious materials, Constr Build Mater 103 (2016) 105-116.
[70] Z. Liu, W. Jiao, A. Sha, J. Gao, Z. Han, W. Xu, Portland Cement Hydration Behavior at Low Temperatures: Views from Calculation and Experimental Study, Adv Mater Sci Eng 2017 (2017) 3927106.
[71] J. Liu, Y. Li, Y. Yang, Y. Cui, Effect of low temperature on hydration performance of the complex binder of silica fume-portland cement, Journal of Wuhan University of Technology-Mater. Sci. Ed. 29(1) (2014) 75-81.
[72] A. Dabarera, W. Saengsoy, K. Kaewmanee, K. Mori, S. Tangtermsirikul, Models for Predicting Hydration Degree and Adiabatic Temperature Rise of Mass Concrete containing Ground Granulated Blast Furnace Slag, Engineering Journal 21 (2017) 157-171.
[73] D. Jeong, T. Kim, J.-H. Ryu, J. Kim, Analytical model to parameterize the adiabatic temperature rise of concrete, Constr Build Mater 268 (2021) 121656.
[74] Y. Huang, G. Liu, S. Huang, R. Rao, C. Hu, Experimental and finite element investigations on the temperature field of a massive bridge pier caused by the hydration heat of concrete, Constr Build Mater 192 (2018) 240-252.
[75] BS EN 206:2013+A2:2021: Concrete — Specification, performance, production and conformity, British Standards Institution, London, UK, 2013.
[76] ACI 301-20: Specifications for Concrete Construction, American Concrete Institute, Farmington Hills, MI, 2020.
[77] J. Bilčík, R. Sonnenschein, N. Gažovičová, Causes of Early-Age Thermal Cracking of Concrete Foundation Slabs and their Reinforcement to Control the Cracking, J Slovak Journal of Civil Engineering, 25(3) (2017) 8-14.
[78] K. Tang, S. Millard, G. Beattie, Technical and economical feasibility of using GGBS in long-span concrete structures, Advances in concrete construction 3 (2015) 1-14.
[79] O. Adeniji, Cracking of Reinforced and Prestressed Precast Concrete Deck Panels on Florida–I Beam Bridges, Master Thesis, Florida Agricultural and Mechanical University, 2019.
[80] K. Kim, S. Chun, B. Park, S. Han, Precast prestressed concrete pavement (PPCP): Effect of thermal gradient on curling deflection and stress, Constr Build Mater 274 (2021) 121966.
[81] Federal Highway Administration. Thermal cracking of concrete and prevention; 2019 Dec 19. U.S. Department of Transportation: Washington, DC. Retrieved 20 Dec. 2023, from. https://www.fhwa.dot.gov/publications/research/infrastructure/pavements/pccp/therm

al.cfm.
[82] CIP 42-Thermal Cracking of Concrete, National Ready Mixed Concrete Association, Silver Spring, MD, 2020.
[83] M. Ghannam, Proposed models for concrete thermal expansion with different aggregate types and saturation conditions, SN Applied Sciences 1(5) (2019) 425.
[84] Y.-x. Hong, W. Chen, J. Lin, J. Gong, H.-d. Cheng, Thermal field in water pipe cooling concrete hydrostructures simulated with singular boundary method, Water Science and Engineering 10(2) (2017) 107-114.
[85] P.R. Singh, D.C. Rai, Effect of Piped Water Cooling on Thermal Stress in Mass Concrete at Early Ages, American Society of Civil Engineers 144(3) (2018) 04017183.
[86] Q. Ma, R. Guo, Z. Zhao, Z. Lin, K. He, Mechanical properties of concrete at high temperature—A review, Constr Build Mater 93 (2015) 371-383.
[87] L. Edwards, P. Donoghue, Concrete temperatures, a review of requirements, specification, and recent case studies, in: Proceedings of the Concrete NZ Conference 2016, Auckland, New Zealand, 2016.
[88] D. Anupama Krishna, R.S. Priyadarsini, S. Narayanan, High temperature effects on different grades of concrete, Sādhanā 46(1) (2021) 31.
[89] M. Malik, S.K. Bhattacharyya, S.V. Barai, Thermal and mechanical properties of concrete and its constituents at elevated temperatures: A review, Constr Build Mater 270 (2021) 121398.
[90] Y.E. Hao, Y.Q. Lan, Analysis on Setting Joints Technology in the Concrete Structure Buildings, Advanced Materials Research 971 (2014) 2052-2056.
[91] X. Gu, X. Song, F. Lin, C. Li, X. Jin, Cracking behaviour of cast in situ reinforced concrete slabs with control joints, Constr Build Mater 25(3) (2011) 1398-1406.
[92] ACI 224.3R-95: Joints in Concrete Construction, American Concrete Institute, Farmington Hills, MI, 1995.
[93] P. Morabito, Adiabatic and semi adiabatic calorimetry to determine the temperature rise in concrete due to hydration heat of the cement, Materials and Structures 30(8) (1994) 451-464.
[94] BS EN 12390-15:2019: Testing hardened concrete, Part 15: Adiabatic method for the determination of heat released by concrete during its hardening process, British Standards Institution, London, UK, 2019.
[95] B. Klemczak, M. Batog, Heat of hydration of low-clinker cements, Journal of Thermal Analysis and Calorimetry 123(2) (2016) 1351-1360.
[96] C.-k. Lim, J.-K. Kim, T.-S. Seo, Prediction of concrete adiabatic temperature rise characteristic by semi-adiabatic temperature rise test and FEM analysis, Constr Build Mater 125 (2016) 679-689.
[97] Y. Lin, H.-L. Chen, Thermal analysis and adiabatic calorimetry for early-age concrete members, Journal of Thermal Analysis and Calorimetry 122(2) (2015) 937-945.
[98] K. Riding, J.L. Poole, A. Schindler, M.C.G. Juenger, K. Folliard, Evaluation of Temperature Prediction Methods for Mass Concrete Members, Aci Mater J 103 (2006)

357-365.
[99] Q. Xu, J.M. Ruiz, J. Hu, K. Wang, R.O. Rasmussen, Modeling hydration properties and temperature developments of early-age concrete pavement using calorimetry tests, Thermochimica Acta 512(1-2) (2011) 76-85.
[100] BS EN 12390-14:2019: Testing hardened concrete, Part 14: Semi-adiabatic method for the determination of heat released by concrete during its hardening process, British Standards Institution, London, UK, 2019.
[101] P. Fjellström, J.-E. Jonasson, M. Emborg, H. Hedlund, Heat loss compensation for semi-adiabatic calorimetric tests, Nordic Concrete Research 47(1) (2013) 39-60.
[102] P.L. Ng, A.K.H. Kwan, Semi-adiabatic Curing Test with Heat Loss Compensation for Evaluation of Adiabatic Temperature Rise of Concrete, HKIE Transactions 19(4) (2013) 11-19.
[103] K. Madupushpa, N. Kahatapitiya, H. Yapa, Numerical prediction of concrete temperature, Proceedings of the 5th International Symposium on Advances in Civil and Environmental Engineering Practices for Sustainable Development, 2017, pp. 347-354.
[104] BS EN 196-11:2018: Methods of testing cement - Part 11: Heat of hydration - Isothermal Conduction Calorimetry method, British Standards Institution, London, UK, 2018.
[105] ASTM C1702-09a, Standard Test Method for Measurement of Heat of Hydration of Hydraulic Cementitious Materials Using Isothermal Conduction Calorimetry, ASTM International, West Conshohocken, PA, 2009.
[106] TAM Air Getting Started Guide.
[107] A. Kuryłowicz-Cudowska, E. Haustein, Isothermal Calorimetry and Compressive Strength Tests of Mortar Specimens for Determination of Apparent Activation Energy, Journal of Materials in Civil Engineering 33(4) (2021) 04021035.
[108] Y. Tan, K. Tang, Finite element modeling of early-age temperature development of in-situ concrete under variable ambient temperatures, Materials Today: Proceedings (2023).
[109] J. Arcenegui-Troya, P.E. Sánchez-Jiménez, A. Perejón, L.A. Pérez-Maqueda, Determination of the activation energy under isothermal conditions: revisited, Journal of Thermal Analysis and Calorimetry 148(4) (2023) 1679-1686.
[110] H. Kada-Benameur, E. Wirquin, B. Duthoit, Determination of apparent activation energy of concrete by isothermal calorimetry, Cement and Concrete Research 30(2) (2000) 301-305.
[111] S.R. Yan, Y. Sun, W.Y. Kuang, K.Q. Wang, Determination of the apparent activation energy for composite binder containing blast furnace ferronickel slag, Journal of Thermal Analysis and Calorimetry 148(15) (2023) 7597-7610.
[112] G. Leon, H.-L. Chen, Thermal Analysis of Mass Concrete Containing Ground Granulated Blast Furnace Slag, CivilEng 2(1) (2021) 254-271.
[113] T.D. Anton K. Schindler, and B. F. McCullough, Temperature Control During Construction to Improve the Long Term Performance of Portland Cement Concrete Pavements, Center for Transportation Research, The University of Texas at Austin,

3208 Red River, Suite 200, Austin, 2002.
[114] K.-H. Kim, S.-E. Jeon, J.-K. Kim, S. Yang, An experimental study on thermal conductivity of concrete, Cement and Concrete Research 33(3) (2003) 363-371.
[115] O. Büyüköztürk, M.A. Taşdemir, D. Mikulić, B. Milovanović, I. Gabrijel, Analysis of Thermal Properties of Cement Paste During Setting and Hardening, Nondestructive testing of materials and structures, Springer, 2013, pp. 465-471.
[116] B. Chen, B. Guan, X. Lu, B. Tian, Y. Li, Thermal conductivity evolution of early-age concrete under variable curing temperature: Effect mechanism and prediction model, Constr Build Mater 319 (2022) 126078.
[117] H. Wang, C. Qi, W. Lopez, H. Farzam, Use of isothermal conduction calorimetric method for measuring the heat of hydration of cement, Journal of ASTM International 6(10) (2009) 1-9.
[118] ASTM C186-05, Standard Test Method for Heat of Hydration of Hydraulic Cement, ASTM International, West Conshohocken, PA, 2005.
[119] ASTM C1074-19e1, Standard Practice for Estimating Concrete Strength by the Maturity Method, ASTM International, West Conshohocken, PA, 2019.
[120] A.G.A. Saul, Principles underlying the steam curing of concrete at atmospheric pressure, Magazine of Concrete Research 2(6) (1951) 127-140.
[121] S. Wade, Evaluation of the maturity method to estimate concrete strength, PhD Thesis, Auburn University, 2005.
[122] C.H. Lee, K. Hover, Compatible Datum Temperature and Activation Energy for Concrete Maturity, Aci Mater J 113(2) (2016) 197-207.
[123] N.J. Carino, The Maturity Method: Theory and Application, Cement, Concrete and Aggregates 6(2) (1984) 61-73.
[124] M. Soutsos, F. Kanavaris, Applicability of the Modified Nurse-Saul (MNS) maturity function for estimating the effect of temperature on the compressive strength of GGBS concretes, Constr Build Mater 381 (2023) 131250.
[125] M. Soutsos, F. Kanavaris, The modified nurse-saul (MNS) maturity function for improved strength estimates at elevated curing temperatures, Case Studies in Construction Materials 9 (2018) e00206.
[126] E. Rastrup, Heat of hydration in concrete, Magazine of concrete research 6(17) (1954) 79-92.
[127] R.C. Tank, N.J. Carino, Rate constant functions for strength development of concrete, Materials Journal 88(1) (1991) 74-83.
[128] Z. Ge, Predicting temperature and strength development of the field concrete, PhD Thesis, Iowa State University, Ames, Iowa 2005.
[129] B.K. Roy, Evaluation of Concrete Strength using Maturity Method, MTech Thesis, National Institute of Technology, Rourkela, India, 2018.
[130] D. Miller, N.-M. Ho, N. Talebian, Monitoring of in-place strength in concrete structures using maturity method–An overview, Structures 44 (2022) 1081-1104.
[131] J.M. Nixon, A.K. Schindler, R.W. Barnes, S.A. Wade, Evaluation of the Maturity Method to Estimate Concrete Strength in Field Applications, ALDOT Research Project,

Alabama Department of Transportation, Auburn University, 2008.
[132] R. Kumar, G.V. Kumar, C.S.K. Raju, S.A. Shehzad, S.V.K. Varma, Analysis of Arrhenius activation energy in magnetohydrodynamic Carreau fluid flow through improved theory of heat diffusion and binary chemical reaction, Journal of Physics Communications 2(3) (2018) 035004.
[133] T. Ratajczak, S. Kurkiewicz, J. Drzymała, A procedure of Arrhenius activation energy determination for salt flotation of particles in the vicinity of one molar salt aqueous solutions, Physicochemical Problems of Mineral Processing 56(6) (2020) 1-5.
[134] G. Li, Y. Yuan, J. Du, Y. Ji, Determination of the apparent activation energy of concrete carbonation, Journal of Wuhan University of Technology-Mater. Sci. Ed. 28(5) (2013) 944-949.
[135] L. D'Aloia, G. Chanvillard, Determining the "apparent" activation energy of concrete: Ea—numerical simulations of the heat of hydration of cement, Cement and Concrete Research 32(8) (2002) 1277-1289.
[136] F.H. P, Pedersen.E.J, Curing of Concrete Structures, Draft DEBGuide to Durable Concrete Structures, Appendix 1, Comité Euro-International du Béton, Lausanne, Switzerland, 1985.
[137] Malhotra, V.M., & Carino, N.J. (2003). Handbook on Nondestructive Testing of Concrete (2nd ed.). CRC Press. https://doi.org/10.1201/9781420040050.
[138] P.F. Hansen, E.J. Pedersen, Maturity computer for controlled curing and hardening of concrete, 10044 Stockholm 70, Sweden, 1977.
[139] E. Martinelli, E.A.B. Koenders, A. Caggiano, A numerical recipe for modelling hydration and heat flow in hardening concrete, Cement and Concrete Composites 40 (2013) 48-58.
[140] H. Reinhardt, J. Blaauwendraad, J. Jongedijk, Temperature development in concrete structures taking account of state dependent properties, Proc. International Conference of Concrete at Early Ages, Paris, France, 1982.
[141] N. J.Carino, Temperature Effects on the Strength–Maturity Relation of Mortar, Report No. NBSIR 81-2244, 1981.
[142] N. J.Carino, H. S.Lew, The maturity method: From theory to application, Cement, Concrete, and Aggregates 6(2) (1984) 61-73.
[143] H. Reinhardt, J. Blaauwendraad, J. Jongedijk, Temperature development in concrete structures taking account of state dependent properties, Proceedings of the 7th International Congress on the chemistry of cements Paris, France, 1982.
[144] E. Gauthier, M. Regourd, The hardening of cement in function of temperature, Proceedings of the RILEM International Conference on Concrete at Early Ages
Ecole Nationale des Ponts et Chausses, Paris, 1982, pp. 145-150.
[145] M. Geiker, Studies of Portland cement hydration by measurements of chemical shrinkage and a systematic evaluation of hydration curves by means of the dispersion model, PhD Thesis, Technical University of Denmark, 1983.
[146] M. Geiker, T. Knudsen, Chemical Shrinkage of Portland Cement Pastes, Cement and Concrete Research 12(5) (1982) 603-610.

[147] D. Roy, Hydration, structure, and properties of blast furnace slag cements, mortars, and concrete, Journal Proceedings, 1982, pp. 444-457.
[148] S.J. Barnett, M.N. Soutsos, S.G. Millard, J.H. Bungey, Strength development of mortars containing ground granulated blast-furnace slag: Effect of curing temperature and determination of apparent activation energies, Cement and Concrete Research 36(3) (2006) 434-440.
[149] R.C. Tank, The rate constant model for strength development of concrete, Polytechnic University, 1988.
[150] W.R.L. da Silva, Šmilauer, Vít, Štemberk, Petr, Upscaling semi-adiabatic measurements for simulating temperature evolution of mass concrete structures, Materials and Structures 48(4) (2013) 1031-1041.
[151] P.J. Andersen, M.E. Andersen, D. Whiting, A guide to evaluating thermal effects in concrete pavements, 1992.
[152] R.H. Bogue, The chemistry of Portland cement, Reinhold publishing corporation, 1947.
[153] T. Kishi, K. Maekawa, F. Spon, Thermal Cracking in Concrete at Early Ages, Proceeeding of the International RILEM Symposium, London, UK, 1994, pp. 11-18.
[154] G. Walenta, T. Füllmann, Advances in quantitative XRD analysis for clinker, cements, and cementitious additions, Powder Diffraction 19(1) (2004) 40-44.
[155] R.K. Bamrah, Evaluation of X-ray Fluorescence Spectroscopy as a tool for Element Analysis in Pea Seeds, University of Saskatchewan, 2018.
[156] S. Khelifi, F. Ayari, H. Tiss, D.B. Hassan Chehimi, X-ray fluorescence analysis of Portland cement and clinker for major and trace elements: accuracy and precision, Journal of the Australian Ceramic Society 53 (2017) 743-749.
[157] M. Azenha, Numerical simulation of the structural behaviour of concrete since its early ages, PhD Thesis, University of Porto, 2009.
[158] M. Azenha, C. Sousa, R. Faria, A. Neves, Thermo–hygro–mechanical modelling of self-induced stresses during the service life of RC structures, Engineering Structures 33(12) (2011) 3442-3453.
[159] J. Baron, J. Byfors, Properties of set concrete at early ages state-of-the-art-report, Mater. Struct 14 (1981) 399-450.
[160] T.C. Hansen, Physical structure of hardened cement paste. A classical approach, Materials and Structures 19(6) (1986) 423-436.
[161] R. Mills, Factors influencing cessation of hydration in water cured cement pastes, Highway Research Board Special Report, 1966.
[162] M. Cervera, J. Oliver, T. Prato, Thermo-Chemo-Mechanical Model for Concrete. I: Hydration and Aging, Journal of Engineering Mechanics 125(9) (1999) 1018-1027.
[163] W.R.L. da Silva, V. Šmilauer, Fuzzy affinity hydration model, Journal of Intelligent & Fuzzy Systems 28(1) (2015) 127-139.
[164] G. Sidebotham, Heat Transfer Modeling, Heat Transfer Modeling: An Inductive Approach, Springer International Publishing, Cham, 2015, pp. 61-93.
[165] P.B. Bamforth, Early-age thermal crack control in concrete, CIRIA, London,

2007.
[166] K. Riding, J. Poole, A. Schindler, M. Juenger, K. Folliard, Temperature Boundary Condition Models for Concrete Bridge Members, Aci Mater J 104(4) (2007) 379-387.
[167] D. Ting, Thermofluids: from nature to engineering, Academic Press, 2022.
[168] R.H.S. Winterton, Newton's law of cooling, Contemporary Physics 40(3) (1999) 205-212.
[169] J.A. Duffie, W.A. Beckman, Solar engineering of thermal processes, John Wiley & Sons, New York, 1980.
[170] L.E. Nevander, B. Elmarsson, Fukthandbok: praktik och teori, Svensk byggtjänst, 1994.
[171] B.F. McCullough, Fast-track paving: concrete temperature control and traffic opening criteria for bonded concrete overlays, Federal Highway Administration, 1999.
[172] R.W. Bliss Jr, Atmospheric radiation near the surface of the ground: a summary for engineers, Solar Energy 5(3) (1961) 103-120.
[173] W. McAdams, Heat Transmission, New York, 1954.
[174] A. Surahyo, Physical Properties of Concrete, in: A. Surahyo (Ed.), Concrete Construction: Practical Problems and Solutions, Springer International Publishing, Cham, 2019, pp. 61-88.
[175] P.K. Mehta, P.J.M. Monteiro, Concrete: Microstructure, Properties, and Materials, 2005.
[176] J. Chan, Thermal properties of concrete with different Swedish aggregate materials, Master Thesis, Division of Building Engineering, Lund University, 2014.
[177] W. Zhang, H. Min, X. Gu, Y. Xi, Y. Xing, Mesoscale model for thermal conductivity of concrete, Constr Build Mater 98 (2015) 8-16.
[178] R. Demirboğa, Thermal conductivity and compressive strength of concrete incorporation with mineral admixtures, Building and Environment 42(7) (2007) 2467-2471.
[179] D. Mikulić, B. Milovanović, I. Gabrijel, Analysis of Thermal Properties of Cement Paste During Setting and Hardening, Nondestruct Test Mater Struct 6 (2013).
[180] T.D. Brown, M. Javaid, The thermal conductivity of fresh concrete, Matériaux et Construction 3 (1970) 411-416.
[181] G. De Schutter, L. Taerwe, Specific-Heat and Thermal-Diffusivity of Hardening Concrete, Magazine of Concrete Research 47 (1995) 203-208.
[182] A.K. Schindler, Concrete hydration, temperature development, and setting at early-ages, The University of Texas at Austin, 2002.
[183] Properties of set concrete at early ages state-of-the-art-report, Matériaux et constructions 14(6) (1981) 399-450.
[184] P.B. Bamforth, Properties of Concrete for Use in Eurocode 2: How to Optimise the Engineering Properties of Concrete in Design to Eurocode 2, Concrete Center, 2008.
[185] Eurocode 2: Design of Concrete Structures : Part 1-1: General Rules and Rules for Buildings, British Standards Institution, London, UK, 2005.
[186] A.A. Khan, W.D. Cook, D. Mitchell, Thermal Properties and Transient Thermal

Analysis of Structural Members During Hydration, Materials Journal 95(3) (1998) 293-303.
[187] A.L. David Whiting, E.G. Stanley, Specific Heat of Selected Concretes, ACI Journal Proceedings 75(7) (1978) 299-305.
[188] K. Van Breugel, Prediction of temperature development in hardening concrete, RILEM REPORT, 1998.
[189] J.E. Jonasson, Modelling of temperature, moisture and stresses in young concrete, PhD Thesis, Lulea University of Technology, 1994.
[190] L. Buffo-Lacarrière, A. Sellier, G. Escadeillas, A. Turatsinze, Multiphasic finite element modeling of concrete hydration, Cement and Concrete Research 37(2) (2007) 131-138.
[191] V.V. Troyan, Prediction of crack resistance of massive concrete structures based on cements different types, Modern Tech. Technol (2) (2015) 89-91.
[192] V. Šmilauer, L. Baquerizo, T. Matschei, P. Havlásek, W.L. Da Silva, K. Hájková, ConTemp–A virtual thermo-mechanical simulator for hydrating reinforced concrete blocks with extension to service life, Service Life of Cement-Based Materials (2016) 463-472.
[193] BS EN 196-2:2013: Method of testing cement. Chemical analysis of cement, British Standards Institution, London, UK, 2013.
[194] Heidelberg Materials UK. Regen GGBS. Heidelberg Materials: United Kingdom. Retrieved 20 Dec. 2023, from. https://www.heidelbergmaterials.co.uk/en/products/regen-ggbs.
[195] BS EN 933-1:2012: Tests for geometrical properties of aggregates. Determination of particle size distribution. Sieving method, British Standards Institution, London, UK, 2012.
[196] BS EN 12620:2013: Aggregates for concrete, British Standards Institution, London, UK, 2013.
[197] AASHTO T 85: Standard Method of Test for Specific Gravity and Absorption of Coarse Aggregate, American Association of State Highway and Transportation Officials, Washington, DC, 2022.
[198] AASHTO T 84: Standard Method of Test for Specific Gravity and Absorption of Fine Aggregate, American Association of State Highway and Transportation Officials, Washington, DC, 2022.
[199] BS EN 1008:2002: Mixing water for concrete. Specification for sampling, testing and assessing the suitability of water, including water recovered from processes in the concrete industry, as mixing water for concrete, British Standards Institution, London, UK, 2002.
[200] BS 8500-1:2015: Concrete. Complementary British Standard to BS EN 206. Method of specifying and guidance for the specifier, British Standards Institution, London, UK, 2015.
[201] BS EN 12350-2:2019: Testing fresh concrete. Slump-test, British Standards Institution, London, UK, 2019.

[202] BS EN 12390-1:2021: Testing hardened concrete. Shape, dimensions and other requirements for specimens and moulds, British Standards Institution, London, UK, 2021.
[203] BS 1881-125:2013: Testing concrete. Methods for mixing and sampling fresh concrete in the laboratory, British Standards Institution, London, UK, 2013.
[204] BS EN 12390-3:2019: Testing hardened concrete, Part 3: Compressive strength of test specimens, British Standards Institution, London, UK, 2019.
[205] BS EN 12390-4:2019: Testing hardened concrete, Part 4: Compressive strength. Specification for testing machines, British Standards Institution, London, UK, 2019.
[206] ASTM C1679, Standard Practice for Measuring Hydration Kinetics of Hydraulic Cementitious Mixtures Using Isothermal Calorimetry, ASTM International, West Conshohocken, PA, 2022.
[207] X. Pang, D.P. Bentz, C. Meyer, G.P. Funkhouser, R. Darbe, A comparison study of Portland cement hydration kinetics as measured by chemical shrinkage and isothermal calorimetry, Cement and Concrete Composites 39 (2013) 23-32.
[208] A. Kuryłowicz-Cudowska, E. Haustein, Isothermal Calorimetry and Compressive Strength Tests of Mortar Specimens for Determination of Apparent Activation Energy, Journal of Materials in Civil Engineering 33(4) (2021).

APPENDIX A Isothermal Calorimetry Micro-concrete and Equivalent Mortar Sample at 20 °C

This section presents the results of the simultaneous measurements of micro-concrete and equivalent mortar specimens at 20 °C (hydration heat and hydration degree). These results are placed in the appendix rather than in the main text (Section 6.4.2) because the hydration heat and degree development curves for micro-concrete and equivalent mortar at 20°C are nearly identical, making them indistinguishable.

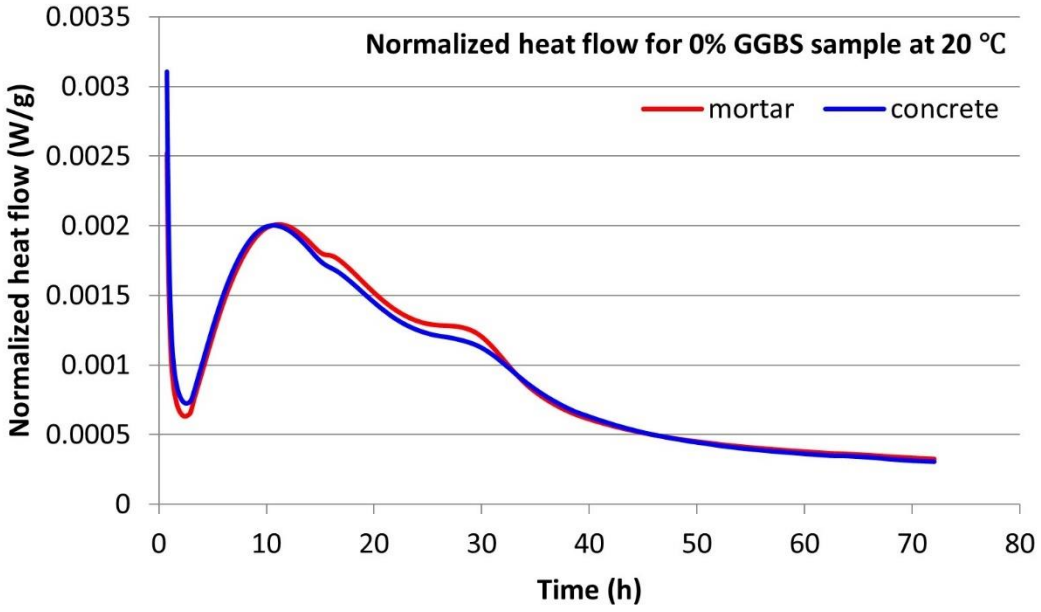

(a)

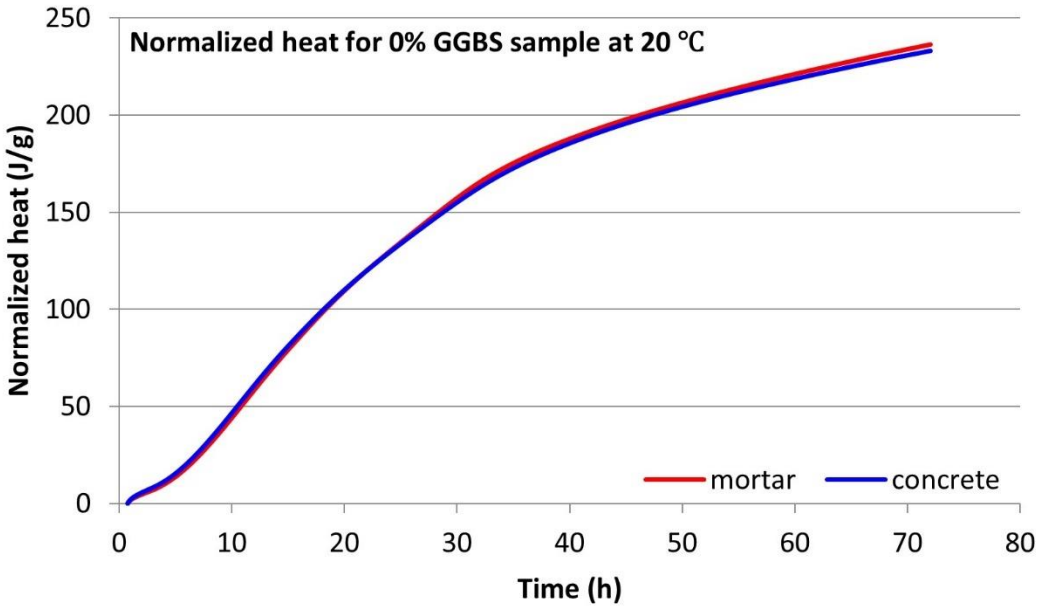

(b)

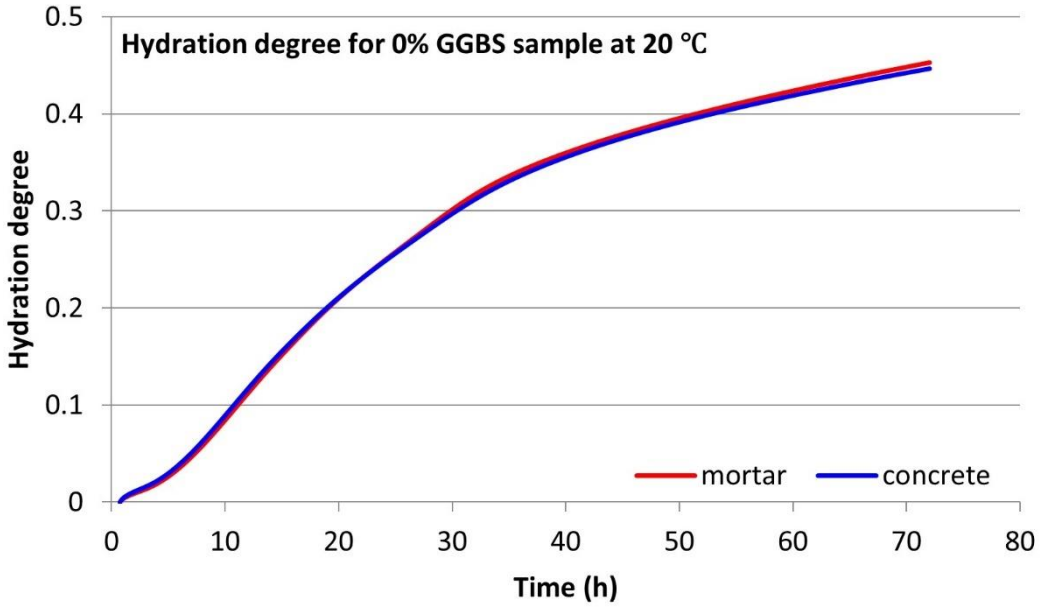

(c)

Figure A.1. Isothermal calorimetry test for 0% GGBS sample: (a) Normalized hydration heat flow; (b) Normalized hydration heat; (c) Hydration degree.

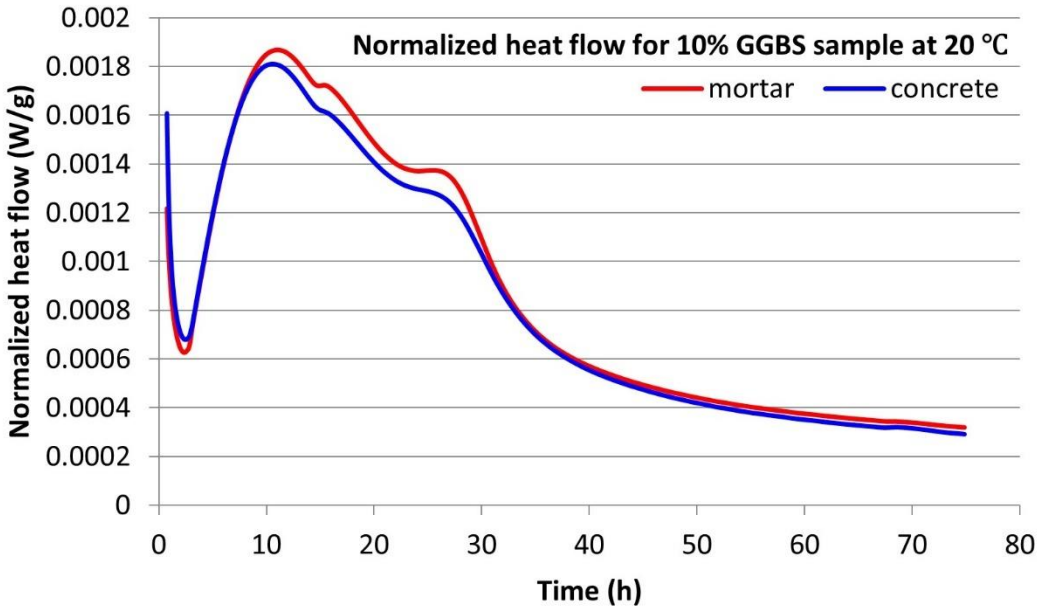

(a)

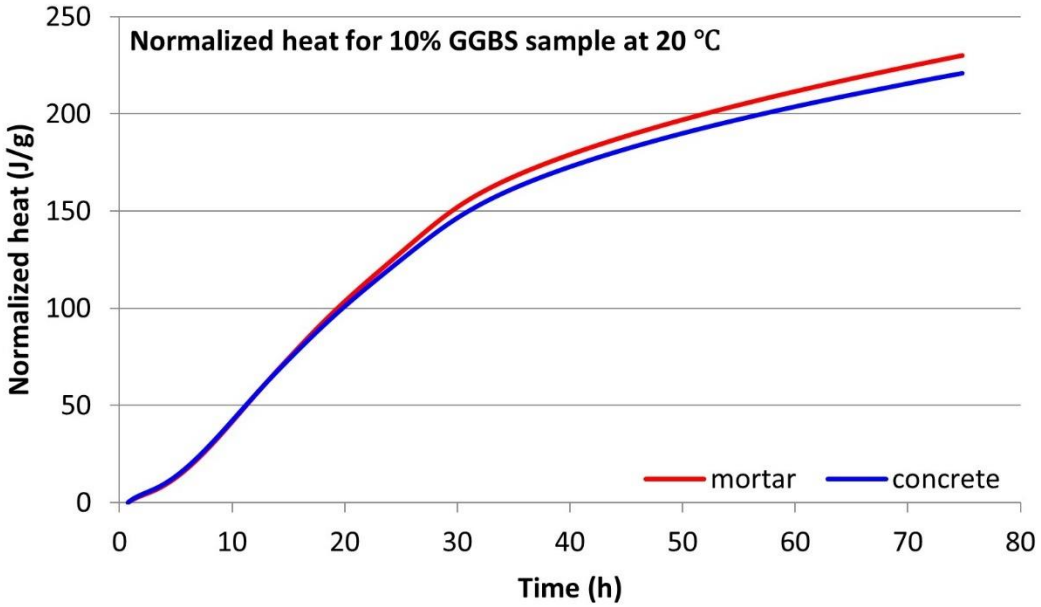

(b)

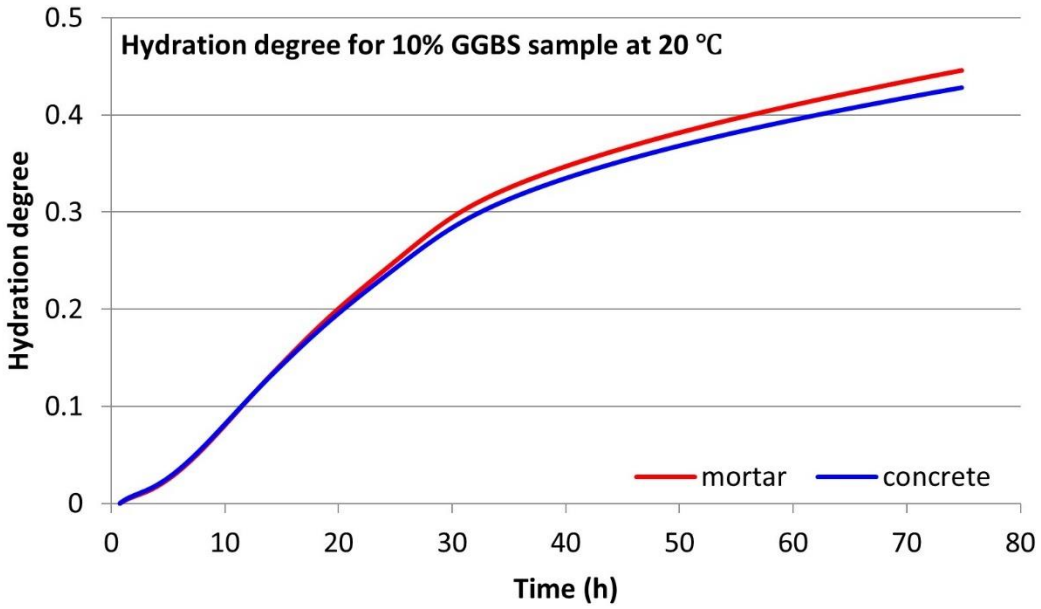

(c)

Figure A.2. Isothermal calorimetry test for 10% GGBS sample: (a) Normalized hydration heat flow; (b) Normalized hydration heat; (c) Hydration degree.

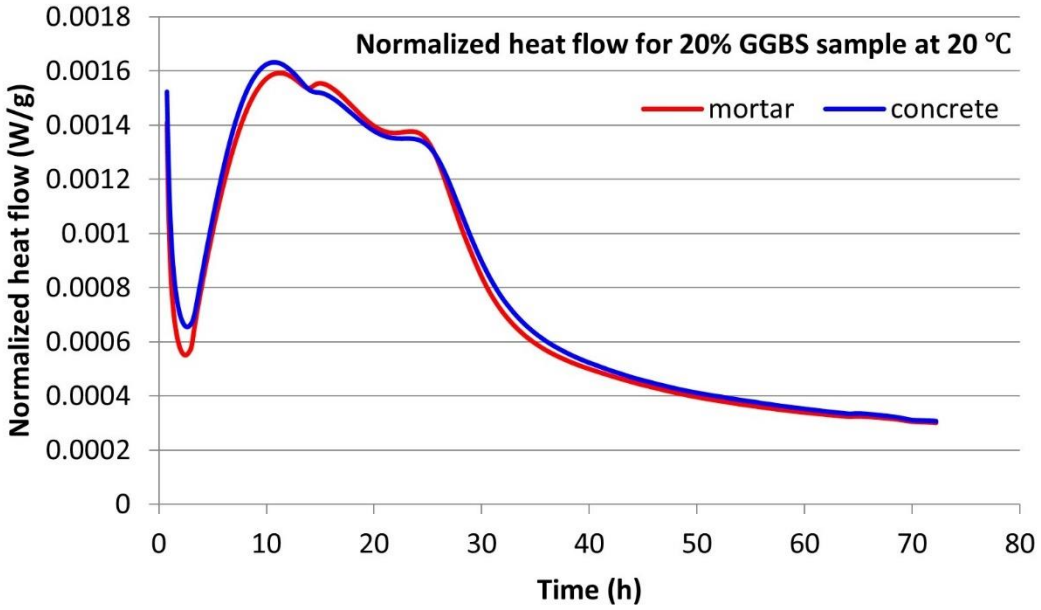
Normalized heat flow for 20% GGBS sample at 20 ℃
mortar
concrete
Normalized heat flow (W/g)
0.0018
0.0016
0.0014
0.0012
0.001
0.0008
0.0006
0.0004
0.0002
0
0
10
20
30
40
50
60
70
80
Time (h)

(a)

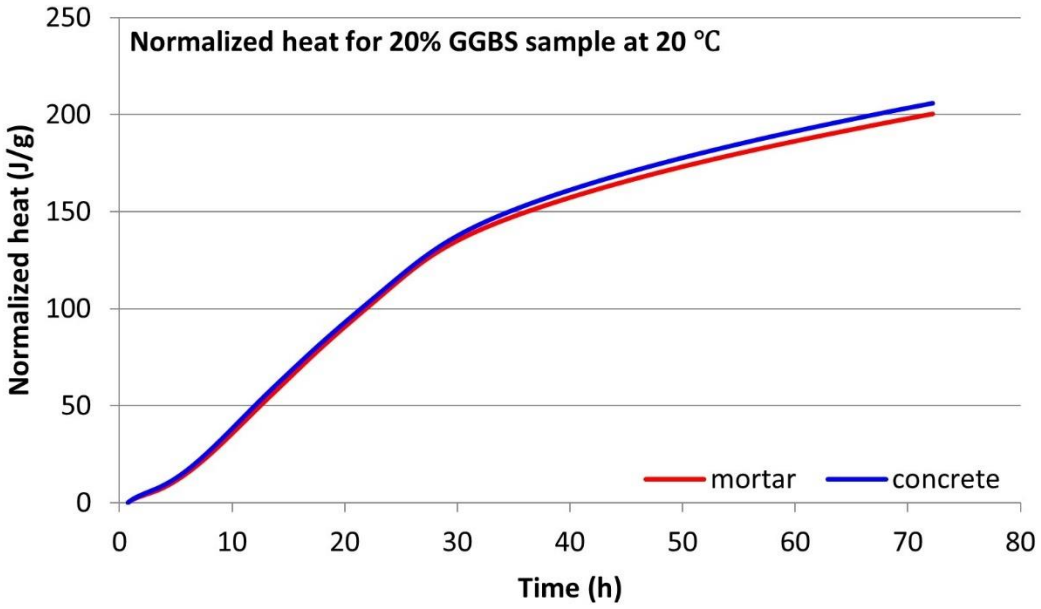
Normalized heat for 20% GGBS sample at 20 ℃
Normalized heat (J/g)
250
200
150
100
50
0
mortar
concrete
0
10
20
30
40
50
60
70
80
Time (h)

(b)

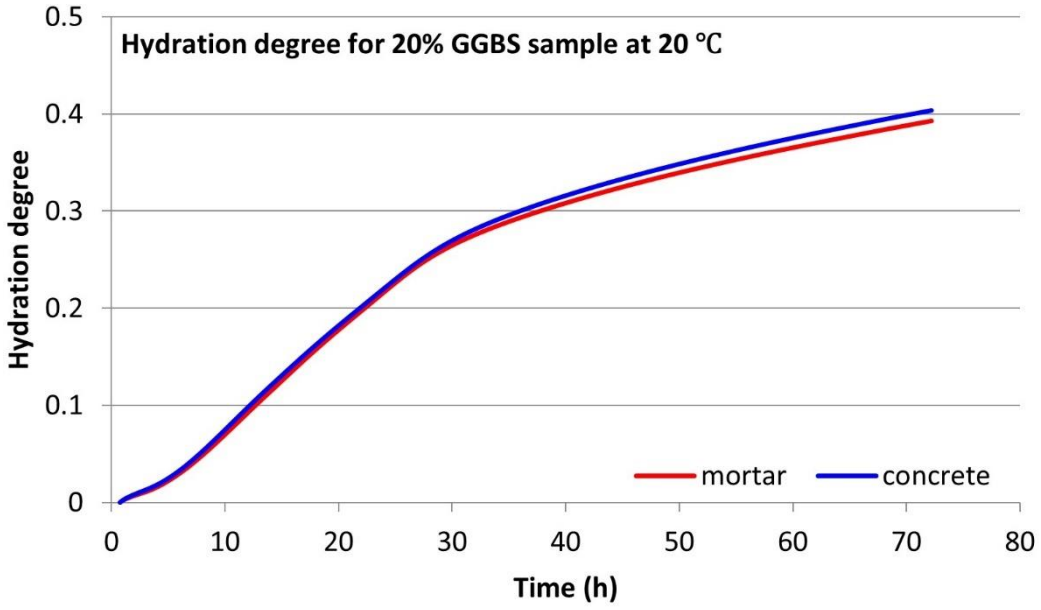

(c)

Figure A.3. Isothermal calorimetry test for 20% GGBS sample: (a) Normalized hydration heat flow; (b) Normalized hydration heat; (c) Hydration degree.

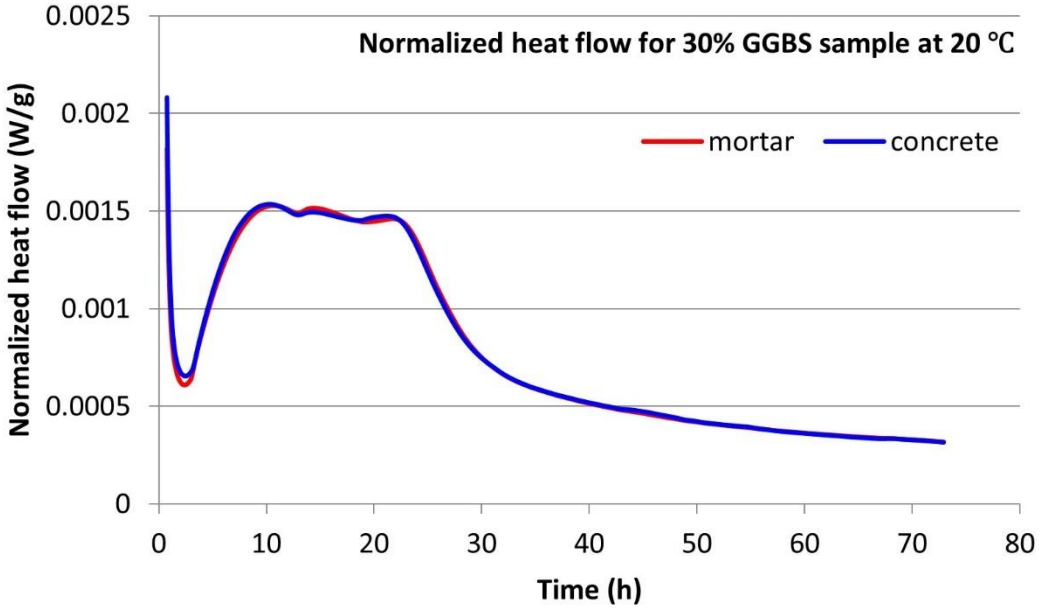

(a)

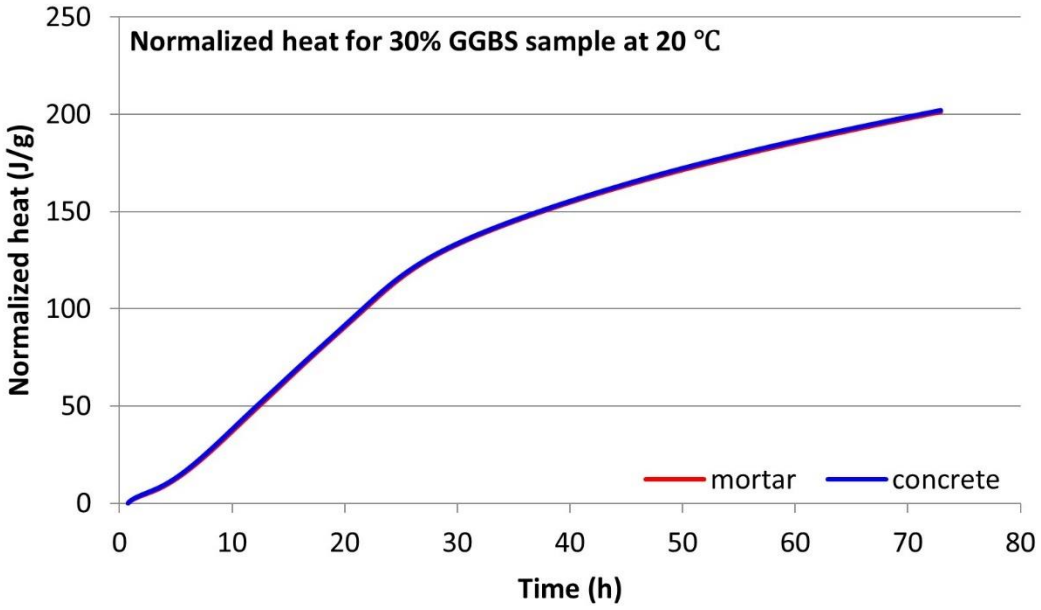

(b)

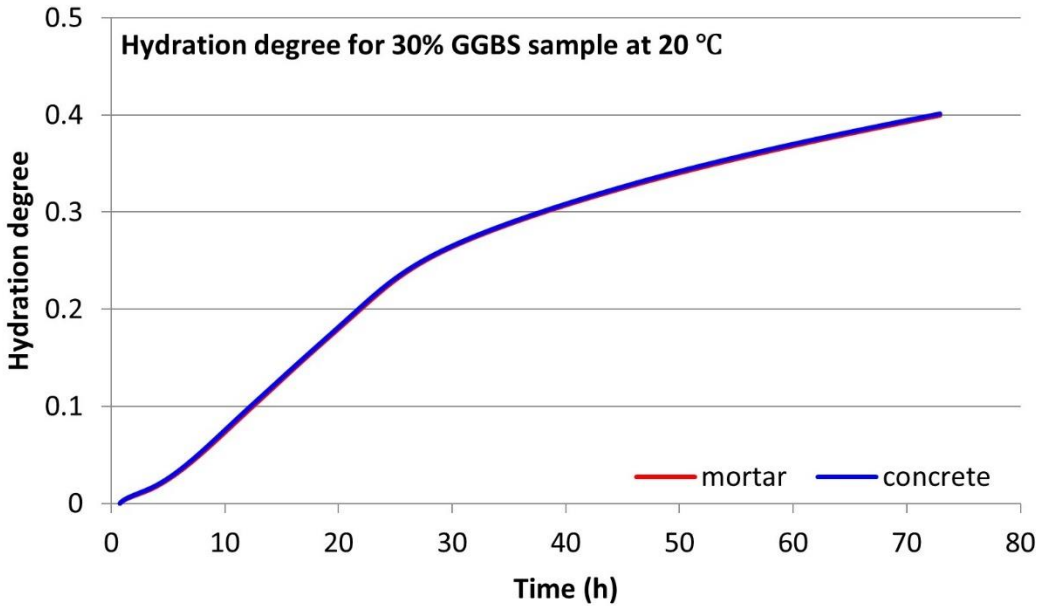

(c)

Figure A.4. Isothermal calorimetry test for 30% GGBS sample: (a) Normalized hydration heat flow; (b) Normalized hydration heat; (c) Hydration degree.

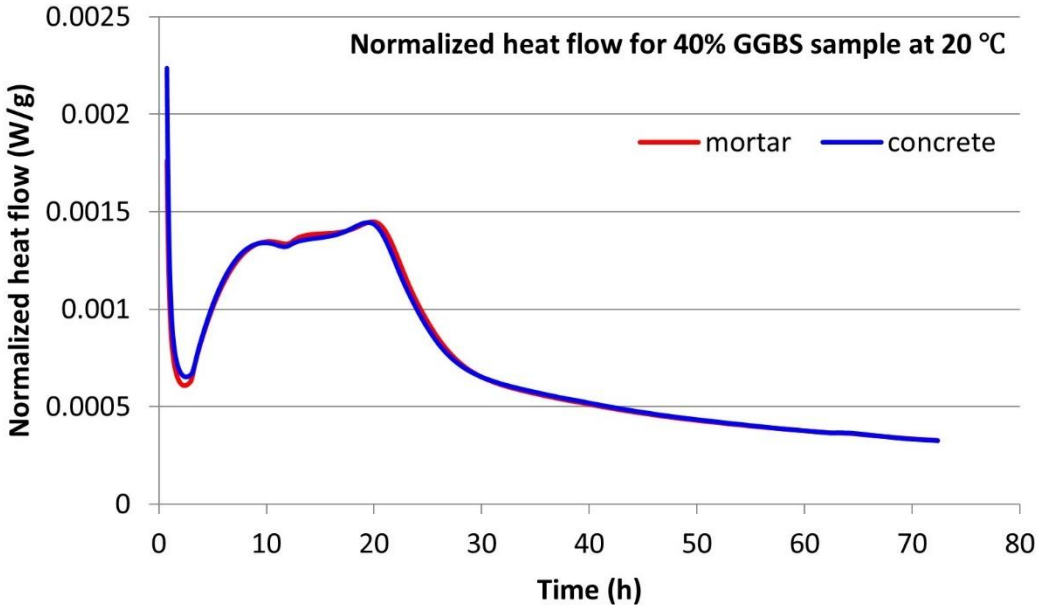
Normalized heat flow for 40% GGBS sample at 20 ℃
Normalized heat flow (W/g)
0.0025
0.002
0.0015
0.001
0.0005
0
mortar
concrete
0
10
20
30
40
50
60
70
80
Time (h)

(a)

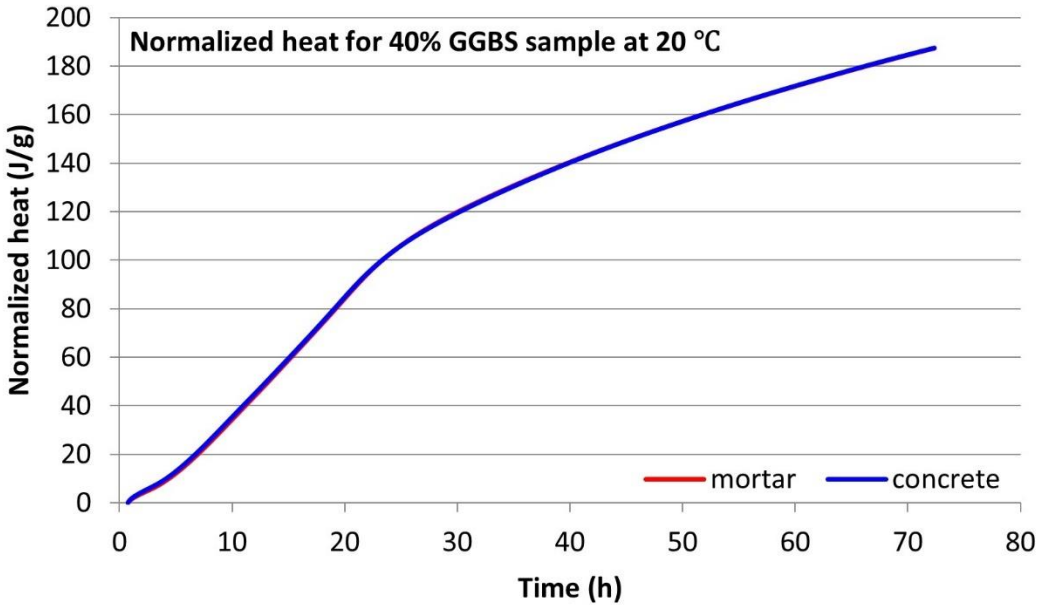
Normalized heat for 40% GGBS sample at 20 ℃
Normalized heat (J/g)
200
180
160
140
120
100
80
60
40
20
0
mortar
concrete
0
10
20
30
40
50
60
70
80
Time (h)

(b)

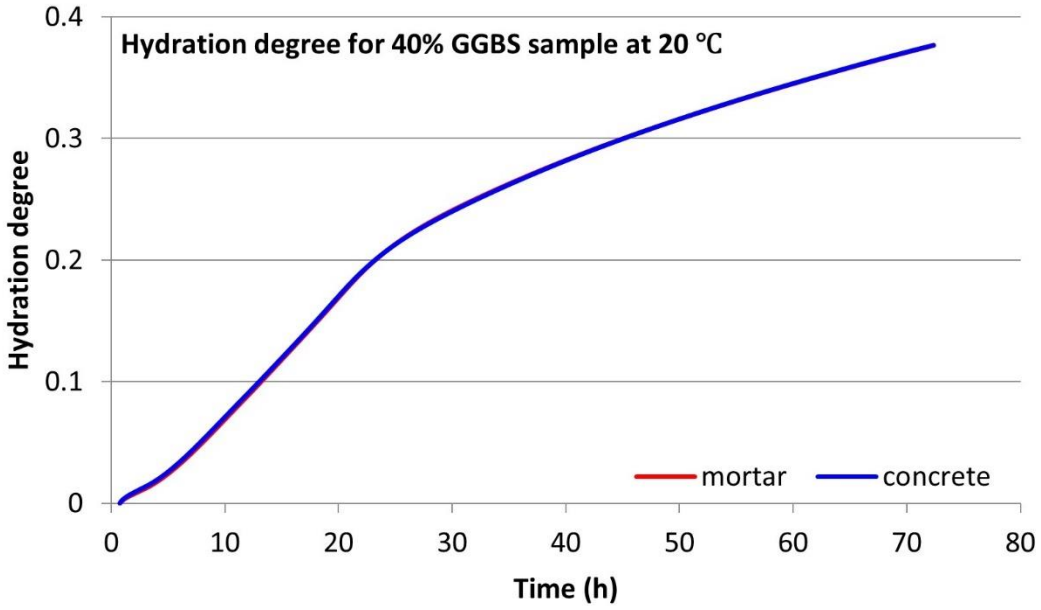

(c)

Figure A.5. Isothermal calorimetry test for 40% GGBS sample: (a) Normalized hydration heat flow; (b) Normalized hydration heat; (c) Hydration degree.

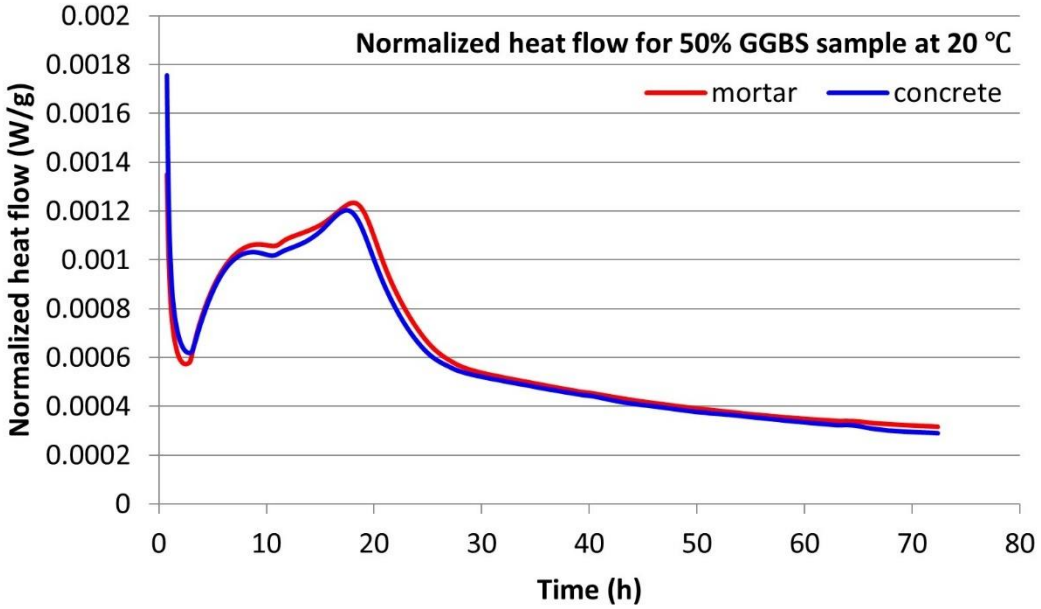

(a)

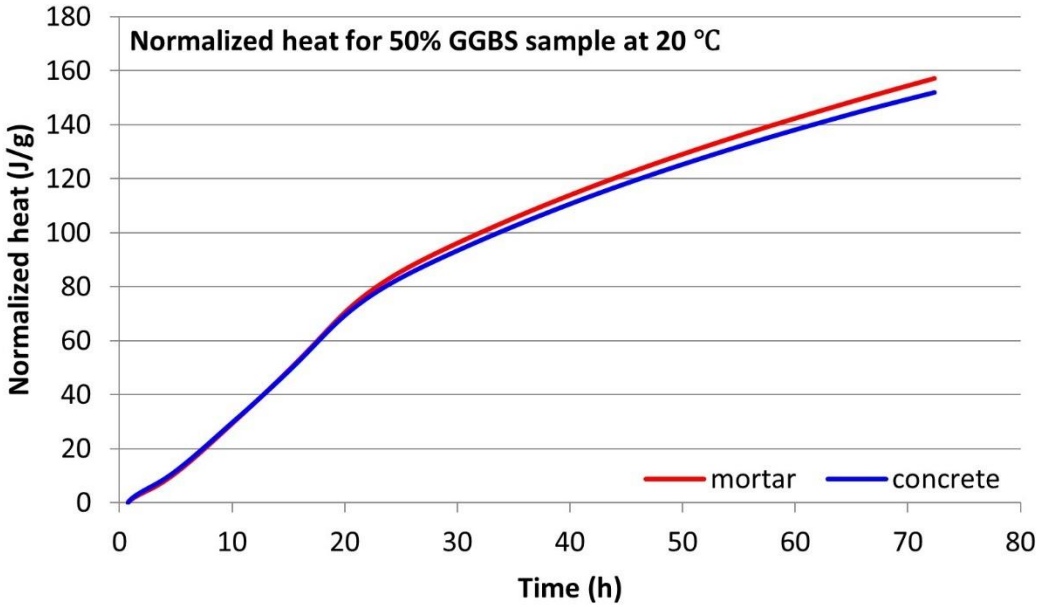

(b)

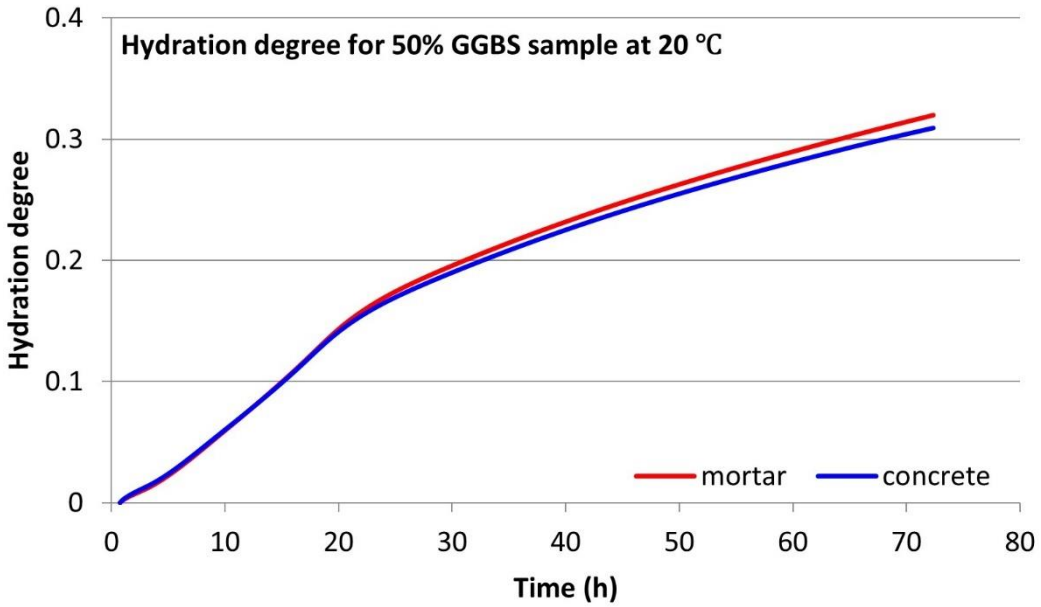

(c)

Figure A.6. Isothermal calorimetry test for 50% GGBS sample: (a) Normalized hydration heat flow; (b) Normalized hydration heat; (c) Hydration degree.

APPENDIX B Linear Regression Analysis for the Calculation of Apparent Activation Energy

This section presents the linear regression results (between $\ln(Q_{max})$ and $1/T_{abs}$) used to calculate the apparent activation energy of the samples based on isothermal calorimetry data, as discussed in Section 6.4.3. These results are included here to provide a detailed account of the regression analysis process and its outcomes.

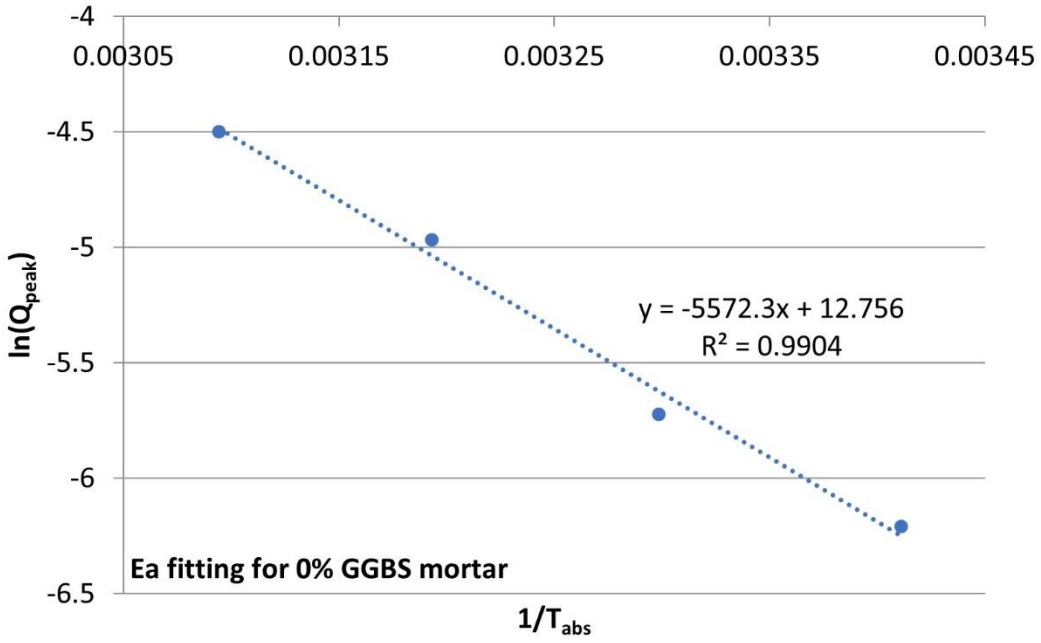

(a)

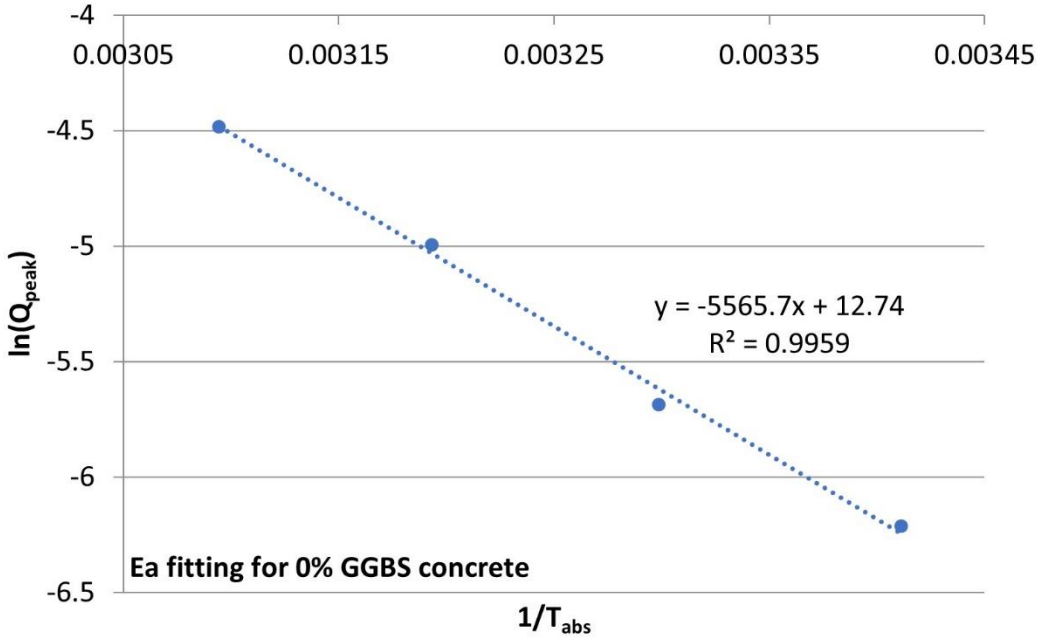

(b)

Figure B.1. Liner regression results between $\ln(Q_{max})$ and $1/T_{abs}$: (a) 0% GGBS mortar; (b) 0% GGBS concrete.

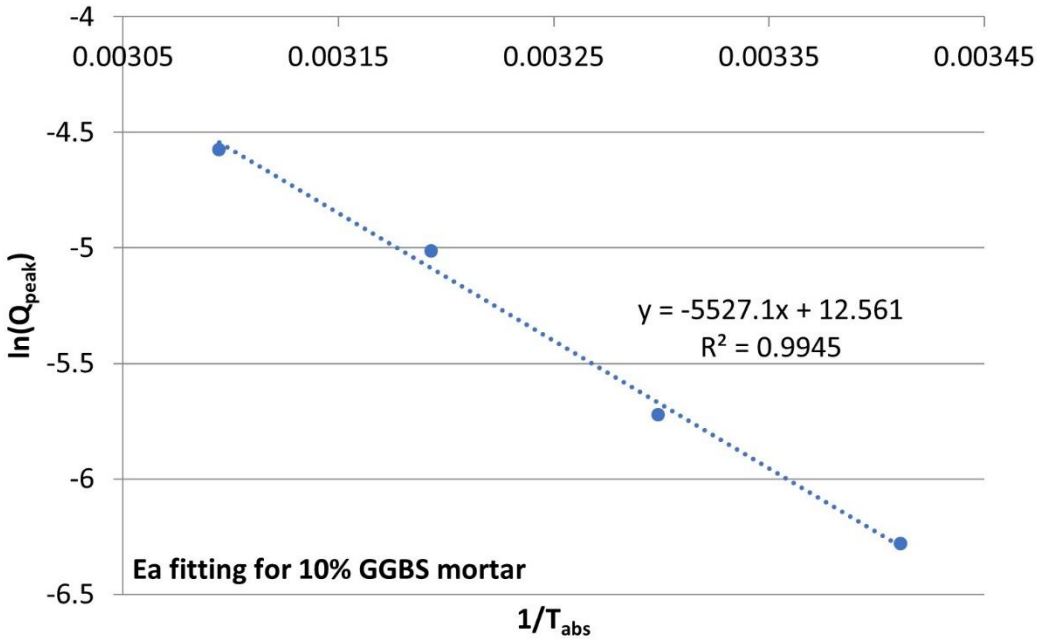

(a)

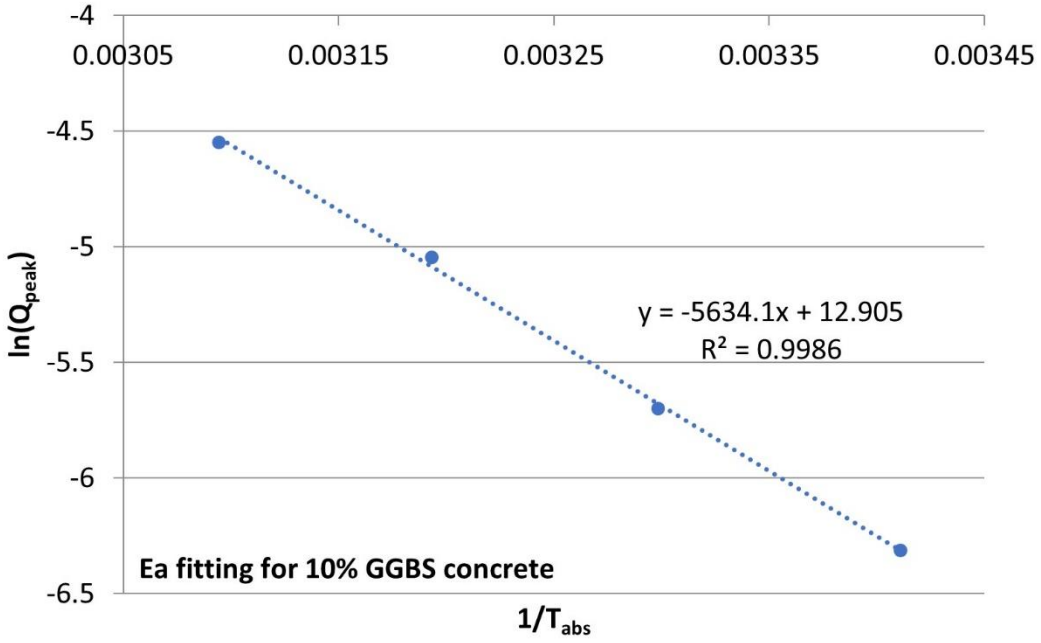

(b)

Figure B.2. Liner regression results between $\ln(Q_{max})$ and $1/T_{abs}$: (a) 10% GGBS mortar; (b) 10% GGBS concrete.

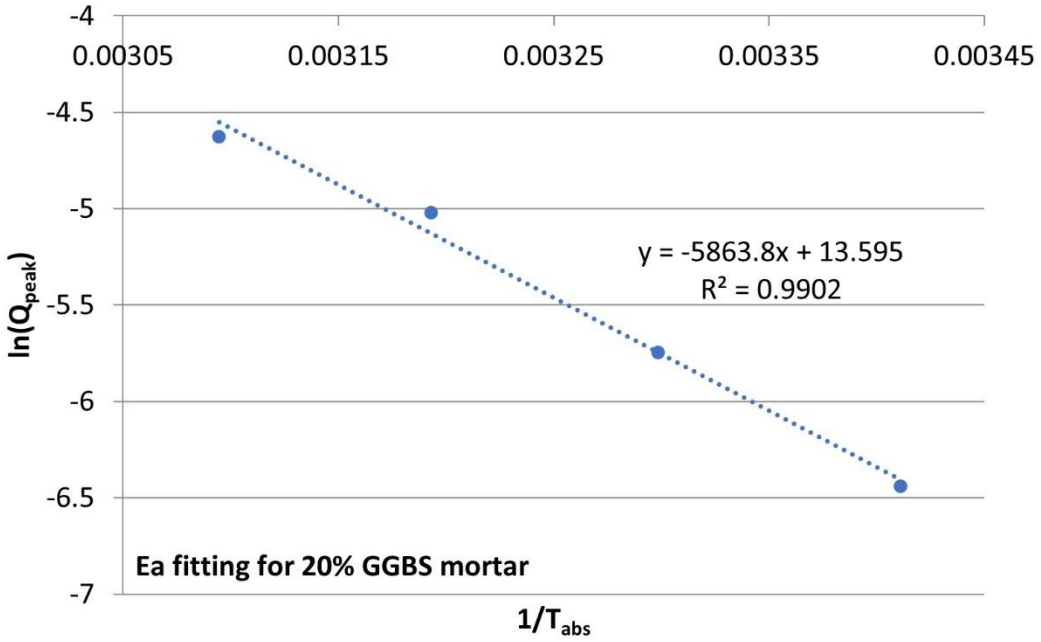

(a)

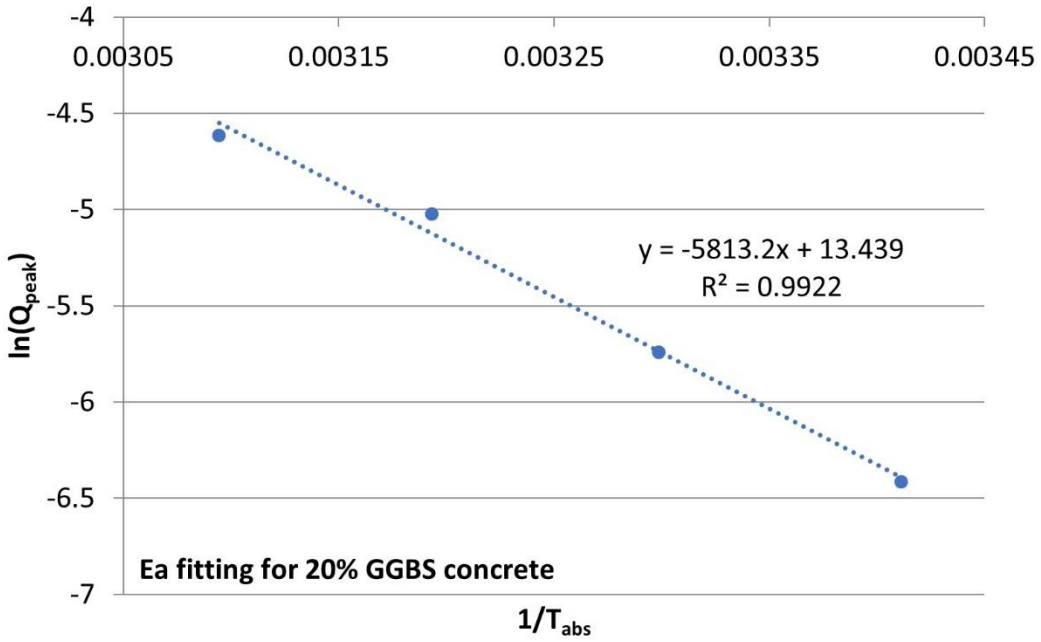

(b)

Figure B.3. Liner regression results between $\ln(Q_{max})$ and $1/T_{abs}$: (a) 20% GGBS mortar; (b) 20% GGBS concrete.

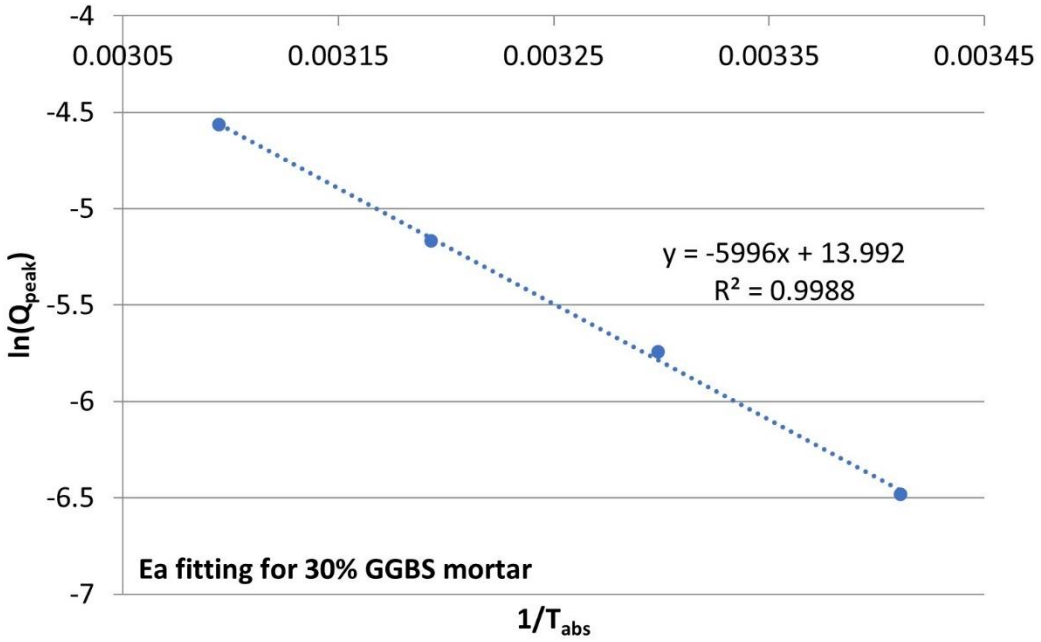

(a)

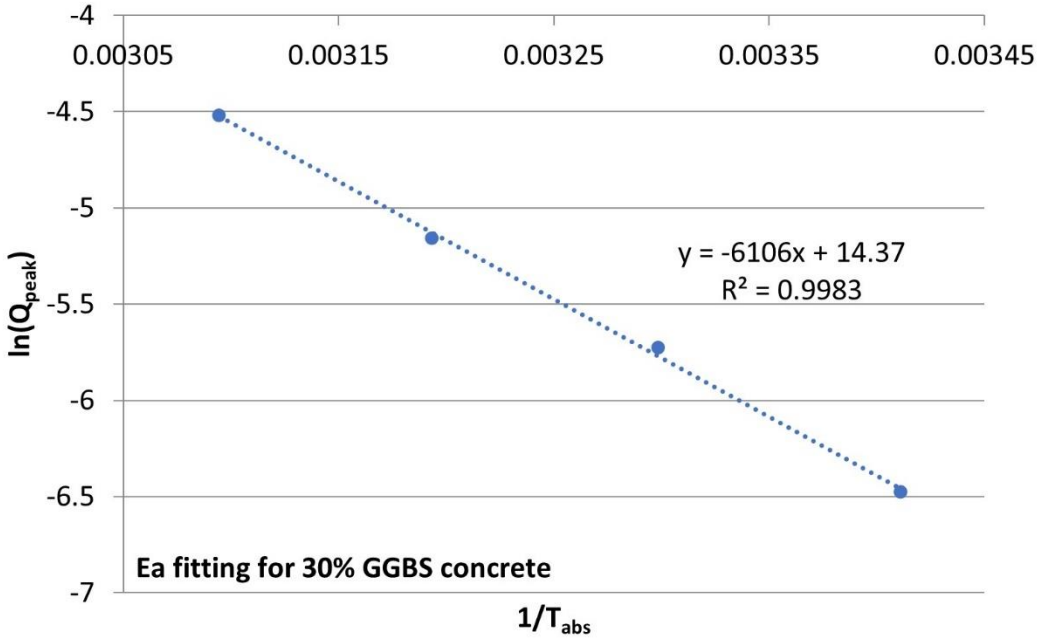

(b)

Figure B.4. Liner regression results between $\ln(Q_{max})$ and $1/T_{abs}$: (a) 30% GGBS mortar; (b) 30% GGBS concrete.

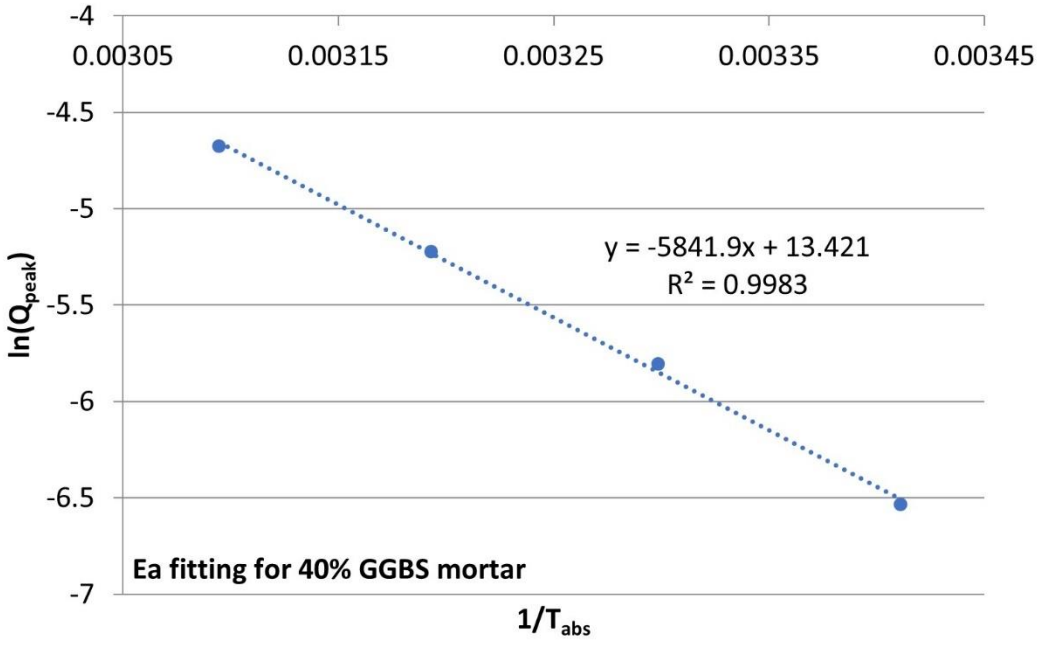

(a)

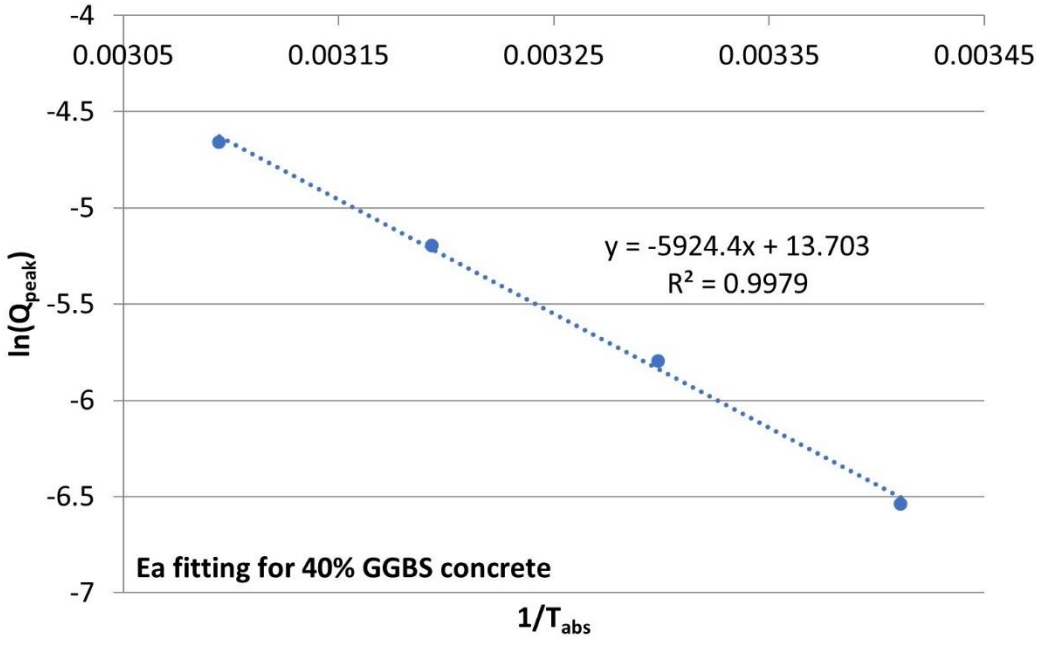

(b)

Figure B.5. Liner regression results between $\ln(Q_{max})$ and $1/T_{abs}$: (a) 40% GGBS mortar; (b) 40% GGBS concrete.

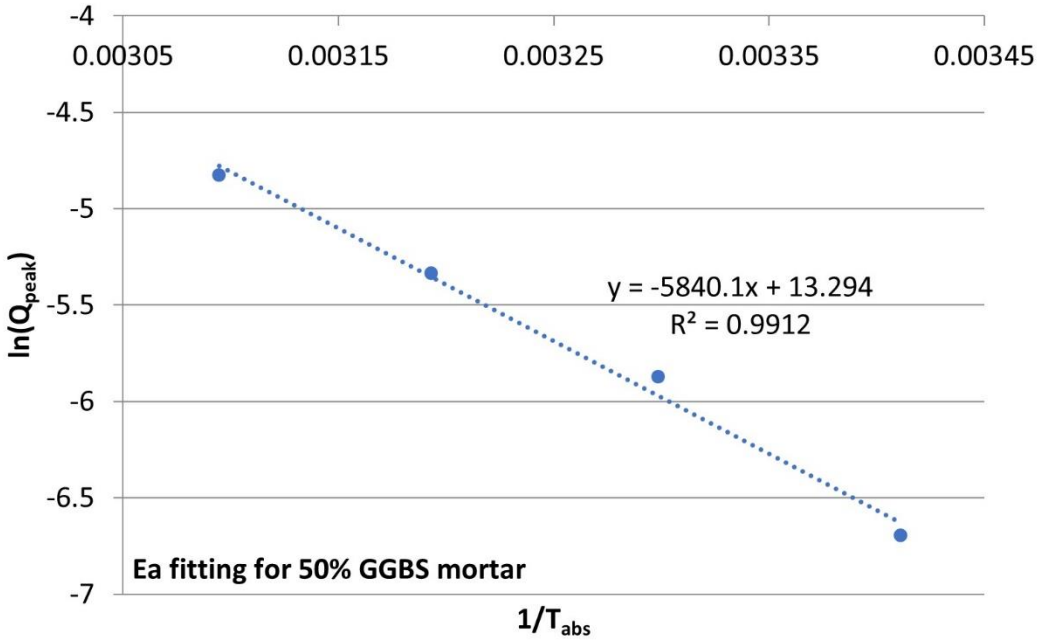

(a)

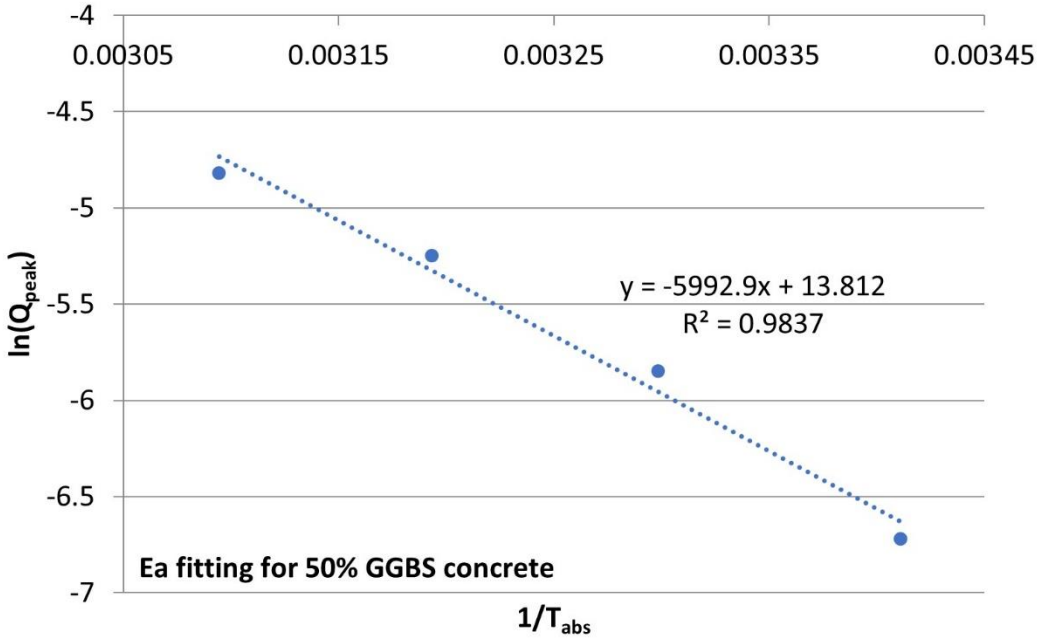

(b)

Figure B.6. Liner regression results between $\ln(Q_{max})$ and $1/T_{abs}$: (a) 50% GGBS mortar; (b) 50% GGBS concrete.